This item was submitted to Loughborough's Research Repository by the author.
Items in Figshare are protected by copyright, with all rights reserved, unless otherwise indicated.

Dynamic interfacial fracture

PLEASE CITE THE PUBLISHED VERSION

PUBLISHER

Loughborough University

LICENCE

CC BY-NC-ND 4.0

REPOSITORY RECORD

Chen, Tianyu. 2021. “Dynamic Interfacial Fracture”. Loughborough University. https://doi.org/10.26174/thesis.lboro.14332817.v1.

Dynamic interfacial fracture

by

Tianyu Chen

DOCTORAL THESIS

Submitted in partial fulfilment of the

requirements for the award of

Doctor of Philosophy

of Loughborough University

March 2021

© by Tianyu Chen 2021

Acknowledgements

I would like to express my sincere gratitude to my supervisors, Dr. Christopher Harvey and Prof. Vadim Silberschmidt. Pursuing a Ph.D. is challenging and sometimes with a few unforeseen frustrations, but the encouragement and patience from my supervisors always help and inspire me to do the best I could.

My gratitude also goes to Prof. Simon Wang and Prof. Gary Critchlow for their kind support through my study. Besides, I would like to thank the Department of Aeronautical and Automotive Engineering for funding my Ph.D. and the conference.

Finally, I would like to thank my parents for their unconditional support.

Abstract

Dynamic interfacial fracture is the branch of fracture mechanics that considers the fracture behaviour of structures with an interface under dynamic loads, such as laminated composites and adhesively bonded or welded structures. In this work, a new and completely analytical framework is developed to determine the dynamic energy release rate (ERR) of pure mode-I and -II fractures in double cantilever beam (DCB) and end-loaded split (ELS) specimens, respectively. For the first time, structural vibration and flexural-wave propagation are accounted for. It is shown that the effect of vibration on interfacial fracture behaviour is significant and cannot be neglected as it conventionally has been. The developed analytical framework is successfully used to study stationary and propagating cracks, cracks at non-rigid elastic interfaces, and to investigate the mode mixity by combining it with a quasi-static mode-partition theory.

The developed analytical framework is established based on the mode-I stationary crack of a DCB and the classical dynamic beam theory with time-dependent boundary conditions. The transverse motion is decomposed into a quasi-static one and a local vibration resulting in three ERR components due to the strain and kinetic energies of quasi-static motion, and the kinetic energy due to motion coupling. It is found that the conventional global approach accounting for the global energy balance method to determine the ERR cannot be used, as it results in non-physical divergence of the vibrating ERR amplitude with addition of more vibration modes. It is discovered that accounting for wave propagation and dispersion of flexural waves and considering the energy flux through a small crack-tip contour solves this divergence, leading to *dispersion-corrected global approach*. For a mode-I propagating crack, the ERR is derived by incorporating an energy-conservation condition and a correction for the Doppler effect. The crack-propagation behaviour and the limiting crack-propagation speed are thereby determined.

Building on this developed analytical framework, an elastic foundation is introduced to represent a crack at a non-rigid elastic interface. This boundary condition not only significantly improves the vibration-phase agreement between the analytical theory and results of the finite-element-method (FEM) simulations but also allows a study of the relationship between dynamic effects and foundation stiffness. For the dynamic mode-II interfacial fracture in an ELS specimen, the dynamic ERR is derived using the vibrating crack-tip loads. It is found that the *i*th modal contribution is dependent on the ratio of the crack length to the total length of the ELS specimen and that for a given ratio, there is a vibration mode with a zero contribution to the ERR.

The developed theory is verified against the results of the FEM simulations and experiments and is in excellent agreement for all the cases considered. The resulting analytical expressions are relatively short, mathematically elegant, physically understandable and convenient-to-use by engineers and researchers. The developed analytical framework provides a detailed physical understanding of dynamic interfacial fracture behaviour. Among other potential uses, it can be employed to predict the extent of interfacial fracture in a dynamically-loaded structure, to post-process the test data on high-loading-rate fracture to determine the loading-rate-dependent interfacial fracture toughness for crack initiation and propagation, and potentially provides solutions for the verification of numerical software.

List of publications

Journal papers

1. T. Chen, C. M. Harvey, S. Wang, and V. V. Silberschmidt, "Dynamic interfacial fracture of a double cantilever beam," *Eng. Fract. Mech.*, vol. 225, p106246, 2020.

2. T. Chen, C. M. Harvey, S. Wang, and V. V. Silberschmidt, "Dynamic delamination on elastic interface," *Compos. Struct.*, vol. 234, p.111670, 2020.

3. T. Chen, C. M. Harvey, S. Wang, and V. V. Silberschmidt, "Delamination propagation under high loading rate," *Compos. Struct.*, vol. 253, p112734, 2020.

4. T. Chen, C. M. Harvey, S. Wang, and V. V. Silberschmidt, "Theory of dynamic mode-II delamination in end-loaded split tests", *Compos. Part C*, vol. 3, p100055, 2020.

Conference presentations and proceedings

1. T. Chen, C. M. Harvey, S. Wang, and V. V. Silberschmidt, "Dynamic interfacial fracture of a thin-layered structure," *Procedia Struct. Integr.*, vol. 13, p613-618, 2018, in 22nd European Conference on Fracture (Serbia, 2018).

2. T. Chen, C. M. Harvey, S. Wang, and V. V. Silberschmidt, "Dynamic interfacial fracture of layered material structures," in 5th International Conference on Mechanics of Composites (Portugal, 2019).

3. T. Chen, C. M. Harvey, S. Wang, and V. V. Silberschmidt, "Dynamic interfacial fracture with higher-order vibration modes," in 3rd International Conference on Advanced Materials & Engineering Applications (China, 2019).

4. T. Chen, C. M. Harvey, S. Wang, and V. V. Silberschmidt, "High-speed mode-I delamination," *Proceedings of the Third International Conference on Theoretical, Applied and Experimental Mechanics* (Greece, 2020).

Table of contents

Acknowledgements .... **ii**

Abstract .... **iii**

List of publications .... **v**

Table of contents .... **vi**

List of figures .... **x**

List of tables .... **xvi**

Nomenclature .... **xvii**

Chapter 1: Introduction **1**

1.1 Background 1

1.2 Aim and objectives 4

1.3 Thesis structure 4

Chapter 2: Vibration and wave propagation **7**

2.1 Introduction 7

2.2 Vibration of beams 8

2.2.1 Equation of motion 9

2.2.2 Free vibration 10

2.2.3 Time-dependent boundary conditions 17

2.3 Wave propagation 19

2.3.1 Waves in 1D waveguides 19

2.3.2 Waves in infinite, semi-infinite and doubly-bounded media 24

2.4 Conclusion 28

Chapter 3: Key concepts of fracture mechanics **30**

3.1 Introduction 30

3.2 Linear-elastic fracture mechanics 30

3.2.1 Global energy balance 30

3.2.2 The Griffith theory and strain energy release rate 31

3.2.3 Stress intensity factor 32
3.2.4 The J-integral 34
3.2.5 Compliance method 35
3.2.6 Fracture mode mixity 38
3.3 Elastodynamic fracture mechanics 39
3.3.1 Dynamic stress intensity factor 39
3.3.2 Dynamic energy release rate 41
3.4 Conclusion 44

Chapter 4: Conventional dynamic interfacial fracture 46
4.1 Introduction 46
4.2 Conventional analytical approach to modelling dynamic interfacial fracture .. 47
4.2.1 Mode-I fracture 47
4.2.2 Mode-II fracture 51
4.3 Numerical method 53
4.3.1 Numerical methods for fracture mechanics 53
4.3.2 Numerical techniques for interfacial fracture mechanics 57
4.4 Conclusion 62

Chapter 5: Dynamic mode-I interfacial fracture for stationary crack 63
5.1 Introduction 63
5.2 Theoretical development with vibration 63
5.2.1 Dynamic response of thin beam 64
5.2.2 Dynamic energy release rate and amplitude divergence 68
5.2.3 Dynamic factor 73
5.3 Theoretical development with wave propagation 75
5.3.1 ERR divergence and energy flux 75
5.3.2 Dynamic energy release rate 76
5.3.3 Simplified dynamic ERR with vibrational deflection 81
5.4 Numerical verification 85
5.4.1 Finite-element model and verification case 85
5.4.2 Verification for developed theory with vibration 86
5.4.3 Verification for developed theory with wave propagation 88
5.5 Crack-tip-rotation compensation for stationary crack 90

5.5.1 Conventional method for compensation of crack-tip rotation 90
5.5.2 Crack-tip rotation compensation for DCB under dynamic loads 91
5.6 Conclusion 95

Chapter 6: Propagation of dynamic mode-I interfacial crack 97
6.1 Introduction 97
6.2 Theoretical development 98
6.2.1 Analytical theory for constant fracture toughness 98
6.2.2 Analytical theory for rate-dependent fracture toughness 99
6.3 Experimental verification 108
6.4 Numerical verification 112
6.4.1 Verification for developed theory for constant fracture toughness 112
6.4.2 Verification for developed theory for rate-dependent fracture toughness 114
6.5 Crack-propagation speed assessment and dynamic ERR 116
6.6 Crack-tip-rotation compensation for propagating crack 119
6.7 Conclusion 120

Chapter 7: Dynamic fracture on elastic interface 122
7.1 Introduction 122
7.2 Theoretical development for stationary crack 122
7.2.1 Dynamic response of beam on elastic foundation 124
7.2.2 Energy stored in the beam on elastic foundation 133
7.2.3 Dynamic energy release rate on elastic foundation 142
7.2.4 Dynamic factor 148
7.3 Numerical verification for stationary crack 150
7.3.1 Verification for rigid interface 151
7.3.2 Verification for non-rigid interface 154
7.3.3 Verification for fracture mode mixity 156
7.4 Theoretical development for propagating crack 157
7.5 Numerical verification for propagating crack 159
7.6 Relation between foundation stiffness and effective crack length 162
7.7 Conclusion 164

Chapter 8: Dynamic mode-II interfacial fracture 166
8.1 Introduction 166

8.2 Theoretical development 167

8.2.1 Dynamic response of ELS specimen 168

8.2.2 Dynamic energy release rate for ELS specimen 176

8.2.3 Dynamic factor 178

8.2.4 Normal modes and crack-tip loading condition 180

8.2.5 *i*th vibration modal contribution to ERR 182

8.3 Numerical verification 184

8.3.1 Verification for isotropic bi-layer composite 184

8.3.2 Verification for orthotropic fibre-reinforced composite 187

8.4 Conclusion 190

Chapter 9: Conclusions and future work 191

9.1 Conclusions 191

9.2 Future work 193

References 195

Appendix A: Formulas for integrals for mode shapes 211

Appendix B: DCB FEM model 212

List of figures

Figure 1.1 (a) Schematic diagram of building-block design approach [4]; (b) fundamental engineering structures for investigation of fracture behaviour in CFRPs 2

Figure 1.2 One-dimensional fractures: (a) coating blister on aero-engine turbine blades [5]; (b) drilling-induced push-out delaminations [6]; (c) delamination of CFRP under impact [7]; (d) Spallation of a thin layer [8]; (e) delamination in wind turbine blade [9] 3

Figure 2.1 (a) Beam on elastic foundation; (b) infinitesimal element for deriving the equation of motion 9

Figure 2.2 First three mode shapes for beams with fixed-pinned boundary conditions . 14

Figure 2.3 First three mode shapes for beams with fixed-fixed boundary conditions.... 15

Figure 2.4 First three mode shapes for beams with pinned-pinned boundary conditions 16

Figure 2.5 Phase speed and group speed of 1D propagating wave................................ 21

Figure 2.6 Illustration for (a) non-dispersive waves; (b) dispersive waves.................... 23

Figure 2.7 Lamb wave modes: (a) symmetric mode; (b) asymmetric modes................. 26

Figure 2.8 Wave speed dispersion for Lamb waves [32] 27

Figure 2.9 Comparison of dispersion relation for axial, flexural, Lamb waves [33]...... 28

Figure 3.1 Three basic fracture modes: (a) opening (mode-I); (b) in-plane shear or sliding (mode-II); (c) out-of-plane shear or tearing (mode-III)... 33

Figure 3.2 Crack-tip contour Ω for J-integral 34

Figure 3.3 Specimen configurations: (a) DCB; (b) ELS; (c) ENF 36

Figure 3.4 Semi-infinite crack problem: (a) crack under sudden pressure with the magnitude of σ, (b) wavefronts generated by suddenly applied pressure, solid lines for dilatational wave and dashed line for shear waves 40

Figure 3.5 Crack-tip contour for determination of energy flux integral 42

Figure 4.1 Typical external load versus time curves for PEEK/carbon-fibre composite DCB tests conducted at a constant opening rate of (a) 3.3×10^{-5} m s^{-1}, (b) 1×10^{-2} m s^{-1}, (c) 5×10^{-1} m s^{-1}, (d) 2 m s^{-1} [19] 49

Figure 4.2 Normalised kinetic-energy contribution to ERR versus crack length ratio... 52

Figure 4.3 Configuration of CNF test specimen 53

Figure 4.4 SPH particle approximations in a 2D domain Ω with a surface S [107]....... 55

Figure 4.5 Quarter-point elements: (a) 8-noded quadrilateral element; (b) 6-noded triangular element 56

Figure 4.6 Enrichment scheme for XFEM: the circled nodes are enriched with discontinuous function and the squared nodes are enriched with crack-tip enrich functions 57

Figure 4.7 VCCT for 2D quadrilateral elements 58

Figure 4.8 Traction-separation laws 59

Figure 4.9 Comparison for an opening crack with (a) cohesive zone; (b) thick level set damage zone [148] 60

Figure 5.1 DCB configuration for stationary crack: (a) symmetric double cantilever beam; (b) effective boundary condition and prescribed coordinates 64

Figure 5.2 Velocity distribution along the DCB arm for the crack region due to applied opening velocity 66

Figure 5.3 Dynamic factor versus characteristic time 74

Figure 5.4 Crack-tip contour Ω for DCB to determine ERR component due to vibration 77

Figure 5.5 Evolution of the relative ERR difference between local and global methods with *n* 83

Figure 5.6 DCB geometry for FEM verification 85

Figure 5.7 (a) ERR solution with element size of 0.1 mm; (b) element size convergence 86

Figure 5.8 Comparison of ERR from results of FEM simulation (grey line) and from the developed analytical theory (black line) using global approach with first (a) and first two (b) vibration modes 86

Figure 5.9 Illustration of crack-tip rotation: (a) no crack-tip rotation under effective boundary condition; (b) crack-tip rotation in 2D FEM model 87

Figure 5.10 Regression of ERR from results of developed analytical theory against FEM simulation using global approach with first (a) and first two (b) vibration modes 88

Figure 5.11 Comparison of ERR from results of FEM simulation (grey line) and from the developed analytical theory (black line) using dispersion-corrected global approach with first (a) and first five (b) vibration modes 88

Figure 5.12 Regression of ERR from results of developed analytical theory against FEM simulation using dispersion-corrected global approach with first (a) and first five (b) vibration modes 89

Figure 5.13 Regression analysis of cube root of compliance with respect to crack length from quasi-static FEM simulation 92

Figure 5.14 Implementation of Δ for compensation of crack-tip rotation: (a) by effective crack length a_{eff}; (b) by effective flexural modulus E_{eff} 92

Figure 5.15 Regression of ERR from results of developed analytical theory against FEM simulation with Δ implemented by (a) by effective crack length a_{eff}; (b) by effective flexural modulus E_{eff} 93

Figure 5.16 Dynamic ERR for stationary crack versus time results from developed theory with effective crack length (black line) and from FEM (grey line) with increasing numbers of vibration modes 94

Figure 5.17 Regression values for slope and R^2 with increasing numbers of vibration modes 95

Figure 6.1 DCB configuration for propagating crack: (a) symmetric DCB; (b) effective boundary conditions and prescribed coordinates 100

Figure 6.2 Crack propagation from a_1 to a_2 over the time interval Δt 101

Figure 6.3 Effect of aspect ratio on limiting crack-propagation speed for various Poisson's ratios 104

Figure 6.4 Comparison of experimentally measured crack-propagation speeds under various opening (loading) rates [19][20] against theoretically predicted limiting speed 106

Figure 6.5 Crack-propagation speeds regressed against aspect ratio: (a) PEEK/carbon-fibre composite and (b) epoxy/carbon-fibre composite 107

Figure 6.6 Evolution of dynamic ERR and crack length for 6.5 m s^{-1} loading rate based on experimentally observed crack-propagation speed 110

Figure 6.7 Evolution of dynamic ERR and crack length for 10 m s^{-1} loading rate based on experimentally observed crack-propagation speed 112

Figure 6.8 Comparison of crack extension obtained from FEM simulation and from the developed analytical theory for material with constant fracture toughness 113

Figure 6.9 Evolution of dynamic ERR and crack length for 6.5 m s^{-1} loading rate based on FEM results of crack-propagation speed 115

Figure 6.10 Evolution of dynamic ERR and crack length for 10 m s^{-1} loading rate based on FEM results of crack-propagation speed 116

Figure 6.11 Mean value of dynamic ERR and its range by three methods of assessing crack-propagation speed 117

Figure 6.12 Dynamic ERR versus crack-propagation speed for sample point t = 2.46 ms 118

Figure 7.1 (a) Symmetric double cantilever beam with $h = h_1 = h_2$; (b) thin-layer-on-thick-substrate configuration with $h_1 = h$ and $h_1 << h_2$ 122

Figure 7.2 Configuration of beam partially supported on elastic foundation and prescribed coordinates 123

Figure 7.3 Crack tip contour Ω for elastic interface to determine ERR component due to vibration 144

Figure 7.4 Normalised dynamic factor due to vibration first ten modes for rigid interface 149

Figure 7.5 Normalised dynamic factors due to vibration versus frequency for various foundation stiffness 150

Figure 7.6 (a) DCB geometry for FEM verification studies (1) and (2); (b) thin-layer-on-thick-substrate geometry for FEM verification study (3) 151

Figure 7.7 Dynamic ERR versus time results from developed theory (black line) and from FEM (grey line) with increasing numbers of vibration modes 153

Figure 7.8 Cohesive element size convergence 154

Figure 7.9 Dynamic ERR versus time results from developed theory (black line) and from FEM (grey line) with the first five vibration modes for different foundation stiffnesses 155

Figure 7.10 Results for (a) total dynamic ERR and (b) its fracture-mode I and fracture-mode II components versus time results from developed theory (black line) and from FEM (grey line). 157

Figure 7.11 Crack propagation from a_1 to a_2 over time interval Δt on elastic interface 158

Figure 7.12 Evolution of dynamic ERR and crack length for 6.5 m s^{-1} loading rate based on FEM results for crack-propagation speed using analytical solution for elastic foundation 161

Figure 7.13 Evolution of dynamic ERR and crack length for 10 m s^{-1} loading rate based on FEM results of crack-propagation speed using analytical solution for elastic foundation 162

Figure 7.14 Dynamic ERR using effective crack length: (a) MCC method; (b) elastic foundation solution 164

Figure 8.1 Configuration of ELS specimen and prescribed coordinates 167

Figure 8.2 Comparison of ERR components of ELS specimen 179

Figure 8.3 Typical value for the parameter Λ_i 179

Figure 8.4 Dynamic factor for the verification case in Section 8.3.1 180

Figure 8.5 Normalised normal modes and slopes for first three vibration modes 181

Figure 8.6 Spatial factor of *i*th vibration mode against crack-length ratio η 183

Figure 8.7 ELS geometry for FEM verification 185

Figure 8.8 Dynamic ERR versus time results from developed theory (black line) and from FEM (grey line) with increasing numbers of vibration modes for an isotropic bi-layer composite 186

Figure 8.9 Dynamic ERR versus time results from developed theory (black line) and from FEM (grey line) with increasing numbers of vibration modes for an orthotropic fibre-reinforced composite 189

List of tables

Table 2.1 Conventional boundary conditions 12

Table 5.1 Boundary conditions for total deflection and its components 65

Table 5.2 Modal parameters for fixed-pinned beam in free vibration 67

Table 5.3 Correction factor for dispersion for stationary crack 79

Table 6.1 Correction factor for dispersion for propagating crack 102

Table 6.2 Experimental values of Δ for the PEEK/carbon-fibre composite 119

Table 7.1 Boundary conditions for the foundation-supported beam section 125

Table 7.2 Boundary conditions for the free beam section 125

Table 7.3 Continuity conditions for total deflection and its components 126

Table 7.4 Boundary conditions for normal modes 127

Table 7.5 Continuity conditions for normal modes 127

Table 7.6 Normalised dynamic factors due to vibration with various foundation stiffnesses 150

Table 7.7 Correction factor for dispersion for propagating crack 159

Table 8.1 Boundary conditions for beam section ① 169

Table 8.2 Boundary conditions for beam section ② 169

Table 8.3 Continuity conditions for total deflection and its components 170

Table 8.4 Boundary conditions for normal modes 171

Table 8.5 Continuity conditions for normal modes 171

Table 8.6 Orthotropic material properties of unidirectional T800H/3900-2 graphite/epoxy 188

Nomenclature

List of Symbols

a	crack length
$\dot{a}$	crack-propagation speed
a_{eff}	effective crack length
A	cross-section area
A_0	crack area
b	width of beams
c	wave speed
C	compliance
C_0	longitudinal wave speed
C_{d}	dilatational or irrotational wave speed
C_{g}	group speed
C_{g}^{i}	group speed of *i*th mode flexural wave
C_{p}	phase speed
C_{p}^{i}	phase speed of *i*th mode flexural wave
C_{R}	Rayleigh wave speed
C_{s}	shear or equivoluminal wave speed
E	Young’s modulus
E_{eff}	effective flexural modulus
E_{vib}	total energy density due to vibration
E_{vib}^{i}	energy density due to *i*th vibration mode
f_{dyn}	dynamic factor
f_{dyn}^{i}	dynamic factor of *i*th vibration mode
f_i, f_i'	correction factor for dispersion
f_{sp}^{i}	spatial factor of *i*th vibration mode
$f_{\mathrm{st}}^{\mathrm{K}}$	reduction factor for ERR component due to kinetic energy of quasi-static motion
$f_{\mathrm{st}}^{\mathrm{U}}$	reduction factor for ERR component due to strain energy of quasi-static motion
$F(x)$	shifting function
$F(\Omega)$	energy flux
$F_{\mathrm{vib}}(\Omega)$	energy flux due to vibration
$F_{\mathrm{vib}}^{i}(\Omega)$	energy flux of *i*th vibration mode
G	energy release rate
G_{c}	critical energy release rate or fracture toughness
G_{dyn}	ERR component accounting for total dynamic effect
$G_{\mathrm{dyn}}^{\mathrm{cp}}$	ERR component due to the coupling between local vibration and quasi-static motion
$G_{\mathrm{dyn}}^{\mathrm{loc}}$	ERR component due to local vibration

G_{vib}	ERR component due to vibration
G_{st}	ERR component due to quasi-static motion
G_{st}^{K}	ERR component due to kinetic energy of quasi-static motion
G_{st}^{U}	ERR component due to strain energy of quasi-static motion
h	thickness of beams
I	second moment of inertia
J	J-integral
k	foundation stiffness
K	kinetic energy/stress intensity factor
L	length of uncracked region/beam length
$M\left(x,t\right)$	bending moment
n	relative time scale
P	external force
P_{c}	external load at crack initiation
$Q\left(x,t\right)$	shear force
r	aspect ratio
S	strain energy stored in elastic foundation
t	time
$T_i\left(t\right)$	*i*th modal displacement
U	strain energy

v	applied loading rate
$w\left(x,t\right)$	deflection
$w_0\left(t\right)$	applied displacement
$w_{\text{fv}}\left(x,t\right)$	free-vibration component of deflection
W_{ext}	external work
$W_i\left(x\right)$	*i*th normal mode

Greek

α_i, β_i	wavenumber
γ_{p}	energy dissipation due to plastic deformation
γ_{s}	surface energy for brittle material
Γ	energy dissipation due to crack growth
δ_{ij}	Kronecker delta
Δ	Additional crack length for crack-tip rotation
η	crack-length ratio
ν	Poisson’s ratio
Π	total mechanical energy
Π_{vib}	mechanical energy component due to vibration
ρ	density

τ	characteristic time
$\phi_i(x)$	*i*th modal shape
φ_i	phase
ω_i	natural frequency

Abbreviations

CAT	crack-arrest toughness
CFRPs	carbon-fibre-reinforced plastics
CIT	crack-initiation toughness
CNF	centre notch flexural
CZM	cohesive zone modelling
DCB	double cantilever beam
EFGM	element-free Galerkin method
ERR	energy release rate
FEM	finite-element method
ITLSM	interfacial thick-level-set modelling
LEFM	linear elastic fracture mechanics
MCC	modified compliance calibration
MLS	moving least squares
PEEK	polyether ether ketone
PMMA	polymethyl methacrylate
SPH	smoothed particle hydrodynamics
SIF	stress intensity factor
VCCT	virtual-crack-closure technique
XFEM	extended-finite-element method

Superscripts

FD	quantity for foundation-supported beam section
FR	quantity for foundation-free beam section

Subscripts

cp	quantity due to coupling between local free vibration and quasi-static motion
I, II, III	fracture mode I, II, III
local	quantity due to local vibration
st	quantity due to quasi-static motion

Chapter 1: Introduction

1.1 Background

The aviation industry has experienced a fast-increasing application of carbon-fibre-reinforced plastics (CFRPs) for the last few decades. This trend is catering for the need to save weight and thus to reduce the fuel consumption thanks to CFRPs' superior properties in terms of their strength and stiffness-to-weight ratios over their metallic counterparts. The examples can be seen in Boeing 787, with more than 50% composite components saving 20% weight, and a CFRP central wing box in Airbus A380, saving 1.5 tons [1]. However, one of the major challenges associated with CFRPs is the prevention of interlaminar delamination, which is reckoned as the most critical damage [2]; it is caused by the interfacial weakness between composite plies. This is also usually the case for other laminated materials, for instance, fibre-metal laminates [3].

The successful prediction and prevention of delamination or interfacial fracture, in general, require an accurate evaluation of a crack-driving force and a crack-resisting force. In fracture mechanics, the former is investigated with the stress intensity factors (SIFs) (Sections 3.2.3 and 3.3.1) or the energy release rate (ERR) (Sections 3.2.2 and 3.3.2), while the latter is called *fracture toughness* or *critical ERR*. For engineering applications, however, the fracture phenomenon can be complicated due to the structural intricacies and complex loading conditions. A feasible and prevalent design guideline for composite structures is the building-block approach (see Figure 1.1a) [4], which studies the properties of composite structures from generic specimens (e.g. coupons), with increasing structural complexity, to non-generic specimens (e.g. a particular component). Fundamentally, the studies for coupon test specimens provide a general understanding in respective physical and mechanical aspects and also a method of determining material properties, which lays out the foundation for the whole design process. In the fracture aspect, the most fundamental engineering structures (Figure 1.1b) for the coupon test for composites in pure fracture modes are double cantilever beam (DCB), end-loaded split (ELS) and end-notched flexure (ENF) specimens, which are usually studied with beam theory (vibration of beam theory is revisited in Chapter 2). These fundamental structures isolate the fracture phenomena, allowing them to be studied without unnecessary interference from other unrelated components. They are therefore suitable for an advanced in-depth mechanical study or experimental test of fracture behaviours.

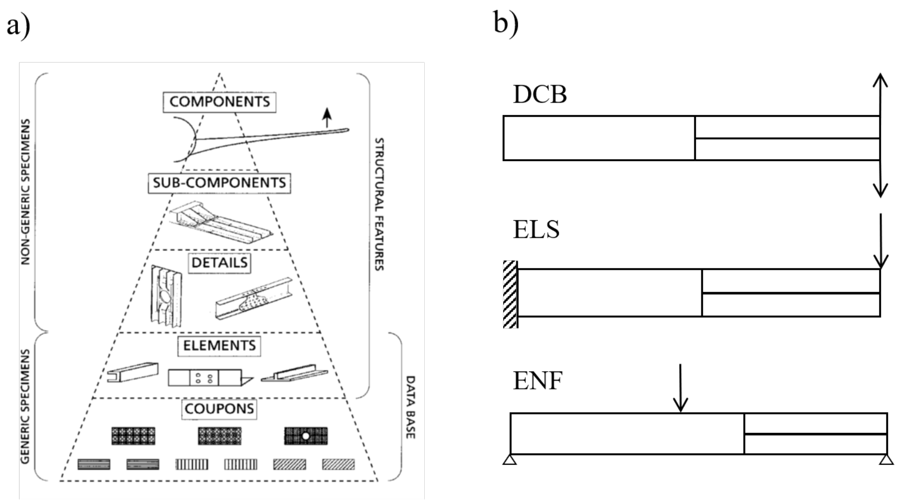

Figure 1.1 (a) Schematic diagram of building-block design approach [4]; (b) fundamental engineering structures for investigation of fracture behaviour in CFRPs

In addition, although the structures in Figure 1.1b are fundamental, they can also represent many real engineering structures (not limited to CFRP structures). For example, the DCB (the geometry of which may also be loaded in the ELS, ENF or otherwise mixed configuration) can represent the domain around a crack tip in a real beam structure with appropriate boundary conditions for the structure where the crack is embedded in. This also applies for narrow (plane-stress) or wide (plane-strain) plates with through-width cracks. In the former case, this can be used to model narrow cross-sectional segments in progressively propagating blisters [5] (Figure 1.2a), for example in telephone cord blisters, worm blisters and varicose blisters. An axisymmetric formulation of the DCB can represent a circular crack, which occurs in many engineering simulations, for example, drilling [6] (Figure 1.2b), impact [7] (Figure 1.2c), spallation of coatings [8] (Figure 1.2d), and even potentially biological cells under needle puncture. Moreover, the DCB as a layered structure can represent a composite laminate with two sub-laminates above and below a delamination, for example, delamination in a wind turbine blade [9] (Figure 1.2e), or a delamination between a stiffened stringer/plate assembly in aero structures.

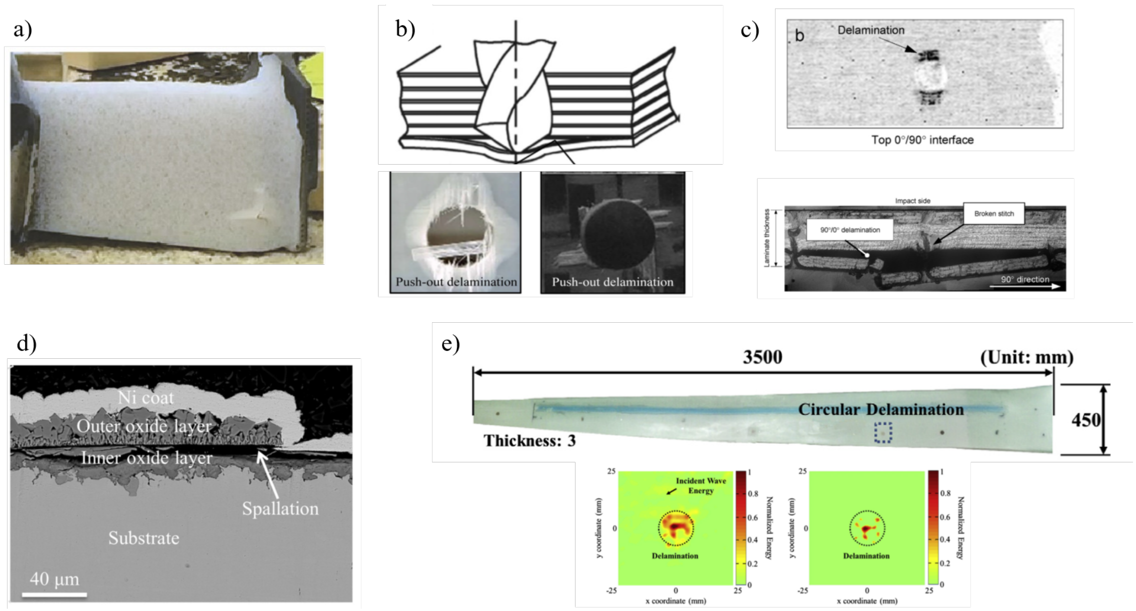
a)
b)
c)
b
Delamination
Top 0°/90° interface
Push-out delamination
Push-out delamination
Impact side
Broken stitch
90°/0° delamination
Laminate thickness
90° direction
d)
Ni coat
Outer oxide layer
Inner oxide layer
Spallation
Substrate
40 μm
e)
3500
(Unit: mm)
Circular Delamination
Thickness: 3
450
Incident Wave Energy
Delamination
Delamination
y coordinate (mm)
x coordinate (mm)
Normalized Energy

Figure 1.2 One-dimensional fractures: (a) coating blister on aero-engine turbine blades [5] Reproduced with permission from Yuan et al. , Theor. Appl. Mech. Lett., 8, 2018 © Elsevier; (b) drilling-induced push-out delaminations [6] Reproduced with permission from Deng et al. , Compos. Struct., 216, 2019 © Elsevier; (c) delamination of CFRP under impact [7] Reproduced with permission from Aymerich and Priolo, Int. J. Impact Eng., 35, 2008 © Elsevier; (d) Spallation of a thin layer [8] Reproduced with permission from Behnamian et al., J. Supercrit. Fluids, 119, 2017 © Elsevier; (e) delamination in wind turbine blade [9] Reproduced with permission from Park and Sohn, Compos. Sci. Technol, 100, 2014 © Elsevier

For a quasi-static loading regime, there were extensive investigations using these fundamental engineering structures – DCB, ELS and ENF configurations – to study fracture behaviours and assess the crack-driving force to measure the crack-resisting force with the fracture criteria; the respective standard testing methods were developed [10][11][12][13][14]. But in the dynamic loading regime, there were few investigations and, therefore, few methods of addressing the dynamic effect. Some studies extended the quasi-static analytical solutions to assess the dynamic fracture toughness, although the oscillating external load was well witnessed as one aspect of the dynamic effect, it was treated as noise, for example in [15][16]. Other investigations aimed at developing new analytical solutions accounting for the kinetic-energy contribution by including the quasi-static motion to study the dynamic effect; this was mostly done without considering structural vibration, with ‘smoothed’ ERR solutions obtained. Usually, the dynamic effect was found to be not significant and could be neglected in these studies, for instance, in

[17][18][19][20] (details in Section 4.2). Still, the oscillating ERR rather than the smoothed one was observed in experiments [21] and numerical simulations [22] due to structural vibration. Therefore, without account for vibration, the assessment of ERR may not be accurate or the fracture toughness measured correctly. Consequently, a new analytical framework is required to study the interfacial fracture under dynamic loads in the context of fundamental engineering structures (Figure 1.1b), i.e. dynamic interfacial fracture, and it is the aim of this thesis. It is referred to as a '*framework*' since the collection of techniques, in general, allows applications to new configurations and fracture phenomena.

1.2 Aim and objectives

This thesis aims to establish a new analytical framework with account for structural vibration and wave propagation to study the dynamic interfacial fracture behaviour in the context of fundamental engineering structures with pure fracture modes. To accomplish this aim, four objectives are suggested:

1. To develop a new analytical framework based on the mode-I stationary crack in DCBs with account for structural vibration and wave propagation to understand the dynamic effects associated with these two phenomena;

2. To develop analytical solutions for the mode-I propagating crack in DCBs based on the established analytical framework to study the dynamic effect in crack propagation;

3. To develop analytical solutions for dynamic interfacial fracture for non-rigid interfaces by introducing elastic foundation to the established analytical framework and to investigate the dynamic effects associated with the elastic interface;

4. To develop analytical solutions for dynamic mode-II fracture in ELS specimens based on the established analytical framework to investigate the dynamic effect in mode-II interfacial fracture.

1.3 Thesis structure

To achieve the aim and objectives, corresponding investigations were conducted and arranged into the following chapters.

Chapter 2 The essential background theories of dynamics are presented for structural vibration and wave propagation.

Chapter 3 The key concepts of fracture mechanics are revisited for both linear-elastic fracture mechanics (LEFM) and elastodynamic fracture mechanics.

Chapter 4 The conventional studies for dynamic interfacial fracture are reviewed. This includes the conventional analytical approach for interfacial fracture in pure fracture modes with account for quasi-static motion together with brief discussions of experimental findings and numerical methods for the interfacial fracture.

Chapter 5 The original work starts in this chapter. The new analytical framework is established for the dynamic mode-I stationary cracks in DCBs. The classical dynamic beam theory is used to solve the problem of the time-dependent boundary with decomposing the dynamic response into a quasi-static motion and a local free vibration. The ERR components are derived based on these two motions and their coupling. The global approach (Section 3.3.2.1) is used together with the consideration of structural vibration to derive the ERR, but the ERR amplitude is found to be divergent with addition of more vibration modes. A correction factor is introduced considering the wave propagation and dispersion to address this issue, and results of this *dispersion-corrected global approach* are verified and confirmed against results from FEM simulations.

Chapter 6 The established analytical framework in Chapter 5 is used to derive analytical solutions for the ERR of the mode-I propagating cracks in DCBs with further assumptions of energy-conservation and a modification due to the Doppler effect to solve the problem of moving boundary. A limiting crack-propagation speed is also proposed and studied. The analytical solutions are verified against the results from experiments as well as FEM simulations.

Chapter 7 The elastic foundation is introduced to the established analytical framework to study the dynamic interfacial fracture at a non-rigid elastic interface. The relation between the dynamic effect and the foundation stiffness is studied. The mode-mixity is also investigated by applying the quasi-static partition theory. The crack propagating on the elastic foundation is also studied by extending the analytical technique and the solution developed in Chapter 6. The analytical solutions are verified against the results from FEM simulations.

Chapter 8 The dynamic mode-II interfacial fracture is studied based on the established analytical framework for ELS specimens using crack-tip loads. The dynamic effects for these specimens are related to the crack-length ratio (the ratio between the crack length and the total ELS specimen’s length), and the crack-tip loading condition is studied with normal modes and their slopes; the dominant vibration mode is identified. The analytical solutions are verified against the results from FEM simulations.

Chapter 9 Conclusions are made according to the main findings, and some important future work is outlined.

The original work is in Chapter 5 to Chapter 8 with original theoretical developments serving each objective.

Chapter 2: Vibration and wave propagation

2.1 Introduction

The dynamic fracture studied in the context of fundamental engineering structures (Figure 1.1b) under dynamic loads, for example, suddenly applied displacement or impact, usually involves structural vibration as a direct observation. And this is the case when a bounded structure is subjected to dynamic loads, structural vibration will form in the long run. To study the vibration phenomenon, equation of motion (Section 2.2.1) is always derived first, which describes the dynamic behaviour of the given structures by providing the relation between forces – both external and inertial – and motions as a function of time. Two essential parameters for structural vibration are the natural frequency and normal modes (Section 2.2.2.2), and the total response of the structure is a superposition of these normal modes with respective modal displacement (Section 2.2.2.3). The main technique to solve the vibration problem is the method of separation of variables, which decomposes the total response into the time and the space domains. The derivation of equation of motion, conventional boundary conditions and method of separation of variables in this chapter can be found in classical book such as [23][24].

However, for transient response of the structure under dynamic loads, the structural vibration theory is not sufficient, since vibration as a standing wave needs time to form, and, therefore, the theory of wave propagation is required. This is also the case for unbounded structures, such as infinite plate, where the waves due to external excitation will propagate towards infinity without forming vibration. The most important parameters in wave propagation theory are the wave propagation speeds and their relation to the natural frequencies, which is essential to understand the characteristics of wave propagation, and this relation is referred to as dispersion.

The vibration and wave propagation theories are associated with the concept of standing waves. In wave propagation analysis, the wave equation shares the same expression of the equation of motion in vibration analysis. The generic solution using d'Alembert's method for the wave equation, for instance, Eq. (2.38), is

$$w(x,t) = f(x-ct) + g(x+ct), \tag{2.1}$$

where $f(x-ct)$ represents the disturbance travelling to the positive x direction and $g(x+ct)$ represents the disturbance travelling to the negative x direction. Unlike the wave propagation in unbounded structure, the wave will be reflected by the boundaries in the bounded structures. Therefore, the wave travelling to the positive *x* direction will be reflected to travel to the negative *x* direction when it arrives at the boundary; and wave travelling to the negative *x* direction will be reflected to travel to the positive *x* direction by the boundary. When these two reflected travelling waves meet under certain conditions, the superposition of these two waves can generate standing waves, and the structure begins to vibrate.

In this chapter, the vibration theory for the classical beam theory is briefly reviewed, including the derivation of the equation of motion, method of separation of variables to solve the free vibration and an approach to solve the time-dependent boundary conditions. Then, the theory of wave propagation in beams is covered with essential concepts, such as phase speed, group speed and dispersion. In addition, the wave propagation is also reviewed for the infinite media, also known as 3D elastodynamic problems, based on which, elastodynamic fracture mechanics is developed; the wave propagation in semi-infinite and doubly-bounded media are also revisited. The wave-propagation related concept in this chapter can be found in classical book such as [25][26].

2.2 Vibration of beams

Usually the fundamental engineering structures, such as DCB and ELS specimens, shown in Figure 1.1b are slender [11][14], where the thickness of beams are smaller than the other two dimensions, i.e. length and width, and, therefore, the classical Euler-Bernoulli beam theory applies, which ignores the rotational inertia and shear. But the notion should be given that the frequency predicted by Euler-Bernoulli beam theory is not correct for higher-order vibration modes, since the frequency goes to infinity with increasing mode numbers (see Figure 2.9 for flexural wave); instead, when the rotational inertia and shear are taken into account, i.e. in Timoshenko beam theory, there exists a cut-off frequency for higher-order vibration modes [27]. However, Euler-Bernoulli beam theory still applies when the lower-frequency vibration modes are dominant where the higher-frequency vibration modes can be ignored, and this is case found in Chapter 5.

Another aspect to note is that normally CFRPs are brittle without significant plastic deformation, and, in addition, the viscoelasticity is usually low (see Section 5.4.1), and, therefore, the material is assumed to be linearly elastic. Currently, in order to generate a fundamental understanding of the effects of structural vibration and wave propagation on dynamic fracture, small deflection is assumed, i.e. structural linearity, and this is also in accordance with conventional studies (see Section 4.2).

2.2.1 Equation of motion

Consider a beam resting on an elastic foundation with a constant foundation stiffness of k and subjected to a distributed force $f(x, t)$ as Figure 2.1a demonstrates. This configuration is a fundamental 1D structure for studying 1D fractures (for example Figure 1.2), which is used to carry out the investigation in the later chapters for theoretical development such as for DCB and ELS specimens; in addition, the elastic foundation can represent adhesives and allows the adhesively bonded structure under dynamic load to be studied, which also gives an advantage that the crack tip can rotate automatically (see Chapter 7). The thickness of the beam is h, width is b and the length is L. It is assumed that thickness is small compared to the length, where $h \ll L$, and the Euler-Bernoulli beam theory applies, that the effects of rotational inertia and shear are not significant and can be ignored.

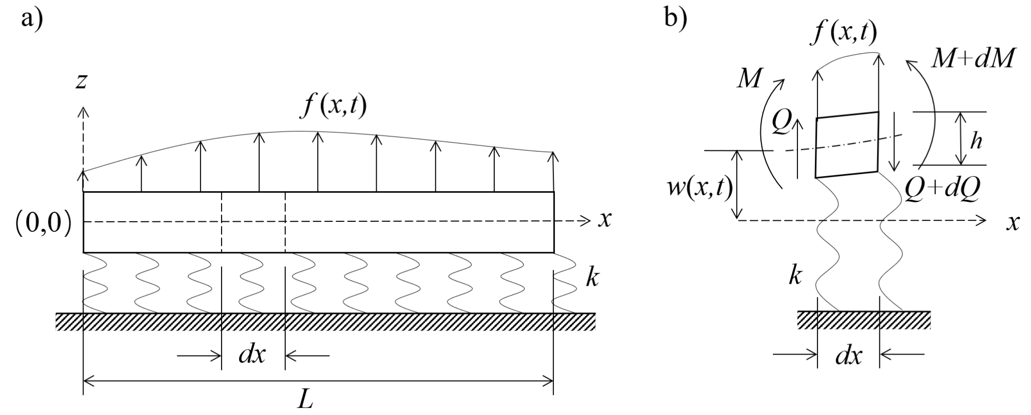

Figure 2.1 (a) Beam on elastic foundation; (b) infinitesimal element for deriving the equation of motion

An infinitesimal element of the beam with the length of dx is considered with its free-body diagram shown in Figure 2.1b, where $Q(x, t)$ is the shear force, $M(x, t)$ is the bending moment and $w(x, t)$ is the transverse deflection. The vertical dynamic force equilibrium can, therefore, be written as Eq. (2.2) with $\rho A dx \ddot{w}(x,t)$ being the transverse inertia force.

$$-(Q+dQ)+f(x,t)dx+Q-k\frac{1}{2}(w+w+dw)dx=\rho A dx\ddot{w}, \tag{2.2}$$

where ρ is the density and A is the area of the cross-section of the beam with $A = bh$. Since the rotational inertia is assumed to be small and negligible, the dynamic moment equilibrium about the y axis is

$$\left(M + dM\right) - \left(Q + dQ\right)dx + f\left(x,t\right)dx\frac{dx}{2} - k\frac{1}{2}\left(w + w + dw\right)dx\frac{dx}{2} - M = 0. \quad (2.3)$$

Combining Eqs. (2.2) and (2.3), together with the relation between the shear force and bending moment, that is, $Q\,(x, t) = M^{(1)}\,(x, t)$, and the relation between deflection and bending moment, that is, $M\,(x, t) = EIw^{(2)}\,(x, t)$, the equation of motion for the thin beam on elastic foundation with external applied distributed force $f\,(x, t)$ is derived:

$$EIw^{(4)}\left(x,t\right) + \rho A\ddot{w}\left(x,t\right) + kw\left(x,t\right) = f\left(x,t\right), \quad (2.4)$$

where I is the second moment of inertia with $I = bh^3/12$. Note that Lagrange's notation is used to represent the differentiation with respect to the x coordinate, and 'over-dot' notation is used to represent the differentiation with respect to time, and these notations are kept through the thesis.

With the absence of external force $f\,(x, t)$, Eq. (2.4) becomes the equation of motion for free vibration:

$$EIw^{(4)}\left(x,t\right) + \rho A\ddot{w}\left(x,t\right) + kw\left(x,t\right) = 0, \quad (2.5)$$

and for the free vibration of a free beam without the support from an elastic foundation, the equation of motion is

$$EIw^{(4)}\left(x,t\right) + \rho A\ddot{w}\left(x,t\right) = 0. \quad (2.6)$$

2.2.2 Free vibration

The general solution of the equation of motion for the free vibration, i.e. Eq. (2.6), is a linear combination of all the characteristic motions, which can be expressed by the separation of variables, and the transverse deflection of the free vibration is of the form as

$$w\left(x,t\right) = \sum_{i=1}^{\infty} W_i\left(x\right)T_i\left(t\right) \quad (2.7)$$

where $W_i\,(x)$ is the ith normal mode and $T_i\,(t)$ is a time-dependent function called the ith modal displacement.

Combining Eqs. (2.6) and (2.7), and introducing the *i*th mode natural frequency ω_i, and rearranging to have

$$\frac{EI}{\rho A}\frac{W_i^{(4)}(x)}{W_i(x)} = -\frac{\ddot{T}_i(t)}{T_i(t)} = \omega_i^2 . \tag{2.8}$$

Therefore, two governing equations for the normal mode and modal displacement are obtained:

$$W_i^{(4)}(x) - \beta_i^4 W_i(x) = 0 , \tag{2.9}$$

$$\ddot{T}_i(t) + \omega_i^2 T_i(t) = 0 , \tag{2.10}$$

where β_i is the *i*th mode wavenumber and is related to the natural frequency ω_i as

$$\beta_i^4 = \omega_i^2 \frac{\rho A}{EI} . \tag{2.11}$$

Note that the method of separation of variables decomposes the dynamic response of the beams into the space domain represented by normal mode and the time domain represented by modal displacement. The parameters link these two domains are the wavenumber β_i and natural frequency ω_i via Eq. (2.11).

The solution for normal modes depends on the boundary conditions. The conventional boundary conditions for the deflection and corresponding normal modes are given in Table 2.1.

Table 2.1 Conventional boundary conditions

Boundary condition	Mechanical interpretation	Free vibration	Normal mode
Free	Bending moment = 0	$EIw^{(2)}(0,t)=0$ or $EIw^{(2)}(L,t)=0$	$W_i^{(2)}(0)=0$ or $W_i^{(2)}(L)=0$
	Shear force = 0	$EIw^{(3)}(0,t)=0$ or $EIw^{(3)}(L,t)=0$	$W_i^{(3)}(0)=0$ or $W_i^{(3)}(L)=0$
Pinned (simply supported)	Deflection = 0	$w(0,t)=0$ or $w(L,t)=0$	$W_i(0)=0$ or $W_i(L)=0$
	Bending moment = 0	$EIw^{(2)}(0,t)=0$ or $EIw^{(2)}(L,t)=0$	$W_i^{(2)}(0)=0$ or $W_i^{(2)}(L)=0$
Fixed (clamped/built-in)	Deflection = 0	$w(0,t)=0$ or $w(L,t)=0$	$W_i(0)=0$ or $W_i(L)=0$
	Slope = 0	$w^{(1)}(0,t)=0$ or $w^{(1)}(L,t)=0$	$W_i^{(1)}(0)=0$ or $W_i^{(1)}(L)=0$

2.2.2.1 Orthogonality of normal modes

Orthogonality of normal modes is of great importance to determine normal modes and to understand the characteristics of the vibration. And it is derived as follows.

Multiplying Eq. (2.9) by $W_j(x)$ and integrating twice by parts over the beam length (0, L) to have

$$\begin{aligned}&\omega_i^2\int_0^L \rho A W_i(x)W_j(x)\,dx\\&=EI\left[W_j(x)W_i^{(3)}(x)\right]\Big|_0^L-EI\left[W_j^{(1)}(x)W_i^{(2)}(x)\right]\Big|_0^L+EI\int_0^L W_i^{(2)}(x)W_j^{(2)}(x)\,dx.\end{aligned}\tag{2.12}$$

With any combination of the conventional boundary conditions listed in Table 2.1, Eq. (2.12) simplifies to

$$\omega_i^2\int_0^L \rho A W_i(x)W_j(x)\,dx=EI\int_0^L W_i^{(2)}(x)W_j^{(2)}(x)\,dx.\tag{2.13}$$

Exchanging subscripts *i* and *j* in Eq. (2.13) and subtracting itself give

$$\left(\omega_i^2-\omega_j^2\right)\int_0^L \rho A W_i\left(x\right)W_j\left(x\right)dx=0. \tag{2.14}$$

The natural frequency is unique, that is, $\omega_i \neq \omega_j$ for $i \neq j$, and therefore

$$\int_0^L \rho A W_i\left(x\right)W_j\left(x\right)dx=0. \tag{2.15}$$

Now, including the case for $i = j$ and normalising Eq. (2.15), the orthogonality condition for the normal modes is

$$\int_0^L \rho A W_i\left(x\right)W_j\left(x\right)dx=\delta_{ij}. \tag{2.16}$$

Another form for the orthogonality can be derived by combining Eqs. (2.13) and (2.16) for $i \neq j$ as

$$\int_0^L W_i^{(2)}\left(x\right)W_j^{(2)}\left(x\right)dx=0. \tag{2.17}$$

2.2.2.2 Normal modes and frequency equation

Normal modes are the spatial distribution of a vibration. The normal modes are derived by solving the governing equation Eq. (2.9). The general solution of Eq. (2.9) takes the form of

$$W_i\left(x\right)=C_{i1}\cosh\left(\beta_i x\right)+C_{i2}\cos\left(\beta_i x\right)+C_{i3}\sinh\left(\beta_i x\right)+C_{i4}\sin\left(\beta_i x\right), \tag{2.18}$$

where C_{i1}, C_{i2}, C_{i3} and C_{i4} are coefficients to be determined by boundary conditions and orthogonality condition.

Fixed-pinned beam

For a beam with fixed-pinned boundary conditions, i.e. fixed at $x = 0$ and pinned at $x = L$, using the boundary conditions in Table 2.1 and solving Eq. (2.18) gives

$$\begin{bmatrix} 1 & 1 & 0 & 0 \\ 0 & 0 & 1 & 1 \\ \cosh\left(\beta_i L\right) & \cos\left(\beta_i L\right) & \sinh\left(\beta_i L\right) & \sin\left(\beta_i L\right) \\ \cosh\left(\beta_i L\right) & -\cos\left(\beta_i L\right) & \sinh\left(\beta_i L\right) & -\sin\left(\beta_i L\right) \end{bmatrix} \begin{pmatrix} C_{i1} \\ C_{i2} \\ C_{i3} \\ C_{i4} \end{pmatrix} = \begin{pmatrix} 0 \\ 0 \\ 0 \\ 0 \end{pmatrix}. \tag{2.19}$$

For the system of the linear equations above to have nonzero solutions, the determinant of the coefficient matrix should be zero, giving

$$\tanh\left(\lambda_i\right)-\tanh\left(\lambda_i\right)=0, \tag{2.20}$$

where $\lambda_i = \beta_i L$. And then the natural frequencies can thus be determined accordingly using Eq. (2.11), i.e. $\omega_i = \beta_i^2 \sqrt{EI/(\rho A)} = \lambda_i^2 L^{-2} \sqrt{EI/(\rho A)}$, and therefore, Eq. (2.20) is also referred to as the *frequency equation*.

Returning to the normal mode solution for fixed-pinned beams, with the boundary conditions applied, it can then be written as

$$W_i(x) = C_{i1}\phi_i(x), \tag{2.21}$$

where $\phi_i(x)$ is the mode shape given as

$$\phi_i(x) = \left[\cosh(\beta_i x) - \cos(\beta_i x)\right] - \sigma_i \left[\sinh(\beta_i x) - \sin(\beta_i x)\right], \tag{2.22}$$

with $\sigma_i = \left[\cosh(\lambda_i) - \cos(\lambda_i)\right] / \left[\sinh(\lambda_i) - \sin(\lambda_i)\right]$. And recall the orthogonality in Section 2.2.2.1, the coefficient C_{i1} can be derived by combining Eqs. (2.16) and (2.21) (Appendix A), and its solution is

$$C_{i1} = \frac{1}{\sqrt{\int_0^L \rho A \left[\phi_i(x)\right]^2 dx}} = \frac{1}{\sqrt{\rho A L}}. \tag{2.23}$$

The mode shapes for the first three vibration modes in Eq. (2.22) are shown in Figure 2.2.

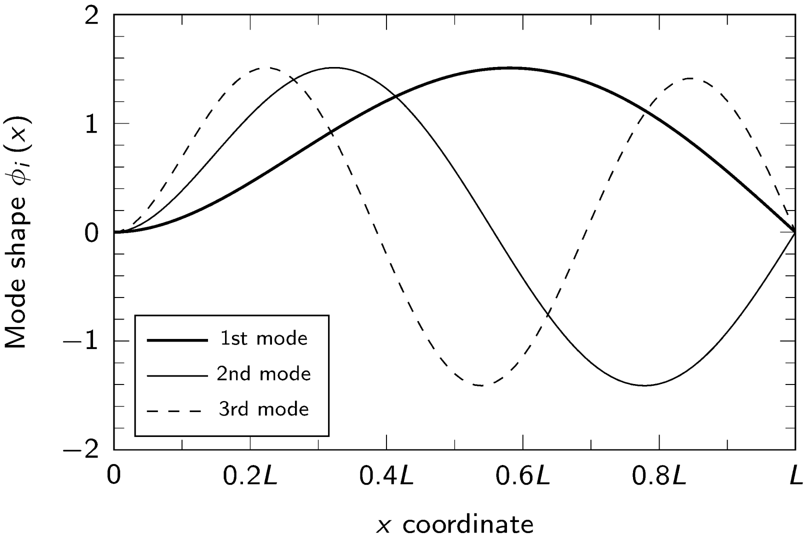

Figure 2.2 First three mode shapes for beams with fixed-pinned boundary conditions

Fixed-fixed beam

For another set of boundary conditions of fixed-fixed, solving the general solution for normal modes in Eq. (2.18) using corresponding boundary conditions in Table 2.1 gives

$$\begin{bmatrix} 1 & 1 & 0 & 0 \\ 0 & 0 & 1 & 1 \\ \cosh(\lambda_i) & \cos(\lambda_i) & \sinh(\lambda_i) & \sin(\lambda_i) \\ \sinh(\lambda_i) & -\sin(\lambda_i) & \cosh(\lambda_i) & \cos(\lambda_i) \end{bmatrix} \begin{pmatrix} C_{i1} \\ C_{i2} \\ C_{i3} \\ C_{i4} \end{pmatrix} = \begin{pmatrix} 0 \\ 0 \\ 0 \\ 0 \end{pmatrix}. \tag{2.24}$$

Therefore, the frequency equation for the beam with fixed-fixed boundary conditions can be derived by setting the determinant of the coefficient matrix of Eq. (2.24) to zero, giving

$$\cosh(\lambda_i)\cos(\lambda_i) - 1 = 0. \tag{2.25}$$

The mode shapes for the first three vibration modes for beams with fixed-fixed boundary conditions are shown in Figure 2.3.

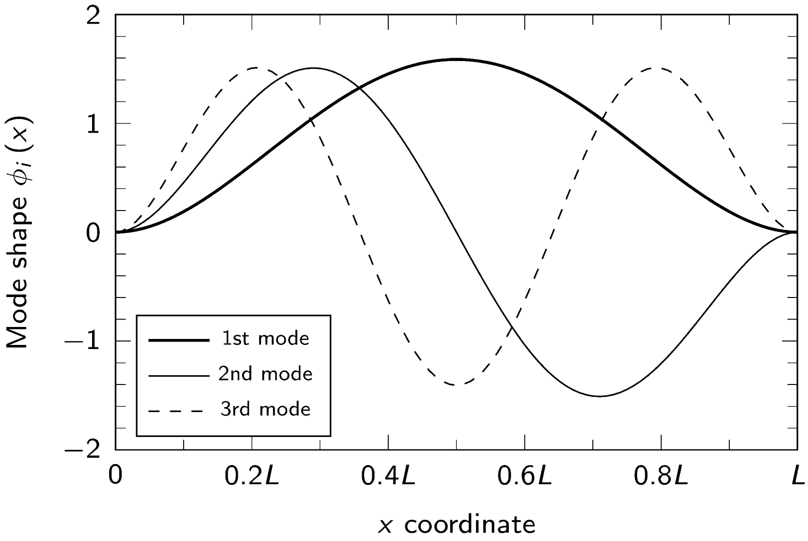

Figure 2.3 First three mode shapes for beams with fixed-fixed boundary conditions

Pinned-pinned beam

For beams with boundary conditions of pinned-pinned, solving the general solution for normal modes in Eq. (2.18) using corresponding boundary conditions in Table 2.1 gives

$$\begin{bmatrix} 1 & 1 & 0 & 0 \\ 1 & -1 & 0 & 0 \\ \cosh(\lambda_i) & \cos(\lambda_i) & \sinh(\lambda_i) & \sin(\lambda_i) \\ \cosh(\lambda_i) & -\cos(\lambda_i) & \sinh(\lambda_i) & -\sin(\lambda_i) \end{bmatrix} \begin{pmatrix} C_{i1} \\ C_{i2} \\ C_{i3} \\ C_{i4} \end{pmatrix} = \begin{pmatrix} 0 \\ 0 \\ 0 \\ 0 \end{pmatrix}. \qquad (2.26)$$

Therefore, the frequency equation for beams with pinned-pinned boundary conditions can be derived by setting the determinant of the coefficient matrix of Eq. (2.26) to zero, giving

$$\sin(\lambda_i) = 0. \qquad (2.27)$$

The mode shapes for the first three vibration modes for beams with pinned-pinned boundary conditions are shown in Figure 2.4.

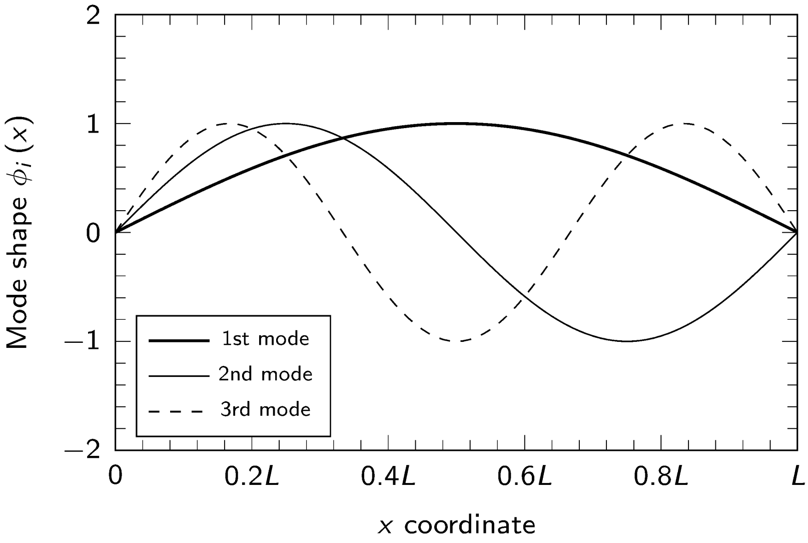

Figure 2.4 First three mode shapes for beams with pinned-pinned boundary conditions

2.2.2.3 Modal displacement

The general solution for the time-dependent modal displacement in Eq. (2.10) is

$$T_i(t) = T_i(0)\cos(\omega_i t) + \frac{\dot{T}_i(0)}{\omega_i}\sin(\omega_i t), \qquad (2.28)$$

where $T_i(0)$ and $\dot{T}_i(0)$ are the initial modal displacement and initial modal velocity for the *i*th vibration mode, respectively. The initial modal displacement and velocity are related to the initial conditions of the beam, and they can be determined in the following procedure.

The initial deflection of the beam according to Eq. (2.7) is

$$w(x,0)=\sum_{i=1}^{\infty}W_i(x)T_i(0). \tag{2.29}$$

Multiplying Eq. (2.29) by $\rho AW_j(x)$ and integrating over beam length (0, L) to have

$$\int_0^L \rho AW_j(x)w(x,0)\,dx=\int_0^L \rho AW_j(x)\sum_{i=1}^{\infty}W_i(x)T_i(0)\,dx. \tag{2.30}$$

Applying the orthogonality in Eq. (2.16) to Eq. (2.30), the initial modal displacement is found to be

$$T_i(0)=\int_0^L \rho AW_i(x)w(x,0)\,dx. \tag{2.31}$$

Following this procedure again, the initial modal velocity is

$$\dot{T}_i(0)=\int_0^L \rho AW_i(x)\dot{w}(x,0)\,dx. \tag{2.32}$$

2.2.3 Time-dependent boundary conditions

For dynamic case, such as suddenly applied displacement or impact, the boundary conditions can be time-dependent rather than the conventional boundary conditions listed in Table 2.1, and solving the vibration with time-dependent boundary conditions is essential to understand the dynamic response of the system and to further investigate the dynamic fracture associated.

Grant [28] introduced shifting functions and assumed that the total dynamic response (i.e. deflection) can be expressed by a combination of free-vibration component and quasi-static component determined by extrapolating the time-dependent boundary conditions via this shifting function along the beam. And corresponding equations of motion and boundary conditions for the free-vibration component and shifting function are obtained by enforcing homogeneous conditions, so that non-homogeneous boundary conditions are avoided, and instead the non-homogeneous (time-dependent) boundary conditions are converted to homogeneous boundary (conventional) conditions.

In [28], Grant provided an illustrative instance that a cantilever beam is subjected to a constant-accelerating displacement $w_0(t)=pt^2$ at its free end and the total deflection was assumed to be

$$w(x,t)=w_{\mathrm{fv}}(x,t)+F_1(x)pt^2+F_2(x)2pt+F_3(x)2p, \tag{2.33}$$

where $w_{\text{fv}}(x, t)$ is the free-vibration component, and $F_1(x)$, $F_2(x)$ and $F_3(x)$ are the shifting functions. Combining Eqs. (2.6) and (2.33), and enforcing homogeneous conditions, the equation of motion for the free-vibration component is found to be

$$EIw_{\text{fv}}^{(4)}\left(x,t\right)+\rho A\ddot{w}_{\text{fv}}\left(x,t\right)=0, \tag{2.34}$$

and system of differential equations for shifting functions are

$$\begin{cases} F_1^{(4)}\left(x\right)=0 \\ F_2^{(4)}\left(x\right)=0 \\ EIF_3^{(4)}\left(x\right)+\rho AF_1\left(x\right)=0 \end{cases}. \tag{2.35}$$

The corresponding boundary conditions can be derived from the deflection assumption in Eq. (2.33) and by enforcing homogeneous conditions, and thus the shifting functions can be solved as well as the free-vibration component as per Section 2.2.2. The only notion should be given to is the treatment of the initial modal displacement and velocity of the free-vibration component: they are determined by the initial displacement $w_{\text{fv}}\left(x,0\right)$ and initial velocity $\dot{w}_{\text{fv}}\left(x,0\right)$ by combining Eq. (2.33) and given as

$$w_{\text{fv}}\left(x,0\right)=w\left(x,0\right)-2F_3\left(x\right)p, \tag{2.36}$$

$$\dot{w}_{\text{fv}}\left(x,0\right)=\dot{w}\left(x,0\right)-2F_2\left(x\right)p. \tag{2.37}$$

Therefore, Grant's method is reckoned to convert the non-homogeneous boundary conditions to homogeneous boundary conditions by introducing shifting functions, and the function of these shifting functions is to distribute the applied displacement or velocity along the beam; and this distribution of the applied displacement and the velocity affects the free-vibration component through the initial modal displacement and velocity as Eqs. (2.31) and (2.32) suggest. By combining Eqs. (2.31), (2.32), (2.36) and (2.37), the modal displacement in Eq. (2.28) can be solved, and then according to Section 2.2.2, the free-vibration component.

2.3 Wave propagation

2.3.1 Waves in 1D waveguides

1D waveguides are the most fundamental waveguides in solid mechanics, such as rods, strings and beams, and relevant concepts important to understanding wave propagation are reviewed in the context of these 1D waveguides.

The analysis of wave propagation provides two essential relations, namely, spectrum relation and dispersion relation. The spectrum relation is the relation for wavenumber and natural frequency, and an example of this for flexural wave in beams is given in Eq. (2.11), i.e. $\beta_i^4 = \omega_i^2 \rho A / (EI)$. The dispersion relation indicates at what speed an excitation travels in the waveguides, and it is a relationship between natural frequency and wave propagation speed, which will be revisited in Section 2.3.1.1 along with other important concepts.

The aforementioned analysis of wave propagation requires solving the wave equation, which is the partial differential equation for the description of motion for a waveguide; in this regard, the wave equation shares the same expression as the equation of motion in vibration analysis (Section 2.2.1). The wave equations for 1D waveguides are usually second-order or fourth-order. For flexural waves in beams, the wave equation is fourth-order as demonstrated in Eq. (2.6). For longitudinal waves in rods and transverse wave in strings, the wave equation is second-order, and a general form is given in Eq. (2.38).

$$u^{(2)}(x,t) = \frac{1}{c^2}\ddot{u}(x,t). \tag{2.38}$$

The second-order system described in Eq. (2.38) is the simplest form for understanding wave propagation behaviour, and important concepts such as phase speed, group speed and modulation are discussed in the context of this second-order system in Section 2.3.1.1, but these concepts are rather general and apply to other systems by slight modifications, for instance, the fourth-order system for flexural waves in beams.

2.3.1.1 Phase speed, group speed and modulation

Consider the second-order wave equation Eq. (2.38) with a characteristic wave speed of *c* and note that *c* is the wave speed as shown later in Eq. (2.41). By the method of separation of variables introduced in Section 2.2.2 and trigonometric transformations, the general solution of Eq. (2.38) by d’Alembert’s method is

$$\begin{aligned} u(x,t) &= C_1 \sin(\beta x + \omega t) + C_2 \sin(\beta x - \omega t) \\ &\quad + C_3 \cos(\beta x + \omega t) + C_4 \cos(\beta x - \omega t), \end{aligned} \tag{2.39}$$

where $\beta = \omega/c$ is the wavenumber.

Consider a typical term in Eq. (2.39) with unit amplitude, given by

$$u(x,t) = \cos(\beta x - \omega t), \tag{2.40}$$

where the term $(\beta x - \omega t)$ is called the *phase of the wave*. And Eq. (2.40) shows that this wave is propagating towards the positive x direction. If the wave travels at constant phase, and speed of this wave is called *phase speed*, which can be determined by

$$C_{\mathrm{p}} = \frac{dx}{dt} = \frac{\omega}{\beta} = c. \tag{2.41}$$

Eq. (2.41) shows that for a typical wave equation written in the form of Eq. (2.38), the parameter c is the wave propagation speed or phase speed of that wave. If Eq. (2.38) represents the longitudinal wave propagation in a rod, the longitudinal wave speed is found to be $C_0 = \sqrt{E/\rho}$.

Now consider the superposition of two waves with slightly different wavenumbers and frequencies in the form of Eq. (2.42).

$$u(x,t) = \cos(\beta_1 x - \omega_1 t) + \cos(\beta_2 x - \omega_2 t). \tag{2.42}$$

By trigonometric relations, and introducing $\Delta\omega = \omega_2 - \omega_1$, $\Delta\beta = \beta_2 - \beta_1$, $\omega = (\omega_1 + \omega_2)/2$ and $\beta = (\beta_1 + \beta_2)/2$, Eq. (2.42) can be written as

$$u(x,t) = 2\cos(\beta x - \omega t)\cos\left(\frac{1}{2}\Delta\beta x - \frac{1}{2}\Delta\omega t\right). \tag{2.43}$$

Hence the superposition of two waves with different frequencies results in two waves: one travels at phase speed of ω/β; and the other travels at speed of $\Delta\omega/\Delta\beta$, which is called *group speed* and denoted C_{g}, where

$$C_{\mathrm{g}} = \frac{\Delta\omega}{\Delta\beta} = \frac{d\omega}{d\beta}. \tag{2.44}$$

The relationship between phase speed C_p and group speed C_g according to Eq. (2.43) is shown in Figure 2.5.

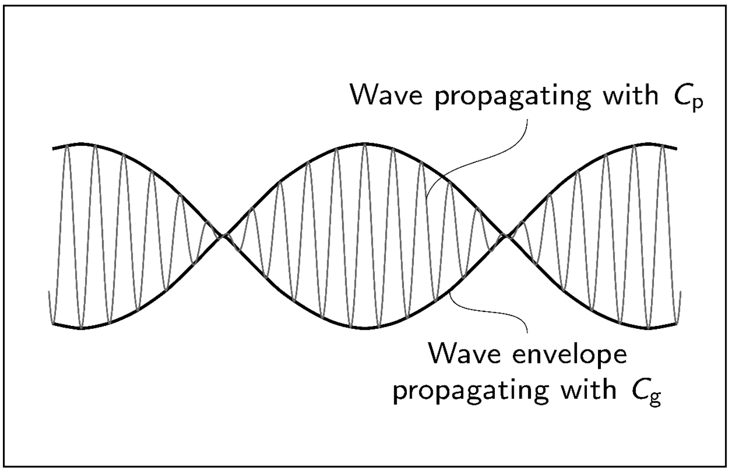
Wave propagating with C_p
Wave envelope propagating with C_g

Figure 2.5 Phase speed and group speed of 1D propagating wave

In Eq. (2.43), the first cosine term with the average wavenumber β and frequency ω has a high frequency, and it propagates at the phase speed of C_p shown in Figure 2.5 with the grey line; the second cosine term with the wavenumber difference $\Delta\beta$ and frequency difference $\Delta\omega$ has a low frequency, and it propagates at the group speed C_g and as an envelope of the high-frequency wave shown in the black line in Figure 2.5. In this manner, the low-frequency wave acts like a carrier to modulate the high-frequency wave.

2.3.1.2 Wave propagation of flexural waves in beams

Now consider the flexural waves in beams. The fourth-order equation of motion Eq. (2.6) is also the wave equation for flexural wave in beams. The spectrum relation between wavenumber β_i and natural frequency ω_i is given in Eq. (2.11).

The solution for wavenumber β_i in Eq. (2.11) are $\beta_i = \pm\sqrt{\omega_i}\sqrt[4]{\rho A/(EI)}$ and $\beta_i = \pm i\sqrt{\omega_i}\sqrt[4]{\rho A/(EI)}$: the first two real roots of β_i are the *propagating modes*, and they correspond to the sine and cosine terms in normal mode solution in Eq. (2.18); however, the other roots of β_i are imaginary, and waves with imaginary wavenumbers do not propagate, and they are called *evanescent modes*. The imaginary roots correspond to the hyperbolic sine and hyperbolic cosine terms in Eq. (2.18).

For the *i*th mode propagating flexural wave, the phase is

$$\varphi_i = \beta_i x \pm \omega_i t, \tag{2.45}$$

where the waves with phase $\varphi_i = \beta_i x - \omega_i t$ travel towards the x positive direction, and waves with phase $\varphi_i = \beta_i x + \omega_i t$ travel towards the negative x direction. The amplitude of these waves is determined by the general solution of vibration analysis in Eq. (2.7).

2.3.1.3 Dispersion of flexural waves in beams

Now consider the speed for the flexural waves to travel in beams as a type of 1D waveguides. The *i*th mode flexural wave travels at its phase speed, which, combining Eqs. (2.11) and (2.41), is

$$C_{\mathrm{p}}^{i} = \frac{\omega_i}{\beta_i} = \sqrt{\omega_i}\sqrt[4]{\frac{EI}{\rho A}}, \tag{2.46}$$

where the superscript *i* on C_{p}^{i} indicates that it is for the *i*th mode flexural wave. Eq. (2.46) indicates that the phase speeds are different among all the flexural waves in beams since they have different natural frequencies, and waves with higher frequencies travel faster.

The group speed for the *i*th mode flexural wave, combining Eqs. (2.11) and (2.44), is

$$C_{\mathrm{g}}^{i} = \frac{d\omega_i}{d\beta_i} = 2\sqrt{\omega_i}\sqrt[4]{\frac{EI}{\rho A}} = 2C_{\mathrm{p}}^{i}, \tag{2.47}$$

where the superscript *i* on C_{g}^{i} indicates that it is for the *i*th mode flexural wave. Eqs. (2.46) and (2.47) suggest that for the beams as a 1D waveguide with the fourth-order wave equation, the group speed is always twice of the phase speed, and this leads to a phenomenon called *dispersion*.

Dispersion happens when $C_{\mathrm{p}}^{i} \neq C_{\mathrm{g}}^{i}$, such as in flexural waves in beams, in which the high-frequency flexural waves travel faster than low-frequency ones, and thus the wave shape or profile will extremely alter as it propagates. And these waves are called *dispersive waves*. The waves without dispersion are called *non-dispersive waves,* and their phase speed is equal to the group speed, that is, $\omega/\beta = d\omega/d\beta$, leading to a linear dispersion, that is, the linear relationship between the wavenumber and frequency. Illustrations of dispersive waves and non-dispersive waves are in Figure 2.6.

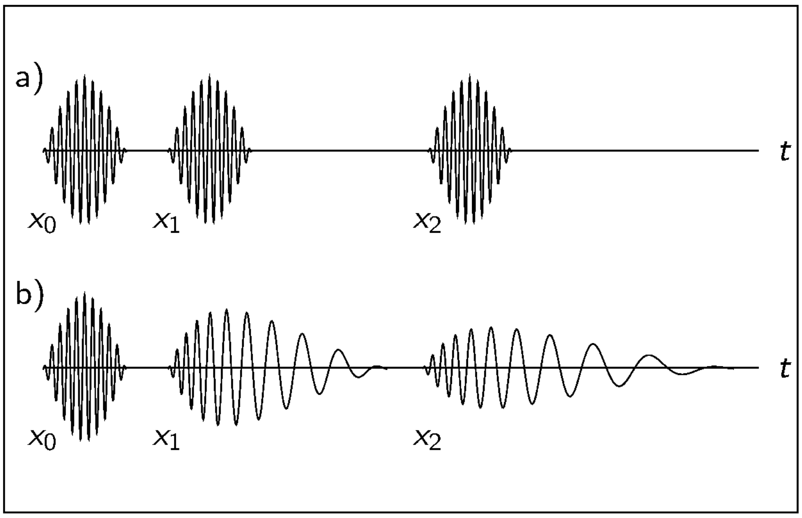

Figure 2.6 Illustration for (a) non-dispersive waves; (b) dispersive waves

Non-dispersive waves will retain their wave profiles while they are travelling (Figure 2.6a), but this is not the case for dispersive waves that their wave profiles undergo extreme distortion as they propagate (Figure 2.6b). Most second-order systems with a hyperbolic wave equation, such as transverse vibration of a string and longitudinal vibration of a rod, are non-dispersive. But the fourth-order system, such as flexural waves in beams, are highly dispersive.

2.3.1.4 Energy transmission speed

For non-dispersive waves, apparently, the speed of energy transmission by these waves is the phase speed or group speed since they are equal. However, for dispersive waves, the speed of energy transmission by these waves should be further investigated.

Consider the same instance for the two waves with slightly different wavenumbers and frequencies shown in Eq. (2.42), the total energy per length is

$$E_0 = U_0 + K_0 = 2K_0 \,, \tag{2.48}$$

where U_0 is the strain energy per length and K_0 is the kinetic energy per length, respectively. Ref. [26] shows that when U_0 and K_0 are considered in a time-averaged concept, they have the same value, $U_0 = K_0$, where K_0 is

$$K_0 = \frac{1}{2}\rho\left[\dot{u}\left(x,t\right)\right]^2 . \tag{2.49}$$

Examining the velocity $\dot{u}(x,t)$ derived from Eq. (2.42) and neglecting the higher-order term with $\Delta\omega$, and combining Eqs. (2.48) and (2.49), E_0 is obtained as

$$E_0 = 4\rho\omega^2 \cos^2\left(\frac{1}{2}\Delta\beta x - \frac{1}{2}\Delta\omega t\right)\sin^2\left(\beta x - \omega t\right). \tag{2.50}$$

Eq. (2.50) suggests that the total energy per length has two variating terms: one with the high frequency ω and the other with the low frequency $\Delta\omega/2$. To avoid the high-frequency influence, consider the time-averaged energy per length for E_0 over a period with $T = 2\pi/\omega$. For the high frequency term $\sin^2(\beta x - \omega t)$, it is found that $\int_0^T \sin^2\left(\beta x - \omega t\right) dt \big/ T = 1/2$. Therefore, Eq. (2.50) can be approximately simplified to Eq. (2.51), for $\Delta\omega << \omega$, and since integration over $T = 2\pi/\omega$ does not change the low-frequency term much.

$$E_0 \approx 2\rho\omega^2 \cos^2\left(\frac{1}{2}\Delta\beta x - \frac{1}{2}\Delta\omega t\right). \tag{2.51}$$

It is demonstrated in Eq. (2.51) that the time-averaged energy travels at a speed of $\Delta\omega/\Delta\beta$, and this is the group speed according to Eq. (2.44). Therefore, the derivation for Eq. (2.51) shows that for dispersive waves, the energy transmits at the group speed C_g rather than phase speed C_p.

2.3.2 Waves in infinite, semi-infinite and doubly-bounded media

Wave propagation in infinite, semi-infinite and doubly-bounded elastic media are essential for the investigation of classical elastodynamic fracture problems, such as semi-infinite crack and central crack in infinite sheets.

2.3.2.1 Waves in infinite elastic media

There are two types of waves, namely dilatational and shear waves, in an infinite 3D elastic structure. Consider the Navier's equation and replace the Laplacian of the displacement vector $\nabla^2 u = \nabla\left(\nabla \cdot u\right) - \nabla \times \nabla \times u$ to have

$$\left(\lambda + \mu\right)\nabla\left(\nabla \cdot u\right) - \mu\nabla \times \nabla \times u = \rho\ddot{u}, \tag{2.52}$$

where λ and μ are the Lamé constants. Relations between the Lamé constants and the Young's modulus and Poisson's ratio are $\lambda = E\nu/[(1 + \nu)(1 - 2\nu)]$ and $\mu = E/[2(1 + \nu)]$.

Consider the irrotational deformation by setting the rotation $\nabla \times u=0$, Eq. (2.52) becomes

$$\nabla^2 u = \frac{1}{C_{\mathrm{d}}^2}\ddot{u}, \tag{2.53}$$

where

$$C_{\mathrm{d}} = \sqrt{\frac{\lambda + 2\mu}{\rho}}. \tag{2.54}$$

Eqs. (2.53) and (2.54) show that the dilatational deformation follows a typical wave equation (recall Eqs. (2.38) and (2.41)), and the corresponding wave speed is C_{d}, which is called *dilatational wave speed* or *irrotational wave speed*.

Now consider the rotational deformation by setting the dilatation $\nabla \cdot u = 0$, Eq. (2.52) becomes

$$\nabla^2 u = \frac{1}{C_{\mathrm{s}}^2}\ddot{u}, \tag{2.55}$$

where

$$C_{\mathrm{s}} = \sqrt{\frac{\mu}{\rho}}. \tag{2.56}$$

Eqs. (2.55) and (2.56) show that the rotational deformation also follows the wave equation, and the corresponding wave travels at a speed of C_{s}, which is called *shear wave speed* or *equivoluminal wave speed*.

2.3.2.2 Waves in semi-infinite elastic media

For a semi-infinite elastic media, that is, with a traction-free surface introduced to the infinite elastic media, a surface wave exists, which can travel near this traction-free surface. This type of wave is Rayleigh wave, first investigated by Lord Rayleigh [29], after whom it is named.

Rayleigh wave is due to the interaction between dilatational and shear waves and is confined on the traction-free surface, and it decays exponentially when the depth into the elastic media from the traction-free surface increases. Consider the dilatational and rotational motions at this free surface, by applying the traction-free boundary condition, the Rayleigh function is derived with the solution being the phase speed of the Rayleigh wave:

$$\left(2-\frac{C_{\mathrm{R}}^2}{C_{\mathrm{s}}^2}\right)^2-4\left(1-\frac{C_{\mathrm{R}}^2}{C_{\mathrm{d}}^2}\right)^{\frac{1}{2}}\left(1-\frac{C_{\mathrm{R}}^2}{C_{\mathrm{s}}^2}\right)^{\frac{1}{2}}=0. \tag{2.57}$$

Note that Eq. (2.57) indicates that the Rayleigh wave speed C_{R} is determined by the dilatational and shear wave speeds and is independent of wavenumber. Therefore, the Rayleigh wave is non-dispersive.

An approximation of the solution for Rayleigh wave speed C_{R} [30] of Eq. (2.57) is

$$C_{\mathrm{R}}=\frac{0.862+1.14\nu}{1+\nu}C_{\mathrm{s}}. \tag{2.58}$$

The Rayleigh wave speed can also be written in terms of longitudinal wave speed for 1D wave propagation (with C_{s} given in Eq. (2.56)) as

$$C_{\mathrm{R}}=\frac{0.862+1.14\nu}{\left(1+\nu\right)\sqrt{2\left(1+\nu\right)}}C_0, \tag{2.59}$$

where $C_0=\sqrt{E/\rho}$ is the longitudinal wave speed for 1D wave propagation.

2.3.2.3 Waves in doubly-bounded elastic media

Upon the semi-infinite elastic media in Section 2.3.2.2, if another traction-free surface is introduced parallel to the existing one, such as for a thick plate, Rayleigh wave degenerates to *Lamb wave*, which is also called *Rayleigh-lamb wave* or *quasi-Rayleigh wave*. But Lamb wave has two modes: symmetric and asymmetric as shown in Figure 2.7.

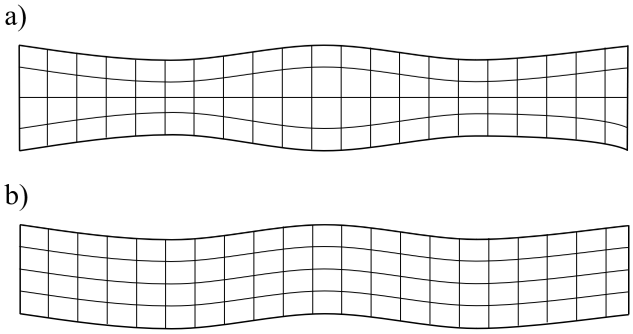

Figure 2.7 Lamb wave modes: (a) symmetric mode; (b) asymmetric modes

In Lamb's original publication [31], the frequency equation for the symmetric modes was derived as shown in Eq. (2.60):

$$\frac{\tan(pd)}{\tanh(qd)} = -\frac{\left(\xi^2 - q^2\right)^2}{4\xi^2 pq}, \tag{2.60}$$

and frequency equation for the asymmetric modes as in Eq. (2.61):

$$\frac{\tan(pd)}{\tan(qd)} = -\frac{4\xi^2 pq}{\left(\xi^2 - q^2\right)^2}, \tag{2.61}$$

where ξ is the wavenumber, d is the half-thickness of the plate, $p^2 = \omega^2 / C_\mathrm{d}^2 - \xi^2$ and $q^2 = \omega^2 / C_\mathrm{s}^2 - \xi^2$. Since the wavenumber and frequency do not have a linear relationship, these symmetric and asymmetric waves are dispersive.

The numerical solutions for Eqs. (2.60) and (2.61) for a given plate configuration provide the wavenumbers for the symmetric and asymmetric modes, but the number of roots for these two equations depends on the product of frequency $f = \omega/(2\pi)$ and half-thickness of the plate d. An example of this for aluminium plate is shown in Figure 2.8 from [32].

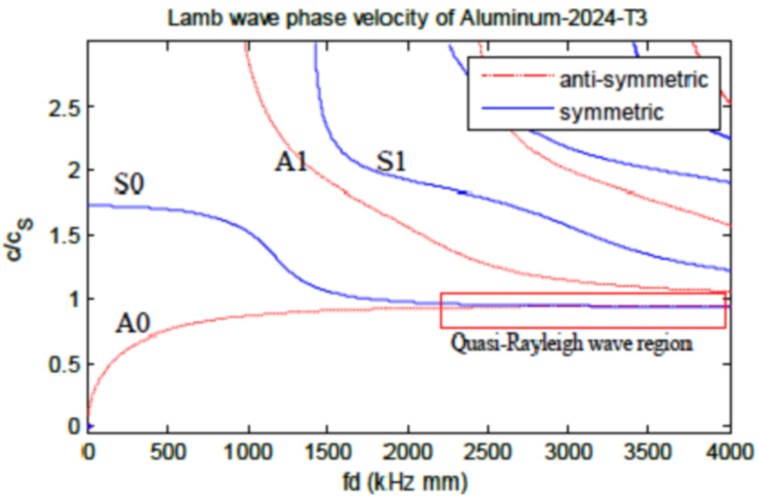

Figure 2.8 Wave speed dispersion for Lamb waves [32]. Reproduced with permission from T. Kamas, V. Giurgiutiu, and B. Lin, Smart Mater. Struct. 24, 2015 © IOP Publishing.

Figure 2.8 implies that for low *fd* value, only S0 and A0 Lamb waves exist, and they are called *zero-order modes*. Correspondingly S0 is also known as the extensional mode, and A0 is the flexural mode. This is important to note for the case of a thin plate with small *d*, only S0 and A0 mode exist.

A comparison of the dispersion relations (i.e. relation between the wave speed and the natural frequency) for axial, flexural, Lamb waves is presented in Figure 2.9 from [33].

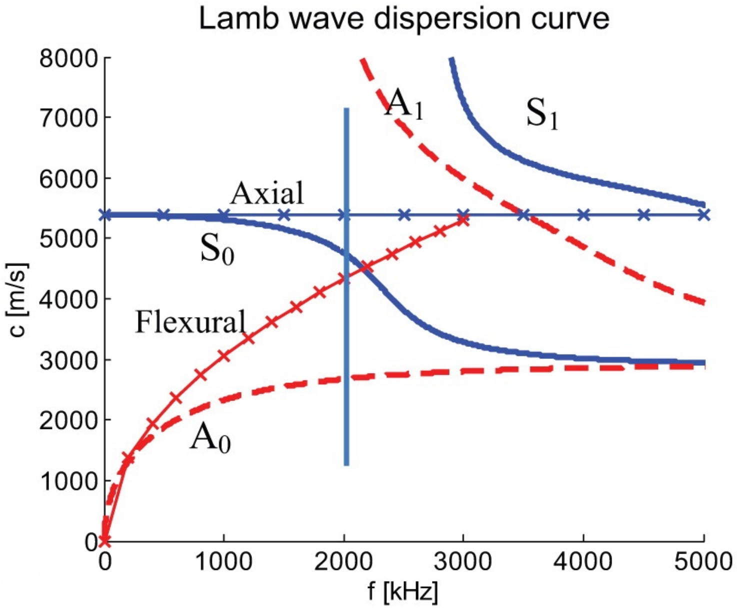

Figure 2.9 Comparison of dispersion relation for axial, flexural, Lamb waves [33]. Reproduced with permission from A. M. Kamal, B. Lin and V. Giurgiutiu, J. Intell. Mater. Syst. Struct., 25, 2014. © SAGE Publications

In Figure 2.9, the axial wave speed is calculated by $C_0 = \sqrt{E/\rho}$, which is the longitudinal wave for rod aforementioned. The Lamb wave A0 mode and S0 mode share the same asymptotes, which has the Rayleigh wave speed (although not noted in the original figure), indicating at high frequency the motion of these Lamb waves is restricted to the surface and therefore they travel with Rayleigh wave speed.

2.4 Conclusion

In this Chapter, the fundamental theories of vibration and wave propagation are briefly reviewed, based on which the following chapters are developed. First, the vibration analysis and method of separation of variables are studied, and Grant's method [28] to solve time-dependent boundary condition is reviewed, which is used through the thesis to determine the dynamic response of respective fundamental engineering structures. Second, the wave propagation theory with concepts, such as phase speed, group speed and dispersion are presented, which are also widely used in later chapters for understanding the energy transmission property of beams as waveguides to study the fracture mechanics.

The wave propagation in infinite elastic media is also revisited, based on which, the classical elastodynamic fracture is developed, and this is reviewed in Chapter 3.

Chapter 3: Key concepts of fracture mechanics

3.1 Introduction

Fracture mechanics is a relatively new scientific discipline dedicated to investigating fracture behaviour of a cracked structure, such as crack initiation and propagation, and aiming at remaining the structural integrity to prevent structural failure with the existence of cracks. Classical books can be found in [34][35] for quasi-static fracture mechanics, and [36][37] for dynamic fracture.

In this chapter, the fundamental concepts of fracture mechanics are presented, both in LEFM (Section 3.2) and elastodynamic fracture mechanics (Section 3.3).

3.2 Linear-elastic fracture mechanics

LEFM assumes the material to be elastic to study the fracture behaviour of cracked structures based on energy or stress criteria. Griffith [38] pioneered the energy-based investigation (Section 3.2.2) for studying crack behaviour of brittle material using global energy balance (Section 3.2.1) and theorem of minimum energy. Irwin [39] studied the crack-tip stress field and gave a stress-based fracture criterion (Section 3.2.3). Cherepanov [40] and Rice [41] focused on the crack-tip local energy and derived the J-integral (Section 3.2.4), which is not only important in LEFM but also is widely used in elastic-plastic fracture problems.

3.2.1 Global energy balance

Global energy balance is important to understand Griffith's approach to study fracture phenomenon, which has been widely used in LEFM. Consider a crack with the area A_0 in an elastic structure, and according to the law of energy conservation [35] without plastic or viscous dissipations

$$\dot{W}_{\text{ext}} = \dot{U} + \dot{K} + \dot{\Gamma}, \tag{3.1}$$

where $\dot{W}_{\text{ext}}$ is the instantaneous power of the external forces; $\dot{U}$ and $\dot{K}$ are the changing rates of strain and kinetic energies, respectively; and $\dot{\Gamma}$ is the rate of energy dissipation due to the increment of crack area. Based on this energy balance, and using the relation of $\partial/\partial t = \partial A_0/\partial t \cdot \partial/\partial A_0 = \dot{A}_0 \cdot \partial/\partial A_0$, Eq. (3.1) can be written as

$$\frac{\partial \Gamma}{\partial A_0} = \frac{\partial W_{\text{ext}}}{\partial A_0} - \frac{\partial U}{\partial A_0} - \frac{\partial K}{\partial A_0}. \tag{3.2}$$

For the elastic structure under quasi-static loads and slow crack growth, where the kinetic-energy contribution is not significant, Eq. (3.2) becomes

$$\frac{\partial \Gamma}{\partial A_0} = \frac{\partial}{\partial A_0}\left(W_{\text{ext}} - U\right). \tag{3.3}$$

3.2.2 The Griffith theory and strain energy release rate

Griffith [42], based on the global energy balance and theorem of minimum energy, proposed a criterion of rupture (fracture) with consideration of equilibrium, that is, the phenomenon of rupture happens with a decrease in potential energy, and this reduction of potential energy transforms to potential surface energy to advance the crack. Griffith studied an infinite plate with a straight crack with a crack length of $2a$, under constant normal stress σ, which is perpendicular to the crack. By applying Inglis' result [43], the strain energy of the system with the crack is

$$U = U_0 - \pi \frac{a^2 \sigma^2}{E}. \tag{3.4}$$

where U_0 is the potential energy of the uncracked plate. The work required to create new surface is $4a\gamma_s$, where γ_s is the surface energy for brittle material, representing the cohesive forces of the molecules. Therefore, the energy dissipated to advance the crack is

$$\Gamma = 4a\gamma_s. \tag{3.5}$$

The total energy of the system is

$$U + \Gamma = U_0 - \pi \frac{a^2 \sigma^2}{E} + 4a\gamma_s. \tag{3.6}$$

Using theorem of minimum energy, $d(U + \Gamma)/dA_0 = 0$, under constant applied stress σ, a critical crack length a_c can be determined, under which crack shall not propagate.

$$a_c = \frac{2E\gamma_s}{\pi \sigma^2}. \tag{3.7}$$

Similarly, for a given crack length $2a$, a critical applied normal stress σ_c is found to be

$$\sigma_{\mathrm{c}} = \sqrt{\frac{2E\gamma_{\mathrm{s}}}{\pi a}}. \tag{3.8}$$

Combining Eqs. (3.3) and (3.6), Griffith's fracture criterion can be written as

$$G = \frac{\partial\left(W_{\mathrm{ext}} - U\right)}{\partial A_0} = G_{\mathrm{c}} = 2\gamma_{\mathrm{s}}. \tag{3.9}$$

In the right-hand side of Eq. (3.9) $G_{\mathrm{c}} = 2\gamma_{\mathrm{s}}$, the coefficient 2 is due to two new material surfaces are formed during crack growth, and G_{c} is called *critical ERR* or *fracture toughness* and is an inherent property of materials that crack growth must overcome and is deemed as the crack-resisting force. The left-hand side of Eq. (3.9) $G = \partial\left(W_{\mathrm{ext}} - U\right)/\partial A_0$ represents the available energy that can be dissipated from the cracked system for crack growth, and is called *ERR*, also known as the crack-driving force. If the external work W_{ext} is zero, for instance, the system under 'fixed-grips' condition when the loaded surface of the cracked structure maintains at a given displacement during crack growth, the ERR becomes $G = -\partial U/\partial A_0$, in this manner, the crack-driving force G comes from the reduction of the strain energy of the cracked system, and thus this G in quasi-static loading regime is also referred to as the strain ERR.

Irwin [39] furthered Griffith's criterion of brittle material to ductile material by incorporating the dissipation due to plastic deformation of γ_{p} to the fracture toughness, giving

$$G_{\mathrm{c}} = 2\left(\gamma_{\mathrm{s}} + \gamma_{\mathrm{p}}\right). \tag{3.10}$$

3.2.3 Stress intensity factor

An alternative method to investigate the fracture behaviour is to examine the crack-tip stress field by using linear elasticity.

Several early analytical studies [39][44][45][46] provided closed-form expressions for the crack-tip stress fields, and in a polar coordinate system, the stress field around a crack tip can all be written as

$$\sigma_{ij} = \frac{K}{\sqrt{2\pi r}} f_{ij}\left(\theta\right) + o\left(\sqrt{r}\right), \tag{3.11}$$

where $f_{ij}(\theta)$ is a dimensionless function of θ and $o\left(\sqrt{r}\right)$ is higher-order term; and K is a constant, which is the SIF defined by Irwin [39].

The SIF in Eq. (3.11) implies it is related with the corresponding stress components, that is, normal stress σ_{xx} and two shear stress τ_{xy} and τ_{xz}, and thus SIF can be categorised into three modes of fracture as Figure 3.1 shows: opening (mode-I), in-plane shear or sliding (mode-II), and out-of-plane shear or tearing (mode-III); and the SIFs are denoted K_{I}, K_{II} and K_{III} for the respective fracture modes.

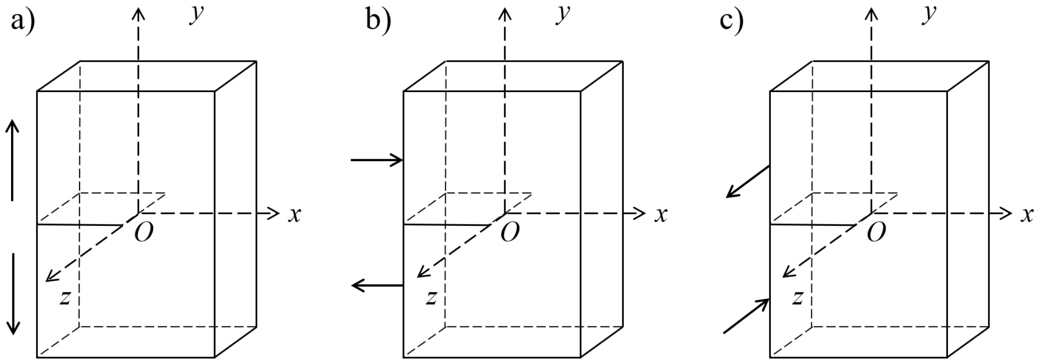

Figure 3.1 Three basic fracture modes: (a) opening (mode-I); (b) in-plane shear or sliding (mode-II); (c) out-of-plane shear or tearing (mode-III)

And therefore, the corresponding SIF of each fracture mode can be determined by

$$\begin{Bmatrix} K_{\mathrm{I}} \\ K_{\mathrm{II}} \\ K_{\mathrm{III}} \end{Bmatrix} = \lim_{r\to 0}\sqrt{2\pi r}\begin{Bmatrix} \sigma_{xx}(r,0) \\ \tau_{xy}(r,0) \\ \tau_{xz}(r,0) \end{Bmatrix}. \tag{3.12}$$

Irwin also identified the ERR according to each fracture mode in Figure 3.1, and derived the relationships between SIFs and ERRs as

$$\begin{Bmatrix} G_{\mathrm{I}} \\ G_{\mathrm{II}} \\ G_{\mathrm{III}} \end{Bmatrix} = \begin{Bmatrix} K_{\mathrm{I}}^2/E \\ K_{\mathrm{II}}^2/E \\ K_{\mathrm{III}}^2/(2\mu) \end{Bmatrix}. \tag{3.13}$$

Eq. (3.13) is for plane-stress condition, and for plane-strain condition, the Young's modulus E in Eq. (3.13) is replaced by $E/(1 - v^2)$.

Turning to the fracture criterion, for the pure fracture mode, for example, fracture mode-I, the fracture criterion is

$$K_{\mathrm{I}} \geq K_{\mathrm{Ic}}, \tag{3.14}$$

where K_{Ic} is the mode-I fracture toughness. Fracture toughness is a material property, which can be determined by testing, and the standardised testing method can be found in [10].

Similarly, for energy-based fracture criterion using ERR, in pure mode-I, it is

$$G_{\mathrm{I}} \geq G_{\mathrm{Ic}}. \tag{3.15}$$

But for mixed-mode fracture, there are several fracture criteria, and simplest is the linear fracture criterion shown in Eq. (3.16). Comprehensive reviews of fracture criteria can be found in [47][48].

$$\frac{G_{\mathrm{I}}}{G_{\mathrm{Ic}}} + \frac{G_{\mathrm{II}}}{G_{\mathrm{IIc}}} + \frac{G_{\mathrm{III}}}{G_{\mathrm{IIIc}}} = 1, \tag{3.16}$$

where G_{Ic}, G_{IIc} and G_{IIIc} are critical ERR in the three respective fracture modes.

3.2.4 The J-integral

Another local approach is the J-integral developed by Cherepanov [40] and Rice [49] using a crack-tip contour integral. This fracture parameter is important not only in linear elastic fracture but also in nonlinear elastic and elastic-plastic fracture.

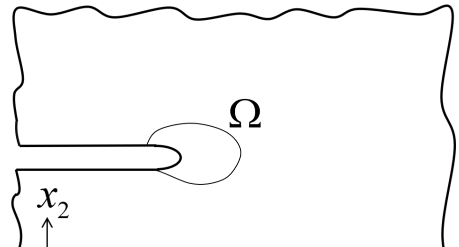

Figure 3.2 Crack-tip contour Ω for J-integral

For a two-dimensional crack shown in Figure 3.2 with a contour Ω around the crack tip, the expression for J-integral is

$$J = \int_{\Omega} \left(W dx_2 - T_i \frac{\partial u_i}{\partial x_1} ds \right), \tag{3.17}$$

where W is the strain energy density, and T_i is the traction component acting on the surface of contour. Rice [49] demonstrated that J-integral is path-independent. In addition, the relation between J-integral and potential energy is given

$$J = -\frac{d\Pi}{dA_0}, \tag{3.18}$$

where $\Pi = (U - W_{\text{ext}})$ is the potential energy. And by comparing the ERR definition in Eq. (3.9), J-integral has the same value of ERR, that is

$$J = G. \tag{3.19}$$

Note that Eq. (3.19) is derived with the assumption that the material is elastic and crack propagates in a self-similar manner.

Eq. (3.19) has an important implication that ERR calculated by global energy balance (Section 3.2.1) equals to the one calculated by local crack-tip energy quantities. Therefore, the energy-based global approach and energy-based local approach are equivalent in LEFM.

3.2.5 Compliance method

To determine the ERR in Eq. (3.9), the potential energy of a cracked structure must be calculated first. A convenient method of determining the potential energy of a given cracked structure is the compliance method. Consider a general force P acting on a cracked elastic structure, and its induced general displacement w. The potential energy can be calculated as follows, which can be therefore used to determine the ERR via Eq. (3.9).

For an elastic plate of uniform thickness b with a crack length a subjected to an external force P, without crack growth, the displacement w is found to be

$$w = CP, \tag{3.20}$$

where C is the compliance of the cracked elastic plate.

Therefore, the infinitesimal external work increment is found to be $dW_{\text{ext}} = Pdw$, and infinitesimal elastic strain energy increment is $dU = (Pdw + wdP)/2$, and considering the definition of ERR in Eq. (3.9), the ERR is found to be

$$G = \frac{1}{2b}\left(\frac{Pdw}{da} - \frac{wdP}{da}\right), \tag{3.21}$$

and substituting the total derivation of displacement w, that is, $dw = CdP + PdC$, the ERR can be written as

$$G = \frac{P^2}{2b}\frac{dC}{da} = \frac{w^2}{2b}\frac{1}{C^2}\frac{dC}{da}. \tag{3.22}$$

Therefore, the ERR G of this cracked elastic structure can be calculated by externally applied load P or displacement w, providing the compliance of the structure $C(a)$, which is a function of crack length a, is known.

Three most common fundamental engineering configurations to study the fracture behaviour and to measure the fracture toughness in pure fracture modes are DCB (Figure 3.3a), ELS (Figure 3.3b) and end-notched flexure (ENF) (Figure 3.3c) specimens. DCB specimens are for mode-I fracture, while ELS and ENF specimens are for mode-II fracture. These three types of specimens are the most common configurations to study the fracture in CFPRs to provide a fundamental understanding of fracture behaviour and a measurement of fracture toughness for building-block design process (also see Section 1.1).

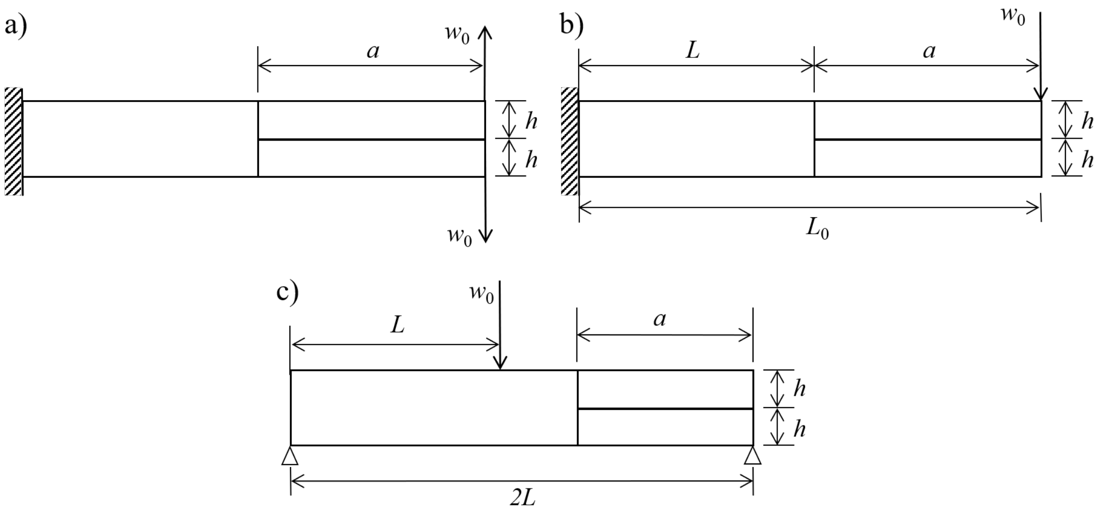

Figure 3.3 Specimen configurations: (a) DCB; (b) ELS; (c) ENF

The compliance for a DCB specimen is a function of crack length a and it is in accordance with power law [50] of $C = A_C a^n$, which can be determined by fitting the experimental data. And then combining Eq. (3.22), the ERR for a DCB is

$$G = \frac{P^2}{b}\frac{dC}{da} = n\frac{w_0 P}{ba}. \tag{3.23}$$

With an effective boundary condition (Figure 5.1b) to assume one DCB arm is fixed at crack tip as a cantilever beam, together with the classical beam theory, the compliance is found to be $C = a^3/(3EI)$, and therefore the ERR solution for a DCB in Eq. (3.23) can be written as

$$G = \frac{3w_0P}{ba} = \frac{9EIw_0^2}{ba^4} = \frac{P^2a^2}{bEI}. \tag{3.24}$$

Note that this compliance is derived from the Euler-Bernoulli beam theory and assumed a fixed boundary condition at the crack tip, further correction for crack-tip rotation is required, and this is discussed in Section 5.5.

For a DCB under constant-rate opening displacement in quasi-static loading regime, where $w_0 = vt$, the ERR in Eq. (3.24) can be written as a function of time t, given by

$$G = \frac{9EIv^2t^2}{ba^4}. \tag{3.25}$$

The compliance for the ELS specimen (Figure 3.3b) is derived in [51] as $C = (4a^3 + 3a^2L + 3aL^2 + L^3)/(24EI)$, and combining Eq. (3.22), the mode-II ERR in ELS specimen is

$$G = \frac{108EIa^2w_0^2}{b\left(L^3 + 3L^2a + 3La^2 + 4a^3\right)^2}, \tag{3.26}$$

where $I = bh^3/12$. Similarly as the DCB above-mentioned, in quasi-static loading regime with applied constant-rate displacement, w_0 is replaced by vt directly and ERR becomes a function of time.

The compliance for ENF specimen is $C = (2L^3 + 3a^3)/(96EI)$, according to [52], and combining Eq. (3.22), the mode-II ERR in ENF specimen as

$$G = \frac{432EIa^2w_0^2}{b\left(2L^3 + 3a^3\right)^2}. \tag{3.27}$$

Note that since $dG/da < 0$ for the ERR solution in Eq. (3.27) for the ENF specimens, indicating that the crack growth is unstable, ENF specimens are only suitable to study the crack initiation and measure the crack initiation toughness.

3.2.6 Fracture mode mixity

The crack in brittle material tends to propagate in pure mode-I despite being under mixed-mode loading conditions due to the ‘criterion of local symmetry’ [53], that is, a mixed-mode crack growth can change to mode-I by kinks. But when a crack propagates along an interface, its path may be confined due to the weakness of the interface and the crack remains under mixed-mode propagation. For an elastic structure with an interfacial crack, the total ERR can be determined, for instance, by compliance method as per Section 3.2.5, the partition of total ERR is vital to understand fracture behaviour considering the fracture criterion, for instance, Eq. (3.16).

Williams [54] pioneered the mode-partition investigation on the asymmetric DCB with the classical beam theory and found that the partition depends on the thickness ratio of the two DCB arms. Schapery and Davidson [55] studied the same problem but no pure modes could be achieved opposite to findings of Williams [54]. Hutchinson and Suo [56] applied SIFs to determine the partition based on the classical beam theory and 2D elasticity for various configurations, among which the partition for a thin-layer-on-thick-substrate (also known as spalling of a surface layer) due to the end bending is $K_{\mathrm{II}}/K_{\mathrm{I}} = 0.7793$, coincided with [57]. The partition for anisotropic material can be found in [58][59].

Wang and Harvey [60][61] derived two orthogonal pairs of locally pure modes based on the classical and the Timoshenko beam theories, and based on same analytical scheme, comprehensive partition theories were developed, such as for rigid interface in composite laminates [62], for the non-rigid interface in isotropic materials [63], for the rigid bi-material interface [64], for orthotropic laminates based on 2D elasticity [65][66]. Using this theoretical development, particularly for a thin-layer-on-thick-substrate configuration, the 2D elasticity partition [67] gives $G_{\mathrm{II}}/G_{\mathrm{I}} = 0.6059$, very close to the partition in [56] for $G_{\mathrm{II}}/G_{\mathrm{I}} = (K_{\mathrm{II}}/K_{\mathrm{I}})^2$ with $K_{\mathrm{II}}/K_{\mathrm{I}} = 0.7793$.

Note that these partition theories were developed in the quasi-static regime, where the inertia and kinetic energy were not considered explicitly. But examination into the two orthogonal pairs of locally pure modes proposed by Wang and Harvey [60][61] reveals the mode partition depends on the crack-tip loading condition and since the crack-tip loads in dynamic regime include inertial effects implicitly, the partition theory may well be further applied in dynamic fracture regime, and this is studied and confirmed in Chapter 7.

3.3 Elastodynamic fracture mechanics

As laid out in [35], there are mainly two aspects in dynamic fracture, that is, one with fast crack propagation and the other with rapidly varying load, such as impact. For impact on composite structure, Davies and Olsson [68] classified the loading rates into low velocity (4 -8 m s^{-1}, for example dropped tool), high velocity (300 -2500 m s^{-1}, for example ballistic impact) and hyper-velocity (30 -70 km s^{-1}, for example impact for satellites and spacecraft). With decreasing of the impact velocities, the response of composite structures changes from dilatational-wave dominant to flexural-wave dominant, and eventually approaches to quasi-static. Therefore, in general, for fracture associated with the dilatational-wave and flexural-wave dominant response, dynamic fracture mechanics have to be applied. Nevertheless, this depends on assessment of each individual case due to complexity for the wave propagation in various structures with different material properties. For the flexural-wave dominant response for dynamic fracture in DCB and ELS configurations, for instance, the dynamic effect can be studied quantitatively using dynamic factor developed in Sections 5.2.3, 7.2.4 and 8.2.3.

Elastodynamic fracture mechanics is the counterpart of LEFM in the dynamic field, which assumes the material is linear elastic. The classical elastodynamic fracture is reviewed in this section, which is developed by including the inertial effect or kinetic energy into account for the elastic cracked structures. Two key concepts in elastodynamic fracture mechanics are dynamic SIF and dynamic ERR, respectively.

3.3.1 Dynamic stress intensity factor

Following Irwin's approach (Section 3.2.3), the near-crack-tip stress field in elastodynamics is time-dependent and for each fracture mode it can be expressed as

$$\sigma_{ij}\left(t\right)=\frac{K\left(t\right)}{\sqrt{2\pi r}}f_{ij}\left(\theta\right), \tag{3.28}$$

where $K(t)$ is time-dependent elastic SIF as the counterpart to the quasi-static SIF in Section 3.2.3, and it is usually referred to as *dynamic SIF*. The determination of dynamic SIF requires a fundamental understanding of stress wave propagation (Section 2.3).

The classical dynamic problem in [36] is a semi-infinite stationary crack under a suddenly applied pressure with the magnitude of σ at $t = 0$ as shown in Figure 3.4a.

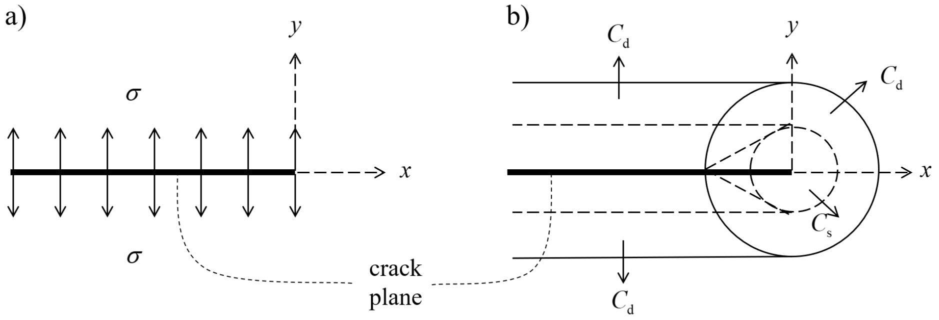

Figure 3.4 Semi-infinite crack problem: (a) crack under sudden pressure with the magnitude of *σ*, (b) wavefronts generated by suddenly applied pressure, solid lines for dilatational wave and dashed line for shear waves

Far from the crack tip, dilatational waves with their wavefronts parallel to the crack plane are emitted due to the suddenly applied pressure. But near the crack tip, both dilatational and shear waves are generated concentrically, with their radii being $C_d t$ and $C_s t$. By Green's method or the Wiener-Hopf technique, the dynamic crack-tip stress field can be solved, and, therefore, the dynamic mode-I SIF is given as

$$K_{\mathrm{I}}(t) = 2\sigma \frac{\sqrt{C_{\mathrm{d}} t(1-2\nu)/\pi}}{(1-\nu)}. \tag{3.29}$$

For the same semi-infinite crack setting, if two opposite and equal tractions with the magnitude of *τ* are applied suddenly to the two crack planes within the *x*-*y* plane from *t* = 0, the dynamic mode-II SIF is given as

$$K_{\mathrm{II}}(t) = 2\tau \sqrt{\frac{2C_s t}{\pi(1-\nu)}}. \tag{3.30}$$

And if these two tractions are applied in the *x*-*z* plane, which indicates the out-of-plane shear condition, the dynamic mode-III SIF is

$$K_{\mathrm{III}}(t) = 2\tau \sqrt{\frac{2C_s t}{\pi}}. \tag{3.31}$$

For a mode-I propagating crack, Freund [69] provided a dynamic SIF solution as

$$K_{\mathrm{I}}(t,a,\dot{a}) = k(\dot{a}) K_{\mathrm{I}}^{0}(t,a), \tag{3.32}$$

where $K_{\mathrm{I}}^{0}(t,a)$ is the dynamic SIF for the stationary crack and $k(\dot{a})$ is the universal function given by

$$k\left(\dot{a}\right)\approx\frac{1-\dot{a}/C_{\mathrm{R}}}{\sqrt{1-\dot{a}/C_{\mathrm{d}}}}. \tag{3.33}$$

3.3.2 Dynamic energy release rate

3.3.2.1 Dynamic ERR using global approach

Early attempt to derive dynamic ERR by extending Griffith's method dates back to Mott [70], where kinetic energy is thought to be significant. Using the global energy balance in Section 3.2.1, the dynamic ERR with account for kinetic energy is

$$G^{\mathrm{global}}=\frac{dW_{\mathrm{ext}}}{dA_0}-\frac{dU}{dA_0}-\frac{dK}{dA_0}, \tag{3.34}$$

where K is the kinetic energy assessed by $K=\int_V \rho\dot{u}_i\dot{u}_i dV\Big/2$. And this dynamic ERR was used to study the classical Griffith's problem of a central crack with the crack length of $2a_0$ in an infinite plate subjected to uniform tension σ. The kinetic energy calculated with a crack-propagation $\dot{a}$ is given as

$$K=\frac{1}{2}k_0\rho a^2\dot{a}^2\left(\frac{\sigma}{E}\right)^2, \tag{3.35}$$

where k_0 is a constant, and its value was given in [71] that $\sqrt{2\pi/k_0}\approx 0.38$ for a Poisson's ratio $v = 0.25$.

Therefore, the dynamic ERR and fracture criterion is

$$G^{\mathrm{global}}=\frac{1}{2}\frac{d}{da}\left(\frac{\pi\sigma^2a^2}{E}-\frac{1}{2}k\rho a^2\dot{a}^2\frac{\sigma^2}{E^2}\right)=2\gamma_{\mathrm{s}}. \tag{3.36}$$

Note that before crack initiation $\dot{a}=0$ and at crack initiation $a_0 = a_\mathrm{c}$, which is given in Eq. (3.7), and therefore, the crack-propagation speed can be derived:

$$\dot{a}=0.38C_0\left(1-\frac{a_0}{a}\right), \tag{3.37}$$

where $C_0=\sqrt{E/\rho}$ is the speed of the longitudinal wave in 1D wave propagation.

Eq. (3.37) indicates that there exists a maximum crack-propagation speed, for $a >> a_0$, and this limiting crack-propagation speed is $0.38C_0$. Examining Rayleigh wave speed in Eq. (2.59) with the Poisson's ratio $v = 0.25$, gives $C_\mathrm{R} = 0.58C_0$, and then the limiting crack-propagation speed estimated by [71] in Eq. (3.37) employing the global energy balance is 0.66C_R, which is smaller than the Rayleigh wave speed.

3.3.2.2 Dynamic ERR using local approach

Alternatively, the dynamic ERR can be determined by crack-tip local quantities, using a contour integral and including the kinetic-energy contribution, the development for dynamic ERR can be found in [72][73][74].

The inclusion of kinetic contribution is by introducing the kinetic-energy density, given by $\rho \dot{u}_i \dot{u}_i / 2$. Now consider the rate of change of mechanical energy for the region R around the crack tip shown in Figure 3.5, the summation of the rate of change of elastic strain energy $\dot{U}$ and rate of change of kinetic energy $\dot{K}$ is

$$\dot{U} + \dot{K} = \frac{d}{dt} \int_R \frac{1}{2} \left(\sigma_{ij} \varepsilon_{ij} + \rho \dot{u}_i \dot{u}_i \right) dA. \tag{3.38}$$

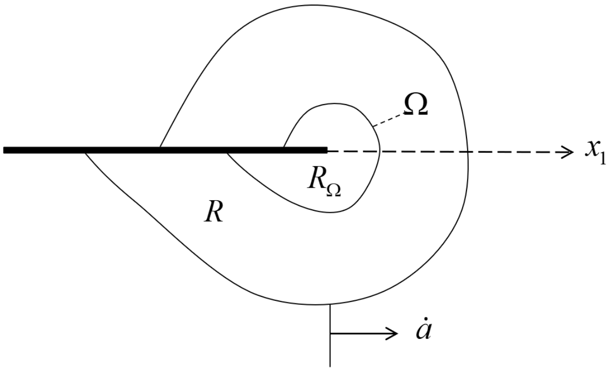

Figure 3.5 Crack-tip contour for determination of energy flux integral

To exclude the singularity at the crack tip, a small contour Ω is made around the crack tip and the total mechanical energy in the region R excluding the region encompassed by the contour Ω is

$$\dot{U} + \dot{K} = \frac{d}{dt} \int_{R - R_\Omega} \frac{1}{2} \left(\sigma_{ij} \varepsilon_{ij} + \rho \dot{u}_i \dot{u}_i \right) dA. \tag{3.39}$$

If the crack propagates towards the x_1 direction with a constant speed $\dot{a}$, by Reynolds transport theorem and divergence theorem, the amount of energy flowing out of the region R and into the crack-tip region through the contour Ω is

$$F(\Omega) = \int_\Omega \left[\sigma_{ij} n_j \dot{u}_i + \frac{1}{2} \left(\sigma_{ij} \varepsilon_{ij} + \rho \dot{u}_i \dot{u}_i \right) \dot{a} n_1 \right] ds. \tag{3.40}$$

The dynamic ERR, therefore, representing the mechanical energy flowing into the crack tip per unit time for crack propagation per unit time, is defined as

$$G^{\text{local}} = \lim_{\Omega \to 0} \frac{F(\Omega)}{\dot{a}} = \lim_{\Omega \to 0} \frac{1}{\dot{a}} \int_{\Omega} \left[\sigma_{ij} n_j \dot{u}_i + \frac{1}{2} \left(\sigma_{ij} \varepsilon_{ij} + \rho \dot{u}_i \dot{u}_i \right) \dot{a} n_1 \right] ds. \tag{3.41}$$

Note that the definition of dynamic ERR in Eq. (3.41) is based on the local approach and its counterpart in LEFM is the J-integral in Section 3.2.4 rather than the ERR derived by reduction of the potential energy of Griffith's global approach in Section 3.2.2.

For a steady-state propagation, the energy flux in Eq. (3.41) is path-independent, and, therefore,

$$G^{\text{local}} = \frac{F(\Omega)}{\dot{a}}. \tag{3.42}$$

Now consider the velocity $\dot{u}_i$ in Eq. (3.41), for a steady state in the moving coordinate system when the partial time derivative is zero, the following relationship with crack-propagation speed $\dot{a}$ can be obtained:

$$\frac{du_i(x,t)}{dt} = \frac{\partial u_i(x,t)}{\partial t} - \dot{a} \frac{\partial u_i(x,t)}{\partial x_1} \approx -\dot{a} \frac{\partial u_i}{\partial x_1}. \tag{3.43}$$

Combining Eqs. (3.40), (3.42) and (3.43) and rearranging, the dynamic ERR using local approach can be written as

$$G^{\text{local}} = \int_{\Omega} \left(\frac{1}{2} \sigma_{ij} \varepsilon_{ij} + \frac{1}{2} \rho \dot{u}_i \dot{u}_i - T_i \frac{\partial u_i}{\partial x_1} \right) ds. \tag{3.44}$$

where T_i is the traction vector given as $T_i = \sigma_{ij} n_j$.

Comparing the J-integral in Eq. (3.17) and dynamic ERR determined by the local approach in Eq. (3.44), if the kinetic-energy contribution is small and can be neglected, which is the case in quasi-static fracture process, the dynamic ERR in Eq. (3.44) becomes the classical J-integral in Eq. (3.17), demonstrating the dynamic ERR defined by local approach is the counterpart of J-integral in LEFM.

The relationship between dynamic ERRs determined by local approach and dynamic SIFs in Section 3.3.1 was derived and given in [36] as

$$G^{\mathrm{local}}=\frac{1-\nu^2}{E}\left[A_{\mathrm{I}}(\dot{a})K_{\mathrm{I}}^2+A_{\mathrm{II}}(\dot{a})K_{\mathrm{II}}^2\right]+\frac{1}{2\mu}A_{\mathrm{III}}(\dot{a})K_{\mathrm{III}}^2, \tag{3.45}$$

where $A_{\mathrm{I}}(\dot{a})$, $A_{\mathrm{II}}(\dot{a})$ and $A_{\mathrm{III}}(\dot{a})$ are universal functions given as

$$A_{\mathrm{I}}(\dot{a})=\frac{\dot{a}^2\alpha_{\mathrm{d}}}{(1-\nu)C_{\mathrm{s}}^2D},\quad A_{\mathrm{II}}(\dot{a})=\frac{\dot{a}^2\alpha_{\mathrm{s}}}{(1-\nu)C_{\mathrm{s}}^2D},\quad A_{\mathrm{III}}(\dot{a})=\frac{1}{\alpha_{\mathrm{s}}}, \tag{3.46}$$

with $\alpha_{\mathrm{d}}=\sqrt{1-\dot{a}^2/C_{\mathrm{d}}^2}$, $\alpha_{\mathrm{s}}=\sqrt{1-\dot{a}^2/C_{\mathrm{s}}^2}$ and $D=4\alpha_{\mathrm{d}}\alpha_{\mathrm{s}}-\left(1+\alpha_{\mathrm{s}}^2\right)^2$.

Combining Eqs. (3.32), (3.33), (3.45) and (3.46) and applying the fracture criterion of $G^{\mathrm{local}} = G_{\mathrm{c}}$, with $G_{\mathrm{c}} = 2\gamma_{\mathrm{s}}$, the following relation for a propagating crack is derived in [36]:

$$\frac{2E\gamma_{\mathrm{s}}}{\left(1-\nu^2\right)\left[K_{\mathrm{I}}^0(t,a)\right]^2}=A_{\mathrm{I}}(\dot{a})\left[k(\dot{a})\right]^2\approx 1-\frac{\dot{a}}{C_{\mathrm{R}}}. \tag{3.47}$$

Eq. (3.47) has a very important implication that crack-propagation speed $\dot{a}$ cannot exceed the Rayleigh wave speed C_{R}. This limiting crack-propagation was also proposed by [75][76].

3.4 Conclusion

Key concepts of fracture mechanics are presented in this chapter, which lays out the foundation of this thesis. In LEFM, there are two approaches to study the fracture behaviour: global approach and local approach. Global approach considers the total energy of the system and reckons the energy required to advance a crack is from the reduction of the potential energy of the system and the ERR is defined. Local approach considers crack-tip quantities, and two fracture parameters are therefore developed: the investigation of stress field near the crack tip leads to SIFs, and study of energy-based crack-tip contour integral gives the J-integral. The relations between ERR and SIF indicates the equivalence between energy-based and stress-based approaches. Also, the relations between ERR and J-integral demonstrates the equivalence between global and local approaches.

In elastodynamic fracture mechanics, the corresponding fracture parameters are developed in a similar way to LEFM to study the dynamic fracture. But these parameters SIFs and ERRs are time-dependent. For dynamic ERR, there are two approaches, i.e.

global and local approaches, to assess its value. The global approach considers the global energy balance as an extension of Griffith's approach, and the dynamic ERR is reckoned as the reduction of the total mechanical energy; the local approach defines dynamic ERR by examining the energy flux flowing into a crack-tip contour as a counterpart of the J-integral in LEFM. However, unlike the equivalence between ERR and J-integral in LEFM, the relation for dynamic ERR using these two approaches (global and local) remains unknown in elastodynamic fracture mechanics, that is, whether G^{global} equals to G^{local} has not been demonstrated. But it is shown that these two approaches predict different limiting crack-propagation speeds at least: $0.66C_{\mathrm{R}}$ in global approach and C_{R} in the local approach. This gap will be partially studied in Chapter 5 (for equivalence between the global and the local approaches) and Chapter 6 (for the limiting crack-propagation speed).

As for the mode-mixity, the partition theories to decompose the total ERR into respective fracture modes has been extensively studied in LEFM, but there is few investigations of partition theory in the dynamic field, and this will be studied by extending a quasi-static partition theory to elastodynamic fracture problem in Chapter 7.

Chapter 4: Conventional dynamic interfacial fracture

4.1 Introduction

The dynamics of interfacial fracture significantly affects fracture behaviour including crack initiation, propagation and arrest, and material properties such as dynamic fracture toughness. There are therefore strong motivations for analytical modelling of dynamic interfacial fracture to achieve a mechanical understanding, or to facilitate post-processing of experimental fracture data for assessment of material properties, vital for maintaining structural integrity and preventing dynamic fracture.

Early investigations into dynamic interfacial fracture did not fully consider the dynamic regime in their analytical models, assuming instead a quasi-static motion. This led to contradictory findings reported in the literature concerning rate effects on fracture toughness. Aliyu and Daniel [77], for instance, conducted tests using DCBs to measure the mode-I fracture toughness of AS4/3501-6 epoxy/carbon-fibre composites at loading rate between 8.5×10^{-6} and 8.5×10^{-3} m s^{-1}, and concluded fracture toughness increased with increasing loading rates. Mall et al. [78] , however, measured the fracture toughness of PEEK/carbon-fibre composite at loading rate between 8.5×10^{-6} and 16.67×10^{-3} m s^{-1} and found the opposite, with fracture toughness decreasing with increasing loading rates. At first thought, material properties might seem a possible explanation, since PEEK as a thermoplastic is relatively ductile compared to the brittle epoxy, with the materials having different rate-dependencies. This is not always the case, however, as when the same material AS4/3501-6 epoxy/carbon-fibre composite was tested in [17] at loading rate range between 4.2×10^{-6} and 6.7×10^{-1} m s^{-1}, the fracture toughness was found to be decrease with increasing opening rates, opposite to the conclusion in [77] for the same material. Comprehensive reviews on the loading effect on fracture toughness can be found in [79][80][81], but no conclusions concerning rate effects on it could be drawn.

Experimental studies for the rate effects on mode-II fracture toughness can be found in [18][82][83][84][85][86][87][88] and in a comprehensive review [89], but – just as for the mode-I investigations – there were no unanimous conclusions regarding fracture-toughness rate effects.

In general, a conventional analytical approach to modelling interfacial fracture is based on [70] (see Section 3.3.2.1). The kinetic energy is considered as significant for the ‘crack-driving force’ or ERR and so included in a global energy-balance approach using

Eq. (3.34), following Griffith (see Section 3.2.1), but based on quasi-static motion without any consideration of vibration. This conventional analytical approach, however, only provides a ‘smoothed’ dynamic ERR. Moreover, the kinetic-energy contribution to the dynamic ERR is simply a baseline shift from its quasi-static component. Surprisingly, experimental data post-processed using this approach appear to show that the dynamic effect under high loading rates is negligible [17][18][20][88]. This contradicts other experimental and numerical investigations [21][90], demonstrating that the dynamic is, in general, oscillating and significant. Meanwhile, in the absence of an analytical modelling capability to properly address the dynamic effect, hybrid experimental-numerical approaches were also used.

In this chapter, the conventional analytical approach for dynamic interfacial fracture is reviewed in Section 4.2; and general numerical method for fracture problem is reviewed briefly in Section 4.3 with an emphasis on numerical techniques for interfacial fracture in Section 4.3.2. Conclusions are given in Section 4.4.

4.2 Conventional analytical approach to modelling dynamic interfacial fracture

The conventional analytical approach to modelling dynamic interfacial fracture accounts for kinetic energy in the global energy balance (Section 3.2.1). Fundamental structures such as those shown in Figure 3.3 are typically considered, including DCB, ELS and ENF specimens. The applied loading velocity is extrapolated along the specimen and then used to determine the kinetic energy. The ERR is subsequently determined using Eq. (3.34) as $G^{\mathrm{global}} = d(W_{\mathrm{ext}} - U - K)/dA_0$.

4.2.1 Mode-I fracture

4.2.1.1 Stationary cracks in DCBs

Smiley and Pipes [17] were the first to account for kinetic energy and derived an expression for the dynamic ERR of a DCB under the opening displacement of constant rate. They used their solution to post-process the experimental data to measure the interlaminar fracture toughness of epoxy/carbon-fibre and PEEK/carbon-fibre composites, and to investigate the effects of loading rates on fracture toughness.

Their analytical model incorporates the kinetic energy of the quasi-static motion of the DCB arms by extrapolating the applied constant-opening velocity v at the free end along the length of the DCB arm. This extrapolation gave the distribution of applied constant-opening velocity along the one DCB arm as

$$\dot{w}(x) = v\left(\frac{3x^2}{2a^2} - \frac{x^3}{2a^3}\right), \tag{4.1}$$

where w (x) is the deflection of the DCB arm with an effective boundary condition (see Figure 5.1b), and $\dot{w}(x)$ is the transverse velocity of the DCB arm, a is the crack length and x is the coordinate along the length of the arm from the crack tip towards the free end with $x = 0$. The kinetic energy for one DCB arm is then calculated as

$$K = \frac{1}{2}\rho A\int_0^a \left[\dot{w}(x)\right]^2 dx = \frac{33}{280}\rho A v^2\,, \tag{4.2}$$

where ρ is the material density, and A is the cross-sectional area. The contribution to the total ERR from the kinetic energy of the quasi-static motion is then $-\,2dK/(bda) = -\,33\rho Av^2/(140b)$, where a factor of two was introduced due to the symmetry of the DCB, and b is the beam width. The total dynamic ERR by the global approach, by combining Eqs. (3.24) and (3.34), is therefore

$$G = \frac{P^2a^2}{bEI} - \frac{33\rho Av^2}{140b}, \tag{4.3}$$

where P is the external load at the location of the applied opening displacement.

Smiley and Pipes used this analytical solution to determine the dynamic ERR in their experiments, but found that the kinetic-energy contribution of $-33\rho Av^2/(140b)$ was negligible.

Blackman et al. [20], using the same technique, derived an equivalent expression for the dynamic ERR of the DCBs under constant-opening-rate displacement as

$$G = \frac{9EIv^2t^2}{ba^4} - \frac{33\rho Av^2}{140b}. \tag{4.4}$$

Eqs. (4.3) and (4.4) are theoretically equivalent as shown by Eq. (3.24) (Section 3.2.5), but they imply a difference of what experimental data should be recorded in DCB tests to determine the fracture toughness (or critical ERR). In Smiley and Pipes's work, the critical load P_c for crack initiation was supposed to be recorded and used in Eq. (4.3), whereas Blackman et al. [20] proposed that the time for crack initiation should be employed instead. This argument came from experimental observations of a considerable oscillation in the externally applied force at high loading rates (Figure 4.1), and so this load could not be accurately recorded for crack initiation. Smiley and Pipes's approach was nevertheless suitable for their own study [17] since the maximum opening rate was 0.67 m s^{-1} whereas the maximum opening rate in Blackman et al.'s study was up to 15 m s^{-1}.

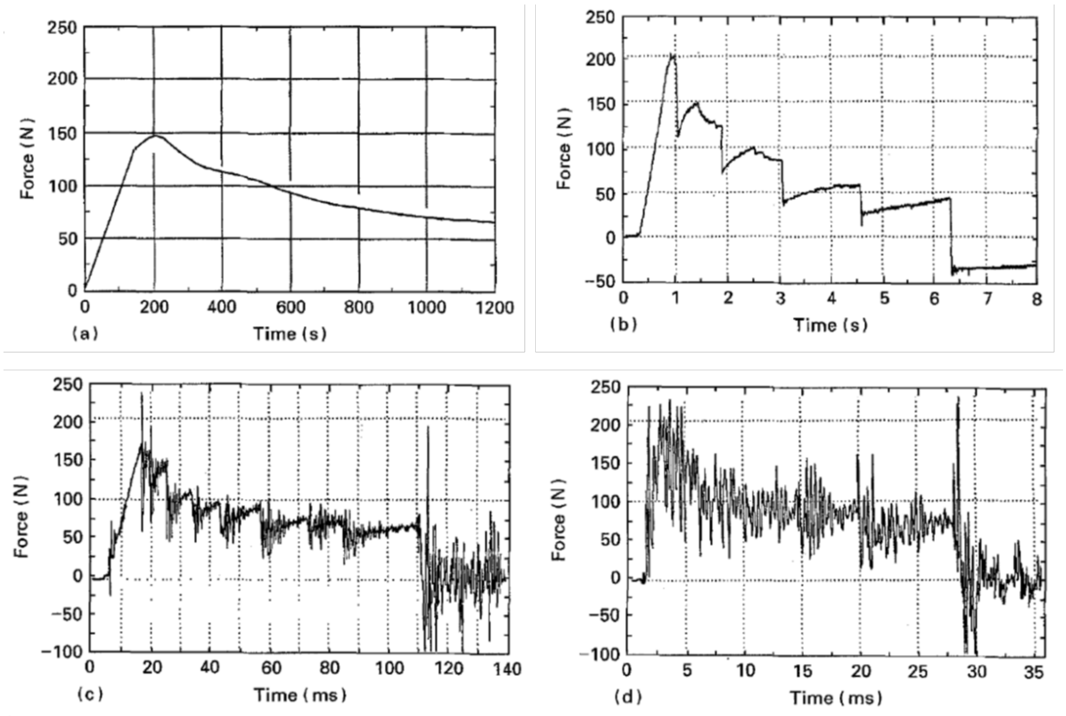

Figure 4.1 Typical external load versus time curves for PEEK/carbon-fibre composite DCB tests conducted at a constant opening rate of (a) 3.3×10^{-5} m s^{-1}, (b) 1×10^{-2} m s^{-1}, (c) 5×10^{-1} m s^{-1}, (d) 2 m s^{-1} [19]. Reproduced with permission from B. R. K. Blackman, J. P. Dear, A. J. Kinloch, H. Macgillivray, Y. Wang, J. G. Williams, and P. Yayla, J. Mater. Sci., 30, 1995. © Springer Nature

4.2.1.2 Propagating cracks in DCBs

Based on the same theoretical principle of including the kinetic energy of the quasi-static motion in the global energy balance, Blackman et al. [20] proposed a dynamic ERR solution for a propagating crack in DCBs. The kinetic energy was calculated from the transverse velocity, but this time including a contribution from crack propagation, that is,

$$\dot{w}(x) = \frac{dw}{dt} + \dot{a}\frac{dw}{da}, \tag{4.5}$$

where $\dot{a}$ is the crack propagation speed and $\dot{a}dw/da$ is the contribution from the crack propagation.

This method seems plausible, but it depends on how the crack-propagation speed $\dot{a}$ is determined. Blackman et al. [20] assumed the continuous crack propagation with $G = G_c$ at all the times after initiation, and constant fracture toughness. According to the quasi-static solution by Eq. (3.25), these assumptions give a crack propagation speed of $\dot{a} = a/(2t)$. Based on this crack-propagation speed, the total kinetic energy (with a factor of two due to symmetry) is

$$K = 2 \cdot \frac{1}{2} \rho A \int_0^a \left(\frac{dw}{dt} + \dot{a} \frac{dw}{da} \right)^2 dx = \frac{111}{280} \rho A a v^2 , \tag{4.6}$$

Thus, using the global approach via Eq. (3.34), the total dynamic ERR for a propagating crack is

$$G = \frac{9EIv^2t^2}{ba^4} - \frac{111\rho A v^2}{280b} . \tag{4.7}$$

Comparing Eqs. (4.4) and (4.7) demonstrates that the ERR of a steadily propagating crack is less than that of a stationary crack due to higher kinetic energy of the former.

This method to determine the ERR of a propagating crack has some intrinsic shortcomings. One is that fracture toughness can be rate-dependent under high loading rates, and another is that experimental observations of DCB tests at high loading rates show that crack propagation is not continuous but, in fact, non-smooth with a mixture of stable growth, fast unstable growth and arrest. This crack-propagation behaviour is referred to as ‘stick-slip’ propagation, and was widely observed in many studies [19][82][91][92][93][94][95]. Together, this means that the crack-propagation speed will not in general follow $\dot{a} = a/(2t)$. That said, however, the kinetic-energy contribution in the second term of Eq. (4.7) is small compared to the strain-energy contribution (first term), and so the method could still be applicable for the low opening rates. In any case, the conventional approach to modelling dynamic interfacial fracture cannot capture stick-slip propagation and instead provides a ‘smoothed’ dynamic ERR.

4.2.2 Mode-II fracture

Dynamic mode-II interfacial fracture, compared to mode-I, received less research attention. The most common configurations to study mode-II fracture in the quasi-static loading regime are ENF [12][93][96] and ELS [14][97][98] specimens. Other specimen configurations can also be used, for instance, centre notch flexural (CNF) specimens [99][100].

The conventional analytical approach to study the dynamic effect in mode-II fracture is to include the kinetic energy of the extrapolated quasi-static motion, similar to as described for mode-I fracture. In this way, ENF [18], ELS [88] and CNF [86] configurations were considered. A crack growth in the ENF configuration is unstable (Section 3.2.5) and, thus, it can only be used to investigate crack initiation. For ELS specimens, as reported in [88], the dynamic effect was negligible, contributing less than 1% to the measured fracture-toughness value. It was therefore assumed in [88] that the dynamic contribution was also negligible for propagating cracks in ELS specimens, and so no analytical model for propagating cracks was developed.

4.2.2.1 Stationary cracks in ENF specimens

Smiley and Pipes [18] conducted tests using ENF specimens to study the rate sensitivity of mode-II interlaminar fracture toughness. To support this, they developed the following analytical solution for the dynamic ERR accounting for the kinetic-energy contribution for the ENF specimen with the crack-length ratio $a/L = 0.5$ (Figure 3.3c):

$$G = \frac{3P^2a^2}{64bEI} + 0.078\frac{\rho A v^2}{b}. \tag{4.8}$$

Eq. (4.8) was still based on global approach $G^{\mathrm{global}} = d(W_{\mathrm{ext}} - U - K)/dA_0$, with the kinetic energy determined by extrapolating the externally applied constant velocity v from the crosshead speed of the test machine.

The kinetic-energy contribution to the fracture toughness measured in their experiments using Eq. (4.8) was, however, negligible [18]. It contributed less than 0.01% for applied velocities between 4.6×10^{-6} and 9.2×10^{-2} m s^{-1}. Kusaka et al. [84] conducted a mode-II fracture test using Hopkinson bars. They measured the kinetic energy term in Eq. (4.8) as ranging from 0.2 to 3%, and concluded that the dynamic effect could be ignored. Cantwell [101] came to the same conclusion as the second term in Eq. (4.8) contributed less than 0.05% in their experiments with loading rates up to 3 m s^{-1}.

4.2.2.2 Stationary cracks in ELS specimens

The conventional dynamic ERR solution for the ELS specimen was given by [88]. The same analytical approach was applied, but the kinetic-energy contribution due to the extrapolated quasi-static motion from the applied constant loading velocity was derived as a function of crack-length ratio η, where $\eta = a/L_0$ (Figure 3.3b). The total ERR was derived as

$$\begin{aligned} G = & \frac{108EIa^2v^2t^2}{b\left(L^3+3L^2a+3La^2+4a^3\right)^2} \\ & -\frac{\rho A v^2}{b}\left[\frac{\eta^2}{\left(1+3\eta^3\right)^3}\left(-\frac{297}{70}+9\eta-\frac{9}{2}\eta^2+\frac{9}{5}\eta^4+\frac{27}{10}\eta^5+\frac{459}{70}\eta^7\right)\right]. \end{aligned} \tag{4.9}$$

The kinetic-energy contribution to the ERR – the last term in Eq. (4.9) – is still very small compared to the ERR component due to the quasi-static component, the first term in Eq. (4.9). As reported in [88], for the epoxy/carbon-fibre composite specimen under 5 m s^{-1} loading rate and with crack length ratio $\eta = 0.6$, the kinetic-energy contribution from the second term in Eq. (4.9) was only 5 N m^{-1}, while the quasi-static component from the first term in Eq. (4.9) was 800 N m^{-1}. It was therefore concluded in [88] that the kinetic-energy contribution could be ignored. Note that the kinetic-energy contribution to the total dynamic ERR in Eq. (4.9) was not always positive or negative but dependent on the crack length ratio η. A plot of normalised kinetic contribution to the ERR against η with the ranging from 0.025 to 0.975 is shown in Figure 4.3, which demonstrates the kinetic contribution to the ERR is (–0.18 ~ 0.15)$\rho A v^2/b$ approximately.

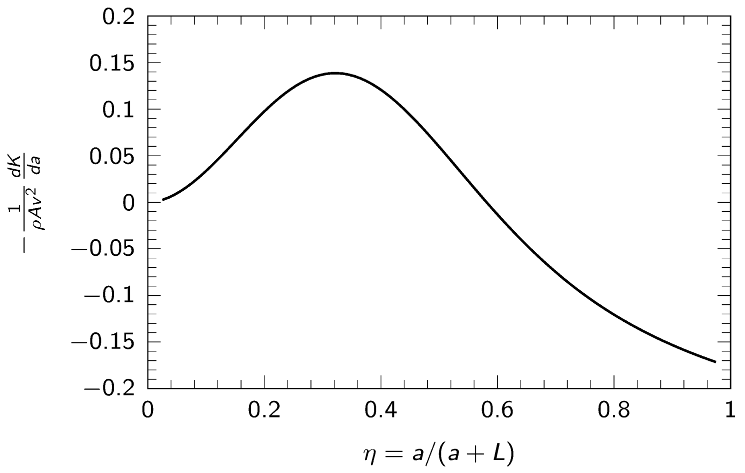

Figure 4.2 Normalised kinetic-energy contribution to ERR versus crack length ratio

4.2.2.3 Stationary cracks in CNF specimens

Maikuma et al. [86] conducted experiments using the CNF specimen (Figure 4.3) under impact loading to study the dynamic mode-II fracture behaviour of CFRPs and developed an analytical solution for the ERR to post-process the experimental data.

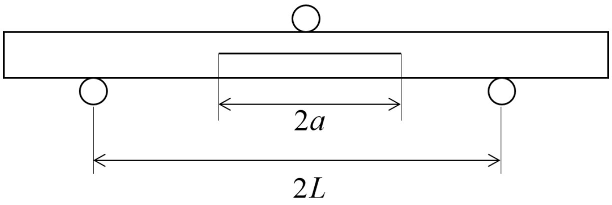

Figure 4.3 Configuration of CNF test specimen

The dynamic ERR solution for the CNF specimen with crack-length ratio $a/L = 0.5$ is

$$G = \frac{3P^2a^2}{256bEI} - 0.633\frac{\rho Av^2}{b}, \tag{4.10}$$

where P is determined by the impact load history, and v is the impact velocity. The latter ranged in their experiments from 1.25 m s^{-1} to 3.00 m s^{-1}, and within this range, they found the kinetic-energy contribution from the second term in Eq. (4.10) to be less than 1%.

4.3 Numerical method

The numerical method, as the third method to study physical and mechanical problems, is a compensation for the limitations of analytical and experimental methods. And computational fracture mechanics as a branch of solid mechanics is established including various numerical techniques to solve the relevant problems in fracture mechanics field [102][103][104].

4.3.1 Numerical methods for fracture mechanics

The numerical method in solid mechanics requires discretising the continuous structure, and there are mainly two methods of doing so: mesh-related methods and meshfree methods (or meshless methods). And then by solving the general equilibrium equations of Eq. (4.11), the displacement field can be obtained and then used to calculate relevant parameters for fracture mechanics.

$$[M]\{\ddot{u}\}+[C]\{\dot{u}\}+[K]\{u\}=\{R\}, \tag{4.11}$$

where $[M]$, $[C]$, $[K]$ are the mass matrix, damping matrix, and stiffness matrix; $\{R\}$ is the external load vector; $\{u\}$ is the displacement vector. Note that for quasi-static problems, the mass matrix and damping matrix are zero; and for linear elastodynamics, the damping matrix is zero.

4.3.1.1 Meshfree method and fracture mechanics

One of the major incentives of using meshfree methods is to overcome the difficulty in mesh-related methods to address the large deformation associated with mesh distortion in crack propagation, material damage, impact and penetration, etc. In fracture modelling, for instance, the FEM does not allow the crack to propagate through the element (except XFEM) and requires re-meshing and mapping, which can be computationally expensive and inaccurate.

Meshfree methods originated from 1977 with the development of smoothed particle hydrodynamics (SPH), which was aimed for modelling astrophysics [105], and has been applied in fluid dynamics and solid mechanics [106].

Generally, the meshfree method discretises the continuous structure into nodal points, which carry the field variables. After discretion, an approximation method is used to estimate the field variable of a particular nodal point through the other nodal points around. For instance, SPH takes the weighted average of the field variables of the other nodal points around within a spatial domain Ω shown in Figure 4.4 via kernel function Eq. (4.12), and the field variable for the given nodal points can be determined as

$$f(x)=\int_{\Omega} f(x')W(x-x',h)\,dx', \tag{4.12}$$

where $W(x-x',h)$ is the kernel function, and h is the smoothing length. As shown in Figure 4.4, $W(x-x',h)$ is used to assess the field variables of the particle i using weighted averaged summations over particle j within the support domain within cut-off distance related to smoothing length h.

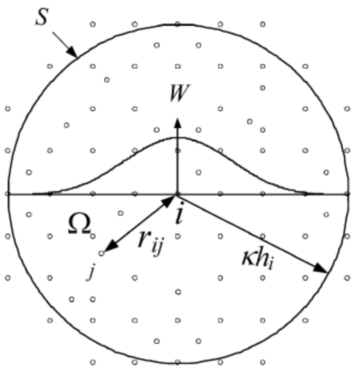

Figure 4.4 SPH particle approximations in a 2D domain Ω with a surface S [107]. Reproduced with permission from M. B. Liu and G. R. Liu, Arch. Comput. Methods Eng, 17, 2010 © Springer Nature

The kernel domain in SPH is truncated by the cut-off distance shown in Figure 4.4, and this can result in inaccuracy when solving fracture problem. Modifying the kernel function to address this issue leads to modified SPH [108] and continuous SPH method [109], and they were used to derive dynamic SIFs for a central crack in a plate subjected to dynamic tensile loading, showing great potential.

Other meshfree methods consider different approximations. For example, using moving least squares (MLS) method leads to element-free Galerkin method (EFGM) [110], and this method was applied to simulate and solve various fracture problems, such as static and dynamic SIFs [111][112][113], mode-mixity [114], delamination in composites [115], impact fracture [116].

4.3.1.2 Finite-element method and fracture mechanics

The FEM is the dominant method in mesh-related numerical methods among the other methods, such as finite-difference method (FDM), finite-volume method (FVM), and it has been integrated into several commercial codes.

In FEM, unlike the meshfree method, the structure is discretised into elements and these elements are connected by nodes. The field variables, for instance, displacements of the nodes are derived by Eq. (4.11) first, and then are used to interpolate inside each element via shape functions in contrast to the kernel function in meshfree methods.

In the field of fracture mechanics, several numerical techniques were developed and well-incorporated into FEM to solve fracture problems, such as quarter-point elements

[117][118], the virtual-crack-extension method [119][120], the virtual-crack-closure technique (VCCT) [121], the extended-finite-element method (XFEM) [122][123], etc.

Quarter-point elements shown in Figure 4.5 were developed with the possibility to simulate the singularity exactly at the crack tip by shifting mid-side nodes to quarter-side position and modifying isoparametric elements with a quadratic shape function, the application of quarter-point elements in the dynamic fracture field to generate dynamic SIFs can be found in [124].

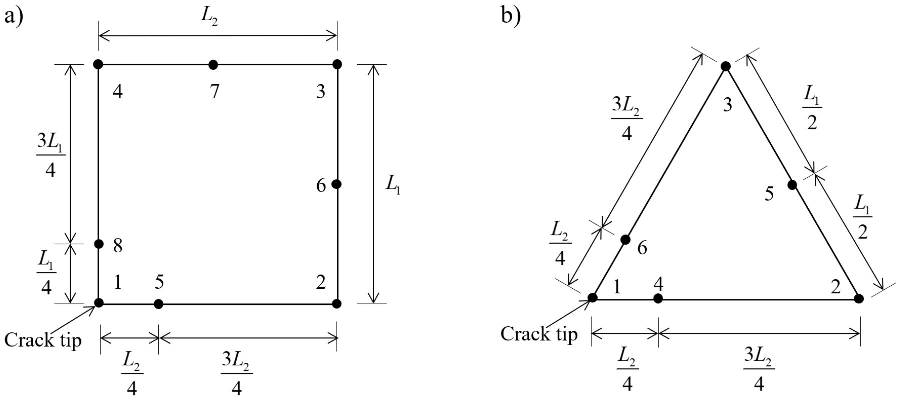

Figure 4.5 Quarter-point elements: (a) 8-noded quadrilateral element; (b) 6-noded triangular element

Virtual-crack-extension method considers a perturbation of crack-tip location Δl as if crack advanced and calculates the response of stiffness matrix, that is, the derivative of stiffness matrix with respect to the crack length perturbation, and this derivative is used to calculate the global energy change, which is the ERR. The limitation of this method is the determination for the length of this virtual extension Δl and derivative of the stiffness matrix needs additional computational process.

XFEM introduces enrichment functions into classical finite elements based on the partition of unity method, and the combined displacement vector becomes

$$u=\sum_{i=1}^{N} N_i\left(x\right)\left[u_i+H\left(x\right)a_i+\sum_{\alpha=1}^{4} F_\alpha\left(x\right)b_i^\alpha\right], \tag{4.13}$$

where $N_i\left(x\right)$ is the classical shape function, u_i is the continuous displacement derived from classical FEM solution, a_i and b_i^α are the nodal enriched degree of freedom vector, $H(x)$ is the discontinuous function, $F_\alpha\left(x\right)$ is the elastic asymptotic crack-tip function. XFEM allows the crack to propagate ‘through’ the classical elements as in Figure 4.6.

The various general dynamic fracture problems have been studied by XFEM [125][126][127][128][129], such as generating dynamic SIFs, dynamic ERRs, dynamic crack propagation and arrest.

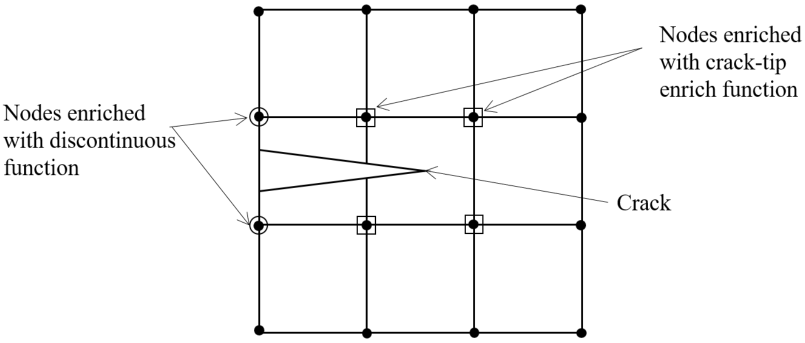
Nodes enriched with crack-tip enrich function
Nodes enriched with discontinuous function
Crack

Figure 4.6 Enrichment scheme for XFEM: the circled nodes are enriched with discontinuous function and the squared nodes are enriched with crack-tip enrich functions

4.3.2 Numerical techniques for interfacial fracture mechanics

4.3.2.1 Virtual-crack-closure technique (VCCT)

The VCCT is based on Irwin's crack closure integral that the energy dissipated with crack extension Δa is equal to the amount of work needed to close the crack. In Cartesian coordinates, for a 2D problem, the mode-I and mode-II crack closure integrals are

$$G_{\mathrm{I}} = \lim_{\Delta a \to 0} \frac{1}{2\Delta a} \int_0^{\Delta a} \sigma_{22}(x) u_2(x - \Delta a) dx, \tag{4.14}$$

$$G_{\mathrm{II}} = \lim_{\Delta a \to 0} \frac{1}{2\Delta a} \int_0^{\Delta a} \sigma_{12}(x) u_1(x - \Delta a) dx. \tag{4.15}$$

To directly incorporate Eqs. (4.14) and (4.15) into FEM, the nodal force at the crack-tip node before crack extension and the nodal displacement after crack extension for the original crack-tip node are needed, and this is referred as "two-step VCCT". To simplify this process, Rybicki and Kanninen [121] proposed that displacement before crack extension behind the crack-tip node can be used to replace the displacement at the crack-tip node after crack extension, assuming crack propagation is self-similar. In the quadrilateral elements shown in Figure 4.7, the mode-I and mode-II ERR components are

$$G_{\mathrm{I}} = -\frac{1}{2\Delta a} F_i^y \left(v_l - v_{l^*} \right), \tag{4.16}$$

$$G_{\mathrm{II}} = -\frac{1}{2\Delta a} F_i^x \left(u_l - u_{l^*} \right), \tag{4.17}$$

where Δa is the element length, F_i^y and F_i^x are the force components at the crack-tip node i, v_l and u_l are the displacement components for the node l, v_{l^*} and u_{l^*} are the displacement components for the node l^*.

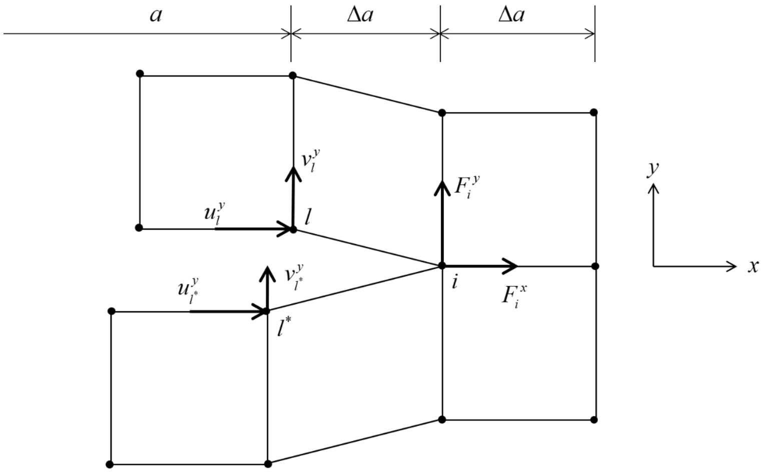

Figure 4.7 VCCT for 2D quadrilateral elements

Note that if the displacements and nodal forces are solved in the dynamic equilibrium as per Eq. (4.11), the displacements and nodal forces will carry the dynamic (inertial) effects implicitly and thus the VCCT has a potential to calculate dynamic ERRs or dynamic SIFs. Jih and Sun [130] used the VCCT to study the dynamic SIF for a central crack in a panel under transient loading, and an excellent agreement with the classical analytical result [36] was achieved. Tsai et al. [131] used the VCCT to calculate dynamic mode-II ERR for ENF specimen using experimentally determined the crack length curve to determine the dynamic fracture toughness. Qian and Xie [132] developed a VCCT interface element to study the dynamic fracture behaviour for the mode-mixity.

4.3.2.2 Cohesive zone modelling (CZM)

The cohesive zone concepts were believed originated by Dugdale [133] and Barenblatt [134]: Dugdale studied a plastic zone ahead of the crack tip of steel slits and assumed the stress is constant as the yield strength, whereas Barenblatt believed that in this softening zone, the stress varies. Hillerborg et al. [135] were the first to incorporate this concept into FEM to study the crack in a concrete beam. Their assumption was that the crack will begin to initiate when the stress at crack tip reaches tensile strength $\sigma_{\max}$, but this stress will not drop to zero immediately; rather, it will fall, for instance, linearly with crack opening width and reach to zero for a given opening width of δ_f as shown in Figure 4.8a, where δ_f represents opening displacement at complete failure. This constitutive behaviour is referred to as bilinear traction-separation law. Other types of traction-separation laws were also developed, such as trapezoidal law [136] (Figure 4.8b), perfectly plastic law [137] (Figure 4.8c), polynomial law [138], exponential law [139] (Figure 4.8d).

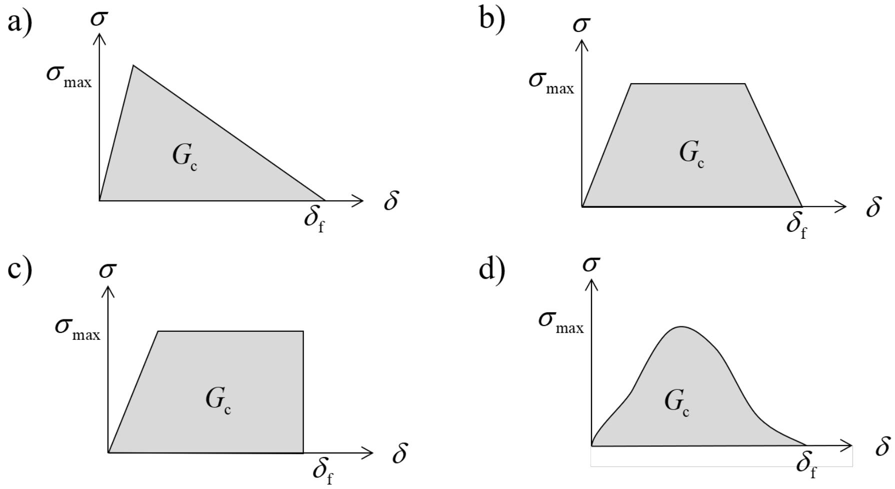

Figure 4.8 Traction-separation laws

Another important aspect of these traction-separation laws is the area that they form represents the energy absorbed by the crack until the complete failure, and in this sense, it is also the critical ERR or fracture toughness, given by

$$G_c = \int_0^{\delta_f} \sigma d\delta, \tag{4.18}$$

where δ is the crack opening displacement.

Therefore, the advantage of CZM over VCCT is that it can predict both crack initiation and propagation. The implementation of CZM into FEM can be achieved by spring elements, cohesive elements and contact algorithms. One of the issues with CZM is the determination of its mesh size, that is, for the accuracy of the simulation the mesh size must be efficiently small than a critical length, and this has been extensively studied, such as in [140][141]. For further application of CZM concepts in dynamic fracture field, rate-dependent cohesive model [142] and time-dependent cohesive segments method [143] were developed.

But a recent study [22] used both rate-independent and rate-dependent CZM to simulate the DCB tests in [19][20] and it is found that CZM could not reproduce the ‘stick-slip’ crack propagation behaviour (see Section 4.2.1.2) observed in experiments, and the researchers then resorted to the interfacial thick-level-set modelling (ITLSM), which demonstrates the ability to capture this non-smooth crack propagation behaviour.

4.3.2.3 Interfacial thick-level-set modelling (ITLSM)

The original motivations to include level-set method [144] to investigate fracture problems numerically are: (1) to overcome the mesh size limitation of CZM for larger elements to be used; (2) to simulate non-self-similar crack propagation in contrast to the VCCT, and related studies can be found in [145][146].

The thick-level-set method was first proposed by Moës et al. [147] in 2011, in which they introduced a fixed damaged band length l_c for the damage zone. A comparison of this damage zone to a cohesive zone is given in Figure 4.9 from [148], and a comprehensive comparison of these two methods is also given in the same reference. By the non-local treatment for this damage zone within the length l_c, thick-level-set model avoids spurious localisation; inside the damaged band, a damage function is assigned to determine the damage variable d with respect to the level-set field, and this distributed damage variable is used to calculate the ERR over the length l_c [149], whereas in CZM the ERR is calculated locally.

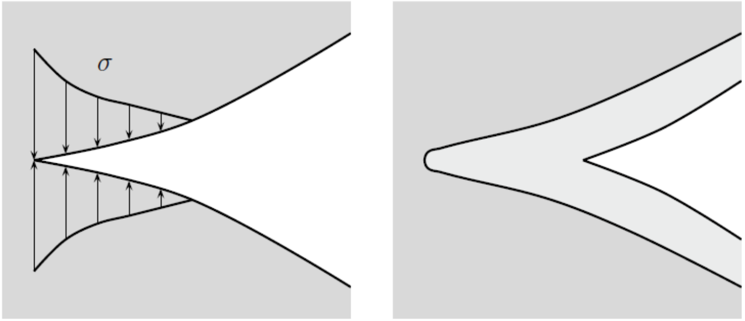

a Cohesive zone. **b** Thick level set model.

Figure 4.9 Comparison for an opening crack with (a) cohesive zone; (b) thick level set damage zone [148]. Reproduced from permission from A. Gómez, N. Moës, and C. Stolz, Adv. Model. Simul. Eng. Sci, 2, 2015. © Springer Nature

Recently, the ITLSM incorporates the thick-level-set concept to study the interfacial fractures [22][149], showing great potential over CZM, especially for the capture of fracture behaviour such as ‘stick-slip’ crack propagation behaviour in DCBs with crack arrest phenomenon. Liu et al. [22] applied rate-independent and rate-dependent CZM to simulate the experimentally observed crack propagation in DCBs under high loading rate from [19][20] as well as using the ITLSM. The comparisons of experimental and numerical results showed that the rate-dependent CZM improved simulation result compared to the rate-independent CZM, but, still, they both cannot capture the crack arrest phenomenon observed in experiments; the ITLSM, however, demonstrated an excellent agreement with the experimental results.

4.3.2.4 Experimental-numerical hybrid method

The experimental-numerical hybrid method is usually used when there are no available analytical solutions to post-process the experimental data. Experimentally measured parameters, such as external force, crack length versus time curve, crack-propagation speed, are incorporated into numerical models, and the desired fracture parameters, e.g. ERR and fracture toughness, are calculated by FEM simulations.

Nishioka and Atluri [150] introduced an experimentally obtained crack length-time curve for a wedge-loaded DCB into finite-element models with their developed singular elements to determine the dynamic SIF. Guo and Sun [151] incorporated a similar curve for a DCB into a finite-element model and developed a scheme of sequentially releasing nodes to calculate the dynamic ERR as

$$G = -\frac{1}{\Delta a}\left(\Delta\mathrm{ALLSE} + \Delta\mathrm{ALLKE}\right), \tag{4.19}$$

where ALLSE is the total elastic strain energy and ALLKE is the total kinetic energy, both directly obtained in FEM simulations. Tsai et al. [131] followed the same approach to study mode-II fracture in ENF specimen. They used the VCCT to calculate the dynamic ERR and obtained results, which were demonstrated to be equivalent to that derived with Eq. (4.19). Kumar and Kishore [152] studied DCBs under impact loading, and used the experimentally measured deflection and crack-propagation speed to calculate the J-integral to determine the fracture toughness. Liu et al. [21] conducted DCB tests under impact using Hopkinson bars, and incorporated experimental data into finite-element model with the VCCT to determine the fracture toughness. Subsequently, Liu et al. [90] also used the CZM to post-process experimental data to determine the fracture toughness.

Note that Refs. [21][90] also confirmed the oscillating characteristic of ERR before crack initiation, which the conventional analytical approaches (Section 4.2) do not capture with their developed ‘smoothed’ ERR solution.

4.4 Conclusion

The conventional analytical approaches for dynamic interfacial fracture are reviewed in this chapter, which are based on the global approach (Section 3.3.2.1) including kinetic energy to account for the dynamic effect. This kinetic energy only considers the quasi-static motion by extrapolating the applied velocity along the beam section of DCB, ENF and ELS configurations. This method provided a ‘smoothed’ dynamic ERR, and the kinetic-energy contribution is a baseline shift for the dynamic ERR from its quasi-static component. But surprisingly post-processing the experimental data using these conventional analytical solutions shows that the dynamic effects under high loading rates are negligible. Other experimental and numerical investigations, however, show that the dynamic ERR, in general, is oscillating, which the conventional analytical approaches do not capture. This oscillation of dynamic ERR is important to understand the contrary rate effects on measured fracture toughness as well as to understand the fracture behaviour, such as crack initiation, propagation and arrest. Therefore, a new analytical framework, which accounts for structural vibration and wave propagation for dynamic interfacial fracture, is required. And this analytical framework is developed in Chapter 5.

In additional, numerical techniques for interfacial fracture are reviewed. The numerical results from these techniques, such as VCCT, CZM and ITLSM, with their ability to study dynamic fracture problems, are used to verify and confirm the developed analytical theories in the later chapters. For a stationary crack, VCCT and CZM are demonstrated adequate to provide accurate numerical results for dynamic ERR; but for a propagating crack, VCCT and CZM could not capture crack arrest behaviour accurately and, therefore, are reckoned not to provide accurate dynamic ERR, and results from ITLSM are desirable.

Chapter 5: Dynamic mode-I interfacial fracture for stationary crack

5.1 Introduction

DCBs are the most fundamental engineering structures to study the mode-I fracture behaviour. The analytical framework for investigating the dynamic interfacial fracture is developed and established on the mode-I stationary cracks in DCBs in this chapter. This is for the first time that structural vibration and wave propagation are taken into consideration to study the dynamic interfacial facture in DCBs. The dynamic response of the DCB is studied analytically by solving the equation of motion together with the time-dependent boundary condition using Grant's method (but derivation is completely new), which allows the dynamic effect due to kinetic energy to be studied; the theoretical development with vibration is found to be erroneous by overlooking the wave propagation properties, i.e. dispersion; to correct this, the energy supplied to the crack-tip for crack propagation is examined in the context of flexural wave propagation, giving *dispersion-corrected global approach*.

5.2 Theoretical development with vibration

To study the dynamic effect on mode-I ERR, equal and opposite time-dependent displacement w_0 (t) are applied to the free-ends of DCB arms (Figure 5.1a). The widely used method for analysing DCB considers the crack region of DCB arm and assumes an effective boundary condition for the crack tip (Figure 5.1b). This condition does not allow the crack tip to rotate and is discussed in Section 5.5. The DCB arm is assumed to be thin, where $h << a$, and a classical idea of Euler-Bernoulli beam applies; the displacement is small, and no longitudinal forces are developed. In addition, no interfacial contact is assumed between two DCB arms, and the DCB arm with the effective boundary condition (Figure 5.1b) can vibrate freely.

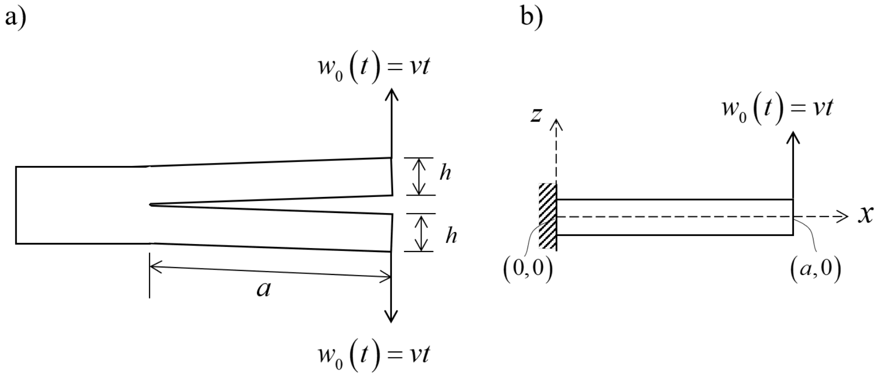

Figure 5.1 DCB configuration for stationary crack: (a) symmetric double cantilever beam; (b) effective boundary condition and prescribed coordinates

The dynamic response of the DCB arm under time-dependent displacement $w_0\ (t)$ is solved by Grant's method for time-dependent boundary condition as per Section 2.2.3, which lays the foundation for the analytical framework to study dynamic interfacial fracture.

5.2.1 Dynamic response of thin beam

For the DCB arms under constant-opening rate v with the corresponding displacement $w_0\ (t) = vt$, the dynamic transverse response (deflection) of the DCB arm shown in Figure 5.1b can be derived by introducing a shifting function, the transverse deflection of the beam is of the form

$$w(x,t)=w_{\mathrm{fv}}(x,t)+F(x)vt\,, \tag{5.1}$$

where $w_{\mathrm{fv}}\ (x, t)$ is the free-vibration component and $F\ (x)$ is the shifting function. Note that the product of applied displacement $w_0\ (t) = vt$ and shifting function $F\ (x)$ represents the quasi-static motion of the DCB arm, and, therefore, the total dynamic response is deemed to be a combination of free vibration and quasi-static motion.

Combining Eqs. (2.6) (the equation of motion for vibration) and (5.1), and enforcing homogeneous conditions, the equation of motion for the free-vibration component $w_{\mathrm{fv}}\ (x, t)$ and governing equation for the shifting function $F\ (x)$ are obtained as

$$EIw_{\mathrm{fv}}^{(4)}(x,t)+\rho A\ddot{w}_{\mathrm{fv}}(x,t)=0\,, \tag{5.2}$$

$$F^{(4)}(x)=0\,. \tag{5.3}$$

The boundary conditions for total deflection $w(x, t)$ are $w(0, t) = 0$, $w^{(1)}(0, t) = 0$, $w(a, t) = vt$ and $w^{(2)}(a, t) = 0$. Using these boundary conditions for $w(x, t)$ in Eq. (5.1) and forcing homogeneous conditions again, the boundary conditions for the free-vibration component $w_{\text{fv}}(x, t)$ and the shifting function $F(x)$ are obtained in Table 5.1.

Table 5.1 Boundary conditions for total deflection and its components

Boundary	Total deflection $w(x,t)$	Free-vibration component $w_{\text{fv}}(x,t)$	Shifting function $F(x)$
$x=0$	$w(0,t)=0$	$w_{\text{fv}}(0,t)=0$	$F(0)=0$
	$w^{(1)}(0,t)=0$	$w_{\text{fv}}^{(1)}(0,t)=0$	$F^{(1)}(0)=0$
$x=a$	$w(a,t)=vt$	$w_{\text{fv}}(a,t)=0$	$F(a)=1$
	$w^{(2)}(a,t)=0$	$w_{\text{fv}}^{(2)}(a,t)=0$	$F^{(2)}(a)=0$

Note that the boundary conditions for the free-vibration component $w_{\text{fv}}(x, t)$ represent a fixed-pinned beam in free vibration.

5.2.1.1 Solution for free-vibration component

The solution for the free vibration for a fixed-pinned beam is a product of normal mode Eq. (2.21) and modal displacement Eq. (2.28) by the method of separation of variables via Eq. (2.7). The only parameters needed now are the initial displacement $w_{\text{fv}}(x,0)$ and initial velocity $\dot{w}_{\text{fv}}(x,0)$ for the free vibration to the determine the initial modal displacement and velocity, respectively.

At $t = 0$, the DCB arm in Figure 5.1b is at rest and thus the transverse deflection at that moment is $w(x,0)=0$ and the transverse velocity is $\dot{w}(x,0)=0$. These initial conditions, together with Eq. (5.1), give the initial conditions for the free-vibration component as $w_{\text{fv}}(x,0)=0$ and $\dot{w}_{\text{fv}}(x,0)=-vF(x)$. The ith initial modal displacement and velocity can thus be determined by Eqs. (2.31) and (2.32), and ith initial modal displacement $T_i(0)$ is found to be zero, and ith initial modal velocity $\dot{T}_i(0)$ depends on the shifting function. Now consider the solution for the shifting function.

5.2.1.2 Solution for shifting function

Solving the governing equation for shifting function $F(x)$ in Eq. (5.3) with the boundary conditions in Table 5.1 gives the shifting function as

$$F\left(x\right)=-\frac{1}{2a^3}x^3+\frac{3}{2a^2}x^2\,. \tag{5.4}$$

The shifting function together with the applied velocity of v gives a velocity distribution along the beam length for the crack region as Figure 5.2 indicates. This velocity distribution $vF(x)$ is also the quasi-static motion of the DCB arm; it has the same expression with the solution for quasi-static motion Eq. (4.1) in the conventional analytical approach, such as in Smiley and Pipes' work [17].

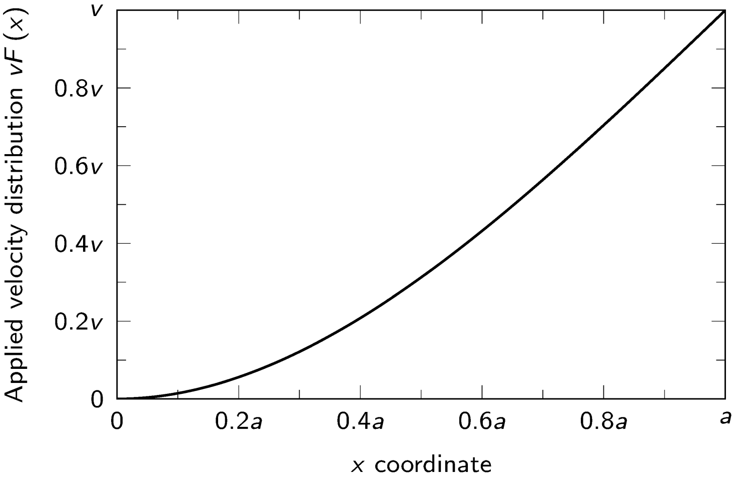

Figure 5.2 Velocity distribution along the DCB arm for the crack region due to applied opening velocity

Therefore, with the initial velocity for the free vibration $\dot{w}_{\text{fv}}\left(x,0\right)=-vF\left(x\right)$, using Eq. (2.32), the *i*th initial modal velocity is found to be

$$\dot{T}_i\left(0\right)=\int_0^a \rho AW_i\left(x\right)\dot{w}_{\text{fv}}\left(x,0\right)dx=v\sqrt{\rho Aa}\,\frac{\Lambda_i}{\lambda_i}, \tag{5.5}$$

where λ_i is the solution for frequency equation Eq. (2.20) and $\Lambda_i=\left(-1\right)^i\sqrt{\sigma_i^2+1}+\sqrt{\sigma_i^2-1}$ with $\sigma_i=\left[\cosh\left(\lambda_i\right)-\cos\left(\lambda_i\right)\right]/\left[\sinh\left(\lambda_i\right)-\sin\left(\lambda_i\right)\right]$. Note that the integration for Eq. (5.5) uses the formulas in Appendix A. The solutions for λ_i, σ_i and Λ_i are given in Table 5.2.

Table 5.2 Modal parameters for fixed-pinned beam in free vibration

Mode number	λ_i	σ_i	Λ_i
1	3.92660231	1.000777304	-1.375327127
2	7.06858275	1.000001445	1.415914585
3	10.21017612	1.000000000	$-\sqrt{2}$
4	13.35176878	1.000000000	$\sqrt{2}$
5	16.49336143	1.000000000	$-\sqrt{2}$
$i > 5$	$(4i + 1)\pi/4$	1.0	$(-1)^i\sqrt{2}$

5.2.1.3 Solution of total deflection

Now, combining solutions in Sections 5.2.1.1 and 5.2.1.2, the total deflection of a DCB arm under the constant-opening rate v at its free end from $t = 0$ is obtained:

$$\begin{aligned} w(x,t) &= va^2\sqrt{\frac{\rho A}{EI}}\sum_{i=1}^{\infty}\frac{\Lambda_i}{\lambda_i^3}\phi_i(x)\sin(\omega_i t)+\left(-\frac{1}{2a^3}x^3+\frac{3}{2a^2}x^2\right)vt \\ &= v\left[a^2\sqrt{\frac{\rho A}{EI}}\sum_{i=1}^{\infty}\frac{\Lambda_i}{\lambda_i^3}\phi_i(x)\sin(\omega_i t)+\left(-\frac{1}{2a^3}x^3+\frac{3}{2a^2}x^2\right)t\right], \end{aligned} \tag{5.6}$$

where $\phi_i(x)$ is the ith mode shape given in Eq. (2.22) and ω_i is the ith mode natural frequency given in Eq. (2.11) for $\omega_i = \lambda_i^2 a^{-2}\sqrt{EI/(\rho A)}$ with $\lambda_i = \beta_i a$.

Note that rather than only accounting for quasi-static motion in the conventional analytical approach in Eq. (4.1), the dynamic response now in Eq. (5.6) also considers the free vibration due to the applied time-dependent displacement, and the significance is that the transverse motion now is a combination of local free vibration and quasi-static motion; their interaction or coupling should also be also considered to study dynamic fracture. Another notion is that the total transverse deflection is proportional to the applied constant-opening rate v, and terms in the bracket in Eq. (5.6) are an inherent property of a given DCB configuration.

5.2.2 Dynamic energy release rate and amplitude divergence

The total transverse deflection in Eq. (5.6) is therefore used to calculate the strain and kinetic energies of the vibrating DCB arm under the applied time-dependent displacement as required to determine the ERR by the global approach in Eq. (3.34) similar to the conventional analytical approach.

5.2.2.1 Strain energy

The strain energy of one DCB arm in Figure 5.1b is $U = \int_0^a M^2\left(x,t\right)dx \Big/ \left(2EI\right)$, where $M(x, t) = EIw^{(2)}(x, t)$, which is the internal bending moment. The strain energy of the vibrating DCB arm with constant-opening rate displacement at its free end by combining the total deflection Eq. (5.6) is therefore

$$U = \frac{1}{2EI}\int_0^a \left\{\left[EIw_{\mathrm{fv}}^{(2)}\left(x,t\right)\right]^2 + 2EIw_{\mathrm{fv}}^{(2)}\left(x,t\right)F^{(2)}\left(x\right)vt + \left[F^{(2)}\left(x\right)vt\right]^2\right\}dx. \qquad (5.7)$$

Let U_{loc}, U_{cp} and U_{st} correspond in order to each of the three terms in Eq. (5.7), representing the strain energy component due to the local vibration, the strain energy component due to the coupling between the local vibration and the quasi-static motion, and the strain energy component due to the quasi-static motion (in the form of the product of the shifting function $F(x)$ and applied velocity v), respectively.

The strain energy component due to the local vibration U_{loc} expands to

$$\begin{aligned} U_{\mathrm{loc}} &= \frac{1}{2EI}\int_0^a \left[a^2 v\sqrt{\rho AEI}\sum_{i=1}^{\infty}\frac{\Lambda_i}{\lambda_i^3}\phi_i^{(2)}\left(x\right)\sin\left(\omega_i t\right)\right]^2 dx \\ &= \frac{1}{2}\rho A a^4 v^2 \int_0^a \lim_{n\to\infty}\left\{\begin{aligned} &\left[\frac{\Lambda_1}{\lambda_1^3}\phi_1^{(2)}\left(x\right)\sin\left(\omega_1 t\right)\right]^2 \\ &+2\frac{\Lambda_1}{\lambda_1^3}\phi_1^{(2)}\left(x\right)\sin\left(\omega_1 t\right)\sum_{j=2}^{n}\frac{\Lambda_j}{\lambda_j^3}\phi_j^{(2)}\left(x\right)\sin\left(\omega_j t\right) \\ &+\left[\frac{\Lambda_2}{\lambda_2^3}\phi_2^{(2)}\left(x\right)\sin\left(\omega_2 t\right)\right]^2 \\ &+2\frac{\Lambda_2}{\lambda_2^3}\phi_2^{(2)}\left(x\right)\sin\left(\omega_2 t\right)\sum_{j=3}^{n}\frac{\Lambda_j}{\lambda_j^3}\phi_j^{(2)}\left(x\right)\sin\left(\omega_j t\right) \\ &+\cdots+\left[\frac{\Lambda_n}{\lambda_n^3}\phi_n^{(2)}\left(x\right)\sin\left(\omega_n t\right)\right]^2 \end{aligned}\right\}dx. \end{aligned} \qquad (5.8)$$

By the orthogonality condition in Eq. (2.17), U_{loc} simplifies to

$$U_{\mathrm{loc}} = \frac{1}{2}\rho A a v^2 \sum_{i=1}^{\infty} \frac{\Lambda_i^2}{\lambda_i^2} \sin^2\left(\omega_i t\right). \tag{5.9}$$

Eq. (5.9) suggests that the total strain energy component due to the local vibration is a summation of each orthogonal vibration mode's strain energy, and there is no coupling between different vibration modes for the total strain energy due to the local vibration.

Next, by expanding the strain energy component due to the coupling between the local vibration and the quasi-static motion, it is found to be zero, i.e. $U_{\mathrm{cp}} = 0$ (the formulas in Appendix A are applied). This shows that for this strain energy component, the local vibration does not affect the quasi-static motion, and vice versa, and their synergy is zero.

And then, by expanding the strain energy component due to the quasi-static motion, U_{st} is found to be

$$U_{\mathrm{st}} = \frac{3EIv^2t^2}{2a^3}. \tag{5.10}$$

Thus, the total strain energy is as follows:

$$U = \frac{1}{2}\rho A a v^2 \sum_{i=1}^{\infty} \frac{\Lambda_i^2}{\lambda_i^2} \sin^2\left(\omega_i t\right) + \frac{3EIv^2t^2}{2a^3}. \tag{5.11}$$

5.2.2.2 Kinetic energy

The kinetic energy of one DCB arm in Figure 5.1b is $K = \rho A \int_0^a \left[\dot{w}\left(x,t\right)\right]^2 dx \big/ 2$, and by combining Eq. (5.6), the total kinetic energy is

$$K = \frac{1}{2}\rho A \int_0^a \left[\dot{w}_{\mathrm{fv}}^2\left(x,t\right) + 2\dot{w}_{\mathrm{fv}}\left(x,t\right)F\left(x\right)v + v^2F^2\left(x\right)\right]dx. \tag{5.12}$$

Note that $\dot{w}_{\mathrm{fv}}\left(x,t\right)$ is the transverse velocity of the local vibration, and the product of $vF(x)$ is transverse velocity due to the quasi-static motion. In a similar way to before as for the strain energy, let K_{loc}, K_{cp}, and K_{st} correspond in order to each three terms in Eq. (5.12), representing the kinetic energy component due to the local vibration, the kinetic energy component due to the coupling between the local vibration and the quasi-static motion, and the kinetic energy component due to the quasi-static motion, respectively.

The local vibration kinetic energy component K_{loc} expands to

$$
\begin{aligned}
K_{\mathrm{loc}} &= \frac{1}{2}\rho A \int_0^a \left[v \sum_{i=1}^{\infty} \frac{\Lambda_i}{\lambda_i} \phi_i(x) \cos(\omega_i t) \right]^2 dx \\
&= \frac{1}{2}\rho A v^2 \int_0^a \lim_{n\to\infty} \left\{
\begin{array}{l}
\left[\dfrac{\Lambda_1}{\lambda_1} \phi_1(x) \sin(\omega_1 t) \right]^2 \\
+2\dfrac{\Lambda_1}{\lambda_1} \phi_1(x) \sin(\omega_1 t) \displaystyle\sum_{j=2}^{n} \dfrac{\Lambda_j}{\lambda_j} \phi_j(x) \sin(\omega_j t) \\
+\left[\dfrac{\Lambda_2}{\lambda_2} \phi_2(x) \sin(\omega_2 t) \right]^2 \\
+2\dfrac{\Lambda_2}{\lambda_2} \phi_2(x) \sin(\omega_2 t) \displaystyle\sum_{j=3}^{n} \dfrac{\Lambda_j}{\lambda_j} \phi_j(x) \sin(\omega_j t) \\
+\cdots+\left[\dfrac{\Lambda_n}{\lambda_n} \phi_n(x) \sin(\omega_n t) \right]^2
\end{array}
\right\} dx.
\end{aligned}
\tag{5.13}
$$

As the same for the strain energy, by applying the orthogonality of normal modes in Eq. (2.16), the kinetic energy component due to the local vibration simplifies to

$$
K_{\mathrm{loc}} = \frac{1}{2}\rho A a v^2 \sum_{i=1}^{\infty} \frac{\Lambda_i^2}{\lambda_i^2} \cos^2(\omega_t t). \tag{5.14}
$$

By expanding the remaining terms, the kinetic energy component due to the coupling between the local vibration and the quasi-static motion is obtained as

$$
K_{\mathrm{cp}} = -\rho A a v^2 \sum_{i=1}^{\infty} \frac{\Lambda_i^2}{\lambda_i^2} \cos(\omega_i t), \tag{5.15}
$$

and the kinetic energy component due to the quasi-static motion is derived as

$$
K_{\mathrm{st}} = \frac{33}{280} \rho A a v^2 . \tag{5.16}
$$

Note that the kinetic energy component due to the quasi-static motion K_{st} is the total kinetic energy used in the conventional analytical approach in Eq. (4.2). In this study, the kinetic energy component due to vibration is also included, which is (K_{loc} + K_{cp}).

Therefore, the total kinetic energy is as follows:

$$
K = \frac{1}{2}\rho A a v^2 \sum_{i=1}^{\infty} \frac{\Lambda_i^2}{\lambda_i^2} \cos^2(\omega_t t) - \rho A a v^2 \sum_{i=1}^{\infty} \frac{\Lambda_i^2}{\lambda_i^2} \cos(\omega_i t) + \frac{33}{280} \rho A a v^2 . \tag{5.17}
$$

5.2.2.3 Dynamic energy release rate

The dynamic ERR of the DCB shown in Figure 5.1a (i.e. comprising two single arms in Figure 5.1b with equal and opposite displacements) is now obtained using the global approach in Eq. (3.34) $G^{\mathrm{global}} = d(W_{\mathrm{ext}} - U - K)/dA_0$, accounting for a global energy balance together with Eqs. (5.11) and (5.17) (under displacement control $W_{\mathrm{ext}} = 0$), which gives

$$\begin{aligned} G &= \frac{1}{b}\frac{d}{da}\left(W_{\mathrm{ext}} - U - K\right) \\ &= \frac{1}{b}\left\{ \begin{aligned} &\frac{9EIv^2t^2}{a^4} \\ &+\frac{4\sqrt{\rho AEI}v^2t}{a^2}\sum_{i=1}^{\infty}\Lambda_i^2\sin\left(\omega_i t\right) + 2\rho Av^2\sum_{i=1}^{\infty}\frac{\Lambda_i^2}{\lambda_i^2}\cos\left(\omega_i t\right) \\ &-\rho Av^2\sum_{i=1}^{\infty}\frac{\Lambda_i^2}{\lambda_i^2} \\ &-\frac{33}{140}\rho Av^2 \end{aligned} \right\}. \end{aligned} \tag{5.18}$$

Note that the natural frequency ω_i is a function of crack length a via Eq. (2.11) with $\lambda_i = \beta_i a$ giving $\omega_i = \lambda_i^2 a^{-2}\sqrt{EI/(\rho A)}$, and this was taken into account when differentiating the corresponding energy terms to derive dynamic ERR in Eq. (5.18).

In Eq. (5.18), the ERR components with their sources are: (1) the first term is the contribution of the strain energy of the quasi-static motion denoted as $G_{\mathrm{st}}^{\mathrm{U}}$; (2) the second and third terms are due to the kinetic energy of coupling between the local vibration and the quasi-static motion, and the fourth term is due to the strain and kinetic energies of the local vibration, and therefore, these three terms are grouped together and denoted G_{vib} since they are vibration-related ERR component; (3) the last term is the ERR component due to the kinetic energy of the quasi-static motion and denoted $G_{\mathrm{st}}^{\mathrm{K}}$. Thus, the total dynamic ERR now can be written accordingly as

$$\begin{aligned} G &= G_{\mathrm{st}} + G_{\mathrm{vib}} \\ &= G_{\mathrm{st}}^{\mathrm{U}} + G_{\mathrm{st}}^{\mathrm{K}} + G_{\mathrm{vib}}, \end{aligned} \tag{5.19}$$

where G_{st} is the ERR component due to quasi-static motion for $G_{\mathrm{st}} = G_{\mathrm{st}}^{\mathrm{U}} + G_{\mathrm{st}}^{\mathrm{K}}$. Note that $G_{\mathrm{st}}^{\mathrm{K}}$ is also the kinetic-energy contribution in the conventional analytical approach and G_{st} has the same expression as the conventional analytical studies in Eq. (4.4); therefore, actually, in the conventional analytical studies, only the ERR due to quasi-static motion was derived by neglecting the vibration-related ERR component G_{vib}.

5.2.2.4 ERR divergence and ERR with first-vibration-mode accuracy

The total dynamic ERR in Eq. (5.18) is based on the global approach (Section 3.3.2.1) accounting for kinetic-energy contribution via Eq. (3.34) $G^{\text{global}} = d(W_{\text{ext}} - U - K)/dA_0$, which was used extensively in LEFM and the conventional analytical approach for dynamic interfacial fracture; thus, it was supposed to be able to predict the ERR accurately. But a close examination of the ERR derived in Eq. (5.18), particular for the ERR component due to vibration G_{vib}, reveals that the ERR determined in Eq. (5.18) provides a non-physical and non-mechanical solution, since the amplitude of the ERR component due to vibration G_{vib} shows a divergent fashion with adding more vibration modes, and its amplitude is with no bound.

This divergence in the ERR amplitude with including more vibration modes comes from the term of $4\sqrt{\rho AEI}v^2ta^{-2}\sum_{i=1}^{\infty}\Lambda_i^2\sin(\omega_i t)$ in G_{vib}. For the *i*th vibration mode, the amplitude of this ERR component is proportional to Λ_i^2. As Table 5.2 shows, the value of Λ_i can be approximately taken as $\Lambda_i \approx (-1)^i\sqrt{2}$, so $\Lambda_i^2 \approx 2$, and this leads to the phenomenon that by adding more vibration modes the amplitude of G_{vib} keeps increasing.

This phenomenon of divergence is also shown in Figure 5.8 (Section 5.4.2). But the verification demonstrates that the dynamic ERR with only the first vibration mode can capture the oscillation in the result from FEM and seems to be the envelope, and, therefore, the dynamic ERR with the first-vibration-mode accuracy is proposed as

$$G = \frac{1}{b}\left\{\begin{aligned} &\frac{9EIv^2t^2}{a^4} - \frac{33}{140}\rho Av^2 \\ &+\frac{4\sqrt{\rho AEI}v^2t}{a^2}\Lambda_1^2\sin(\omega_1 t) + 2\rho Av^2\frac{\Lambda_1^2}{\lambda_1^2}\cos(\omega_1 t) - \rho Av^2\frac{\Lambda_1^2}{\lambda_1^2}\end{aligned}\right\}. \tag{5.20}$$

Note that the first vibration mode has the lowest natural frequency, and therefore Eq. (5.20) is approximately applicable when the duration of the external load is long for low-frequency vibration mode is significant.

5.2.3 Dynamic factor

Based on the derived dynamic ERR in Eq. (5.20), a dynamic factor can be defined to investigate the dynamic effects.

In the derived dynamic ERR with the first-vibration-mode accuracy in Eq. (5.20), the first term is the ERR component due to the strain energy of the quasi-static motion $G_{\mathrm{st}}^{\mathrm{U}}$, which is also the strain ERR in the quasi-static loading regime without any dynamic effect (see Eq. (3.25)), and accordingly, the remaining terms can be grouped together as the dynamic component G_{dyn}, so that the total dynamic ERR is $G = G_{\mathrm{st}}^{\mathrm{U}} + G_{\mathrm{dyn}}$, where

$$G_{\mathrm{dyn}} = \frac{1}{b}\left\{\begin{aligned} &\frac{4\sqrt{\rho AEI}v^2 t}{a^2}\Lambda_1^2 \sin\left(\omega_1 t\right) + 2\rho A v^2 \frac{\Lambda_1^2}{\lambda_1^2}\cos\left(\omega_1 t\right) \\ &-\rho A v^2 \frac{\Lambda_1^2}{\lambda_1^2} - \frac{33}{140}\rho A v^2 \end{aligned}\right\}. \tag{5.21}$$

Therefore, the dynamic factor f_{dyn} is defined by $f_{\mathrm{dyn}} = G_{\mathrm{dyn}} / G_{\mathrm{st}}^{\mathrm{U}}$. A characteristic time can be introduced to study the property of f_{dyn}, that is, $\tau = ta^{-2}\sqrt{EI/(\rho A)}$. Then the dynamic factor can be written as a function of this characteristic time:

$$\begin{aligned} f_{\mathrm{dyn}} &= \frac{G_{\mathrm{dyn}}}{G_{\mathrm{st}}^{\mathrm{U}}} \\ &= \frac{4}{9}\frac{1}{\tau}\Lambda_1^2 \sin\left(\lambda_1^2 t\right) + \frac{1}{9}\frac{\Lambda_1^2}{\lambda_1^2}\frac{1}{\tau^2}\left[2\cos\left(\lambda_1^2 t\right) - 1\right] - \frac{11}{420}\frac{1}{\tau^2}. \end{aligned} \tag{5.22}$$

Based on the above definition, the total dynamic ERR is then given by $G = G_{\mathrm{st}}^{\mathrm{U}}\left(1 + f_{\mathrm{dyn}}\right)$. The ERR is proportional to the static ERR with the dynamic factor, which is determined by the characteristic time only. Note that the characteristic time is an inherent and universal property of the DCB with given material properties and structural configuration. And thus, the dynamic factor defined by Eq. (5.22) is also inherent and universal for DCBs.

As the Eq. (5.22) suggests, the dynamic factor f_{dyn} attenuates significantly with respect to the characteristic time τ with oscillation, and it is plotted against the characteristic time as the solid line in Figure 5.3 together with dynamic factor in the conventional analytical approach represented by the dashed line. The conventional dynamic factor is derived from Eq. (4.4) and related to the characteristic time τ, which is found to be $f_{\text{dyn}} = -11\tau^{-2}/420$, and this is also the last term of Eq. (5.22). As expected, the dynamic factor due to structural vibration oscillates, while the dynamic factor defined by the conventional analytical approach is an inverse function of time without any oscillation; both dynamic factors decay with time.

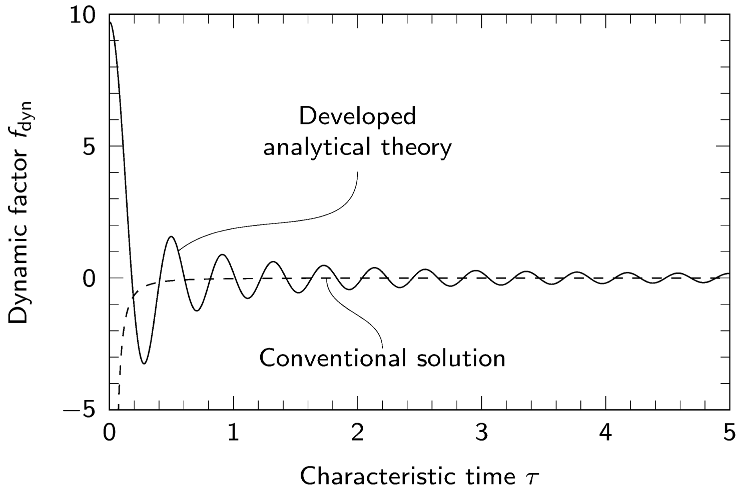

Figure 5.3 Dynamic factor versus characteristic time

The oscillating dynamic factor is less than -1 during parts of the first two vibration periods, which leads to the negative ERR. This finding is consistent with conventional analytical investigations by Smiley and Pipes [17] and Blackman et al. [20], although an infinite negative dynamic factor at $t = 0$ or $\tau = 0$ are seen based on their analytical solutions, whereas thanks to the dynamic ERR with the first-vibration-mode accuracy in Eq. (5.22) the dynamic factor is always finite. In the literature, a negative ERR was also witnessed in the test for DCB under impact load [152] before crack initiation. According to the energy consideration, the negative ERR impedes crack propagation [153], because in this case the crack growth increases the potential energy rather than decreasing it [154].

At $\tau = 0$, the dynamic effect is at its maximum, and the limit of f_{dyn} at $\tau = 0$ is

$$\lim_{\tau \to 0} f_{\text{dyn}}(\tau) \approx 9.721. \tag{5.23}$$

The dynamic factor, however, decays to $-1.0 < f_{\text{dyn}} < 1.0$ after one characteristic time period. It then continues to drop steadily. After around 10 characteristic time periods, the dynamic factor reduces to $-0.1 < f_{\text{dyn}} < 0.1$, which can be regarded as insignificant. Note that this dynamic factor is independent of the applied opening rate. Also note that the dynamic factor is a direct quantitative measurement of dynamic effect, and, in general, is a function of characteristic time, and, therefore, it can be employed to study the dynamic effect under different loading rates: for low loading rate, the dynamic factor is associated with large characteristic time and dynamic effect is small; and for high loading rate, the dynamic is with low characteristic time and dynamic effect large.

5.3 Theoretical development with wave propagation

5.3.1 ERR divergence and energy flux

In Section 5.2.2.4, the ERR determined with the global approach (Section 3.3.2.1), that is, $G^{\text{global}} = d(W_{\text{ext}} - U - K)/dA_0$ (Eq. (3.34)) to include the contribution to ERR from kinetic energy, is shown to be divergent in the ERR amplitude as more vibration modes are added. This is contrary to the physical and mechanical reality that the unbounded ERR would lead to immediate rupture for any applied loading rate. This phenomenon of divergent ERR therefore implies that the global approach is not viable to study the dynamic fracture mechanics with beams or 1D waveguides in the context of wave propagation. This is an interesting finding since the global approach, or global energy balance proposed by Griffith has long been used to study the fracture behaviour in the quasi-static loading regime of LEFM. Moreover, the strain ERR derived from the global energy balance is equivalent to the crack-tip related magnitudes of SIF and J-integral.

Smiley and Pipes [17] and Blackman et al. [20] extended the approach to include kinetic energy in the global energy balance, as proposed by Mott [70] (Section 3.3.2.1), to study the dynamic interfacial fracture. They did not, however, include vibration and, thus, they did not encounter this divergent ERR issue since their ERR is ‘smoothed’ and not oscillating.

Recall the alternative definition of dynamic ERR based on a crack-tip energy flux integral with Eq. (3.42), that is, $G^{\text{local}} = F(\Omega) / \dot{A}_0$, which is a local approach (Section 3.3.2.2). If this local approach provides the correct dynamic ERR, as demonstrated in this section, and the global approach provides an unbounded non-physical ERR since the amplitude is divergent as more vibration modes are added, then the following inequality can be written:

$$\frac{1}{b}\frac{F(\Omega)}{\dot{a}} < \frac{1}{b}\frac{d}{da}\left(W_{\text{ext}} - U - K\right). \tag{5.24}$$

This inequality of Eq. (5.24) shows that the actual amount of energy flowing into the crack tip (the left-hand side) is less than the amount of energy that can be potentially dissipated from the system (the right-hand side). In dynamics, beams are 1D waveguides and have a dispersive property, that is, flexural waves with higher frequencies travel faster (Section 2.3.1.3). The global approach for the global energy balance needs to be reconsidered in consideration of this, since it treats the energy term from each vibration mode (flexural wave) indiscriminately by reckoning they can be dissipated simultaneously. This, however, is not the case when looking at the crack tip for an infinitesimal time interval. The energy supplied to the crack tip by each vibration mode (flexural wave) is highly dependent on the speed of the flexural wave.

A further analytical theory to address this issue with consideration for dispersion of wave propagation is developed, and it is called the *dispersion-corrected global approach*.

5.3.2 Dynamic energy release rate

Combining Eqs. (5.11) and (5.17), the total mechanical energy Π of the half DCB at a given time *t* is

$$\begin{aligned}\Pi &= U + K \\ &= \frac{3EIv^2t^2}{2a^3} + \frac{33\rho Aav^2}{280} + \frac{\rho Aav^2}{2}\sum_{i=1}^{\infty}\frac{\Lambda_i^2}{\lambda_i^2} - \rho Aav^2\sum_{i=1}^{\infty}\frac{\Lambda_i^2}{\lambda_i^2}\cos\left(\omega_i t\right).\end{aligned} \tag{5.25}$$

Note that the first and second terms in Eq. (5.25) are the strain and kinetic energies, respectively, due to the quasi-static motion; and last two terms are the energy due to vibration. To aid in the following analytical development, these contributions are denoted $\Pi_{\mathrm{st}}^{\mathrm{U}}$, $\Pi_{\mathrm{st}}^{\mathrm{K}}$ and Π_{vib}, respectively.

5.3.2.1 ERR components due to quasi-static motion

Since the quasi-static motion is not dispersive, the ERR component due to the strain energy of the quasi-static motion can be directly derived using $G_{\mathrm{st}}^{\mathrm{U}} = -d\Pi_{\mathrm{st}}^{\mathrm{U}} \big/ dA_0$, and so does the ERR component due to the kinetic energy of the quasi-static motion with $G_{\mathrm{st}}^{\mathrm{K}} = -d\Pi_{\mathrm{st}}^{\mathrm{K}} \big/ dA_0$. These give the same solutions as the global approach provides in Eq. (4.4), where $G_{\mathrm{st}}^{\mathrm{U}} = 9EIv^2t^2 \big/ \left(ba^4\right)$ and $G_{\mathrm{st}}^{\mathrm{K}} = -33\rho Av^2 \big/ (140b)$ (a factor of two is applied for the symmetry).

5.3.2.2 ERR component due to vibration

The ERR component due to vibration G_{vib} cannot be determined by $-d\Pi_{\mathrm{vib}}/dA_0$, which leads to divergence as discussed before. Considering the definition in the local approach (Section 3.3.2.2) for dynamic ERR in Eq. (3.42) $G^{\mathrm{local}} = F(\Omega)/\dot{A}_0$, where $F(\Omega)$ is the energy flux into a contour around the crack tip, and accordingly, the ERR component due to vibration G_{vib} is calculated as

$$G_{\mathrm{vib}} = \frac{F_{\mathrm{vib}}(\Omega)}{\dot{A}_0}, \tag{5.26}$$

where $F_{\mathrm{vib}}(\Omega)$ is the energy flux due to vibration through the contour Ω shown in Figure 5.4 where $\varepsilon << a$.

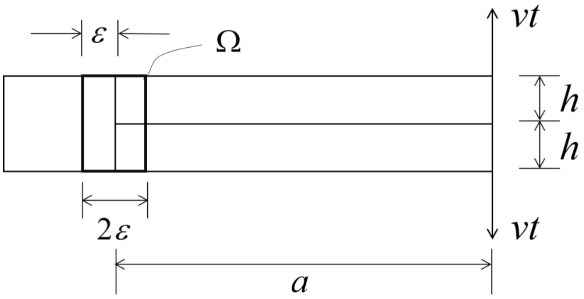

Figure 5.4 Crack-tip contour Ω for DCB to determine ERR component due to vibration

The energy flux due to vibration through the contour Ω can be calculated as

$$F_{\mathrm{vib}}(\Omega) = E_{\mathrm{vib}} C_{\mathrm{p}}^{1}, \tag{5.27}$$

where E_{vib} is the total energy density due to vibration and C_{p}^{1} is the phase speed of the first-mode flexural wave, since the first-mode flexural wave modulates all the other waves with higher frequencies (Section 2.3.1.1), and, therefore, the average speed of total energy flux is C_{p}^{1}.

To determine the total energy density due to vibration E_{vib}, a small region $0 < x < \varepsilon$ in front of the crack tip is considered (the energy density in the small region $-\varepsilon < x < 0$ behind the crack tip is zero due to the effective boundary condition). The sign of the spatial distribution (represented by the normal modes) of the free vibration in this region is proportional to Λ_i, which alternates with vibration mode numbers since $\Lambda_i \approx (-1)^i \sqrt{2}$

(Table 5.2). Note that for each vibration mode (flexural wave), its free-vibration component has contributions from both the space and time domains. The contribution from the space domain is the spatial distribution of free vibration, which is proportional to Λ_i; and the contribution from the time domain oscillates with sin ($\omega_i t$). Therefore, $\Lambda_i \approx (-1)^i \sqrt{2}$ means that the contribution of vibration modes (flexural waves) with odd mode numbers tend to close the crack and decrease the total energy density in the space domain, while those with even mode numbers tend to open the crack and increase the total energy density. The total energy density due to vibration E_{vib} in the contour is therefore

$$E_{\text{vib}} = \sum_{i=1}^{\infty} (-1)^i E_{\text{vib}}^i \,, \tag{5.28}$$

where E_{vib}^i is the energy density due to the *i*th mode flexural wave (*i*th vibration mode).

Note that Λ_i comes from the initial modal velocity Eq. (5.5), which is the coupling of the normal mode $W_i\,(x)$ (representing the free vibration) and the quasi-static motion $vF\,(x)$ along the beam. The physical interpretation of Eq. (5.28) is therefore that when the spatial velocity of free vibration (flexural wave), represented by the normal mode, is in the same direction as the applied opening velocity, this vibration mode (flexural wave) opens the crack and increases the energy density in the contour in the space domain. Likewise, when the spatial velocity of free vibration (flexural wave), represented by the normal mode, is in the opposite direction to the applied opening velocity, this vibration mode (flexural wave) closes the crack and decreases the energy density in the contour in the space domain.

The energy flux of the *i*th mode flexural wave $F_{\text{vib}}^i(\Omega)$ is $F_{\text{vib}}^i(\Omega) = E_{\text{vib}}^i C_{\text{g}}^i$, where C_{g}^i is the wave's group speed, since the energy of a wave propagates at its group speed (Section 2.3.1.4). Now, combining Eqs. (5.27) and (5.28) gives

$$F_{\text{vib}}(\Omega) = \sum_{i=1}^{\infty} (-1)^i F_{\text{vib}}^i(\Omega)\, f_i \,, \tag{5.29}$$

where $f_i = C_{\text{p}}^1 / C_{\text{g}}^i$. The *i*th mode flexural wave energy flux is $F_{\text{vib}}^i(\Omega) = -d\Pi_{\text{vib}}^i / dt$, where $\Pi_{\text{vib}}^i = \rho A a v^2\, \Lambda_i^2/\lambda_i^2 - 2\rho A a v^2\, \Lambda_i^2/\lambda_i^2 \cos(\omega_i t)$ from Eq. (5.25) (but with a factor of two applied since Eq. (5.25) is for a half DCB). Substituting these results into Eq. (5.29) and combining Eq. (5.26) gives the ERR component due to vibration as

$$\begin{aligned} G_{\mathrm{vib}} = & \frac{4\sqrt{\rho AEI}v^2 t}{ba^2}\sum_{i=1}^{\infty}(-1)^i \Lambda_i^2 f_i \sin(\omega_i t) \\ & + \frac{2\rho Av^2}{b}\sum_{i=1}^{\infty}(-1)^i \frac{\Lambda_i^2}{\lambda_i^2} f_i \cos(\omega_i t) - \frac{\rho Av^2}{b}\sum_{i=1}^{\infty}(-1)^i \frac{\Lambda_i^2}{\lambda_i^2} f_i . \end{aligned} \tag{5.30}$$

5.3.2.3 Correction factor for dispersion

In deriving the ERR component due to vibration in Section 5.3.2.2, a factor f_i is introduced in Eqs. (5.29) and (5.30), which is used to address the dispersive property of beams as highly dispersive waveguides. This factor is for accurate assessment of the amount of energy supplied to the crack tip to determine ERR based on the global approach. Note that the global approach accounting for global energy balance overestimates the energy supplied to the crack tip, and f_i corrects this by considering the dispersive property of wave propagation. Therefore, this factor is called the *correction factor for dispersion*.

The phase speed of the first-mode flexural wave is $C_{\mathrm{p}}^1 = \sqrt{\omega_1}\sqrt[4]{EI/(\rho A)}$ from Eq. (2.46), group speed of the *i*th mode flexural wave is $C_{\mathrm{g}}^i = 2\sqrt{\omega_i}\sqrt[4]{EI/(\rho A)}$ from Eq. (2.47); the relationship between the natural frequencies and frequency parameters λ_i is $\omega_i = \lambda_i^2 a^{-2}\sqrt{EI/(\rho A)}$, so the correction factor for dispersion can be written as

$$f_i = \frac{C_{\mathrm{p}}^1}{C_{\mathrm{g}}^i} = \frac{1}{2}\sqrt{\frac{\omega_1}{\omega_i}} = \frac{\lambda_1}{2\lambda_i}. \tag{5.31}$$

The value for the correction factor for dispersion f_i is presented in Table 5.3 for different vibration mode numbers.

Table 5.3 Correction factor for dispersion for stationary crack

Mode number	1	2	3	4	5	$i > 5$
Correction factor f_i	0.5	0.27775	0.19229	0.14704	0.11904	$\frac{2.49975}{(4i+1)}$

The correction factor for dispersion f_i decreases with increasing mode number as Table 5.3 shows. Also, note that the amplitude of each mode for the ERR component due to vibration G_{vib} is proportional to f_i as shown in Eq. (5.30). This allows the amplitude ratio to be studied, for instance, the amplitude of the fifth vibration mode is only 12% of that for the first mode. This indicates that the dominant mode is the first, which partially justifies approximation for the ERR with first-mode-accuracy in Section 5.2.2.4; in addition, higher modes (i.e. $i > 5$) are not significant and can be reckoned as noise since the amplitudes are smaller and frequencies are higher than for the first five vibration modes.

Another important aspect of this correction factor for dispersion is that it characterises the energy transmission ability of beams as waveguides to generate the ERR, and it is an inherent property of beams with a given set of boundary conditions as Eq. (5.31) suggests. The effective boundary assumption to study DCB gives fixed-pinned boundary conditions, and the correction factor for dispersion f_i is dimensionless and universal for DCBs with its value given in Table 5.3.

5.3.2.4 Total dynamic ERR

By combining results from Sections 5.3.2.1 to 5.3.2.3 for each ERR component and the correction factor for dispersion, for a stationary crack in DCBs, the total dynamic ERR is, therefore:

$$\begin{aligned} G_{\text{stationary}}^{\text{global}} = {} & \frac{9EIv^2t^2}{ba^4} - \frac{33\rho A v^2}{140b} + \frac{4\sqrt{\rho AEI}\,v^2 t}{ba^2}\sum_{i=1}^{\infty}(-1)^i \Lambda_i^2 f_i \sin(\omega_i t) \\ & + \frac{2\rho A v^2}{b}\sum_{i=1}^{\infty}(-1)^i \frac{\Lambda_i^2}{\lambda_i^2} f_i \cos(\omega_i t) - \frac{\rho A v^2}{b}\sum_{i=1}^{\infty}(-1)^i \frac{\Lambda_i^2}{\lambda_i^2} f_i \,. \end{aligned} \tag{5.32}$$

Note that this ERR expression was derived based on global approach accounting for global energy balance along with a correction for the dispersive properties of beams as waveguides; it is therefore referred to as *dispersion-corrected global ERR*, and this approach is called *dispersion-corrected global approach* to distinguish it from the global approach in Section 3.3.2.1.

5.3.3 Simplified dynamic ERR with vibrational deflection

5.3.3.1 Local approach with vibrational deflection

For a DCB under quasi-static loads, the ERR can be calculated by $G = M^2(a, t)/(bEI)$, where $M(a, t) = EIw^{(2)}(a, t)$ is the crack-tip bending moment. The static ERR is a local quantity related to the crack tip since it is only a function of the crack-tip bending moment.

Similarly, for a crack propagating in a DCB under dynamic loads, Freund derived the ERR using the crack-tip energy flux integral Eq. (3.41) as

$$G_{\text{propagation}}^{\text{local}} = \frac{M^2(a,t)}{bEI}\left(1 - \frac{\dot{a}^2}{C_0^2}\right), \tag{5.33}$$

where C_0 is the longitudinal wave speed with $C_0 = \sqrt{E/\rho}$. The dynamic ERR of a propagating crack is only a function of the crack-propagation speed $\dot{a}$ and the crack-tip bending moment.

Since the ERR under quasi-static loads and the ERR of a propagating crack under dynamic loads can both be determined by the crack-tip local quantities, it is an interesting question whether the dynamic ERR of stationary crack can be determined by setting $\dot{a} = 0$ in Eq. (5.33) and using the vibrational deflection in Eq. (5.6) derived in this study to determine $M(a,t)$. This would give a simplified solution for dynamic ERR for a stationary crack compared to Eq. (5.32).

It should be recognised that Eq. (5.6) is a vibrational solution, which assumes adequate time for all the flexural waves to form standing waves. Eq. (5.33), however, considers the actual values of the crack-tip quantities at a given time. This means that the stationary dynamic ERR calculated with Eqs. (5.6) and (5.33) together can only become accurate after a certain period of time after $t = 0$, at least after the establishment of all the standing waves. Furthermore, the calculated ERR is overestimated during this initial period since the calculation assumes that the energies of all flexural waves are immediately available at the crack tip, when, in fact, flexural waves need time to travel along the beam (with lower-frequency ones travelling more slowly due to the dispersive property of flexural waves in 1D waveguides). By comparison, the dispersion-corrected global ERR in Eq. (5.32) accounts for wave dispersion (by considering the energy flux into a contour around the crack tip), even though it is also based on the vibrational deflection of Eq. (5.6).

By combining Eqs. (5.6) and (5.33) and setting $\dot{a}=0$, the simplified dynamic ERR for a stationary crack of a DCB under dynamic loads is

$$G^{\text{local}}_{\text{stationary}}=\frac{9EIv^2t^2}{ba^4}+\frac{12\sqrt{\rho AEI}\,v^2t}{ba^2}\sum_{i=1}^{\infty}\frac{\Lambda_i}{\lambda_i}\sin\left(\omega_i t\right)+\frac{4\rho Av^2}{b}\left[\sum_{i=1}^{\infty}\frac{\Lambda_i}{\lambda_i}\sin\left(\omega_i t\right)\right]^2. \tag{5.34}$$

This dynamic ERR is referred to as *local ERR* in this study since it is determined by the crack-tip bending moment only and derived by the local approach in Section 3.3.2.2 but with the assumption that vibrational deflection is applicable. It consists of three components: the first term is the ERR component due to the quasi-static motion, the second term is the ERR component due to the coupling between the local vibration and the quasi-static motion, and the third term is the ERR component due to the local vibration. Note that Eq. (5.34) will overestimate ERR for a short period of time in the beginning as discussed, since it assumes all the flexural waves are immediately available at the crack tip using the vibrational deflection when actually flexural waves need time to travel, and ones with lower frequencies travel slower due to dispersion.

5.3.3.2 Equivalence of local and dispersion-corrected global approaches

Now consider the equivalence between the simplified ERR with the local approach in Eq. (5.34) in Section 5.3.3.1 and dispersion-corrected global ERR in Eq. (5.32) in Section 5.3.2.4, that is, under which condition Eq. (5.34) is applicable and potentially equivalent to Eq. (5.32). To achieve this, a relative ERR difference between $G^{\text{local}}_{\text{stationary}}$ .and $G^{\text{global}}_{\text{stationary}}$ is defined as

$$\frac{\Delta G}{G^{\text{U}}_{\text{st}}}=\frac{\left(G^{\text{local}}_{\text{stationary}}-G^{\text{global}}_{\text{stationary}}\right)}{G^{\text{U}}_{\text{st}}}. \tag{5.35}$$

It is the difference between the ERRs from the two methods, divided by G^{U}_{st} (the ERR component due to strain energy of quasi-static motion, or equivalently, the static ERR without any dynamic effect). Both methods give the same $G^{\text{U}}_{\text{st}}=9EIv^2t^2\big/\left(ba^4\right)$, which makes it an appropriate choice as the normalisation factor when defining the relative ERR difference.

To study the characteristics of this relative difference, a relative time scale *n* is also defined: $n = t/\tau_0 = \lambda_1 a^2 t^{-1}\sqrt{EI/(\rho A)}$. It is the time *t* divided by the time taken for the first-mode flexural wave to travel the crack length *a*. The phase speed of the first-mode flexural wave is $C_\mathrm{p}^1 = \lambda_1 a^{-1}\sqrt{EI/(\rho A)}$ (combining Eqs. (2.11) and (2.46)) and the time for this wave to travel from the excitation point (i.e. the free end of the beam) to the crack tip is $\tau_0 = a/C_\mathrm{p}^1$.

Based on Eqs. (5.32), (5.34) and (5.35) as well as the definition for relative time scale *n* above, the relative ERR difference becomes

$$\begin{aligned}\frac{\Delta G}{G_\mathrm{st}^\mathrm{U}} = &\frac{2}{9}\frac{\lambda_1}{n}\sum_{i=1}^{\infty}\left[\frac{6\Lambda_i}{\lambda_i} - (-1)^i \Lambda_i^2 \frac{\lambda_1}{\lambda_i}\right]\sin\left(\lambda_i \frac{n}{\lambda_1}\right) \\ &+ \frac{1}{18}\frac{\lambda_1^2}{n^2}\sum_{i=1}^{\infty}(-1)^i \frac{\lambda_1\Lambda_i^2}{\lambda_i^3}\left[1 - 2\cos\left(\lambda_i \frac{n}{\lambda_1}\right)\right] \\ &+ \frac{4}{9}\frac{\lambda_1^2}{n^2}\left[\sum_{i=1}^{\infty}\frac{\Lambda_i}{\lambda_i}\sin\left(\lambda_i \frac{n}{\lambda_1}\right)\right]^2 + \frac{11}{420}\frac{\lambda_1^2}{n^2}.\end{aligned} \tag{5.36}$$

Eq. (5.36) is dimensionless and universal for DCBs. Evolution of the relative ERR difference $\Delta G/G_\mathrm{st}^\mathrm{U}$ with the relative time scale *n* is shown in Figure 5.5a based on the first ten mode flexural waves (or vibration modes). Figure 5.5b shows the same data, but with the *y* axis transformed to enhance low-amplitude variations of the relative ERR difference for both positive and negative values.

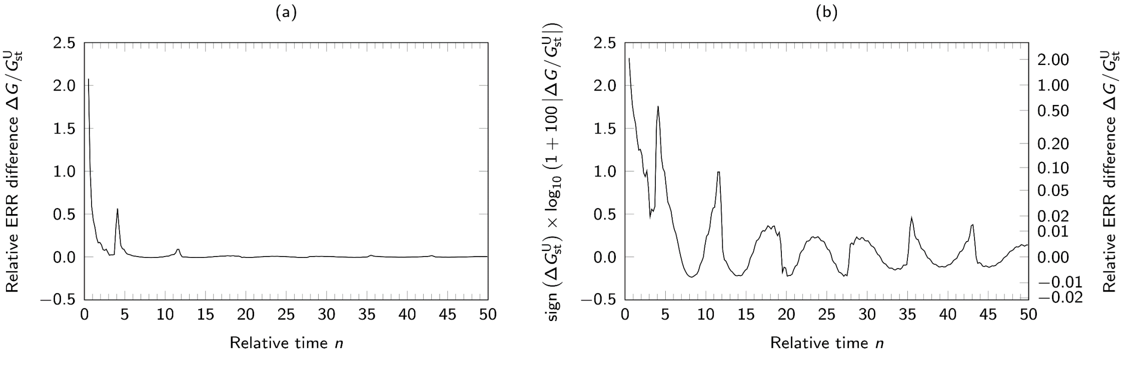

Figure 5.5 Evolution of the relative ERR difference between local and global methods with *n*

Apparently, the relative ERR difference is mainly positive. This indicates that the local ERR is larger than the dispersion-corrected global ERR, consistent with the discussion in Section 5.3.3.1. The most significant overestimation happens in the range $0 < n < 5$; for $n > 5$, it rapidly decreases to close to zero. For $n > 12$, the relative ERR difference is within approximately $-0.7\% < \Delta G / G_{\mathrm{st}}^{\mathrm{U}} < 1.9\%$. The dispersion-corrected global and local ERR solutions can, therefore, be considered as equivalent for predicting the dynamic ERR provided that enough time has passed, with $0 \le n \le 12$ being the transition period for the vibrational solution to be applicable. Note that when $n = 2$, the first-mode flexural wave returns to the free end, with all the standing waves established (also the establishment of vibration). The local ERR solution, however, still needs time to 'even out' the additional 'artificial' energy in comparison to the dispersion-corrected global ERR solution, explaining the duration of the transition period beyond $n = 12$.

Another important aspect of this equivalence is that it provides some insight into whether global (Section 3.3.2.1) and local approaches (Section 3.3.2.2) give an equivalent assessment of dynamic ERR. Generally, in dispersive waveguides, as demonstrated in this chapter, the global approach (Section 3.3.2.1) using Eq. (3.34) $G^{\mathrm{global}} = d(W_{\mathrm{ext}} - U - K)/dA_0$ does not provide a physically and mechanically sound definition of dynamic ERR. In dispersive waveguides, the dynamic ERR should be defined with the dispersion-corrected global approach instead, accounting for dispersion of the waveguides. It is demonstrated in this section that dynamic ERR defined by the dispersion-corrected global approach is equivalent to that defined by the local approach.

5.3.3.3 Simplified dynamic ERR for stationary crack

One further simplification can be made to Eq. (5.34) for its third term: since $\left[\sum_{i=1}^{\infty} \Lambda_i / \lambda_i \sin\left(\omega_i t\right)\right]^2 \le \left(\sum_{i=1}^{\infty} \Lambda_i / \lambda_i\right)^2$, with the value of Λ_i and λ_i given in Table 5.2, this third term of Eq. (5.34) can be no larger than $0.2295\rho A v^2/b$. This term is therefore small in comparison to the second term of Eq. (5.34) when $n > 12$, in which case the dynamic ERR further simplifies to

$$G_{\mathrm{stationary}}^{\mathrm{local}} = \frac{9EIv^2t^2}{ba^4} + \frac{12\sqrt{\rho AEI}\,v^2 t}{ba^2} \sum_{i=1}^{\infty} \frac{\Lambda_i}{\lambda_i} \sin\left(\omega_i t\right). \tag{5.37}$$

Eq. (5.37) provides the simplified dynamic ERR based on the local bending moment and vibrational deflection. When $n > 12$, it is equivalent to Eq. (5.32), but for an accurate calculation of ERR when $n < 12$, it is advisable to use Eq. (5.32) instead, which accounts for wave dispersion.

5.4 Numerical verification

5.4.1 Finite-element model and verification case

To verify the analytical solutions for ERR of stationary crack with vibration in Section 5.2 and with wave propagation in Section 5.3, the symmetric DCB (Figure 5.6) was considered; its width is 1 mm. An isotropic elastic material was used with the Young's modulus of 10 GPa, the Poisson's ratio of 0.3, and the density of 10^3 kg m^{-3}.

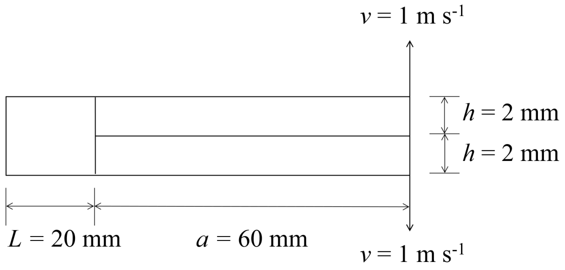

Figure 5.6 DCB geometry for FEM verification

A 2D finite-element model was built employing plane-stress elements (CPS4R) in Abaqus/Explicit solver, which includes the inertia effects. All the viscous parameters were set to zero to avoid unnecessary damping. This is in accordance with literature, that the damping factor of CFRPs is found to be very low due to the low viscoelastic nature of carbon fibre [155][156]; and this is also in line with the conventional studies (see Section 4.2) and standardised testing methods such as ASTM D5528, D7905, that the damping is not accounted for. The VCCT was used to determine the dynamic ERR numerically. The uncracked region was formed by sharing nodes of two DCB arms, and no contact was modelled. A FEM model can be seen in Figure B.1 in Appendix B.

Uniform squared elements were used, and the effects of element size were studied for 4 levels of elements sizes, (i.e. 1 mm, 0.5 mm, 0.2 mm and 0.1 mm) and no significant improvement was seen by decreasing mesh size from 1 mm to 0.1 mm, and ERR solution with 0.1 mm element size is shown in Figure 5.7a. There was a very slight frequency shift with decreasing the element size, since with increasing continuous of the structure, the natural frequency deceases. To study the element size convergence, the amplitudes of the first vibration mode were used, which were derived by performing fast Fourier Transform on the ERRs derived with 4 levels of element sizes. The element size convergence is shown in Figure 5.7b, where the amplitudes of first vibration mode are plotted against the inversed element size.

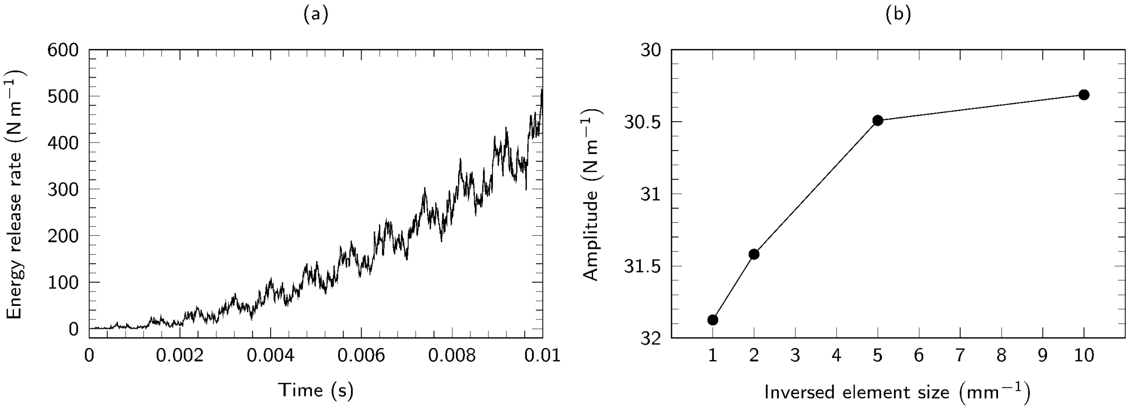

Figure 5.7 (a) ERR solution with element size of 0.1 mm; (b) element size convergence

It is seen that the ERR shows convergence for the element smaller than 0.2 mm, and, therefore, the ERR from the finite-element model with the mesh size of 0.1 mm is used, which also provides ERR with more accurate frequency, to verify the analytical results both for the theories with vibration and wave propagation.

5.4.2 Verification for developed theory with vibration

As discussed in Section 5.2, the ERR derived directly from the global approach with consideration of vibration accounting for the global energy balance shows a divergent amplitude, and only the ERR with the first-vibration-mode accuracy can be used; this result is compared to the FEM result in Figure 5.8a.

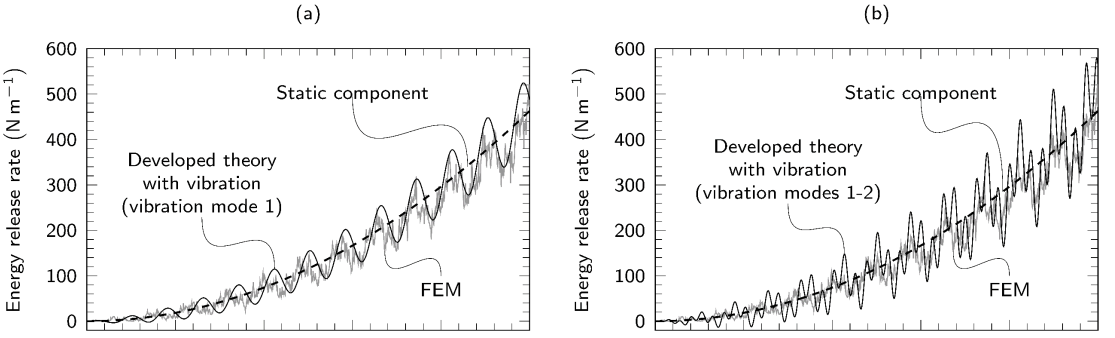

Figure 5.8 Comparison of ERR from results of FEM simulation (grey line) and from the developed analytical theory (black line) using global approach with first (a) and first two (b) vibration modes

The results based on the developed analytical theory with vibration and with the first-vibration-mode accuracy are in good agreement with the results from the numerical simulation: the analytical results capture the amplitude and frequency of ERR variation predicted by the FEM. The analytical theory is slightly out-of-phase with the FEM result, which is due to the difference in boundary conditions: the finite-element model simulates a full DCB, whereas the developed theory models the effective boundary condition shown in Figure 5.1b. The effective boundary condition does not allow crack tip to rotate as illustrated in Figure 5.9a, but in reality for 2D FEM or experiments, the crack tip can rotate as shown in Figure 5.9b.

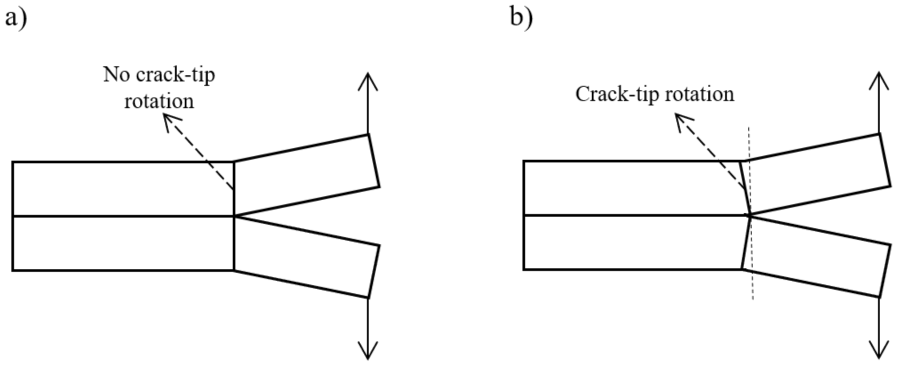

Figure 5.9 Illustration of crack-tip rotation: (a) no crack-tip rotation under effective boundary condition; (b) crack-tip rotation in 2D FEM model

It is worth noting that the ERR with dynamic effects oscillates about a mean value of $G_{\mathrm{st}}^{\mathrm{U}}$ (the ERR component due to strain energy of quasi-static motion or static ERR without any dynamic effect). In Eq. (5.22), the dynamic factor decays quickly with time, but in Figure 5.8a, the oscillating amplitude actually increases with time. This indicates that the dominant contribution to this vibration amplitude is the increasing of $G_{\mathrm{st}}^{\mathrm{U}}$ .When the first two vibration modes are included in the analytical result as shown in Figure 5.8b, the amplitude of ERR oscillation begins to diverge as predicted.

A quantitative measurement of the deviation of analytical result from that of FEM can be made by regressing the analytical result against FEM result for every time point as shown in Figure 5.10, using the data from Figure 5.8. Ideally, if analytical agrees FEM completely, the slope of the regression line should be 1, and R^2 indicates the extent of analytical solution deviating from FEM solution, which can be taken as a measurement of the frequency difference.

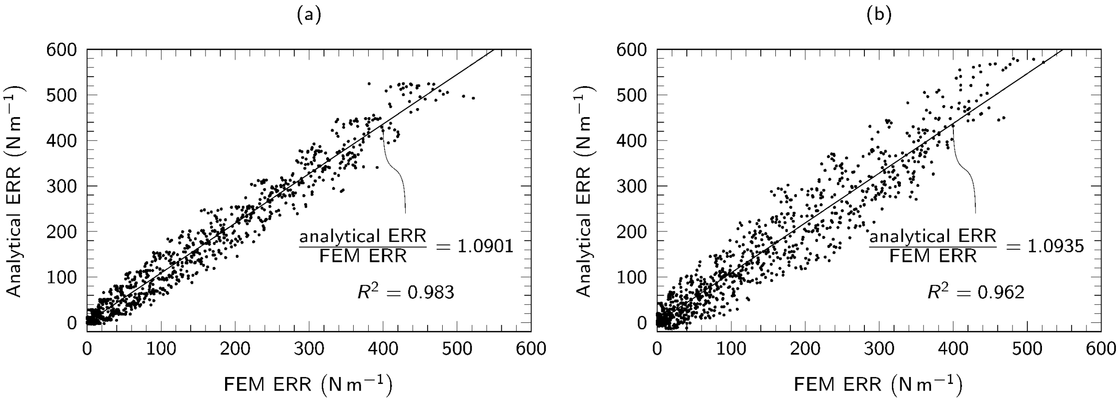

Figure 5.10 Regression of ERR from results of developed analytical theory against FEM simulation using global approach with first (a) and first two (b) vibration modes

Clearly, for both subfigures of Figure 5.10, the analytical solution provides a higher ERR solution as the slopes are larger than 1 since the analytical model is stiffer than the FEM model due to effective boundary condition. In addition, comparison between Figure 5.10a and b shows that by adding the contribution of the second vibration mode the analytical solution deviates from FEM solution even more with an increased slope and a decreased R^2.

5.4.3 Verification for developed theory with wave propagation

The theory developed based on the dispersion-corrected global approach in Eq. (5.32) in Section 5.3, is compared against results from FEM in Figure 5.11 for the first vibration mode (a) and first five vibration modes (b).

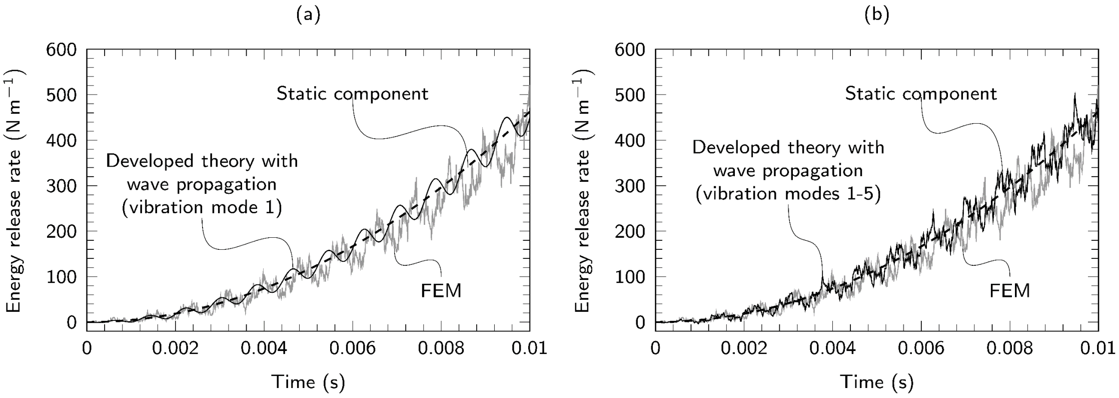

Figure 5.11 Comparison of ERR from results of FEM simulation (grey line) and from the developed analytical theory (black line) using dispersion-corrected global approach with first (a) and first five (b) vibration modes

Apparently, the divergence of ERR amplitude as more vibration modes are added is resolved by accounting for dispersion (Figure 5.11b); this contrasts with Figure 5.8b, calculated using the conventional global approach. By adding more vibration modes, the ERR from the analytical theory approaches the FEM simulation results, as expected. This can also be seen in the regression of ERR from analytical solution against FEM solution in Figure 5.12. The slope of the regression for the first five vibration modes using dispersion-corrected global approach shown in Figure 5.12 is smaller than that for first vibration modes using global approach shown in Figure 5.10b.

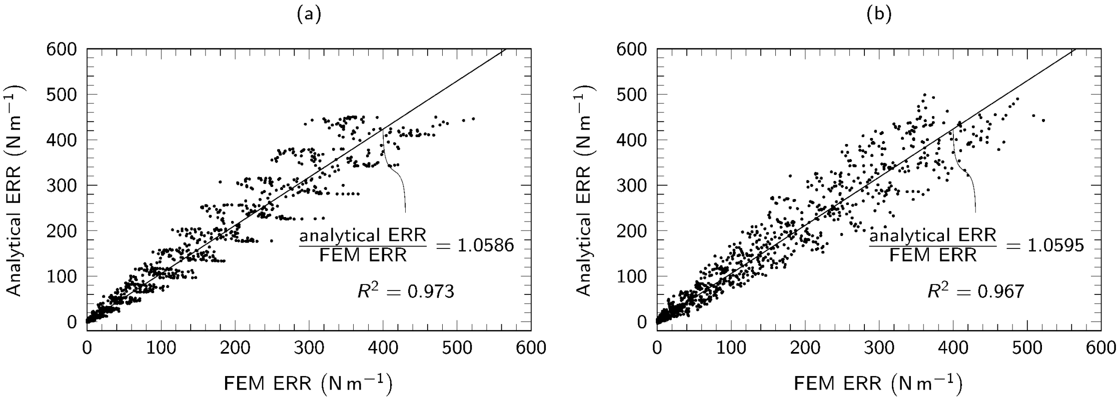

Figure 5.12 Regression of ERR from results of developed analytical theory against FEM simulation using dispersion-corrected global approach with first (a) and first five (b) vibration modes

Recall that the ERR amplitude from each vibration mode is proportional to the correction factor for dispersion f_i given in Table 5.3. Based on this, the first five vibration modes are reckoned sufficient to predict the amplitude of the ERR. This is confirmed by Figure 5.11b; adding more vibration modes does not significantly alter the ERR although may provide more details of the ERR.

By examining Figure 5.11, a slight phase difference between the analytical and FEM simulation results is observed, which can also be seen by comparing Figure 5.12a and b, that adding more vibration modes leading to significant decline in R^2. In addition, the analytical results are slightly higher than the FEM simulation results, which can also be seen in Figure 5.12a and b with a slope larger than 1. Both these discrepancies are due to the effective boundary condition. This can be resolved either by using an effective crack length for crack-tip-rotation compensation, as per Section 5.5, or by treating the intact section of the beam as resting on an elastic foundation; the latter is one of the motivations for Chapter 7.

5.5 Crack-tip-rotation compensation for stationary crack

5.5.1 Conventional method for compensation of crack-tip rotation

When using the effective boundary condition, the dynamic ERR result is slightly overestimated, and the frequency is not accurately predicted; crack-tip-rotation compensation can be used to resolve this. In this section, the viability of making the required compensation by using an additional crack length Δ is investigated. This Δ is determined in the quasi-static regime following the modified compliance calibration (MCC) method from ASTM D5528 [11], originally from [157].

In DCB tests under quasi-static loading condition, MCC method measures the external forces at various crack lengths and calculated the corresponding compliances. These compliances are then plotted against corresponding crack lengths, and, based on the relation $C^{1/3} = \left(a + \Delta\right) \Big/ \sqrt[3]{3EI}$ from beam theory, the negative intercept corresponding to the zero compliance is the additional crack length Δ for crack-tip-rotation compensation. This experiment-based method to compensate for crack-tip rotation has been widely used in the quasi-static regime and incorporated into standard testing methods, such as ASTM D5528.

There are two methods of implementing this additional crack length Δ in ASTM D5528: one method increases the crack length by Δ to give an effective crack length of $a_{\mathrm{eff}} = a+\Delta$, while the other method uses an effective flexural modulus of $E_{\mathrm{eff}} = a^3E/(a+\Delta)^3$; and it is believed that these two methods, using effective crack length a_{eff} and using effective flexural modulus E_{eff}, give the equivalent ERR solution under quasi-static loads.

However, in dynamic DCB test, this compensation method has two difficulties:

(1) Oscillating compliance:

The cube root of the compliance $C^{1/3}$ is not linear related to the crack length in dynamic DCB test, as the externally applied load oscillates dramatically (as shown in experimental observation in Figure 4.1) under high opening rates, giving oscillating compliance; this is also demonstrated by the analytical solution using vibrational deflection Eq. (5.6), for a given crack length, the compliance is

$$\begin{aligned} C &= \frac{w_0(t)}{P} = \frac{vt}{-EIw^{(3)}(a,t)} \\ &= \frac{a^3}{3EI - \frac{a^5}{t}\sqrt{\rho AEI}\sum_{i=1}^{\infty}\frac{\Lambda_i}{\lambda_i^3}\phi_i^{(3)}(a)\sin(\omega_i t)}. \end{aligned} \tag{5.38}$$

The MCC method requires to measure the external load with respect to each crack length to derive compliance for DCB, but with the indication in Figure 4.1 and Eq. (5.38), the compliance calculated for each crack length is not accurate due to the oscillation of the external force.

(2) Contradicting solutions for natural frequency:

The natural frequency for the DCB arm is $\omega_i = \lambda_i^2 a^{-2}\sqrt{EI/(\rho A)}$ with its uncorrected crack length a. If the effective crack length $a_{\mathrm{eff}} = a+\Delta$ is applied, the modified natural frequency is $\omega_i = \lambda_i^2 (a+\Delta)^{-2}\sqrt{EI/(\rho A)}$; however, using the effective flexural modulus gives the natural frequency as $\omega_i = \lambda_i^2 (a+\Delta)^{-2}\sqrt{EI(a+\Delta)/(\rho Aa)}$. Note that these two solutions of natural frequencies are not equal, and thus the implementation of the MCC method to address the crack-tip rotation needs further investigation.

5.5.2 Crack-tip rotation compensation for DCB under dynamic loads

The MCC method must be used in the context of quasi-static cases to avoid oscillating compliances. In this section, the viability of using Δ determined by the MCC method quasi-statically to the dynamic case is assessed by using the effective crack length as well as the effective flexural modulus against FEM results.

Following the quasi-static MCC method to determine Δ, the external force acting on the DCB at various crack lengths under constant-opening rate is measured. Quasi-static FEM simulation is used (using Abaqus/Standard, where the inertia of the DCB is not accounted for), and the compliances are calculated for each crack length. Then, according to the MCC method, the cube root of compliance is plotted against the corresponding crack length. The results for the verification case in Section 5.4.1 are shown in Figure 5.13, and linear regression is used to find the additional crack length corresponding to zero compliance: Δ = 1.34 mm.

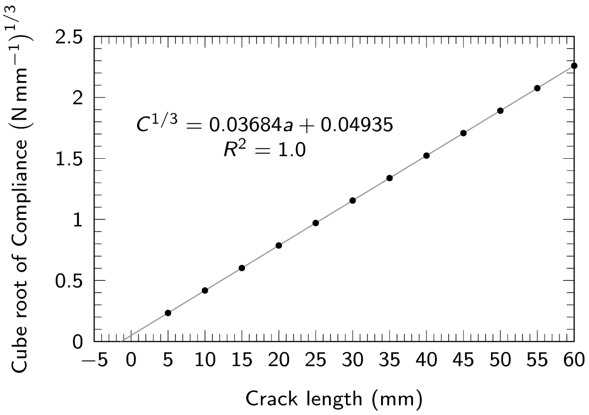

Figure 5.13 Regression analysis of cube root of compliance with respect to crack length from quasi-static FEM simulation

Considering the verification case in Section 5.4.1, two methods for implementing additional crack length Δ, that is, using effective crack length and effective flexural modulus, are tried, first replacing *a* in Eq. (5.32) with effective crack length a_{eff}, and then replacing *E* in Eq. (5.32) with effective flexural modulus E_{eff}. The ERR results for these two methods are compared against the results of FEM simulation in Figure 5.14.

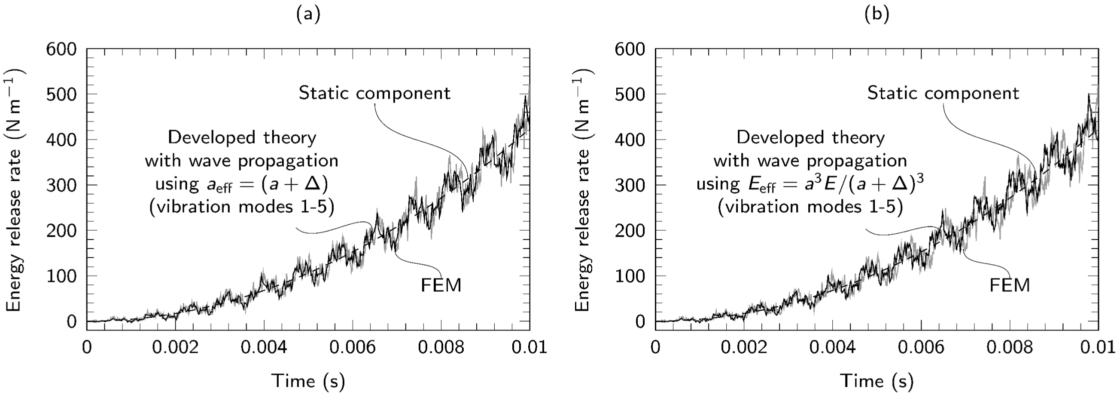

Figure 5.14 Implementation of Δ for compensation of crack-tip rotation: (a) by effective crack length a_{eff}; (b) by effective flexural modulus E_{eff}

Apparently, employing the effective crack length a_{eff} is more accurate than the use of the effective flexural modulus E_{eff}. This can also be seen in the regression of analytical solution against FEM solution in Figure 5.15 that R^2 with a_{eff} is larger than that with E_{eff} indicating a better agreement in frequency. For the former, there is still a very small difference between the analytical solution and the results from FEM simulation. Note that the two methods are proposed in ASTM D5528 and deemed equivalent for quasi-static loads, but as shown, they are not equivalent for dynamic fracture.

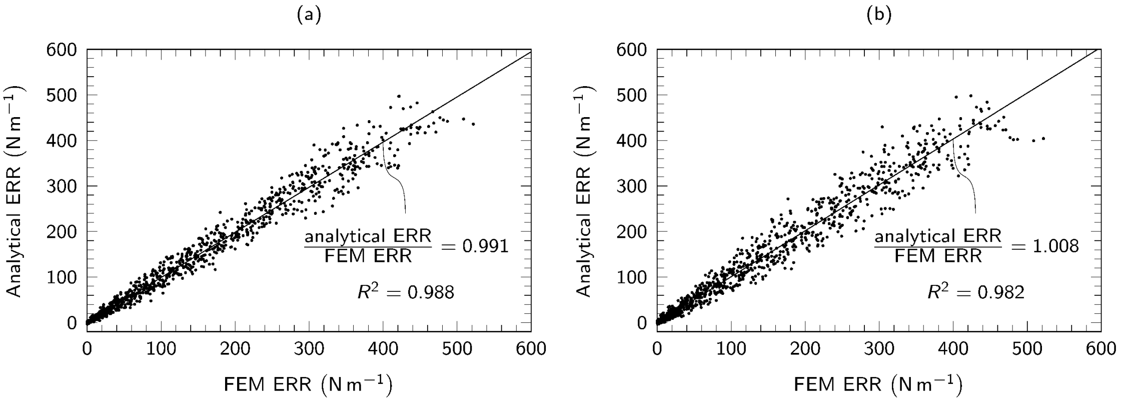

Figure 5.15 Regression of ERR from results of developed analytical theory against FEM simulation with Δ implemented by (a) by effective crack length a_{eff}; (b) by effective flexural modulus E_{eff}

Including the additional crack length Δ for crack-tip rotation compensation also allows accurate calculation of the ERR contribution from each vibration mode. The analytical results based on the effective crack length a_{eff} for the first one, two, three, four, five, ten, 15 and 20 vibration modes (or flexural waves) are shown in Figure 5.16a-h, respectively. As more vibration modes are included, analytical solution becomes increasingly close to the FEM results in terms of the overall magnitude of ERR as well as the frequencies. It also demonstrates that the first five vibration modes (Figure 5.16e) are adequate to capture the dynamic ERR accurately.

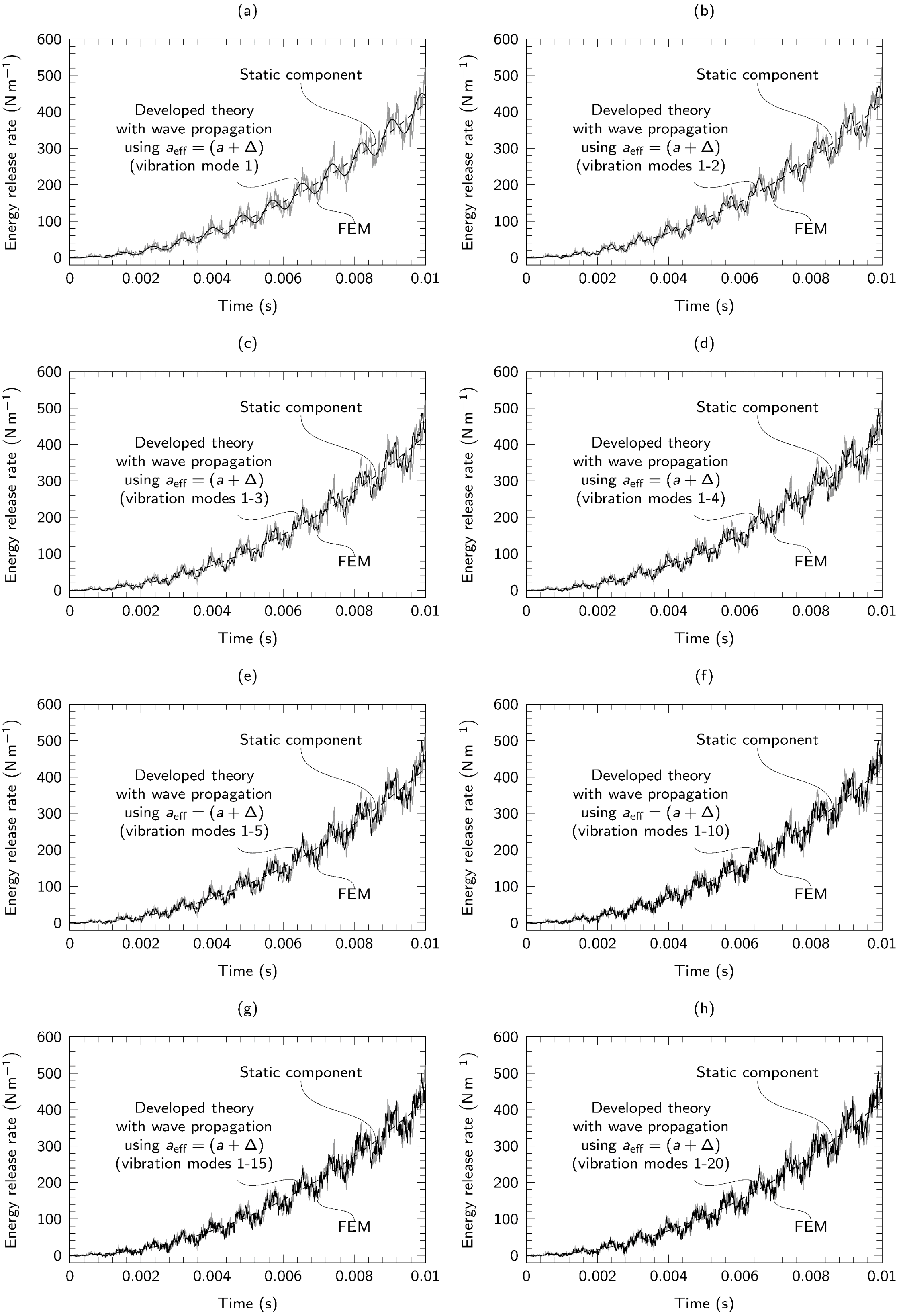

Figure 5.16 Dynamic ERR for stationary crack versus time results from developed theory with effective crack length (black line) and from FEM (grey line) with increasing numbers of vibration modes

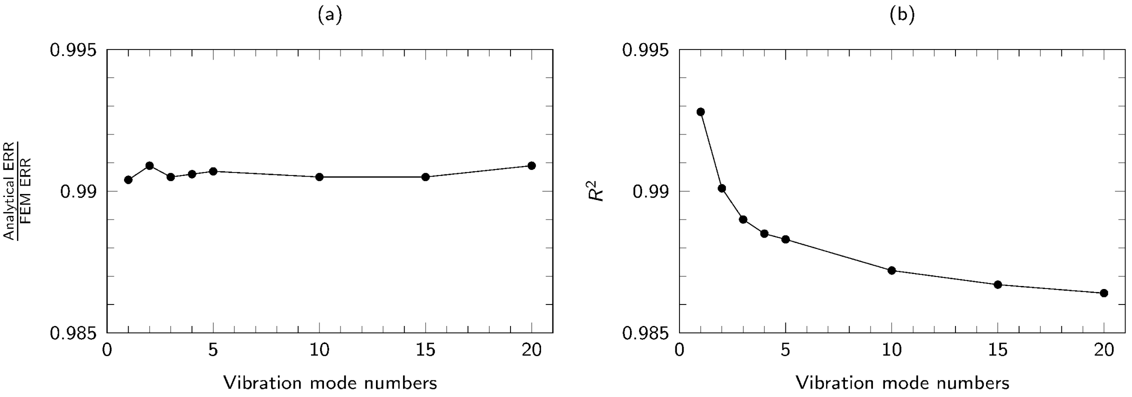

Figure 5.17 Regression values for slope and R^2 with increasing numbers of vibration modes

The regression of analytical solution against FEM solution with the increasing numbers of vibration is conducted and results are shown in Figure 5.17a for the slope and in Figure 5.17b for R^2. In Figure 5.17a, the slope of regression does not change significantly after the fifth vibration mode indicating the contribution from higher vibration mode is not significant. But there is a decline in R^2 with increasing vibration mode number as shown in Figure 5.17b, where it decreases monotonically in the first five vibration mode and change then becomes insignificant after. This is due to the very slight frequency difference between the analytical and numerical solutions, but the general agreement is still excellent.

Note that the additional crack length Δ cannot be determined using compliance calibration and results of DCB tests under dynamic loads because the compliance measured in such experiments is not accurate due to oscillation of the external loads. Parallel quasi-static experiments or FEM simulations must therefore be conducted to derive the additional crack length Δ to use this method for experiments under dynamic loads. Further analytical models are desirable to allow the crack tip to rotate rather than the effective boundary condition, and this is one of the motivations of introducing elastic foundation in Chapter 7.

5.6 Conclusion

In this chapter, the analytical framework for dynamic interfacial fracture is established for a mode-I stationary crack in DCBs by considering vibration and wave propagation. The analytical framework is based on solving the equation of motion with time-dependent boundary conditions, which represents the applied displacement; and strain and kinetic energies can be thus calculated.

By global approach, the strain and kinetic energies are therefore used to determine the dynamic ERR, which leads to a non-physical divergent ERR for including more vibration modes. Examination of this reveals the limitation of global approach accounting for global energy balance assuming all the flexural waves arrive at crack tip simultaneously, but this is not the case for Euler-Bernoulli beams as 1D waveguides, which are highly dispersive that waves with different frequencies travel at different speeds. Therefore, a correction factor for dispersion is derived to account for the dispersive properties of Euler-Bernoulli beams by investigating the energy flux into the crack tip, and this method is called *dispersion-corrected global approach*. And dispersion-corrected dynamic ERR by this factor shows good agreement with results from FEM. But the analytical solution is slightly out-of-phase with numerical results due to the effective boundary condition, which assumes a perfectly fixed boundary condition at the crack tip allowing no rotation, and this is addressed by extending the quasi-static MCC method, and analytical solution shows excellent agreement with numerical results. But the MCC method cannot be directly used for DCB tests under dynamic load and parallel quasi-static experiments or FEM simulations are needed. Further analytical model allowing the crack tip to rotation is still desirable, and this is achieved in Chapter 7.

In addition, the findings in this chapter also help answer the question left in Chapter 3, whether dynamic ERR defined by global approach (Section 3.3.2.1) is equivalent to the one defined by local approach (Section 3.3.2.2) in elastodynamic fracture. Clearly, for the dynamic ERR derived in the context of dispersive waveguides, e.g. Euler-Bernoulli beams, these two approaches are not equivalent; and rather, the dynamic ERR defined by global approach is erroneous. Instead, dispersion-corrected global approach must be used, and this dispersion-corrected global approach is demonstrated to be equivalent to the local approach.

Chapter 6: Propagation of dynamic mode-I interfacial crack

6.1 Introduction

In Chapter 5, the dynamic ERR of a stationary crack was derived and the framework to study dynamic interfacial fracture is developed and established. The equation of motion was solved with a time-dependent boundary condition, and the global approach including kinetic energy with correction for dispersion was used, forming the dispersion-corrected global approach. According to the fracture criterion, the crack begins to propagate when the dynamic ERR reaches the crack-initiation toughness. Then, while the crack propagates, the dynamic ERR equals or exceeds the crack-propagation toughness. These criteria are, however, complicated by the fact that dynamic fracture toughness is not, in general, constant.

It is generally believed that dynamic fracture toughness is dependent on crack-propagation speed based on experimental observations and results, that is, $G_{\mathrm{c}} = f\left(\dot{a}\right)$. In early experimental results from experiments with a low crack-propagation speed, fracture toughness was shown to be approximately constant, but with increasing crack-propagation speed the dynamic fracture toughness increased exponentially after a limiting value of $\dot{a}_{\mathrm{L}}$. A comprehensive review of these early experiments is given in [158], and it was concluded that the relationship between the dynamic fracture toughness and the crack-propagation speed might be a material property.

Zhou et al. [142] reported their experimental results for the dynamic fracture toughness of PMMA versus crack-propagation speed and fitted the respective relation as

$$G_{\mathrm{c}}\left(\dot{a}\right) = G_0 \log\left(\frac{\dot{a}_{\mathrm{L}}}{\dot{a}_{\mathrm{L}} - \dot{a}}\right), \tag{6.1}$$

where G_0 and $\dot{a}_{\mathrm{L}}$ are the fitting parameters. The microstructures of failure for various crack-propagation speeds were also examined to explain the relationship between G_{c} and $\dot{a}$ together with the failure mechanisms.

Based on the literature discussed, the fracture toughness for slow crack propagation can be considered as approximately constant, but for fast crack propagation, the fracture toughness depends on the crack-propagation speed or rate. Therefore, here, for mode-I crack propagation, two scenarios of constant and rate-dependent fracture toughness are investigated separately, with analytical solutions developed for each.

6.2 Theoretical development

6.2.1 Analytical theory for constant fracture toughness

For a steadily propagating crack, consider the fracture criterion of $G - G_\mathrm{c} = 0$, and its total derivative at a given time *t*, and corresponding crack length *a* is

$$\frac{\partial\left(G-G_\mathrm{c}\right)}{\partial a}da+\frac{\partial\left(G-G_\mathrm{c}\right)}{\partial t}dt=0. \tag{6.2}$$

Rearranging Eq. (6.2), the crack-propagation speed at this given time *t* is

$$\dot{a}=\frac{da}{dt}=-\frac{\partial\left(G-G_\mathrm{c}\right)/\partial t}{\partial\left(G-G_\mathrm{c}\right)/\partial a}. \tag{6.3}$$

Assuming that the contribution to strain and kinetic energies due to the crack-propagation speed is small, the ERR solution for the stationary crack can be used to study the crack-propagation speed derived in Eq. (6.3). Since the analytical ERR solution with the first-mode accuracy in Eq. (5.20) predicts the envelope of ERR compared to results from FEM simulation, it can be used to obtain crack-propagation speed in Eq. (6.3) approximately.

Evaluating respective terms in Eq. (6.3): $\partial G_\mathrm{c}/\partial a$ and $\partial G_\mathrm{c}/\partial t$ are found to be zero due to the constant G_c, and terms $\partial G/\partial a$ and $\partial G/\partial t$ are derived from Eq. (5.20), giving the approximate crack-propagation speed as

$$\dot{a}=-\frac{\partial G/\partial t}{\partial G/\partial a}=\frac{a}{2t}. \tag{6.4}$$

For oscillating ERR in Eq. (5.20), the crack-propagation speed does not oscillate as Eq. (6.4) shows, since all of the oscillatory terms in $\partial G/\partial t$ and $\partial G/\partial a$ cancel out. Note that Eq. (6.4) only applies under the steady and slow crack propagation without contact. Physically it means that during crack propagation, the time-oscillation of the ERR is balanced by the gradient of ERR.

The crack-propagation speed in Eq. (6.4) is the same as that obtained for a DCB under quasi-static loads. Nevertheless, it was derived using the theory developed for dynamic interfacial fracture and is therefore also valid for dynamic crack propagation under the stated assumptions and limitations. Integrating Eq. (6.4) gives the solution for a crack length versus time curve as

$$a - a_0 = A_1 \sqrt{t - t_0}\,, \tag{6.5}$$

where a_0 is the initial crack length, t_0 is the time for crack initiation. The crack-initiation time can be determined using the condition for the stationary crack of $G = G_c$, and therefore, the coefficient A_1 is determined accordingly by crack-initiation condition. Note that Eq. (6.4) has an interesting implication that the crack-propagation speed is independent of fracture toughness once it starts to propagate and crack extension follows a fixed pattern as Eq. (6.5) indicates. But the coefficient A_1 is dependent on fracture toughness G_c.

Eqs. (6.4) and (6.5) are only applicable to brittle materials with a moderate material density and a constant fracture toughens G_c. If the material density is high, the inertial effect can cause the crack surfaces to close, causing crack arrests. This theory for constant G_c, however, cannot predict crack arrest phenomenon for two reasons: (1) The condition used in deriving Eqs. (6.4) and (6.5) is that $G = G_c$ at all times after crack initiation, meaning that the crack must always propagate. (2) The theory does not consider contact between crack surfaces, and furthermore, the interpenetration of crack surfaces gives non-zero ERR. For materials with high density, Eq. (6.5) can still accurately predict the slope of the crack length-time curve.

6.2.2 Analytical theory for rate-dependent fracture toughness

6.2.2.1 Problem description

For a DCB of a material with a rate-dependent fracture toughness $G_c(\dot{a})$, that is, the fracture toughness depends on the crack-propagation speed, the fracture criterion is $G(a,\dot{a},t) - G_c(\dot{a}) = 0$, where the dynamic ERR is treated as a function of crack length a, crack-propagation speed $\dot{a}$ and time t. Considering the total derivative of this fracture criterion and differentiating it with regard to t, give

$$\frac{\partial G(a,\dot{a},t)}{\partial a}\dot{a} + \frac{\partial G(a,\dot{a},t)}{\partial \dot{a}}\ddot{a} + \frac{\partial G(a,\dot{a},t)}{\partial t} - \frac{dG_c(\dot{a})}{d\dot{a}}\ddot{a} = 0\,, \tag{6.6}$$

where $\ddot{a}$ is the acceleration of crack propagation.

Note that the last term in Eq. (6.6) is the contribution of dynamic interfacial fracture toughness, and it is neither always known nor with mature constitutive models, that is, for different materials they can take different forms and expressions. Therefore, solving Eq. (6.6) analytically to derive a solution for crack-propagation speed and then crack-length curve is generally infeasible in contrast to the case with constant fracture toughness in Section 6.2.1. Rather, the theory developed hereby is to provide analytical solutions to determine the dynamic ERR, and then to measure and study the dynamic interfacial fracture toughness and fracture behaviours accordingly.

To achieve this, the assumption is made that crack length a is a given parameter, which can be measured in experiments. And since the crack propagates, Freund's formula in Eq. (5.33) can be applied to determine the dynamic ERR; however, it depends on the crack-tip bending moment. This requires solving partial differential equations with a moving boundary condition to determine the deflection at the crack tip and then the crack-tip bending moment as the crack propagates. This cannot be achieved by rigorous mathematics due to the unknown expression for crack length $a\,(t)$ [159][160][161]; however, a general analytical engineering solution is developed, which can be applied for a given crack-length curve, for example, from experimental results.

6.2.2.2 Theoretical derivation

Consider the DCB in Figure 6.1a and one DCB arm with effective boundary in Figure 6.1b with prescribed coordinate, so that the crack can propagate in the x positive direction.

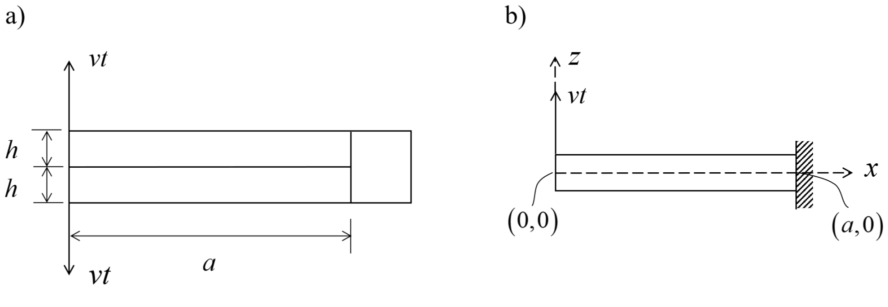

Figure 6.1 DCB configuration for propagating crack: (a) symmetric DCB; (b) effective boundary conditions and prescribed coordinates

The deflection of the DCB arm in Figure 6.1b is obtained by coordinate transformation of the solution in Eq. (5.6) as

$$w\left(x,t\right)=va^{2}\sqrt{\frac{\rho A}{EI}}\sum_{i=1}^{\infty}\frac{\Lambda_{i}}{\lambda_{i}^{3}}\phi_{i}\left(a-x\right)\sin\left(\omega_{i}t\right)+\left(\frac{x^{3}}{2a^{3}}-\frac{3x}{2a}+1\right)vt. \tag{6.7}$$

For a propagating crack of instantaneous length a_1, by assuming the deflection given in Eq. (6.7) holds, the bending moment at the crack tip is $M\,(a_1, t) = EIw^{(2)}\,w(a_1, t)$. Then by combining Eqs. (5.33) and (6.7) and employing the simplification described in Section 5.3.3.3, the dynamic ERR is

$$G_{\text{propagation}}^{\text{local}}=\frac{9EIv^{2}t^{2}}{ba^{4}}\left(1-\frac{\dot{a}_{1}^{2}}{C_{0}^{2}}\right)+\frac{12\sqrt{\rho AEI}\,v^{2}t}{ba_{1}^{2}}\left(1-\frac{\dot{a}_{1}^{2}}{C_{0}^{2}}\right)\sum_{i=1}^{\infty}\frac{\Lambda_{i}}{\lambda_{i}}\sin\left(\omega_{i}t\right). \tag{6.8}$$

The first term is due to the strain energy of quasi-static motion and its expression keeps the same for any given crack length, and, therefore, does not need to be adjusted for dispersion. The second term, however, is related to vibration and wave propagation, and so does need to be adjusted to account for dispersion and the Doppler effect [162].

By combining Eqs. (5.26) ($G_{\text{vib}}=F_{\text{vib}}\left(\Omega\right)/\dot{A}_{0}$) and (6.8) for a crack length of a_1, the vibration energy flux into a contour around the crack tip (Figure 6.2) is

$$F_{1}\left(\Omega\right)=\dot{a}_{1}b\sum\nolimits_{i=1}^{\infty}G_{\text{vib}}^{i}\left(a_{1}\right), \tag{6.9}$$

where $G_{\text{vib}}^{i}\left(a_{1}\right)=12\sqrt{\rho AEI}\,v^{2}t\left(C_{0}^{2}-\dot{a}_{1}^{2}\right)\Lambda_{i}\sin\left(\omega_{i}t\right)/\left(\lambda_{i}ba_{1}^{2}C_{0}^{2}\right)$.

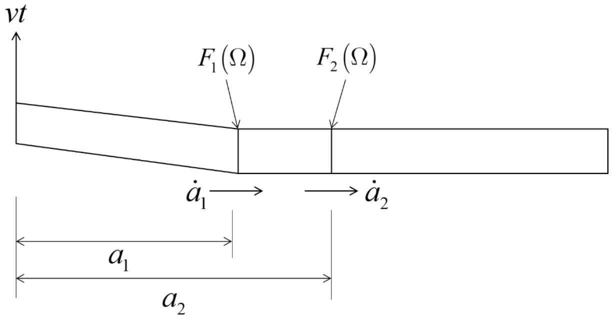

Figure 6.2 Crack propagation from a_1 to a_2 over the time interval Δt

Now consider crack propagation from a_1 to a_2 over the time interval Δt. Ahead of the initial crack-tip position at $x = a_1$, a new beam section of length ($a_2 - a_1$) is formed as shown in Figure 6.2, with the total energy related to vibration (or wave propagation) supplied to this new beam section being $F_1\,(\Omega)\Delta t$. Following the same arguments and techniques developed for consideration of dispersion in Section 5.3.2.3, the energy flux due to $F_1\,(\Omega)\Delta t$ at the new crack-tip position at $x = a_2$ is

$$F_2\left(\Omega\right)=\dot{a}_1 b\sum\nolimits_{i=1}^{\infty} f_i' G_{\text{vib}}^{i}\left(a_1\right), \tag{6.10}$$

where f_i' is the correction factor that accounts for the dispersion of flexural waves in the new beam section of ($a_2 - a_1$); it is a function of the new beam section's boundary conditions only.

By combining Eqs. (5.26) ($G_{\text{vib}} = F_{\text{vib}}\left(\Omega\right)/\dot{A}_0$) and (6.10), the ERR component due to vibration at the new crack length of a_2 is therefore

$$G_{\text{vib}}\left(a_2\right)=\frac{F_2\left(\Omega\right)}{b\dot{a}_2}=\frac{12\sqrt{\rho AEI}v^2 t}{ba_1^2}\frac{\dot{a}_1}{\dot{a}_2}\left(1-\frac{\dot{a}_1^2}{C_0^2}\right)\sum_{i=1}^{\infty}\frac{\Lambda_i}{\lambda_i}f_i'\sin\left(\omega_i t\right). \tag{6.11}$$

The ratio f_i' or correction factor for dispersion for propagating crack is determined in the same way as f_i in Section 5.3.2.3. Note that the boundary conditions for the new beam section of ($a_2 - a_1$), formed by crack propagation, are different to the boundary conditions for the stationary crack in Section 5.3.2.3, f_i' must be different to f_i. If ($a_2 - a_1$) is small then $\dot{a}_1 \approx \dot{a}_2$ and the boundary conditions for the new beam section can be taken as approximately fixed-fixed, where the deflections and slopes at both $x = a_1$ and $x = a_2$ are all zero. From Section 5.3.2.3, f_i' is still derived as $f_i' = \lambda_1'/\left(2\lambda_i'\right)$, but now λ_i' is determined from the frequency equation of a beam with fixed-fixed boundary condition, that is, $\cos\left(\lambda_i'\right)\cosh\left(\lambda_i'\right)-1=0$ (Eq. (2.25)). The value of λ_i' and the corresponding correction factor for dispersion for propagating crack are given in Table 6.1.

Table 6.1 Correction factor for dispersion for propagating crack

Mode number	1	2	3	4	5	i > 5
Frequency solution λ_i'	4.73004	7.85320	10.99561	14.13717	17.27876	$\frac{\left(2i+1\right)\pi}{2}$
Correction factor f_i'	0.5	0.30115	0.21509	0.16729	0.13687	$\frac{1.50562}{\left(2i+1\right)}$

The frequency of the ith mode flexural wave is $\omega_i = \lambda_i^2 a^{-2}\sqrt{EI/\left(\rho A\right)}$ (from Eq. (2.11) with $\lambda_i = \beta_i a$). The excitation point is at the free end of the DCB arms, and these waves travel toward to crack tip; since the crack propagates, the frequency of each flexural wave that the crack tip observes needs to be modified due to the Doppler effect. The frequencies of flexural waves observed at the crack tip decrease with increasing crack-propagation speeds. For a propagating crack, the actual frequency of the *i*th mode flexural wave observed at the crack tip is

$$\omega_i' = \left(1 - \frac{\dot{a}}{C_\mathrm{p}^i}\right)\omega_i . \tag{6.12}$$

Combining Eqs. (6.8), (6.11) and (6.12), the total dynamic ERR for a propagating crack is

$$\begin{aligned} G_\text{propagation}^\text{local} &= \frac{9EIv^2t^2}{ba^4}\left(1 - \frac{\dot{a}^2}{C_0^2}\right) \\ &+ \frac{12\sqrt{\rho AEI}v^2t}{ba^2}\left(1 - \frac{\dot{a}^2}{C_0^2}\right)\sum_{i=1}^{\infty}\frac{\Lambda_i}{\lambda_i} f_i'\sin\left[\left(1 - \frac{\dot{a}}{C_\mathrm{p}^i}\right)\omega_i t\right]. \end{aligned} \tag{6.13}$$

6.2.2.3 Limiting speed of crack propagation in DCBs

For the first term of Eq. (6.13), which is the ERR component due to the strain energy of quasi-static motion, the crack propagation speed $\dot{a}$ should be no larger than $C_0 = \sqrt{E/\rho}$. This component of ERR would otherwise become negative, inhibiting crack propagation. For the second term of Eq. (6.13), which is the ERR component due to vibration, there is another constraint in addition to $\dot{a} \le C_0$: the crack propagation speed $\dot{a}$ must be no greater than C_p^1, that is, $\dot{a} \le C_\mathrm{p}^1$. Vibration energy would otherwise not be supplied to the propagating crack tip (recall that C_p^1 is the phase speed of the first-mode flexural wave, which carries all the other higher mode waves). This speed is

$$C_\mathrm{p}^1 = \frac{\lambda_1}{a}\sqrt{\frac{EI}{\rho A}} = \frac{\lambda_1}{\sqrt{12}} r \sqrt{\frac{E}{\rho}}, \tag{6.14}$$

where $r = h/a$ is the aspect ratio the half DCB, and so the limiting speed of crack propagation in DCBs is proportional to r; and $\lambda_1 \approx 3.9266$ (Table 5.2).

Freund [36] derived that for mode-I fracture, the crack-propagation speed cannot surpass the Rayleigh wave speed C_R, where $C_\mathrm{R} = (0.862 + 1.14v)C_\mathrm{s}/(1 + v)$ in Eq. (2.58) approximately (see Section 3.3.2.2). The ratio of these two limiting speeds, C_p^1 and C_R, is

$$\frac{C_\mathrm{p}^1}{C_\mathrm{R}} = \frac{\lambda_1}{\sqrt{6}} \frac{1+\nu}{\left(0.862+1.14\nu\right)\sqrt{1-\nu}} r. \tag{6.15}$$

These two different limiting speeds, C_p^1 and C_R, are not in contradiction to each other: instead, C_p^1 is a development of C_R when applied to a DCB with a given aspect ratio. Freund's original derivation of the limiting crack-propagation speed as the Rayleigh wave speed C_R was based on a crack in an infinite sheet (see Eq. (3.47)). The crack provides a traction-free surface on a semi-infinite medium, where Rayleigh waves can form (Section 2.3.2.2). If, however, additional structural constraints are included, for example, in the form of another traction-free surface imposed parallel to the existing one, the semi-infinite medium develops into a plate. For a thick plate, Rayleigh waves become Rayleigh-Lamb waves, which are the superposition of A0 (asymmetric mode) and S0 (symmetric mode) Lamb waves [163] (Section 2.3.2.3). A0 Lamb waves resemble flexural waves and S0 Lamb waves resemble axial waves [26]. For a thin plate, A0 Lamb waves become the 2D counterpart of flexural waves in Euler-Bernoulli beams [164] (Figure 2.9), and, if axial motion is absent, the influence of S0 Lamb waves can be ignored.

For the increasingly constrained structure described above, as it develops from a semi-infinite sheet to an Euler-Bernoulli beam, Rayleigh waves develop into flexural waves in a beam, and accordingly, the Rayleigh wave speed drops to the phase speed of flexural waves. This leads to a reduction in the limiting speed of crack propagation, as determined by Eq. (6.15).

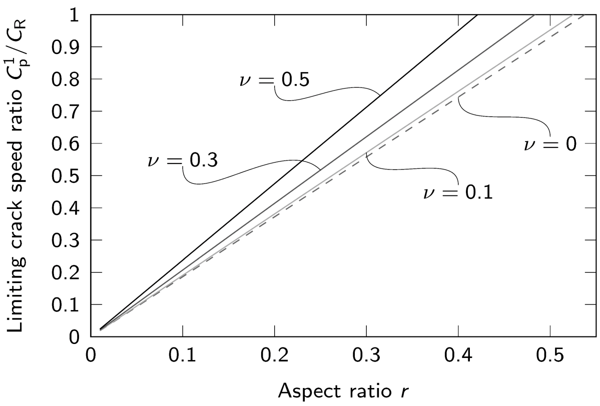

Figure 6.3 Effect of aspect ratio on limiting crack-propagation speed for various Poisson's ratios

According to the assessment in Eq. (6.15), the limiting crack-propagation speed decreases with decreasing aspect ratio and decreasing Poisson's ratio as shown in Figure 6.3. The limiting speed of crack in a DCB, therefore, decreases with the increasing crack length. For the conventional DCB test employed to determine the mode-I fracture toughness in CFRPs, the aspect ratio magnitude typically ranges from 0.01 to 0.1 [11], and so, from Eq. (6.15), the corresponding limiting speed of crack propagation is therefore in the range from $0.02C_R$ to $0.25C_R$.

There are currently relatively few experimental data on dynamic crack propagation available in the literature [81] for CFRPs in DCBs, at least partly due to the challenges such as tests pose for experimental setup design. Experimental data for high loading rates are available in [19] and [20], which used a servo-hydraulic test machine with a 'lost motion device' to achieve opening rates up to 15 m s^{-1} and in [90], that employed an electromagnetic Hopkinson bar to obtain opening rates up to 30 m s^{-1}.

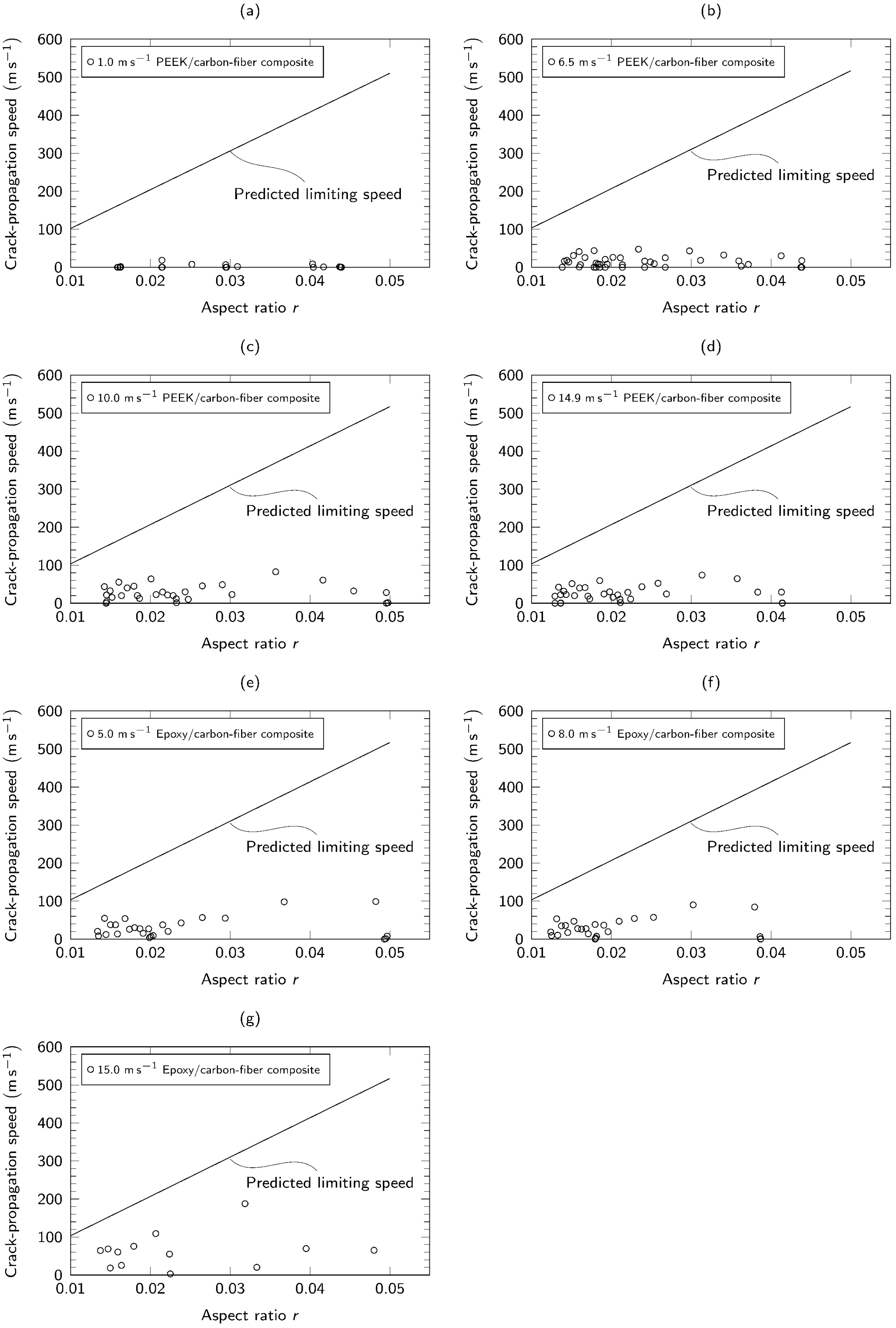

Figure 6.4 Comparison of experimentally measured crack-propagation speeds under various opening (loading) rates [19][20] against theoretically predicted limiting speed

The crack-propagation speeds measured in [19] and [20] under various loading rates for two kinds of CFRPs, PEEK/carbon-fibre and epoxy/carbon-fibre composites, are plotted in Figure 6.4. The theoretical limiting speed of crack propagation, predicted by Eq. (6.14), is also plotted. The measured crack-propagation speeds are well below the predicted limiting speed for all the opening rates up to 15 m s^{-1}. Note that the experimentally measured crack-propagation speeds are in a distance to the proposed limiting crack-propagation speed, the reason for this distance is due to the low applied loading rate. To investigate this, the crack-propagation speeds for each loading rate are regressed against the corresponding aspect ratios, and results for PEEK/carbon-fibre composite and epoxy/carbon-fibre composite are shown in Figures 6.5a and b, respectively. Note that according to Eqs. (6.4) and (6.5), which provides a mean value for crack-propagation speed, as well as the relationship $r = h/a$, the crack-propagation speed is proportional to the aspect ratio, and, therefore, the crack-propagation speed is linearly regressed against the aspect ratio.

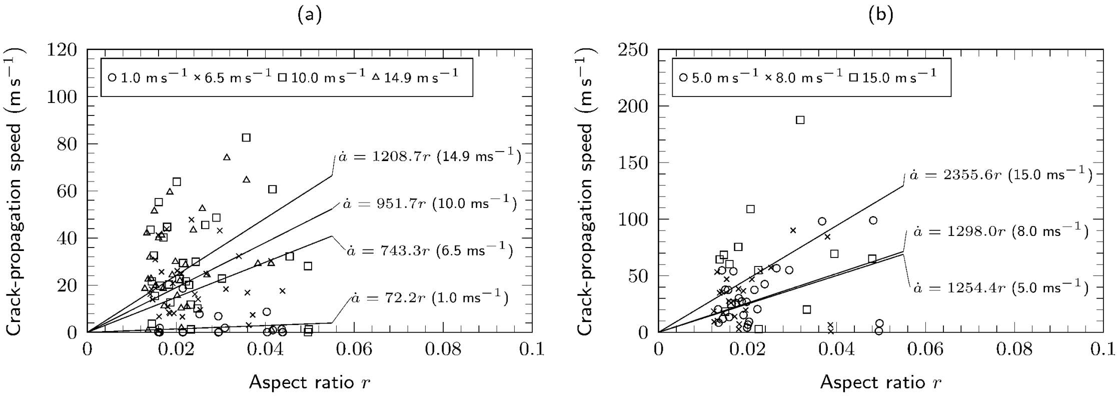

Figure 6.5 Crack-propagation speeds regressed against aspect ratio: (a) PEEK/carbon-fibre composite and (b) epoxy/carbon-fibre composite

Apparently, crack-propagation speeds increase with loading rates, and decrease with reduced aspect ratios, which is in accordance with the proposed limiting crack-propagation speed in Figure 6.3; based on the tendency shown in Figure 6.5, it is sensible to predict that with an increasing loading rate, the crack-propagation speed can increase closer to the proposed crack-propagation speed reducing the distance shown in Figure 6.4; and if the applied loading rate is adequate high, the crack-propagation speed can approach to the proposed limiting crack-propagation speed but cannot surpass it, since when crack propagates faster than limiting crack-propagation speed, the energy cannot be supplied to the crack tip for crack growth.

Ref. [90] reports crack-propagation speeds for 18 specimens of unidirectional epoxy/carbon-fibre composite, ranging from 108 m s^{-1} to 253 m s^{-1}. For the given opening rates of up to 30 m s^{-1}, the lowest predicted the limiting crack propagation speed from Eq. (6.14) is 385 m s^{-1}, and so the measured crack-propagation speeds are also within the predicted limit.

A further two points should be noted concerning Eq. (6.15). First, for aspect ratios in the range from 0.4 to 0.5 when the thickness and crack length are of the same order, it might appear that the limiting crack-propagating speed can reach C_R as Rayleigh waves can form [30]. The Euler-Bernoulli beam assumption, however, requires that $r = h/a < 0.1$. Second, when the aspect ratio approaches zero, it might appear that the limiting crack-propagation speed should also approach zero, which would mean that crack cannot propagation. For zero aspect ratio, however, the structure instead behaves like a string and is unable to bear compression or bending loads. This should not be the case with real DCB configurations.

6.3 Experimental verification

Fracture toughness is generally rate-dependent as shown by the slip-stick non-smooth propagation behaviour under high loading rates; this is also demonstrated by the experimental results in [19] and [20], which are used to verify the analytical solution for rate-dependent fracture toughness developed in Section 6.2.2.

There are relatively few experimental studies of DCBs under high loading rates in the literature [81]. Blackman et al. [19][20], however, performed a comprehensive series of experiments under high opening rates of up to 15 m s^{-1}. Two of these DCB experiments, with PEEK/carbon-fibre composite under opening rates of 6.5 m s^{-1} and 10 m s^{-1}, were selected to verify the analytical solution developed in Section 6.2.2. For this composite, the longitudinal modulus is taken as 115 GPa, the Poisson's ratio as 0.28 and the density as 1540 kg m^{-3} [19][20]. The half DCB thickness is 1.5 mm, and the width is 20 mm. A plane-strain condition is therefore assumed in the analytical calculations with the effective Young's modulus taken as $E/(1-\nu^2) = 124.78$ GPa.

Before crack propagation, that is, for a stationary crack, the solution of Eq. (5.32) in Section 5.3.2.4 was used, which provides a continuous ERR with respect to time since the crack length does not increase. During crack propagation, Eq. (6.13) developed in Section 6.2.2.2 for rate-dependent fracture toughness was used to calculate the dynamic

ERR. The first five vibration modes were considered in both cases, which Section 5.3.2.3 and Section 5.5.2 showed to be adequate.

The original experimental data of crack length versus time curves in [19] and [20] includes 51 data points at evenly spaced intervals for the test with the 6.5 m s^{-1} opening rate, and 31 points for the test with the 10 m s^{-1} opening rate. A central difference calculation was therefore used to estimate the crack-propagation speed with $\dot{a}\left(t_n\right)=\left[a\left(t_{n+1}\right)-a\left(t_{n-1}\right)\right]\big/\left(t_{n+1}-t_{n-1}\right)$, since there are not enough data points to get an accurate estimation otherwise (further study for assessment of crack-propagation speed is in Section 6.5). When calculating the ERR, the effective crack length of $a_{\text{eff}} = a+\Delta$ was used, where a is the actual crack length and Δ is an additional crack length aimed to compensate for crack-tip rotation [19][20], which otherwise is not captured by Euler-Bernoulli beams with effective boundary condition. The corresponding values of Δ for each test are from [19] and [20]. The Δ for 6.5 m s^{-1} opening rate is 4.4 mm (see Table 6.2), and that for 10 m s^{-1} opening rate is calculated by linear interpolating for opening rates 6.5 m s^{-1} and 14.9 m s^{-1}, giving Δ = 5 mm.

Experimental verification for DCB under 6.5 m s^{-1} loading rate

The theoretical results of the dynamic ERR for the DCB test with the 6.5 m s^{-1} opening rate are plotted in Figure 6.6. They are based on the experimentally observed crack length and propagation speeds (the crack length is also plotted in Figure 6.6 with values on the secondary axis). Note that Ref. [22] simulates Blackman et al.'s [19][20] experiments using FEM with ITLSM (Section 4.3.2.3), and in these simulations, the crack initiation time is higher than the actual crack initiation time in the experiments. This is because "the lost motion device was set to allow a period of pre-travel to ensure that the test was conducted at constant velocity" in experiments [19][20], and so this pre-travel period should be taken into consideration. The FEM results in [22] were therefore used to shift the initiation time in the experimental data. The experimental results in Figure 6.6 are plotted on this shifted time scale in order to make a valid comparison with the theory. The crack-initiation toughness (CIT) of 1400 N m^{-1} and crack-arrest toughness (CAT) of 670 N m^{-1} are taken from the same reference [22], in which Liu et al. performed a parametric FEM study of different values of CIT and CAT aiming to match the experimentally measured crack length versus time curve. These values are not required in the calculation of dynamic ERR and are only shown for comparison.

Using the developed analytical solutions – Eq. (5.32) for stationary crack and Eq. (6.13) for propagating crack – and the experimentally observed crack length and propagation speed, the dynamic ERR was calculated for both stationary and propagating cracks. For the stationary crack, it is expected that crack should not propagate until the ERR exceeds the CIT (1400 N m^{-1}). For propagating crack, it is expected that the crack should propagate if the ERR exceeds the CAT (670 N m^{-1}) and should be arrested otherwise. Moreover, once the dynamic ERR drops below the CAT and crack propagation is arrested, it is expected that it re-initiates (i.e. continue propagating again) only once the dynamic ERR builds up and exceeds the CIT again.

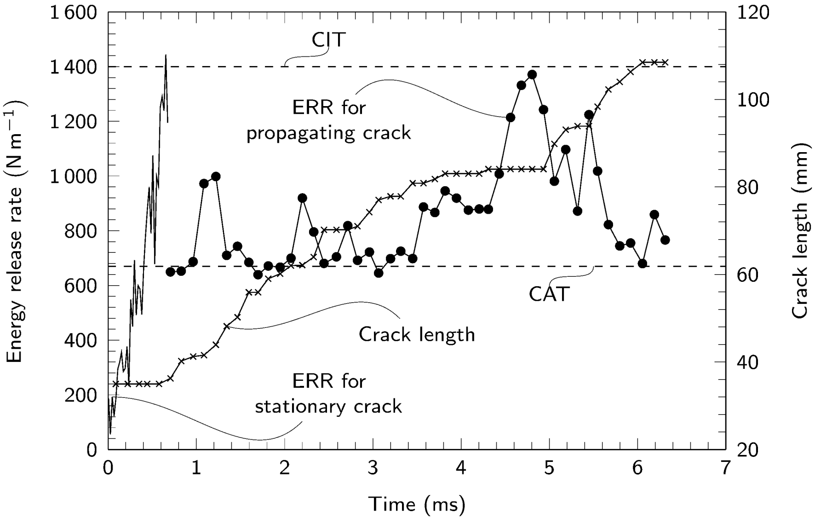

Figure 6.6 Evolution of dynamic ERR and crack length for 6.5 m s^{-1} loading rate based on experimentally observed crack-propagation speed

Apparently, the developed analytical theory is generally in excellent agreement with the experimental results (Figure 6.6): (1) The crack initiates and begins to propagate once the dynamic ERR reaches the expected CIT (i.e. after 0.6 ms). (2) The dynamic ERR is equal to or greater than the CAT, while it propagates continuously between about 0.6 ms and 3.5 ms. Note that a small number of data points in this period are slightly below the CAT and that in the period between 2.4 ms and 2.7 ms (with three sample points), there appears to be a very short period of arrest. Nevertheless, the general tendency in the period from 0.6 ms to 3.5 ms is that of propagation with the dynamic ERR equal to or greater than the CAT. There are several considerations, which indicates that the general tendency is more important than close attention to singular or small groups of data points when interpreting these experimental results. In both cases, at least part of the cause is the relatively few experimental sample points, which prevented accurate estimation of the crack-propagation speed (detailed discussion in Section 6.5). Also, concerning the short arrest period, the FEM simulation shows its absence (see Figure 6.9). Generally, dynamic tests are well-known to be probabilistic in nature [165], particularly where damage is concerned, and on small scales of time and space, whereas the developed theory is deterministic. For all these reasons, it is sensible to consider that the crack propagates during the short period between 2.4 ms and 2.7 ms with the dynamic ERR equal to or greater than the CAT (thus permitting continued propagation). (3) At about 3.5 ms, for the reasons described above, it is also within the probable error margin that the dynamic ERR drops below the CAT, and the propagation is arrested. (4) Once propagation is arrested, the dynamic ERR needs to exceed the CIT again in order to re-initiate. Indeed, there is a crack arrest period between 3.5 ms and about 4.8 ms, where the dynamic ERR is lower than the CIT. (5) At about 4.8 ms, the dynamic ERR reaches the CIT again and then the crack propagates until about 6 ms with the dynamic ERR within the limits set by the CIT and the CAT. (6) At 6 ms, the dynamic ERR drops below the CAT and the propagation arrests once more.

Experimental verification for DCB under 10 m s^{-1} loading rate

The theoretical results of dynamic ERR for the DCB test with the 10 m s^{-1} opening rate are presented in Figure 6.7. These results are based on the experimentally observed crack length and propagation speeds (the crack length is also plotted in Figure 6.7 with values on the secondary axis). As previously explained, to account for the period of pre-travel in the experiment, the experimental results are plotted on a shifted time scale, with the required amount of shift determined using the FEM results in [22]. The values of CIT and CAT were also determined in the same reference as 1300 N m^{-1} and 300 N m^{-1}, respectively. These toughness values are not required in the calculation of dynamic ERR and are only shown for comparison.

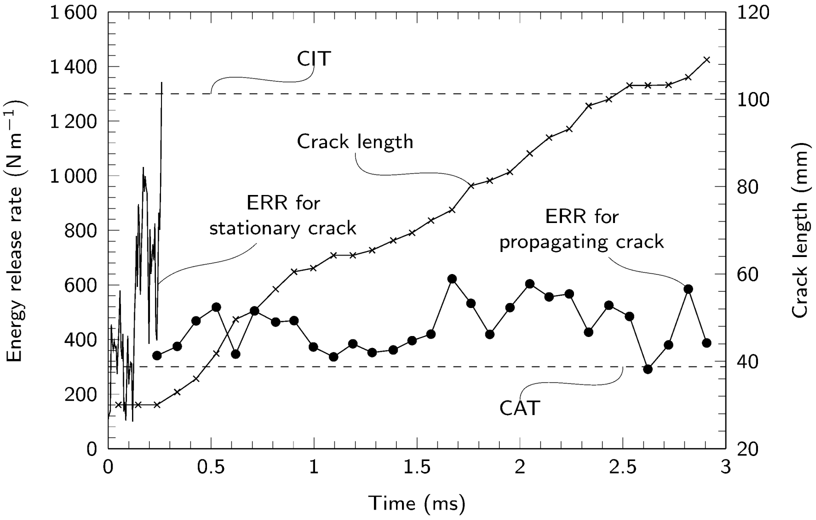

Figure 6.7 Evolution of dynamic ERR and crack length for 10 m s^{-1} loading rate based on experimentally observed crack-propagation speed

Figure 6.7 again demonstrates an excellent agreement between the developed analytical theory and the experimental results: (1) The crack initiates and begins to propagate once the dynamic ERR reaches the expected CIT. (2) After crack initiation, there is a significant drop of dynamic ERR, which remains above the CAT until $t = 2.6$ ms, when the propagation arrests.

In both comparisons with dynamic DCB experiments at different opening rates, the developed analytical theory predicts dynamic ERRs that are in line with the observed crack-propagation behaviour. This is a strong confirmation that the developed analytical theory accurately predicts the values of CIT and CAT at times of the crack initiation or re-initiation, and arrest.

6.4 Numerical verification

6.4.1 Verification for developed theory for constant fracture toughness

For the crack propagation in the DCB with constant fracture, the same geometry in Figure 5.6 and material properties in Section 5.4.1 were used, but the fracture toughness of the material was set to 200 N m^{-1}, and the width of the specimen set to 0.05 mm. 3D finite-element model was built with 3D stress elements (C3D8R) with one element in the widthwise direction. Widthwise displacement was constrained, which simulated a plain-strain condition, Consequently, the effective Young's modulus of $E/(1–\nu^2)$ was used in the analytical calculations. The VCCT method was used to model the crack propagation.

In the analytical model, crack initiation time is predicted by analytical solution for stationary crack in Eq. (5.20) and crack length is derived by Eq. (6.5) with crack extension being $A_1\sqrt{t-t_0}$. Note that the coefficient A_1 is determined by the crack initiation condition.

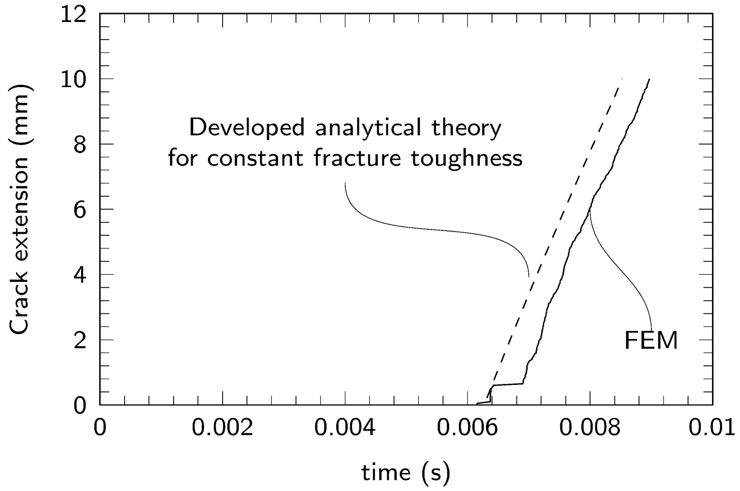

Figure 6.8 Comparison of crack extension obtained from FEM simulation and from the developed analytical theory for material with constant fracture toughness

The comparison for the crack extension from the analytical solution and the FEM simulation is shown in Figure 6.8. Both analytical and numerical methods predict the same crack initiation time, and they also agree well with each other for the period just following crack initiation. This is as expected since the analytical solution for stationary crack with the first-mode accuracy has already been shown to agree well with the FEM in predicting the ERR in Section 5.4.2. Subsequently, however, the FEM shows a period of a crack arrest of about 0.0005 s after crack initiation, after which the crack grows steadily with a slope that is well predicted by the theory. The FEM captures the crack arrest period, but the analytical theory does not for the reasons explained in Section 6.2.1.

This comparison shows that, for brittle materials with moderate density, the analytical theory developed for constant fracture toughness based on the ERR with the first-mode accuracy can predict the ERR well (and thus the crack initiation time), as well as the slope of the crack-extension curve.

6.4.2 Verification for developed theory for rate-dependent fracture toughness

The experimental verification (Section 6.3) for the theory developed for rate-dependent fracture toughness of Eq. (6.13) can accurately predict the main features of fracture behaviour such as initiation, propagation and arrest. More detailed comparisons between the developed analytical theory and experiment were not possible, however, since dynamic ERR cannot be measured directly from experiments without post-processing (for example, using the developed theory), and because of the insufficient number of sample points for accurate measurement of the crack propagation speed.

Instead, the results from FEM analysis in [22], which simulated the same experiments in [19] and [20] considered in Section 6.3, were used to further verify the developed analytical theory. The FEM analysis by Liu et al. [22] used ITLSM (see Section 4.3.2.3) to simulate 3D DCB under different loading rates. Full details are given in [22]. Following the same procedure described in Section 6.3 for experimental verification, the FEM results for crack length and crack propagation speed were used together with the developed analytical theory for rate-dependent fracture toughness to determine the analytical dynamic ERR, which could then be compared directly with the dynamic ERR of the respective FEM results.

Numerical verification for DCB under 6.5 m s^{-1} loading rate

The dynamic ERR calculated with developed analytical theory (based on the crack length versus time curve obtained from the FEM simulation as well as the crack propagation speed) and the FEM results for the 6.5 m s^{-1} loading case are compared in Figure 6.9.

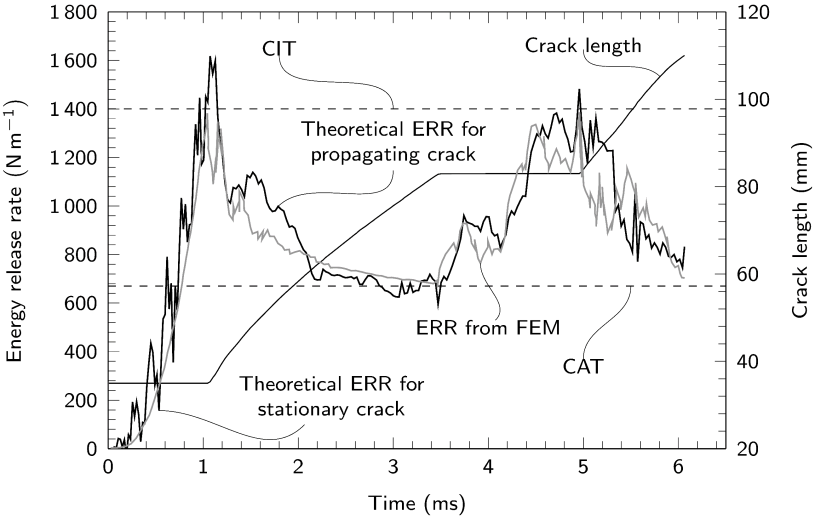

Figure 6.9 Evolution of dynamic ERR and crack length for 6.5 m s^{-1} loading rate based on FEM results of crack-propagation speed

They are in excellent agreement for both stationary crack and propagating cracks. Note that the developed analytical theory predicts a slightly higher ERR in comparison to the result from FEM. This is reasonable since the FEM model used a 3D formulation with the anisotropic material properties of E_{11} = 115 GPa and E_{22} = 8 GPa, making this model less stiff than the analytical one. The discrepancy is not significant.

Numerical verification for DCB under 10 m s^{-1} loading rate

The dynamic ERR determined with the developed analytical theory (based on the evolution of the crack length calculated with the FEM result as well as the crack propagation speed) and the numerical result are compared in Figure 6.10 for 10 m s^{-1} loading case. They are in excellent agreement for both regimes of crack – stationary and propagation.

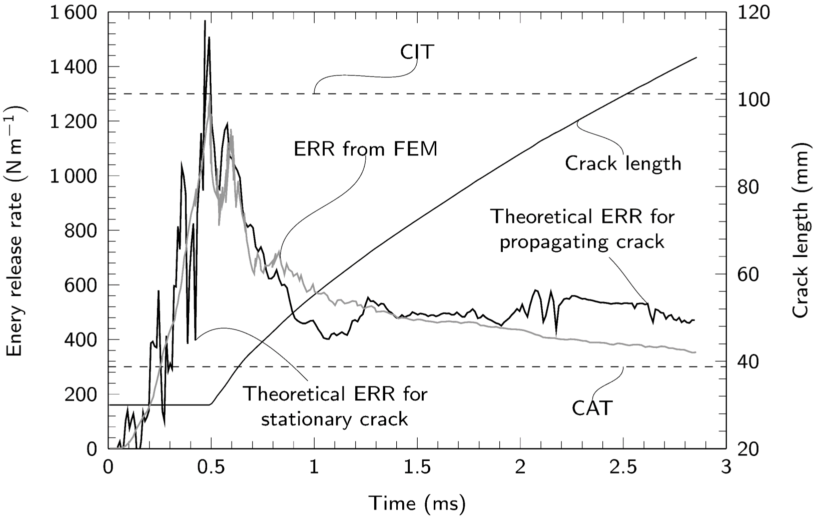

Figure 6.10 Evolution of dynamic ERR and crack length for 10 m s^{-1} loading rate based on FEM results of crack-propagation speed

The analytical theory developed for the material with rate-dependent fracture toughness is therefore verified and can accurately predict the dynamic ERR in DCB tests under high loading rate, and also to characterise the main feature of fracture behaviour such as crack initiation, propagation and arrest.

6.5 Crack-propagation speed assessment and dynamic ERR

An accurate prediction of dynamic ERR requires an accurate estimation of crack-propagation speed. Due to the relatively small number of experimental sample points, central difference method was used in Section 6.3 to assess the crack-propagation speed at a given time based on two crack-length measurements to avoid sudden jumps in the crack-propagation speed, so $\dot{a}(t_n)=\left[a(t_{n+1})-a(t_{n-1})\right]/(t_{n+1}-t_{n-1})$ was used.

Another two possible methods to assess the crack-propagation speed include backward difference method with $\dot{a}(t_n)=\left[a(t_n)-a(t_{n-1})\right]/(t_n-t_{n-1})$, and forward difference method with $\dot{a}(t_n)=\left[a(t_{n+1})-a(t_n)\right]/(t_{n+1}-t_n)$. Ideally, these three methods would give values of crack-propagation speed in close agreement, but this may not be the case in real experiments under high loading rates when the actual number of sample points for the crack length is determined by the capability of the experimental setup, for example, high-speed cameras.

For the experimental verification in Section 6.3 (i.e. PEEK/carbon-fibre composite under the opening rate of 6.5 m s^{-1}), the three methods of determining the crack-propagation speed are examined. At $t = 3.065$ ms, the crack-propagation speed is 15.15 m s^{-1} by central difference method, 26.81 m s^{-1} by backward difference and 6.14 m s^{-1} by the forward difference; the dynamic ERR predicted with these crack-propagation speeds are 645.33 N m^{-1}, 809.01 N m^{-1} and 625.19 N m^{-1}, respectively, and the mean and range of these dynamic ERR values is therefore 693.18±82.32 N m^{-1}. Following this approach, the dynamic ERR for every sample point is calculated, and the mean and range results of the dynamic ERR are shown in Figure 6.11.

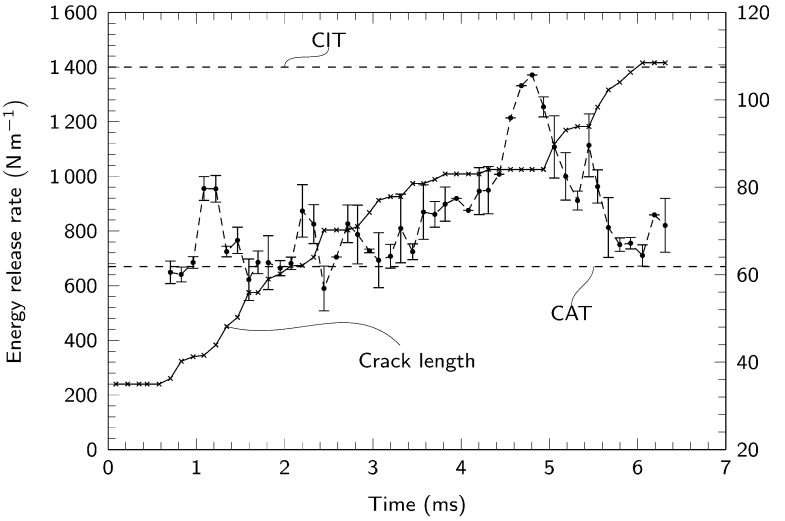

Figure 6.11 Mean value of dynamic ERR and its range by three methods of assessing crack-propagation speed

Apparently, precise prediction of the dynamic ERR based on the developed analytical solution of Eq. (6.13) in Section 6.2.2 depends on the accurate determination of the crack-propagation speed. The mean value of the dynamic ERR from the three estimation methods of the crack-propagation speed can capture the main crack-propagation behaviours including its arrest and re-initiation. The CAT measured from the experimental results in this way is a range rather than the single value of 670 N m^{-1} determined by the FEM simulation. The crack re-initiation value at $t = 4.81$ ms is not affected by estimation of the crack-propagation speed, however, because it is zero before re-initiation.

There is a particular point at $t = 2.46$ ms, where the mean dynamic ERR drops significantly below the CAT value of 670 N m^{-1} (the value determined by the FEM simulation). This one point is not considered problematic for several reasons: (i) the overall crack behaviour around this time is one of crack propagation (see Section 6.3); (ii) the range still allows for a dynamic ERR that exceeds the CAT; and, furthermore, (iii) there are other contributions to the experimental error besides estimation of the crack-propagation speed, which is the one considered here.

At t = 2.46 ms, the forward and backward differences for crack-propagation speed give a lower limit of 0 m s^{-1} and an upper one of 53.31 m s^{-1}, respectively, and the central difference gives 24.12 m s^{-1}. To study the sensitivity of the dynamic ERR to the crack-propagation speed, the dynamic ERR is calculated for this particular point at t = 2.46 ms with the crack-propagation speed ranging from 0 to 55 m s^{-1} while keeping other parameters same; the results are shown in Figure 6.12.

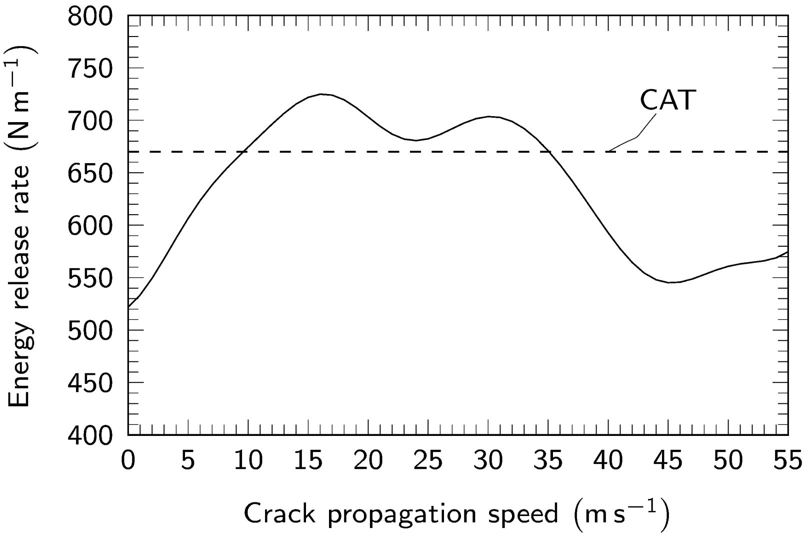

Figure 6.12 Dynamic ERR versus crack-propagation speed for sample point t = 2.46 ms

The dynamic ERR ranges from 521.9 N m^{-1} to 724.9 N m^{-1}. For the crack-propagation speeds between 10 m s^{-1} and 35 m s^{-1}, the dynamic ERR is above the CAT value of 670 N m^{-1}. Note that the lower limit of crack-propagation speed at this point is 0, while the upper one is 53.31 m s^{-1}. The mean value gives the dynamic ERR above 670 N m^{-1}; this is as expected since the general crack behaviour around this point is propagation.

In conclusion, application of the theoretical solution developed in this chapter clearly requires the accurate estimation of the crack-propagation speed. For a relatively small number of experimental sample points, however, the central difference method may offer a reasonable prediction of the dynamic ERR.

6.6 Crack-tip-rotation compensation for propagating crack

In Section 6.3 experimental and Section 6.4 numerical verifications, when applying Eq. (6.13), the effective crack length $a_{\mathrm{eff}} = a+\Delta$ is used, aiming at compensating the crack-tip rotation. The additional crack lengths Δ were from [19] and [20] as shown in Table 6.2 corresponding to various opening rates.

Table 6.2 Experimental values of Δ for the PEEK/carbon-fibre composite

Opening rate	1.67×10^{-5} m s^{-1}	1.10 m s^{-1}	6.50 m s^{-1}	14.90 m s^{-1}	18.40 m s^{-1}
Δ	3.6 mm	2.0 mm	4.4 mm	6.0 mm	8.5 mm

In Table 6.2, Δ = 3.6 mm was determined by the MCC method (Section 5.5.1), with the opening rate of 1.67×10^{-5} m s^{-1} being as the quasi-static loading rate. The other values for Δ, however, were not determined by the MCC method, since the MCC method cannot be used in dynamic DCB tests due to the inaccurate assessment of compliance from the oscillating external forces under high loading rates. Instead, these values for Δ under high loading rates were derived by Blackman et al. [20] as they used another method of linearly regressing the experimentally measured crack length a against the square root of time $t^{1/2}$ with the Δ being the negative intercept corresponding to $t = 0$. It is noteworthy that the additional crack length Δ for propagating cracks determined in this way under high loading rates is rate-dependent as shown in Table 6.2 whereas the additional crack length Δ for stationary cracks determined by the MCC method is rate-independent. The reason for the rate-dependency of Δ is the presumption that the crack length a is linearly related to square root of time $t^{1/2}$ while in reality the crack length is in a stick-slip fashion, and this linearly regression fits all the crack behaviours (propagation, arrest, re-initiation) all together against the root time, making the additional crack length Δ a representation of the average crack behaviour rather than only compensation for crack-tip rotation; under different high loading rate, the crack behaves differently with different combinations of crack propagation, arrest and re-initiation, and this explains the rate-dependency of the additional crack length Δ.

The experimental (Section 6.3) and numerical (Section 6.4) verifications have shown for the propagating cracks, with the rate-dependent Δ in Table 6.2, the analytical solution can accurately predict the dynamic ERR. However, these Δ, representing the average crack propagation behaviour rather than only compensating for crack-tip rotation, might disguise some local crack behaviour, and therefore further investigation is desirable. And this is one objective in Chapter 7 to introduce the elastic foundation into the analytical framework, which allows the crack tip to rotate to avoid using the compensation.

6.7 Conclusion

In this chapter, analytical theories for dynamic mode-I crack propagation are developed for a DCB with constant and rate-dependent fracture toughness under high loading rates based on the established analytical framework in Chapter 5.

For a propagating crack in a DCB with constant fracture toughness material, crack propagation speed is determined by fracture criterion $G = G_c$ and it is found that crack-propagation speed is $\dot{a} = a/(2t)$ and integration of this crack-propagation speed gives the crack length as $a = a_0 + A_1\sqrt{t - t_0}$. These analytical solutions are in accordance with conventional solutions for interfacial fracture but including dynamic effects of vibration. The crack length curve predicted by this analytical solution is verified against FEM simulations. The analytical result predicts the same slope for crack length curve indicating the accurate crack propagation speed assessment, but it cannot predict a short crack arrest near crack initiation observed by FEM simulation. However, in the long run, this short crack arrest is not significant, and the analytical solution for the constant toughness is still applicable under the stated assumptions.

For a propagating crack in a DCB with rate-dependent fracture toughness material, dynamic ERR is derived using crack-tip bending moment and simplification method in Chapter 5, as well as an assumption of energy conservation at the crack tip, also accounting for dispersion and the Doppler effect. The developed analytical solution is also used to study the limiting speed of crack propagation in DCBs. For a conventional DCB test with a magnitude of aspect ratio $r = h/a$ ranging from 0.01 to 0.1 typically (where h is the DCB's arm thickness, a is the crack length), the limiting speed of crack propagation is determined to be in the range from $0.02C_R$ to $0.25C_R$, where C_R is the Rayleigh wave speed. The developed analytical theory for rate-dependent fracture toughness is verified against both experimental data and results of FEM simulations. It accurately predicts the dynamic ERR in comparison to FEM simulations; and it provides the correct assessment of fracture behaviour, including crack initiation, arrest and re-initiation observed in the experiments. The theory can, therefore, be used to determine the CIT and CAT values.

The developed analytical solution is based on effective boundary condition assumption of a fixed boundary condition at the crack tip, and compensation for crack-tip rotation is required via effective crack length $a_{\mathrm{eff}} = a+\Delta$. But the result in [20] shows that the additional crack length Δ for the propagating cracks is rate-dependent and also an average representation of crack behaviours rather than only a compensation for crack-tip rotation, which might limit its applications. Therefore, further analytical models are desirable to allow crack-tip rotation rather than using the compensation method, and this is achieved by introducing the elastic foundation in Chapter 7.

Chapter 7: Dynamic fracture on elastic interface

7.1 Introduction

The analytical framework of dynamic mode-I fracture for the rigid interface has been established in Chapter 5 for stationary cracks and Chapter 6 for propagating cracks in DCBs with effective boundary condition, which requires using effective crack length to compensate for crack-tip rotation; and there are some limitations in determining this crack-tip rotation compensation in the dynamic regime, and further analytical models that allow the crack tip to rotate is desirable. This can be achieved by introducing an elastic foundation into the established analytical framework, which allows the crack-tip to rotate. But more importantly, the dynamic fracture on the non-rigid interface can, therefore, be studied by this introduced elastic foundation.

The derived analytical solution for dynamic fracture on an elastic foundation can be directly applied to study the following structures: adhesively bonded or welded symmetric DCB (Figure 7.1a) and thin-layer-on-thick-substrate configuration (or spalling of a surface layer) (Figure 7.1b).

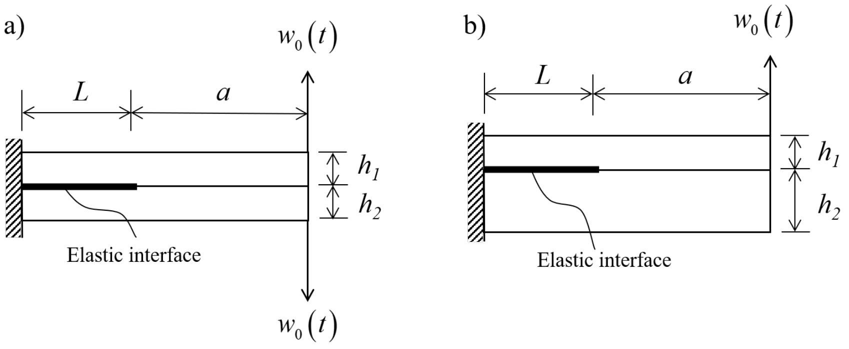

Figure 7.1 (a) Symmetric double cantilever beam with $h = h_1 = h_2$; (b) thin-layer-on-thick-substrate configuration with $h_1 = h$ and $h_1 << h_2$.

7.2 Theoretical development for stationary crack

The two configurations in Figure 7.1 can be represented by the configuration of Figure 7.2. And the dynamic ERR of this stationary crack shown in Figure 7.2 is derived analytically considering both vibration and wave propagation. Figure 7.2 shows that a beam in its initial undeformed condition rests on a partial elastic foundation with constant foundation stiffness k, with a time-dependent displacement $w_0(t)$ applied to the midplane of its free end. A constant opening rate v is selected, that is, $w_0(t) = vt$. The length of the beam section resting on the foundation representing the uncracked region is *L*. The length of the free beam section is *a*, which represents the crack length. The coordinate system is set so that the *x* axis is to the right with the crack tip at $x = L$, and the *z* axis is upwards, with the beam's transverse deflection in the *x*-*z* plane. The deflection of the foundation-supported beam section is represented by $w^{\mathrm{FD}}(x, t)$, and the deflection of the free beam section is represented by $w^{\mathrm{FR}}(x, t)$. It is assumed that there is no interfacial contact between the free beam section and the foundation and that the beam thickness *h* is small enough compared to *a* and *L* ($h/a<0.1$, $h/L<0.1$) for the Euler-Bernoulli beam theory to apply. At (0,0) it is assumed a fixed boundary, since deflection is constrained due to the symmetry, and when the foundation stiffness is large, the rotation is also constrained. Note that for thick beams with *h* not small compared to *a* and *L* the rotational inertia and shear can be significant, and Rayleigh beam theory (accounting for rotational inertia) and Timoshenko beam theory (accounting for rotational inertia and shear) have to be adopted, but this is beyond the scope of this thesis.

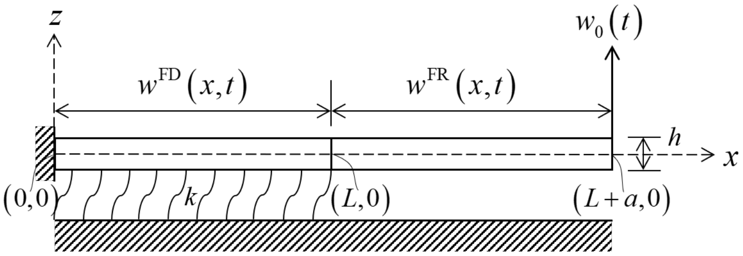

Figure 7.2 Configuration of beam partially supported on elastic foundation and prescribed coordinates

Now the global energy balance based on conservation of energy for this elastic structure with the crack area of A_0 (corresponding to crack length *a*) is

$$W_{\mathrm{ext}} = U + K + S + \Gamma, \tag{7.1}$$

where W_{ext} is the time-accumulated work done by the external forces; *U* and *K* are the instantaneous strain and kinetic energies of the beam, respectively; *S* is the instantaneous strain energy stored in the elastic foundation, and Γ is the time-accumulated energy, dissipated from the whole system in advancing the crack. At $t = 0$, the system is in its initial condition and all the energy terms are zero. Under displacement control, the applied displacement is held during the crack opening and so $dW_{\mathrm{ext}}/dA_0 = 0$. The energy dissipated from the system in incrementing the crack area by dA_0 is, therefore, the reduction in total mechanical energy of the system Π, where

$$\Pi = U + K + S\,. \tag{7.2}$$

Note that Π is the total mechanical energy of the system in Figure 7.2 at a given time t that could potentially be dissipated from the system during crack growth.

7.2.1 Dynamic response of beam on elastic foundation

By introducing shifting functions (Section 2.2.3), the dynamic transverse deflections of the beam sections shown in Figure 7.2 with applied constant-rate displacement $w_0(t) = vt$ takes the form of

$$w^{\text{FD}}\left(x,t\right) = w_{\text{fv}}^{\text{FD}}\left(x,t\right) + F^{\text{FD}}\left(x\right)vt\,, \tag{7.3}$$

$$w^{\text{FR}}\left(x,t\right) = w_{\text{fv}}^{\text{FR}}\left(x,t\right) + F^{\text{FR}}\left(x\right)vt\,, \tag{7.4}$$

where $w_{\text{fv}}^{\text{FD}}\left(x,t\right)$ and $w_{\text{fv}}^{\text{FR}}\left(x,t\right)$ are the free-vibration components of the foundation-supported beam section and the free beam section, respectively; $F^{\text{FD}}(x)$ and $F^{\text{FR}}(x)$ are the corresponding shifting functions. The shifting functions distribute the externally applied displacement along the beam.

The equation of motion for the vibration of an Euler-Bernoulli beam on an elastic foundation with constant foundation stiffness k is given in Eq. (2.5). Combining Eqs. (2.5) and (7.3), and enforcing homogeneous condition, the governing equation for the free-vibration component $w_{\text{fv}}^{\text{FD}}\left(x,t\right)$ and the corresponding shifting function $F^{\text{FD}}(x)$ for the foundation-supported beam section are obtained:

$$EIw_{\text{fv}}^{\text{FD}(4)}\left(x,t\right) + \rho A\ddot{w}_{\text{fv}}^{\text{FD}}\left(x,t\right) + kw_{\text{fv}}^{\text{FD}}\left(x,t\right) = 0\,, \tag{7.5}$$

$$EIF^{\text{FD}(4)}\left(x\right) + kF^{\text{FD}}\left(x\right) = 0\,. \tag{7.6}$$

Likewise, using Eqs. (2.6) and (7.4) for the free beam section, the governing equations for the free-vibration component $w_{\text{fv}}^{\text{FR}}\left(x,t\right)$ and the shifting function $F^{\text{FR}}(x)$ are

$$EIw_{\text{fv}}^{\text{FR}(4)}\left(x,t\right) + \rho A\ddot{w}_{\text{fv}}^{\text{FR}}\left(x,t\right) = 0\,, \tag{7.7}$$

$$F^{\text{FR}(4)}\left(x\right) = 0\,. \tag{7.8}$$

For the foundation-supported beam section, the boundary conditions for the total deflection $w^{\mathrm{FD}}(x, t)$ are $w^{\mathrm{FD}}(0, t) = 0$ and $w^{\mathrm{FD}(1)}(0, t) = 0$. By using these boundary conditions for $w^{\mathrm{FD}}(x, t)$ in Eq. (7.3), and enforcing homogeneous conditions, the boundary conditions for the free-vibration component $w_{\mathrm{fv}}^{\mathrm{FD}}(x,t)$ and the shifting function $F^{\mathrm{FD}}(x)$ are obtained in Table 7.1.

Table 7.1 Boundary conditions for the foundation-supported beam section

Boundary	Total deflection $w^{\mathrm{FD}}(x,t)$	Free-vibration component $w_{\mathrm{fv}}^{\mathrm{FD}}(x,t)$	Shifting function $F^{\mathrm{FD}}(x)$
$x=0$	$w^{\mathrm{FD}}(0,t)=0$	$w_{\mathrm{fv}}^{\mathrm{FD}}(0,t)=0$	$F^{\mathrm{FD}}(0)=0$
	$w^{\mathrm{FD}(1)}(0,t)=0$	$w_{\mathrm{fv}}^{\mathrm{FD}(1)}(0,t)=0$	$F^{\mathrm{FD}(1)}(0)=0$

For the free beam section with boundary conditions $w^{\mathrm{FR}}(L + a, t) = vt$ and $w^{\mathrm{FR}(2)}(L + a, t) = 0$, following a similar approach with Eq. (7.4), the corresponding boundary conditions for the free-vibration component $w_{\mathrm{fv}}^{\mathrm{FR}}(x,t)$ and shifting function $F^{\mathrm{FR}}(x)$ are obtained in Table 7.2.

Table 7.2 Boundary conditions for the free beam section

Boundary	Total deflection $w^{\mathrm{FR}}(x,t)$	Free-vibration component $w_{\mathrm{fv}}^{\mathrm{FR}}(x,t)$	Shifting function $F^{\mathrm{FR}}(x)$
$x=L+a$	$w^{\mathrm{FR}}(L+a,t)=vt$	$w_{\mathrm{fv}}^{\mathrm{FR}}(L+a,t)=0$	$F^{\mathrm{FR}}(L+a)=1$
	$w^{\mathrm{FR}(2)}(L+a,t)=0$	$w_{\mathrm{fv}}^{\mathrm{FR}(2)}(L+a,t)=0$	$F^{\mathrm{FR}(2)}(L+a)=0$

Considering continuity at the crack-tip location, $x = L$, since the two beam sections share the same deflection, slope, bending moment and shear force at this location, the continuity condition for the free-vibration components $w_{\mathrm{fv}}^{\mathrm{FD}}(x,t)$ and $w_{\mathrm{fv}}^{\mathrm{FR}}(x,t)$ as well as the shifting functions $F^{\mathrm{FD}}(x)$ and $F^{\mathrm{FR}}(x)$ are derived by enforcing homogeneous conditions, given in Table 7.3.

Table 7.3 Continuity conditions for total deflection and its components

Continuity	Total deflection	Free-vibration component	Shifting function
Deflection	$w^{\mathrm{FD}}(L,t)=w^{\mathrm{FR}}(L,t)$	$w_{\mathrm{fv}}^{\mathrm{FD}}(L,t)=w_{\mathrm{fv}}^{\mathrm{FR}}(L,t)$	$F^{\mathrm{FD}}(L)=F^{\mathrm{FR}}(L)$
Slope	$w^{\mathrm{FD}(1)}(L,t)=w^{\mathrm{FR}(1)}(L,t)$	$w_{\mathrm{fv}}^{\mathrm{FD}(1)}(L,t)=w_{\mathrm{fv}}^{\mathrm{FR}(1)}(L,t)$	$F^{\mathrm{FD}(1)}(L)=F^{\mathrm{FR}(1)}(L)$
Bending moment	$w^{\mathrm{FD}(2)}(L,t)=w^{\mathrm{FR}(2)}(L,t)$	$w_{\mathrm{fv}}^{\mathrm{FD}(2)}(L,t)=w_{\mathrm{fv}}^{\mathrm{FR}(2)}(L,t)$	$F^{\mathrm{FD}(2)}(L)=F^{\mathrm{FR}(2)}(L)$
Shear force	$w^{\mathrm{FD}(3)}(L,t)=w^{\mathrm{FR}(3)}(L,t)$	$w_{\mathrm{fv}}^{\mathrm{FD}(3)}(L,t)=w_{\mathrm{fv}}^{\mathrm{FR}(3)}(L,t)$	$F^{\mathrm{FD}(3)}(L)=F^{\mathrm{FR}(3)}(L)$

7.2.1.1 Solutions for free-vibration components and orthogonality

By the method of separation of variables, the solutions for the free-vibration components $w_{\mathrm{fv}}^{\mathrm{FD}}(x,t)$ in Eq. (7.5) and $w_{\mathrm{fv}}^{\mathrm{FR}}(x,t)$ in Eq. (7.7) are

$$w_{\mathrm{fv}}^{\mathrm{FD}}(x,t)=\sum_{i=1}^{\infty}W_i^{\mathrm{FD}}(x)T_i(t), \tag{7.9}$$

$$w_{\mathrm{fv}}^{\mathrm{FR}}(x,t)=\sum_{i=1}^{\infty}W_i^{\mathrm{FR}}(x)T_i(t), \tag{7.10}$$

where $W_i(x)$ represents the *i*th normal mode for the respective beam section, which is derived in Section 7.2.1.2, and $T_i(t)$ is the time-dependent modal displacement of the *i*th vibration mode, which is solved in Section 7.2.1.3. Substituting these solutions into Eqs. (7.5) and (7.7), introducing natural frequency ω_i and rearranging provide two ordinary differential equations for the normal modes, $W_i^{\mathrm{FD}}(x)$ and $W_i^{\mathrm{FR}}(x)$, and one ordinary differential equation for the modal displacement $T_i(t)$:

$$W_i^{\mathrm{FD}(4)}(x)+\left(\frac{k}{EI}-\omega_i^2\frac{\rho A}{EI}\right)W_i^{\mathrm{FD}}(x)=0, \tag{7.11}$$

$$W_i^{\mathrm{FR}(4)}(x)-\omega_i^2\frac{\rho A}{EI}W_i^{\mathrm{FR}}(x)=0, \tag{7.12}$$

$$\ddot{T}_i(t)+\omega_i^2T_i(t)=0. \tag{7.13}$$

The corresponding boundary conditions for the normal modes $W_i^{\mathrm{FD}}(x)$ and $W_i^{\mathrm{FR}}(x)$ are derived from the boundary conditions of their free-vibration components shown in Table 7.4 from Table 7.1 and Table 7.2.

Table 7.4 Boundary conditions for normal modes

Boundary	Normal modes	
	$W_i^{\mathrm{FD}}(x)$	$W_i^{\mathrm{FR}}(x)$
$x=0$	$W_i^{\mathrm{FD}}(0)=0$	-
	$W_i^{\mathrm{FD}(1)}(0)=0$	-
$x=L+a$	-	$W_i^{\mathrm{FR}}(L+a)=0$
	-	$W_i^{\mathrm{FR}(2)}(L+a)=0$

The continuity conditions at the crack tip *x* = *L* are given in Table 7.5 derived from Table 7.3.

Table 7.5 Continuity conditions for normal modes

Continuity	Normal modes
Deflection	$W_i^{\mathrm{FD}}(L)=W_i^{\mathrm{FR}}(L)$
Slope	$W_i^{\mathrm{FD}(1)}(L)=W_i^{\mathrm{FR}(1)}(L)$
Bending moment	$W_i^{\mathrm{FD}(2)}(L)=W_i^{\mathrm{FR}(2)}(L)$
Shear force	$W_i^{\mathrm{FD}(3)}(L)=W_i^{\mathrm{FR}(3)}(L)$

Now consider the orthogonality condition. For the foundation-supported beam section, multiplying Eq. (7.11) by $W_j^{\mathrm{FD}}(x)$, integrating over the length of the beam section from 0 to L twice by parts, and applying the boundary conditions in Table 7.4, gives

$$\begin{aligned}&W_j^{\mathrm{FD}}(L)W_i^{\mathrm{FD}(3)}(L)-W_j^{\mathrm{FD}(1)}(L)W_i^{\mathrm{FD}(2)}(L)+\int_0^L W_j^{\mathrm{FD}(2)}(x)W_i^{\mathrm{FD}(2)}(x)dx\\&=-\frac{k}{EI}\int_0^L W_i^{\mathrm{FD}}(x)W_j^{\mathrm{FD}}(x)dx+\omega_i^2\frac{\rho A}{EI}\int_0^L W_i^{\mathrm{FD}}(x)W_j^{\mathrm{FD}}(x)dx.\end{aligned} \tag{7.14}$$

For the free beam section, multiplying Eq. (7.12) by $W_j^{\mathrm{FR}}(x)$, integrating over the length of free beam section from L to $L + a$ twice by parts, and applying the boundary conditions in Table 7.4, gives

$$\begin{aligned}&-W_j^{\mathrm{FR}}(L)W_i^{\mathrm{FR}(3)}(L)+W_j^{\mathrm{FR}(1)}(L)W_i^{\mathrm{FR}(2)}(L)+\int_L^{L+a} W_j^{\mathrm{FR}(2)}(x)W_i^{\mathrm{FR}(2)}(x)dx\\&=\omega_i^2\frac{\rho A}{EI}\int_L^{L+a} W_i^{\mathrm{FR}}(x)W_j^{\mathrm{FR}}(x)dx.\end{aligned} \tag{7.15}$$

Summing Eqs. (7.14) and (7.15), applying continuity at the crack tip in Table 7.5, and then subtracting this from itself with the subscripts i and j exchanged, gives

$$\left(\omega_i^2-\omega_j^2\right)\left[\int_0^L \rho A W_i^{\mathrm{FD}}(x)W_j^{\mathrm{FD}}(x)dx+\int_L^{L+a}\rho A W_i^{\mathrm{FR}}(x)W_j^{\mathrm{FR}}(x)dx\right]=0. \tag{7.16}$$

Since the natural frequency of the system is unique, that is, $\omega_i \neq \omega_j$ for $i \neq j$, therefore

$$\int_0^L \rho A W_i^{\mathrm{FD}}(x)W_j^{\mathrm{FD}}(x)dx+\int_L^{L+a}\rho A W_i^{\mathrm{FR}}(x)W_j^{\mathrm{FR}}(x)dx=0. \tag{7.17}$$

Including the case of $i = j$ and normalising Eq. (7.17), finally, the orthogonality of the free vibration of a beam partially supported on an elastic foundation is written as

$$\int_0^L \rho A W_i^{\mathrm{FD}}(x)W_j^{\mathrm{FD}}(x)dx+\int_L^{L+a}\rho A W_i^{\mathrm{FR}}(x)W_j^{\mathrm{FR}}(x)dx=\delta_{ij}. \tag{7.18}$$

7.2.1.2 Solutions for normal modes and frequency equation

For the ith normal mode of the free-vibration component of the foundation-supported beam section, $W_i^{\mathrm{FD}}(x)$ in Eq. (7.11), the general solution with the available boundary conditions in Table 7.4 applied is

$$\begin{aligned}W_i^{\mathrm{FD}}(x)=&\,C_{i1}\left[\cosh(\alpha_i x)\sin(\alpha_i x)-\sinh(\alpha_i x)\cos(\alpha_i x)\right]\\&+C_{i2}\sinh(\alpha_i x)\sin(\alpha_i x),\end{aligned} \tag{7.19}$$

where $4\alpha_i^4 = k/EI - \omega_i^2\,\rho A/(EI)$ with $k/EI - \omega_i^2\,\rho A/(EI) > 0$ for the foundation stiffness k being relatively large, C_{i1} and C_{i2} are coefficients to be determined.

For the ith normal mode of the free-vibration component for the free beam section, $W_i^{\mathrm{FR}}(x)$ in Eq. (7.12), the general solution with available boundary conditions in Table 7.4 applied is

$$W_i^{\mathrm{FR}}(x) = C_{i3}\sinh\left[\beta_i\left(x-L-a\right)\right] + C_{i4}\sin\left[\beta_i\left(x-L-a\right)\right], \tag{7.20}$$

where $\beta_i^4 = \omega_i^2\rho A/(EI)$, C_{i3} and C_{i4} are coefficients to be determined.

The frequency equation is derived by applying the four continuity conditions at the crack tip, $x = L$, listed in Table 7.5, to these general solutions for $W_i^{\mathrm{FD}}(x)$ and $W_i^{\mathrm{FR}}(x)$, which gives

$$\begin{bmatrix} \begin{pmatrix} \cosh(\alpha_i L)\sin(\alpha_i L) \\ -\sinh(\alpha_i L)\cos(\alpha_i L) \end{pmatrix} & \sinh(\alpha_i L)\sin(\alpha_i L) & \sinh(\beta_i a) & \sin(\beta_i a) \\ 2\alpha_i \sinh(\alpha_i L)\sin(\alpha_i L) & \alpha_i \begin{pmatrix} \sinh(\alpha_i L)\cos(\alpha_i L) \\ +\cosh(\alpha_i L)\sin(\alpha_i L) \end{pmatrix} & -\beta_i\cosh(\beta_i a) & -\beta_i\cos(\beta_i a) \\ 2\alpha_i^2 \begin{pmatrix} \sinh(\alpha_i L)\cos(\alpha_i L) \\ +\cosh(\alpha_i L)\sin(\alpha_i L) \end{pmatrix} & 2\alpha_i^2\cosh(\alpha_i L)\cos(\alpha_i L) & \beta_i^2\sinh(\beta_i a) & -\beta_i^2\sin(\beta_i a) \\ 4\alpha_i^3\cosh(\alpha_i L)\cos(\alpha_i L) & 2\alpha_i^3 \begin{pmatrix} \sinh(\alpha_i L)\cos(\alpha_i L) \\ -\cosh(\alpha_i L)\sin(\alpha_i L) \end{pmatrix} & -\beta_i^3\cosh(\beta_i a) & \beta_i^3\cos(\beta_i a) \end{bmatrix} \begin{pmatrix} C_{i1} \\ C_{i2} \\ C_{i3} \\ C_{i4} \end{pmatrix} = \begin{pmatrix} 0 \\ 0 \\ 0 \\ 0 \end{pmatrix}. \tag{7.21}$$

For this homogeneous system of linear equations above to have nonzero solutions, the determinant of the coefficient matrix must be zero, and this gives the frequency equation. Let D_i be the determinant of the coefficient matrix of Eq. (7.21). From $D_i = 0$, the wavenumbers β_i can be determined and thus the angular frequency of each mode is $\omega_i = \beta_i^2\sqrt{EI/(\rho A)}$.

By Gaussian elimination, the coefficients C_{i1}, C_{i2} and C_{i3} can be expressed linearly in terms of C_{i4}. Then, by substituting the general solutions in Eqs. (7.19) and (7.20) into the orthogonality condition in Eq. (7.18), C_{i4} can be determined, and, therefore, C_{i1}, C_{i2} and C_{i3} also.

7.2.1.3 Solution for time-dependent modal displacement

The general solution for the time-dependent modal displacement of the ith vibration mode in Eq. (7.13) is

$$T_i\left(t\right)=\frac{\dot{T}_i\left(0\right)}{\omega_i}\sin\left(\omega_i t\right)+T_i\left(0\right)\cos\left(\omega_i t\right),\tag{7.22}$$

where $T_i\left(0\right)$ and $\dot{T}_i\left(0\right)$ are the initial values of the modal displacement and modal velocity of the *i*th vibration mode.

The initial modal displacement $T_i\,(0)$ can be determined by the following procedure: Substitute Eq. (7.22) into Eqs. (7.9) and (7.10), and combining Eqs. (7.3) and (7.4) to obtain the following equations for foundation-supported beam and free beam sections, respectively:

$$w^{\mathrm{FD}}\left(x,t\right)=\sum_{i=1}^{\infty}W_i^{\mathrm{FD}}\left(x\right)\left[\frac{\dot{T}_i\left(0\right)}{\omega_i}\sin\left(\omega_i t\right)+T_i\left(0\right)\cos\left(\omega_i t\right)\right]+F^{\mathrm{FD}}\left(x\right)vt,\tag{7.23}$$

$$w^{\mathrm{FR}}\left(x,t\right)=\sum_{i=1}^{\infty}W_i^{\mathrm{FR}}\left(x\right)\left[\frac{\dot{T}_i\left(0\right)}{\omega_i}\sin\left(\omega_i t\right)+T_i\left(0\right)\cos\left(\omega_i t\right)\right]+F^{\mathrm{FR}}\left(x\right)vt.\tag{7.24}$$

The initial displacements of these two beam sections are therefore $w^{\mathrm{FD}}\left(x,0\right)=\sum_{i=1}^{\infty}W_i^{\mathrm{FD}}\left(x\right)T_i\left(0\right)$ and $w^{\mathrm{FR}}\left(x,0\right)=\sum_{i=1}^{\infty}W_i^{\mathrm{FR}}\left(x\right)T_i\left(0\right)$, respectively. Multiply $w^{\mathrm{FD}}\left(x,0\right)$ by $\rho AW_j^{\mathrm{FD}}\left(x\right)$ and integrate over the foundation-supported beam length (from 0 to L); multiply $w^{\mathrm{FR}}\left(x,0\right)$ by $\rho AW_j^{\mathrm{FR}}\left(x\right)$ and integrate over the free beam length (from L to $L + a$); and sum these two integrals to have

$$\begin{aligned}&\int_0^L\rho AW_j^{\mathrm{FD}}\left(x\right)w^{\mathrm{FD}}\left(x,0\right)dx+\int_L^{L+a}\rho AW_j^{\mathrm{FR}}\left(x\right)w^{\mathrm{FR}}\left(x,0\right)dx\\&=\int_0^L\rho AW_j^{\mathrm{FD}}\left(x\right)\sum_{i=1}^{\infty}W_i^{\mathrm{FD}}\left(x\right)T_i\left(0\right)dx+\int_L^{L+a}\rho AW_j^{\mathrm{FR}}\left(x\right)\sum_{i=1}^{\infty}W_i^{\mathrm{FR}}\left(x\right)T_i\left(0\right)dx.\end{aligned}\tag{7.25}$$

By applying the orthogonality in Eq. (7.18) together with the initial conditions that $w^{\mathrm{FD}}\,(x,\,0) = 0$ and $w^{\mathrm{FR}}\,(x,\,0) = 0$, the *i*th modal displacement is found to be zero, that is, $T_i\,(0) = 0$. Following a similar procedure, the initial value of the *i*th modal velocity is found to be

$$\begin{aligned}\dot{T}_i\left(0\right)&=-v\left[\int_0^L\rho AW_i^{\mathrm{FD}}\left(x\right)F^{\mathrm{FD}}\left(x\right)dx+\int_L^{L+a}\rho AW_i^{\mathrm{FR}}\left(x\right)F^{\mathrm{FR}}\left(x\right)dx\right]\\&=-vH_i,\end{aligned}\tag{7.26}$$

where

$$H_i = \int_0^L \rho A W_i^{\mathrm{FD}}(x) F^{\mathrm{FD}}(x)\,dx + \int_L^{L+a} \rho A W_i^{\mathrm{FR}}(x) F^{\mathrm{FR}}(x)\,dx. \tag{7.27}$$

The quantity H_i represents the coupling of free vibration and applied constant opening velocity, that is, the response of the free vibration of the beam to the applied excitation. It is shown in Section 7.2.1.4 that the shifting functions, $F^{\mathrm{FD}}(x)$ and $F^{\mathrm{FR}}(x)$, are independent of the applied velocity v; therefore, H_i is also independent of the applied velocity and is instead an inherent property of the beam configuration. In addition, H_i is also a counterpart of Λ_i in Eq. (5.5).

7.2.1.4 Solutions for shifting functions

The shifting functions are obtained by solving the ordinary differential equations in Eqs. (7.6) and (7.8), together with the available boundary conditions in Table 7.1 and Table 7.2 as well as the continuity conditions at the crack tip in Table 7.3.

The general solution for $F^{\mathrm{FD}}(x)$ with available boundary conditions in Table 7.1 applied is

$$\begin{aligned} F^{\mathrm{FD}}(x) = {} & P_1\left[\cosh(\gamma x)\sin(\gamma x) - \sinh(\gamma x)\cos(\gamma x)\right] \\ & + P_2 \sinh(\gamma x)\sin(\gamma x), \end{aligned} \tag{7.28}$$

where $4\gamma^4 = k/(EI)$, and where P_1 and P_2 are coefficients to be determined.

The general solution for $F^{\mathrm{FR}}(x)$ with available boundary conditions in Table 7.2 applied is

$$F^{\mathrm{FR}}(x) = P_3(x - L - a)^3 + P_4(x - L - a) + 1, \tag{7.29}$$

where P_3 and P_4 are coefficients to be determined.

By applying the four continuity conditions at the crack tip $x = L$ in Table 7.3, to the general solutions for $F^{\mathrm{FD}}(x)$ and $F^{\mathrm{FR}}(x)$, the following system of equations is obtained:

$$\begin{bmatrix} \begin{pmatrix} \cosh(\gamma L)\sin(\gamma L) \\ -\cos(\gamma L)\sinh(\gamma L) \end{pmatrix} & \sinh(\gamma L)\sin(\gamma L) & a^3 & a \\ 2\gamma\sinh(\gamma L)\sin(\gamma L) & \gamma\begin{pmatrix} \cosh(\gamma L)\sin(\gamma L) \\ +\cos(\gamma L)\sinh(\gamma L) \end{pmatrix} & -3a^2 & -1 \\ 2\gamma^2\begin{pmatrix} \cosh(\gamma L)\sin(\gamma L) \\ +\cos(\gamma L)\sinh(\gamma L) \end{pmatrix} & 2\gamma^2\cosh(\gamma L)\sin(\gamma L) & 6a & 0 \\ 4\gamma^3\cosh(\gamma L)\cos(\gamma L) & 2\gamma^3\begin{pmatrix} \cos(\gamma L)\sinh(\gamma L) \\ -\cosh(\gamma L)\sin(\gamma L) \end{pmatrix} & -6 & 0 \end{bmatrix} \begin{pmatrix} P_1 \\ P_2 \\ P_3 \\ P_4 \end{pmatrix} = \begin{pmatrix} 1 \\ 0 \\ 0 \\ 0 \end{pmatrix}. \tag{7.30}$$

Solving this system of equations gives the coefficients P_1, P_2, P_3 and P_4 as

$$P_1 = \frac{-6\begin{bmatrix} \cosh(\gamma L)\cos(\gamma L) \\ +a\gamma\sinh(\gamma L)\cos(\gamma L) - a\gamma\cosh(\gamma L)\sin(\gamma L) \end{bmatrix}}{P_0}, \tag{7.31}$$

$$P_2 = \frac{-6\begin{bmatrix} \sinh(\gamma L)\cos(\gamma L) \\ +\cosh(\gamma L)\sin(\gamma L) + 2a\gamma\cosh(\gamma L)\cos(\gamma L) \end{bmatrix}}{P_0}, \tag{7.32}$$

$$P_3 = \frac{-\gamma^3\left[\cosh(2\gamma L) + \cos(2\gamma L) + 2\right]}{P_0}, \tag{7.33}$$

$$P_4 = \frac{3\gamma\begin{Bmatrix} a^2\gamma^2\left[\cosh(2\gamma L) + \cos(2\gamma L) + 2\right] \\ +2a\gamma\left[\sinh(2\gamma L) + \sin(2\gamma L)\right] + \left[\cosh(2\gamma L) - \cos(2\gamma L)\right] \end{Bmatrix}}{P_0}, \tag{7.34}$$

where $P_0 = \begin{Bmatrix} 2a^3\gamma^3\left[\cos(2\gamma L) + \cosh(2\gamma L) + 2\right] + 6a^2\gamma^2\left[\sin(2\gamma L) + \sinh(2\gamma L)\right] \\ +6a\gamma\left[\cosh(2\gamma L) - \cos(2\gamma L)\right] + 3\left[\sinh(2\gamma L) - \sin(2\gamma L)\right] \end{Bmatrix}.$

The shifting function solutions, given in Eqs. (7.28) and (7.29) together with their coefficients from Eqs. (7.31) to (7.34) show that they are independent of the applied opening velocity v. This indicates that the shifting functions, which represent the distribution of the externally applied displacement or velocity along the beam, are inherent properties of the beam configuration.

7.2.1.5 Total deflections

The combined results from Sections 7.2.1.1 to 7.2.1.4 give the total deflections for foundation-supported beam and free beam sections in Eqs. (7.3) and (7.4) as

$$\begin{aligned} w^{\mathrm{FD}}(x,t) &= w_{\mathrm{fv}}^{\mathrm{FD}}(x,t) + F^{\mathrm{FD}}(x)vt \\ &= v\left\{-\sum_{i=1}^{\infty}\left[\frac{H_i}{\omega_i}W_i^{\mathrm{FD}}(x)\sin(\omega_i t)\right] + F^{\mathrm{FD}}(x)t\right\}, \end{aligned} \tag{7.35}$$

$$\begin{aligned} w^{\mathrm{FR}}(x,t) &= w_{\mathrm{fv}}^{\mathrm{FR}}(x,t) + F^{\mathrm{FR}}(x)vt \\ &= v\left\{-\sum_{i=1}^{\infty}\left[\frac{H_i}{\omega_i}W_i^{\mathrm{FR}}(x)\sin(\omega_i t)\right] + F^{\mathrm{FR}}(x)t\right\}. \end{aligned} \tag{7.36}$$

It is demonstrated that the beam system’s response is proportional to the externally applied constant opening velocity v. The terms contained in the braces are determined by the beam configuration alone. And the total deflection in Eqs. (7.35) and (7.36) are used to derive the respective energy terms in Section 7.2.2 and then to determine the dynamic ERR in Section 7.2.3.

7.2.2 Energy stored in the beam on elastic foundation

7.2.2.1 Strain energy of beam

The strain energy of a thin beam section is calculated using $U = \int M^2(x,t)\,dx \big/ (2EI)$, where $M(x,t) = EIw^{(2)}(x,t)$, which is the internal bending moment. The strain energy stored in the foundation-supported beam section is therefore

$$U^{\mathrm{FD}} = \frac{1}{2}EI\left\{\begin{array}{l} \int_0^L \left[w_{\mathrm{fv}}^{\mathrm{FD}(2)}(x,t)\right]^2 dx \\ +2\int_0^L \left[w_{\mathrm{fv}}^{\mathrm{FD}(2)}(x,t)F^{\mathrm{FD}(2)}(x)vt\right]dx \\ +\int_0^L \left[F^{\mathrm{FD}(2)}(x)vt\right]^2 dx \end{array}\right\}, \tag{7.37}$$

and the strain energy stored in the free beam section is

$$U^{\mathrm{FR}} = \frac{1}{2}EI\left\{\begin{array}{l} \int_L^{L+a} \left[w_{\mathrm{fv}}^{\mathrm{FR}(2)}(x,t)\right]^2 dx \\ +2\int_L^{L+a} \left[w_{\mathrm{fv}}^{\mathrm{FR}(2)}(x,t)F^{\mathrm{FR}(2)}(x)vt\right]dx \\ +\int_L^{L+a} \left[F^{\mathrm{FR}(2)}(x)vt\right]^2 dx \end{array}\right\}. \tag{7.38}$$

Let $U_{\mathrm{loc}}^{\mathrm{FD}}$, $U_{\mathrm{cp}}^{\mathrm{FD}}$ and $U_{\mathrm{st}}^{\mathrm{FD}}$ correspond in order to each of the three terms in Eq. (7.37), representing the strain energy due to the local vibration, the strain energy due to the coupling between the local vibration and the quasi-static motion, and the strain energy due to the quasi-static motion, respectively. Similar definitions are applied to Eq. (7.38), with the corresponding strain energy terms being $U_{\text{loc}}^{\text{FR}}$, $U_{\text{cp}}^{\text{FR}}$ and $U_{\text{st}}^{\text{FR}}$.

The total strain energy of the whole beam is, therefore, $U = U^{\text{FD}} + U^{\text{FR}}$, which can then be partitioned into the total strain energy due to the local vibration, $U_{\text{loc}} = U_{\text{loc}}^{\text{FD}} + U_{\text{loc}}^{\text{FR}}$; the total strain energy due to the coupling between the local vibration and the quasi-static motion, $U_{\text{cp}} = U_{\text{cp}}^{\text{FD}} + U_{\text{cp}}^{\text{FR}}$; and the total strain energy due to the quasi-static motion, $U_{\text{st}} = U_{\text{st}}^{\text{FD}} + U_{\text{st}}^{\text{FR}}$.

$$\begin{aligned} U &= U^{\text{FD}} + U^{\text{FR}} \\ &= \left(U_{\text{loc}}^{\text{FD}} + U_{\text{cp}}^{\text{FD}} + U_{\text{st}}^{\text{FD}}\right) + \left(U_{\text{loc}}^{\text{FR}} + U_{\text{cp}}^{\text{FR}} + U_{\text{st}}^{\text{FR}}\right) \\ &= \left(U_{\text{loc}}^{\text{FD}} + U_{\text{loc}}^{\text{FR}}\right) + \left(U_{\text{cp}}^{\text{FD}} + U_{\text{cp}}^{\text{FR}}\right) + \left(U_{\text{st}}^{\text{FD}} + U_{\text{st}}^{\text{FR}}\right) \\ &= U_{\text{loc}} + U_{\text{cp}} + U_{\text{st}}. \end{aligned} \tag{7.39}$$

The total strain energy due to the local vibration is

$$U_{\text{loc}} = \frac{1}{2} EI \int_0^L \left[w_{\text{fv}}^{\text{FD}(2)}\left(x,t\right) \right]^2 dx + \frac{1}{2} EI \int_L^{L+a} \left[w_{\text{fv}}^{\text{FR}(2)}\left(x,t\right) \right]^2 dx. \tag{7.40}$$

The combined results from Sections 7.2.1.1 to 7.2.1.3 allow $w_{\text{fv}}^{\text{FD}}\left(x,t\right)$ and $w_{\text{fv}}^{\text{FR}}\left(x,t\right)$ in Eqs. (7.9) and (7.10) to be substituted into Eq. (7.40) and expanded, giving

$$\begin{aligned} U_{\text{loc}} = {} & \frac{1}{2} EI \int_0^L \left\{ -v \sum_{i=1}^{\infty} \left[\frac{H_i}{\omega_i} W_i^{\text{FD}(2)}\left(x\right) \sin\left(\omega_i t\right) \right] \right\}^2 dx \\ & + \frac{1}{2} EI \int_L^{L+a} \left\{ -v \sum_{i=1}^{\infty} \left[\frac{H_i}{\omega_i} W_i^{\text{FR}(2)}\left(x\right) \sin\left(\omega_i t\right) \right] \right\}^2 dx, \end{aligned} \tag{7.41}$$

which then further expands to

$$
\begin{aligned}
U_{\mathrm{loc}} = \frac{1}{2} EIv^2 \lim_{n\to\infty}\int_0^L \left\{
\begin{aligned}
&\left[\frac{H_1}{\omega_1} W_1^{\mathrm{FD}(2)}\left(x\right)\sin\left(\omega_1 t\right)\right]^2 \\
&\ +2\frac{H_1}{\omega_1} W_1^{\mathrm{FD}(2)}\left(x\right)\sin\left(\omega_1 t\right)\sum_{j=2}^{n}\frac{H_j}{\omega_j} W_j^{\mathrm{FD}(2)}\left(x\right)\sin\left(\omega_j t\right) \\
&+\left[\frac{H_2}{\omega_2} W_2^{\mathrm{FD}(2)}\left(x\right)\sin\left(\omega_2 t\right)\right]^2 \\
&\ +2\frac{H_2}{\omega_2} W_2^{\mathrm{FD}(2)}\left(x\right)\sin\left(\omega_2 t\right)\sum_{j=3}^{n}\frac{H_j}{\omega_j} W_j^{\mathrm{FD}(2)}\left(x\right)\sin\left(\omega_j t\right) \\
&+\dots \\
&+\left[\frac{H_{n-1}}{\omega_{n-1}} W_{n-1}^{\mathrm{FD}(2)}\left(x\right)\sin\left(\omega_{n-1} t\right)\right]^2 \\
&\ +2\frac{H_{n-1}}{\omega_{n-1}} W_{n-1}^{\mathrm{FD}(2)}\left(x\right)\sin\left(\omega_{n-1} t\right)\frac{H_n}{\omega_n} W_n^{\mathrm{FD}(2)}\left(x\right)\sin\left(\omega_n t\right) \\
&+\left[\frac{H_n}{\omega_n} W_n^{\mathrm{FD}(2)}\left(x\right)\sin\left(\omega_n t\right)\right]^2
\end{aligned}
\right\} dx \\
+\frac{1}{2} EIv^2 \lim_{n\to\infty}\int_L^{L+a} \left\{
\begin{aligned}
&\left[\frac{H_1}{\omega_1} W_1^{\mathrm{FR}(2)}\left(x\right)\sin\left(\omega_1 t\right)\right]^2 \\
&\ +2\frac{H_1}{\omega_1} W_1^{\mathrm{FR}(2)}\left(x\right)\sin\left(\omega_1 t\right)\sum_{j=2}^{n}\frac{H_j}{\omega_j} W_j^{\mathrm{FR}(2)}\left(x\right)\sin\left(\omega_j t\right) \\
&+\left[\frac{H_2}{\omega_2} W_2^{\mathrm{FR}(2)}\left(x\right)\sin\left(\omega_2 t\right)\right]^2 \\
&\ +2\frac{H_2}{\omega_2} W_2^{\mathrm{FR}(2)}\left(x\right)\sin\left(\omega_2 t\right)\sum_{j=3}^{n}\frac{H_j}{\omega_j} W_j^{\mathrm{FR}(2)}\left(x\right)\sin\left(\omega_j t\right) \\
&+\dots \\
&+\left[\frac{H_{n-1}}{\omega_{n-1}} W_{n-1}^{\mathrm{FR}(2)}\left(x\right)\sin\left(\omega_{n-1} t\right)\right]^2 \\
&\ +2\frac{H_{n-1}}{\omega_{n-1}} W_{n-1}^{\mathrm{FR}(2)}\left(x\right)\sin\left(\omega_{n-1} t\right)\frac{H_n}{\omega_n} W_n^{\mathrm{FR}(2)}\left(x\right)\sin\left(\omega_n t\right) \\
&+\left[\frac{H_n}{\omega_n} W_n^{\mathrm{FR}(2)}\left(x\right)\sin\left(\omega_n t\right)\right]^2
\end{aligned}
\right\} dx\ .
\end{aligned}
\tag{7.42}
$$

Rearranging Eq. (7.42) gives

$$U_{\text{loc}} = \frac{1}{2} EIv^2 \sum_{i=1}^{\infty} \frac{H_i^{\,2}}{\omega_i^{\,2}} \sin^2\left(\omega_i t\right) \left\{ \int_0^L \left[W_i^{\text{FD}(2)}\left(x\right) \right]^2 dx + \int_L^{L+a} \left[W_i^{\text{FR}(2)}\left(x\right) \right]^2 dx \right\}$$
$$+ EIv^2 \lim_{n\to\infty} \left\{ \begin{array}{l} \displaystyle\int_0^L \sum_{i=1}^{n-1} \left[\frac{H_i}{\omega_i} W_i^{\text{FD}(2)}\left(x\right) \sin\left(\omega_i t\right) \sum_{j=i+1}^{n} \frac{H_j}{\omega_j} W_j^{\text{FR}(2)}\left(x\right) \sin\left(\omega_j t\right) \right] dx \\ \displaystyle + \int_L^{L+a} \sum_{i=1}^{n-1} \left[\frac{H_i}{\omega_i} W_i^{\text{FR}(2)}\left(x\right) \sin\left(\omega_i t\right) \sum_{j=i+1}^{n} \frac{H_j}{\omega_j} W_j^{\text{FR}(2)}\left(x\right) \sin\left(\omega_j t\right) \right] \end{array} \right\}. \quad (7.43)$$

The first term in Eq. (7.43) is the summation of strain energy due to each individual local vibration, and denoted as $U_{\text{loc/S}}$; the second term is the strain energy due to the coupling between different local vibration modes $U_{\text{loc/C}}$, so

$$U_{\text{loc}} = U_{\text{loc/S}} + U_{\text{loc/C}}\,, \quad (7.44)$$

where

$$U_{\text{loc/S}} = \frac{1}{2} EIv^2 \sum_{i=1}^{\infty} \frac{H_i^{\,2}}{\omega_i^{\,2}} \sin^2\left(\omega_i t\right) \left\{ \int_0^L \left[W_i^{\text{FD}(2)}\left(x\right) \right]^2 dx + \int_L^{L+a} \left[W_i^{\text{FR}(2)}\left(x\right) \right]^2 dx \right\}, \quad (7.45)$$

$$U_{\text{loc/C}} = EIv^2 \lim_{n\to\infty} \left\{ \begin{array}{l} \displaystyle\int_0^L \sum_{i=1}^{n-1} \left[\frac{H_i W_i^{\text{FD}(2)}\left(x\right) \sin\left(\omega_i t\right)}{\omega_i} \sum_{j=i+1}^{n} \frac{H_j W_j^{\text{FR}(2)}\left(x\right) \sin\left(\omega_j t\right)}{\omega_j} \right] dx \\ \displaystyle + \int_L^{L+a} \sum_{i=1}^{n-1} \left[\frac{H_i W_i^{\text{FR}(2)}\left(x\right) \sin\left(\omega_i t\right)}{\omega_i} \sum_{j=i+1}^{n} \frac{H_j W_j^{\text{FR}(2)}\left(x\right) \sin\left(\omega_j t\right)}{\omega_j} \right] dx \end{array} \right\}. \quad (7.46)$$

The total strain energy due to the coupling between the local vibration and the quasi-static motion, that is, $U_{\text{cp}} = U_{\text{cp}}^{\text{FD}} + U_{\text{cp}}^{\text{FR}}$, is

$$\begin{aligned} U_{\text{cp}} &= EI \int_0^L \left[w_{\text{fv}}^{\text{FD}(2)}\left(x,t\right) F^{\text{FD}(2)}\left(x\right) vt \right] dx \\ &\quad + EI \int_L^{L+a} \left[w_{\text{fv}}^{\text{FR}(2)}\left(x,t\right) F^{\text{FR}(2)}\left(x\right) vt \right] dx. \end{aligned} \quad (7.47)$$

The total strain energy due to the quasi-static motion, that is, $U_{\text{st}} = U_{\text{st}}^{\text{FD}} + U_{\text{st}}^{\text{FR}}$, is

$$U_{\text{st}} = \frac{1}{2} EI \int_0^L \left[F^{\text{FD}(2)}\left(x\right) vt \right]^2 dx + \frac{1}{2} EI \int_L^{L+a} \left[F^{\text{FR}(2)}\left(x\right) vt \right]^2 dx. \quad (7.48)$$

7.2.2.2 Kinetic energy of beam

The transverse velocities of the foundation-supported beam and the free beam sections are $\dot{w}^{\text{FD}}\left(x,t\right) = \dot{w}_{\text{fv}}^{\text{FD}}\left(x,t\right) + F^{\text{FD}}\left(x\right)v$ and $\dot{w}^{\text{FR}}\left(x,t\right) = \dot{w}_{\text{fv}}^{\text{FR}}\left(x,t\right) + F^{\text{FR}}\left(x\right)v$. The kinetic energy of a thin beam section is calculated using $K = \rho A/2\int_0^L \left[\dot{w}\left(x,t\right)\right]^2 dx$, and, therefore, the corresponding kinetic energies are

$$K^{\mathrm{FD}} = \frac{1}{2}\rho A\left\{\begin{array}{l}\int_0^L \left[\dot{w}_{\mathrm{fv}}^{\mathrm{FD}}\left(x,t\right)\right]^2 dx\\ +2\int_0^L \left[\dot{w}_{\mathrm{fv}}^{\mathrm{FD}}\left(x,t\right)F^{\mathrm{FD}}\left(x\right)v\right]dx\\ +\int_0^L \left[F^{\mathrm{FD}}\left(x\right)v\right]^2 dx\end{array}\right\}, \tag{7.49}$$

$$K^{\mathrm{FR}} = \frac{1}{2}\rho A\left\{\begin{array}{l}\int_L^{L+a} \left[\dot{w}_{\mathrm{fv}}^{\mathrm{FR}}\left(x,t\right)\right]^2 dx\\ +2\int_L^{L+a} \left[\dot{w}_{\mathrm{fv}}^{\mathrm{FR}}\left(x,t\right)F^{\mathrm{FR}}\left(x\right)v\right]dx\\ +\int_L^{L+a} \left[F^{\mathrm{FR}}\left(x\right)v\right]^2 dx\end{array}\right\}. \tag{7.50}$$

Let $K_{\mathrm{loc}}^{\mathrm{FD}}$, $K_{\mathrm{cp}}^{\mathrm{FD}}$ and $K_{\mathrm{st}}^{\mathrm{FD}}$ correspond in order to each of the three terms in Eq. (7.49), representing the kinetic energy due to the local vibration, the kinetic energy due to the coupling between the local vibration and the quasi-static motion, and the kinetic energy due to the quasi-static motion, respectively. Similar definitions are applied to Eq. (7.50) with the corresponding kinetic energy terms being $K_{\mathrm{loc}}^{\mathrm{FR}}$, $K_{\mathrm{cp}}^{\mathrm{FR}}$ and $K_{\mathrm{st}}^{\mathrm{FR}}$.

The total kinetic energy of the whole beam is, therefore, $K = K^{\mathrm{FD}} + K^{\mathrm{FR}}$, which can be partitioned into the total kinetic energy due to the local vibration, $K_{\mathrm{loc}} = K_{\mathrm{loc}}^{\mathrm{FD}} + K_{\mathrm{loc}}^{\mathrm{FR}}$; the total kinetic energy due to the coupling between the local vibration and the quasi-static motion, $K_{\mathrm{cp}} = K_{\mathrm{cp}}^{\mathrm{FD}} + K_{\mathrm{cp}}^{\mathrm{FR}}$; and the total kinetic energy due to the quasi-static motion, $K_{\mathrm{st}} = K_{\mathrm{st}}^{\mathrm{FD}} + K_{\mathrm{st}}^{\mathrm{FR}}$. And, therefore,

$$\begin{aligned} K &= K^{\mathrm{FD}} + K^{\mathrm{FR}}\\ &= \left(K_{\mathrm{loc}}^{\mathrm{FD}} + K_{\mathrm{cp}}^{\mathrm{FD}} + K_{\mathrm{st}}^{\mathrm{FD}}\right) + \left(K_{\mathrm{loc}}^{\mathrm{FR}} + K_{\mathrm{cp}}^{\mathrm{FR}} + K_{\mathrm{st}}^{\mathrm{FR}}\right)\\ &= \left(K_{\mathrm{loc}}^{\mathrm{FD}} + K_{\mathrm{loc}}^{\mathrm{FR}}\right) + \left(K_{\mathrm{cp}}^{\mathrm{FD}} + K_{\mathrm{cp}}^{\mathrm{FR}}\right) + \left(K_{\mathrm{st}}^{\mathrm{FD}} + K_{\mathrm{st}}^{\mathrm{FR}}\right)\\ &= K_{\mathrm{loc}} + K_{\mathrm{cp}} + K_{\mathrm{st}}. \end{aligned} \tag{7.51}$$

The total kinetic energy due to the local vibration is

$$K_{\mathrm{loc}} = \frac{1}{2}\rho A\int_0^L \left[\dot{w}_{\mathrm{fv}}^{\mathrm{FD}}\left(x,t\right)\right]^2 dx + \frac{1}{2}\rho A\int_L^{L+a} \left[\dot{w}_{\mathrm{fv}}^{\mathrm{FR}}\left(x,t\right)\right]^2 dx. \tag{7.52}$$

Like the case for the strain energy due to the local vibration U_{loc} in Eq. (7.40), and by the equivalent derivation for Eq. (7.44), the total kinetic energy due to the local vibration can be expressed as the sum of kinetic energy contributions from each individual vibration mode $K_{\mathrm{loc/S}}$ and kinetic energy contributions from the coupling between different vibration modes $K_{\mathrm{loc/C}}$. In this case, however, the orthogonality condition in Eq. (7.18) can also be applied, allowing $K_{\mathrm{loc/S}}$ and $K_{\mathrm{loc/C}}$ to simplify further to $K_{\mathrm{loc/S}} = v^2 / 2 \sum_{i=1}^{\infty} H_i^2 \cos^2\left(\omega_i t\right)$ and $K_{\mathrm{loc/C}} = 0$, giving

$$K_{\mathrm{loc}} = \frac{1}{2} v^2 \sum_{i=1}^{\infty} H_i^2 \cos^2\left(\omega_i t\right). \tag{7.53}$$

The total kinetic energy due to the coupling between the local vibration and the quasi-static motion, that is, $K_{\mathrm{cp}} = K_{\mathrm{cp}}^{\mathrm{FD}} + K_{\mathrm{cp}}^{\mathrm{FR}}$, with the orthogonality condition in Eq. (7.18) also applied, is

$$\begin{aligned} K_{\mathrm{cp}} &= \rho A \int_0^L \left[\dot{w}_{\mathrm{fv}}^{\mathrm{FD}}\left(x,t\right) F^{\mathrm{FD}}\left(x\right) v\right] dx + \rho A \int_L^{L+a} \left[\dot{w}_{\mathrm{fv}}^{\mathrm{FR}}\left(x,t\right) F^{\mathrm{FR}}\left(x\right) v\right] dx \\ &= -v^2 \sum_{i=1}^{\infty} H_i^2 \cos\left(\omega_i t\right). \end{aligned} \tag{7.54}$$

The total kinetic energy due to the quasi-static motion, that is, $K_{\mathrm{st}} = K_{\mathrm{st}}^{\mathrm{FD}} + K_{\mathrm{st}}^{\mathrm{FR}}$, is

$$K_{\mathrm{st}} = \frac{1}{2} \rho A \int_0^L \left[F^{\mathrm{FD}}\left(x\right) v\right]^2 dx + \frac{1}{2} \rho A \int_L^{L+a} \left[F^{\mathrm{FR}}\left(x\right) v\right]^2 dx. \tag{7.55}$$

7.2.2.3 Strain energy of elastic foundation

The strain energy of the elastic foundation is $S = k \int_0^L \left[w^{\mathrm{FD}}\left(x,t\right)\right]^2 dx / 2$, which expands to

$$S = \frac{1}{2} k \left\{ \begin{aligned} & \int_0^L \left[w_{\mathrm{fv}}^{\mathrm{FD}}\left(x,t\right)\right]^2 dx \\ & + 2 \int_0^L \left[w_{\mathrm{fv}}^{\mathrm{FD}}\left(x,t\right) F^{\mathrm{FD}}\left(x\right) vt\right] dx \\ & + \int_0^L \left[F^{\mathrm{FD}}\left(x\right) vt\right]^2 dx \end{aligned} \right\}. \tag{7.56}$$

Let S_{loc}, S_{cp} and S_{st} correspond in order to each of the three terms in Eq. (7.56), representing the strain energy of the foundation due to the local vibration, the strain energy of the foundation due to the coupling between the local vibration and the quasi-static motion, and the strain energy of the foundation due to the quasi-static motion, respectively.

The strain energy stored in the foundation due to the local vibration is

$$S_{\mathrm{loc}} = \frac{1}{2}k\int_0^L \left\{ -v\sum_{i=1}^{\infty}\left[\frac{H_i}{\omega_i} W_i^{\mathrm{FD}}(x)\sin(\omega_i t) \right] \right\}^2 dx. \tag{7.57}$$

Like the case for the strain energy due to local vibration U_{loc} in Eq. (7.40), and by the equivalent derivation for Eq. (7.44), the total strain energy of the foundation due to local vibration can be expressed as the sum of strain energy contributions from each individual vibration mode $S_{\mathrm{loc/S}}$ and strain energy contributions from the coupling between different vibration modes $S_{\mathrm{loc/C}}$. This is expressed as

$$S_{\mathrm{loc}} = S_{\mathrm{loc/S}} + S_{\mathrm{loc/C}}\,, \tag{7.58}$$

where

$$S_{\mathrm{loc/S}} = \frac{1}{2}kv^2\left\{ \sum_{i=1}^{\infty} \frac{H_i^2}{\omega_i^2}\sin^2(\omega_i t)\int_0^L \left[W_i^{\mathrm{FD}}(x) \right]^2 dx \right\}, \tag{7.59}$$

$$S_{\mathrm{loc/C}} = kv^2 \lim_{n\to\infty}\sum_{i=1}^{n-1}\left\{ \int_0^L \frac{H_i W_i^{\mathrm{FD}}(x)\sin(\omega_i t)}{\omega_i} \sum_{j=i+1}^{n}\left[\frac{H_j W_j^{\mathrm{FD}}(x)\sin(\omega_j t)}{\omega_j} \right] dx \right\}. \tag{7.60}$$

The total strain energy of the foundation due to the coupling between the local vibration and the quasi-static motion is

$$S_{\mathrm{cp}} = -kv^2 t\sum_{i=1}^{\infty}\left\{ \frac{H_i}{\omega_i}\sin(\omega_i t)\int_0^L \left[W_i^{\mathrm{FD}}(x) F^{\mathrm{FD}}(x) \right] dx \right\}. \tag{7.61}$$

The total strain energy of the foundation due to the quasi-static motion is

$$S_{\mathrm{st}} = \frac{1}{2}kv^2 t^2 \int_0^L \left[F^{\mathrm{FD}}(x) \right]^2 dx. \tag{7.62}$$

7.2.2.4 Total mechanical energy

The total mechanical energy Π is by summing all the energy terms derived from Sections 7.2.2.1 to 7.2.2.3 as per Eq. (7.2). The relations between relevant energy terms are derived first, which can be used to simplify the final solution for total mechanical energy.

(1) Relation between U_{loc} and S_{loc}

For simplifying the strain energy of local vibration U_{loc} , the following relationship in Eq. (7.63) for normal modes of $W_i^{\text{FD}}\left(x\right)$ and $W_i^{\text{FR}}\left(x\right)$ is derived first by summing Eqs. (7.14) and (7.15) together with the continuity condition in Table 7.5 and also by letting *i* = *j* and applying orthogonality in Eq. (7.18).

$$\int_0^L \left[W_i^{\text{FD}(2)}\left(x\right)\right]^2 dx + \int_L^{L+a} \left[W_i^{\text{FR}(2)}\left(x\right)\right]^2 dx = -\frac{k}{EI}\int_0^L \left[W_i^{\text{FD}}\left(x\right)\right]^2 dx + \frac{\omega_i^2}{EI}. \quad (7.63)$$

Using Eq. (7.63), the local vibration strain-energy contributions from individual mode vibration, that is, $U_{\text{loc/S}}$ in Eq. (7.45) can be simplified to

$$\begin{aligned} U_{\text{loc/S}} &= -\frac{1}{2}kv^2\sum_{i=1}^{\infty}\left\{\frac{H_i^2}{\omega_i^2}\sin^2\left(\omega_i t\right)\int_0^L \left[W_i^{\text{FD}}\left(x\right)\right]^2 dx\right\} + \frac{1}{2}v^2\sum_{i=1}^{\infty}H_i^2\sin^2\left(\omega_i t\right) \\ &= -S_{\text{loc/S}} + \frac{1}{2}v^2\sum_{i=1}^{\infty}H_i^2\sin^2\left(\omega_i t\right). \end{aligned} \quad (7.64)$$

Using the summation of Eqs. (7.14) and (7.15) again, the local vibration strain-energy contributions from the coupling between different mode vibrations, that is, $U_{\text{loc/C}}$ in Eq. (7.46) can be simplified to

$$\begin{aligned} U_{\text{loc/C}} &= -kv^2\lim_{n\to\infty}\sum_{i=1}^{n-1}\left\{\int_0^L \frac{H_i\sin\left(\omega_i t\right)W_i^{\text{FD}}\left(x\right)}{\omega_i}\sum_{j=i+1}^{n}\left[\frac{H_j W_j^{\text{FD}}\left(x\right)\sin\left(\omega_j t\right)}{\omega_j}\right]dx\right\} \\ &= -S_{\text{loc/C}}\,. \end{aligned} \quad (7.65)$$

(2) Relation between U_{cp} and S_{cp}

Expanding $U_{\text{cp}}^{\text{FD}}$, which is the first term of Eq. (7.47), with Eq. (7.9) and integrating twice by parts gives

$$U_{\text{cp}}^{\text{FD}} = -EIv^2t\sum_{i=1}^{\infty}\frac{H_i}{\omega_i}\sin\left(\omega_i t\right)\left\{\begin{array}{l}\left[W_i^{\text{FD}(1)}\left(x\right)F^{\text{FD}(2)}\left(x\right)\right]\Big|_0^L \\ -\left[W_i^{\text{FD}}\left(x\right)F^{\text{FD}(3)}\left(x\right)\right]\Big|_0^L \\ +\int_0^L \left[W_i^{\text{FD}}\left(x\right)F^{\text{FD}(4)}\left(x\right)\right]dx\end{array}\right\}. \quad (7.66)$$

Then, by using the boundary conditions for $W_i^{\text{FD}}\left(x\right)$ in Table 7.4 and for F^{FD} (*x*) in Table 7.1, and substituting Eq. (7.6), $U_{\text{cp}}^{\text{FD}}$ simplifies to

$$U_{\mathrm{cp}}^{\mathrm{FD}} = -EIv^2 t \sum_{i=1}^{\infty} \frac{H_i}{\omega_i} \sin\left(\omega_i t\right) \begin{Bmatrix} \left[W_i^{\mathrm{FD}(1)}\left(L\right) F^{\mathrm{FD}(2)}\left(L\right)\right] \\ -\left[W_i^{\mathrm{FD}}\left(L\right) F^{\mathrm{FD}(3)}\left(L\right)\right] \\ -\dfrac{k}{EI}\displaystyle\int_0^L \left[W_i^{\mathrm{FD}}\left(x,t\right) F^{\mathrm{FD}}\left(x\right)\right] dx \end{Bmatrix}. \tag{7.67}$$

By using the same procedure with Eqs. (7.8) and (7.10), $U_{\mathrm{cp}}^{\mathrm{FR}}$, which is the second term in Eq. (7.47), simplifies to

$$U_{\mathrm{cp}}^{\mathrm{FR}} = -EIv^2 t \sum_{i=1}^{\infty} \frac{H_i}{\omega_i} \sin\left(\omega_i t\right) \begin{Bmatrix} -W_i^{\mathrm{FR}(1)}\left(L\right) F^{\mathrm{FR}(2)}\left(L\right) \\ +W_i^{\mathrm{FR}}\left(L\right) F^{\mathrm{FR}(3)}\left(L\right) \end{Bmatrix}. \tag{7.68}$$

By summing Eqs. (7.67) and (7.68) as for Eq. (7.47) and applying the continuity conditions at the crack tip in Table 7.3 and Table 7.5, U_{cp} is simplified to

$$\begin{aligned} U_{\mathrm{cp}} &= kv^2 t \sum_{i=1}^{\infty} \left\{ \frac{H_i}{\omega_i} \sin\left(\omega_i t\right) \int_0^L W_i^{\mathrm{FD}}\left(x\right) F^{\mathrm{FD}}\left(x\right) dx \right\} \\ &= -S_{\mathrm{cp}} . \end{aligned} \tag{7.69}$$

(3) Relation between U_{st} and S_{st}

Partially integrating $U_{\mathrm{st}}^{\mathrm{FD}}$, the first term in Eq. (7.48), twice and using the boundary condition in Table 7.1 together with Eq. (7.6), gives

$$U_{\mathrm{st}}^{\mathrm{FD}} = \frac{EIv^2 t^2}{2} \begin{Bmatrix} F^{\mathrm{FD}(1)}\left(L\right) F^{\mathrm{FD}(2)}\left(L\right) - F^{\mathrm{FD}(3)}\left(L\right) F^{\mathrm{FD}}\left(L\right) \\ -\dfrac{k}{EI}\displaystyle\int_0^L \left[F^{\mathrm{FD}}\left(x\right)\right]^2 dx \end{Bmatrix}. \tag{7.70}$$

By the same procedure for $U_{\mathrm{st}}^{\mathrm{FR}}$, the second term in Eq. (7.48), but using Eq. (7.8) and Table 7.2, $U_{\mathrm{st}}^{\mathrm{FR}}$ simplifies to

$$U_{\mathrm{st}}^{\mathrm{FR}} = \frac{EIv^2 t^2}{2} \begin{bmatrix} -F^{\mathrm{FR}(1)}\left(L\right) F^{\mathrm{FR}(2)}\left(L\right) \\ +F^{\mathrm{FR}(3)}\left(L\right) F^{\mathrm{FR}}\left(L\right) - F^{\mathrm{FR}(3)}\left(L+a\right) \end{bmatrix}. \tag{7.71}$$

Summing Eqs. (7.70) and (7.71) and applying the continuity at the crack tip for shifting functions in Table 7.3, U_{st} is found to be

$$\begin{aligned} U_{\mathrm{st}} &= -\frac{1}{2}EIv^2t^2F^{\mathrm{FR}(3)}\left(L+a\right)-\frac{1}{2}kv^2t^2\int_0^L\left[F^{\mathrm{FD}}\left(x\right)\right]^2dx \\ &= -\frac{1}{2}EIv^2t^2F^{\mathrm{FR}(3)}\left(L+a\right)-S_{\mathrm{st}}\,. \end{aligned} \tag{7.72}$$

Thus, by substituting results from Sections 7.2.2.1 to 7.2.2.3 to Eq. (7.2), and combining Eqs. (7.64), (7.65), (7.69) and (7.72), the total mechanical energy of the system at a given time *t* that could potentially be dissipated during crack growth is

$$\begin{aligned} \Pi = &-v^2\sum_{i=1}^{\infty}{H_i}^2\cos\left(\omega_i t\right)+\frac{1}{2}v^2\sum_{i=1}^{\infty}{H_i}^2 \\ &-\frac{1}{2}EIv^2t^2F^{\mathrm{FR}(3)}\left(L+a\right) \\ &+\frac{1}{2}\rho A\int_0^L\left[F^{\mathrm{FD}}\left(x\right)v\right]^2dx+\frac{1}{2}\rho A\int_L^{L+a}\left[F^{\mathrm{FR}}\left(x\right)v\right]^2dx. \end{aligned} \tag{7.73}$$

7.2.3 Dynamic energy release rate on elastic foundation

The energy that can potentially be dissipated from the system during crack growth comes from the mechanical energy of the system. The total mechanical energy is given by Π is Eq. (7.73). Let $\Pi=\Pi_{\mathrm{vib}}+\Pi_{\mathrm{st}}^{\mathrm{U}}+\Pi_{\mathrm{st}}^{\mathrm{K}}$, where

$$\Pi_{\mathrm{vib}}=-v^2\sum_{i=1}^{\infty}H_i^2\cos\left(\omega_i t\right)+\frac{1}{2}v^2\sum_{i=1}^{\infty}H_i^2\,, \tag{7.74}$$

$$\Pi_{\mathrm{st}}^{\mathrm{U}}=-\frac{1}{2}EIv^2t^2F^{\mathrm{FR}(3)}\left(L+a\right), \tag{7.75}$$

$$\Pi_{\mathrm{st}}^{\mathrm{K}}=\frac{1}{2}\rho A\int_0^L\left[F^{\mathrm{FD}}\left(x\right)v\right]^2dx+\frac{1}{2}\rho A\int_L^{L+a}\left[F^{\mathrm{FR}}\left(x\right)v\right]^2dx, \tag{7.76}$$

in which Π_{vib} is the vibration-related energy component, $\Pi_{\mathrm{st}}^{\mathrm{U}}$ is the strain energy component due to the quasi-static motion, and $\Pi_{\mathrm{st}}^{\mathrm{K}}$ is the kinetic energy component due to the quasi-static motion.

They dynamic ERR can also be expressed as the sum of respective components, that is, $G=G_{\mathrm{st}}^{\mathrm{U}}+G_{\mathrm{st}}^{\mathrm{K}}+G_{\mathrm{vib}}$, where $G_{\mathrm{st}}^{\mathrm{U}}$ and $G_{\mathrm{st}}^{\mathrm{K}}$ are the ERR components due to the strain and kinetic energies of the quasi-static motion, respectively, and G_{vib} is the ERR component due to the vibration. Note that this partition is also in accordance with Section 5.3.2. The ERR components due to the quasi-static motion $G_{\mathrm{st}}^{\mathrm{U}}$ and $G_{\mathrm{st}}^{\mathrm{K}}$ can be readily determined as $G_{\mathrm{st}}^{\mathrm{U}}=-d\Pi_{\mathrm{st}}^{\mathrm{U}}/dA_0$ and $G_{\mathrm{st}}^{\mathrm{K}}=-d\Pi_{\mathrm{st}}^{\mathrm{K}}/dA_0$. But for the ERR component G_{vib}, in general, $G_{\mathrm{vib}} \neq -d\Pi_{\mathrm{vib}}/dA_0$, and instead the dispersive properties for the propagation of flexural waves must be considered as Section 5.3.2 and dispersion-corrected global approach must be applied, or otherwise G_{vib} will not be accurately determined.

7.2.3.1 ERR component due to quasi-static motion

The ERR component due to the strain energy of the quasi-static motion $G_{\mathrm{st}}^{\mathrm{U}}$ is

$$G_{\mathrm{st}}^{\mathrm{U}} = -\frac{d\Pi_{\mathrm{st}}^{\mathrm{U}}}{dA_0} = \frac{EIv^2t^2}{2b}\frac{dF^{\mathrm{FR}(3)}\left(L+a\right)}{da}, \tag{7.77}$$

where, from Eq. (7.29), $F^{\mathrm{FR}(3)}\,(L + a) = 6P_3$. Assuming the product of the foundation stiffness k and the length of the foundation-supported beam section L (also the uncracked region length) is large enough to satisfy $\tanh(2\gamma L) \approx 1$ (that is, $\gamma L \gtrapprox 3$ so that $\tanh(6) \approx 0.999999$), and then P_3 in Eq. (7.33) approximates to

$$P_3 = \frac{-\gamma^3}{2a^3\gamma^3 + 6a^2\gamma^2 + 6a\gamma + 3}, \tag{7.78}$$

and $G_{\mathrm{st}}^{\mathrm{U}}$ simplifies to

$$G_{\mathrm{st}}^{\mathrm{U}} = \frac{9EIv^2t^2 f_{\mathrm{st}}^{\mathrm{U}}}{2ba^4}, \tag{7.79}$$

where

$$f_{\mathrm{st}}^{\mathrm{U}} = \frac{4a^4\gamma^4\left(a\gamma+1\right)^2}{\left(2a^3\gamma^3 + 6a^2\gamma^2 + 6a\gamma + 3\right)^2}. \tag{7.80}$$

For a rigid interface, the foundation stiffness k and γ approach to infinity, and so $f_{\mathrm{st}}^{\mathrm{U}} = 1$ and $G_{\mathrm{st}}^{\mathrm{U}}$ becomes $G_{\mathrm{st}}^{\mathrm{U}} = 9EIv^2t^2/\left(2ba^4\right)$. Therefore, $f_{\mathrm{st}}^{\mathrm{U}}$ can be viewed as a static ERR reduction factor for non-rigid linear elastic interfaces, and this can be readily used for the quasi-static case, for example, a DCB bonded with adhesives under quasi-static loads.

Based on Eq. (7.76), the ERR component due to the kinetic energy of the quasi-static motion, $G_{\mathrm{st}}^{\mathrm{K}} = -d\Pi_{\mathrm{st}}^{\mathrm{K}}/dA_0$, is constant and only gives the total ERR a downward shift. As above, if $\tanh(2\gamma L) \approx 1$, then $G_{\mathrm{st}}^{\mathrm{K}}$ is

$$G_{\text{st}}^{\text{K}} = -\frac{33\rho A v^2 f_{\text{st}}^{\text{K}}}{280b}, \tag{7.81}$$

where

$$f_{\text{st}}^{\text{K}} = \frac{\begin{pmatrix} 88a^9\gamma^9 + 792a^8\gamma^8 + 3168a^7\gamma^7 + 7420a^6\gamma^6 + 11256a^5\gamma^5 \\ +12180a^4\gamma^4 + 10920a^3\gamma^3 + 8820a^2\gamma^2 + 5040a\gamma + 1260 \end{pmatrix}}{11\left(2a^3\gamma^3 + 6a^2\gamma^2 + 6a\gamma + 3\right)^3}. \tag{7.82}$$

It is worth noting that if $a\gamma \gtrapprox 4.7$ then $f_{\text{st}}^{\text{K}} > 0.995$. For a rigid interface, $f_{\text{st}}^{\text{K}} = 1$, and this ERR component becomes $G_{\text{st}}^{\text{K}} = -33\rho A v^2 \big/ \left(280b\right)$, which is the same as the contribution from kinetic energy in the conventional method (half of the last term in Eq. (4.4)) and as the contribution from the kinetic energy of the quasi-static motion in Section 5.3.2.1.

7.2.3.2 ERR component due to vibration

The ERR component due to vibration is determined by the energy flux $F_{\text{vib}}(\Omega)$ due to vibration through a crack tip contour Ω as shown in Figure 7.3 with $\varepsilon \ll a$ and $\varepsilon \ll L$.

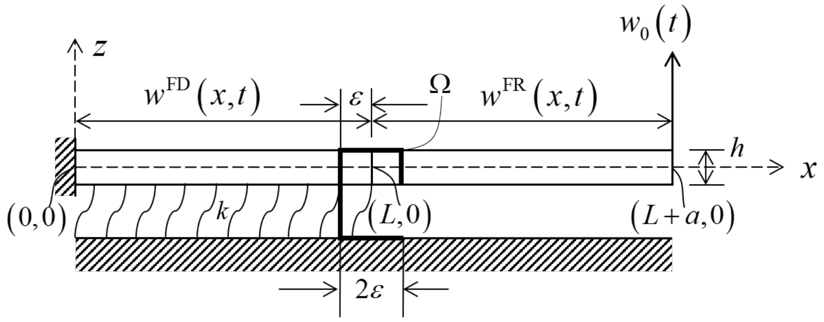

Figure 7.3 Crack tip contour Ω for elastic interface to determine ERR component due to vibration

Similar to Section 5.3.2.2, $F_{\text{vib}}(\Omega)$ can be determined by $F_{\text{vib}}\left(\Omega\right) = E_{\text{vib}} C_{\text{p}}^{1}$, where E_{vib} is the energy density and C_{p}^{1} is the phase speed of the first-mode flexural wave. This is due to the dispersive property of flexural waves in beams, and first-mode flexural wave modulates all the other waves with higher frequencies [25] (Sections 2.3.1.1 and 5.3.2.2).

To determine the total energy density E_{vib}, and hence via Eq. (5.26) for $G_{\text{vib}} = F_{\text{vib}}\left(\Omega\right) \big/ \dot{A}_0$, the ERR component due to vibration G_{vib}, consider Π_{vib} in Eq. (7.74) as having two components, $\Pi_{\mathrm{vib}} = \Pi_{\mathrm{C}} + \Pi_{\mathrm{S}}$, which give rise to E_{vib} with two corresponding components, $E_{\mathrm{vib}} = E_{\mathrm{C}} + E_{\mathrm{S}}$.

The E_{C} component of E_{vib} comes from Π_{C}, which is the first term in Eq. (7.74) and is the kinetic energy due to the coupling between local vibration and quasi-static motion. For the *i*th mode flexural wave, the energy flux from the coupling between local vibration and quasi-static motion is $F_{\mathrm{C}}^{i}\left(\Omega\right) = E_{\mathrm{C}}^{i} C_{\mathrm{g}}^{i}$, and $F_{\mathrm{C}}^{i}\left(\Omega\right) = -d\Pi_{\mathrm{C}}^{i}/dt$. However, $E_{\mathrm{C}} \neq \sum_{i=1}^{\infty} E_{\mathrm{C}}^{i}$, and so also, $F_{\mathrm{C}}\left(\Omega\right) \neq \sum_{i=1}^{\infty} F_{\mathrm{C}}^{i}\left(\Omega\right)$; The E_{S} component of E_{vib} comes from Π_{S}, which is the second term in Eq. (7.74) and is the strain and kinetic energy due to local vibration. For the *i*th mode flexural wave, the energy flux from the strain and kinetic energy due to local vibration is $F_{\mathrm{S}}^{i}\left(\Omega\right) = E_{\mathrm{S}}^{i} C_{\mathrm{g}}^{i}$, and $F_{\mathrm{S}}^{i}\left(\Omega\right) = -d\Pi_{\mathrm{S}}^{i}/dt$. Nevertheless, $E_{\mathrm{S}} \neq \sum_{i=1}^{\infty} E_{\mathrm{S}}^{i}$, and so also, $F_{\mathrm{S}}\left(\Omega\right) \neq \sum_{i=1}^{\infty} F_{\mathrm{S}}^{i}\left(\Omega\right)$.

Now consider the net contribution from all the flexural waves to E_{C}. If the foundation stiffness k is relatively large, then the shifting function for the foundation-supported beam section is approximately zero. Therefore, by simplifying Eq. (7.54) with $F^{\mathrm{FD}}(x) \approx 0$, expanding $\dot{w}_{\mathrm{fv}}^{\mathrm{FR}}\left(x,t\right)$ using Eq. (7.36), and substituting in Π_{C}, which is the first term of Eq. (7.74), then Π_{C}^{i} (the *i*th mode flexural wave contribution to Π_{C}) is obtained as

$$\Pi_{\mathrm{C}}^{i} = K_{\mathrm{cp}}^{i} \approx -\rho A v^{2} \int_{L}^{L+a} \left\{ \sum_{i=1}^{\infty} \left[H_{i} W_{i}^{\mathrm{FR}}\left(x\right) F^{\mathrm{FR}}\left(x\right) \right] \right\} dx \cos\left(\omega_{i} t\right). \qquad (7.83)$$

The integrand of Eq. (7.83) represents the spatial coupling of the normal modes and the shifting function due to the velocity coupling between local vibration and applied velocity. For the small contour Ω around the crack tip as shown in Figure 7.3, inside this contour in a region behind the crack tip, that is, $L \leq x \leq L+\varepsilon$, it can be shown that $F^{\mathrm{FR}}(x) > 0$ and $W_{i}^{\mathrm{FR}}\left(x\right) > 0$, but that the sign of H_i alternates with vibration mode numbers with $H_i < 0$ for odd modes and $H_i > 0$ for even modes. This can be seen by referring to Λ_{i} in Table 5.2, which has the effective boundary condition i.e. fixed at the crack tip. For relatively large foundation stiffness, the beam partially on elastic foundation is equivalent to the fixed effective boundary condition, and thus H_i is equivalent to Λ_{i} (see Section 7.2.1.3), which alternates with vibration mode numbers. The integrand of Eq. (7.83) is therefore negative for odd modes, which means that the corresponding Π_{C}^{i}

reduces the energy density, and is positive for even modes, which means that the corresponding Π_{C}^{i} increases the energy density. Therefore, the total energy density due to Π_{C}^{i} is

$$E_{\mathrm{C}} = \sum_{i=1}^{\infty} (-1)^{i} E_{\mathrm{C}}^{i} . \tag{7.84}$$

The physical interpretation of Eq. (7.84) is that, near to the crack tip spatially, when the transverse velocity of the free vibration represented by normal modes is in the same direction as the applied velocity, the energy flux tends to open the crack and increase the total energy density and the ERR. When, however, near to the crack tip spatially, the transverse velocity of the free vibration represented by normal mode is in the opposite direction to the applied velocity, the energy flux tends to close the crack and decrease the total energy density and the ERR.

The energy density of E_{S} due to Π_{S}, similarly, can be determined by $E_{\mathrm{S}} = \sum_{i=1}^{\infty} (-1)^{i} E_{\mathrm{S}}^{i}$ with an alternating H_i. The total energy density due to vibration E_{vib} is therefore

$$E_{\mathrm{vib}} = \sum_{i=1}^{\infty} (-1)^{i} E_{\mathrm{C}}^{i} + \sum_{i=1}^{\infty} (-1)^{i} E_{\mathrm{S}}^{i} . \tag{7.85}$$

By substituting Eq. (7.85) into Eq. (5.26) for $G_{\mathrm{vib}} = F_{\mathrm{vib}}(\Omega) / \dot{A}_0$, the ERR component due to vibration is

$$\begin{aligned} G_{\mathrm{vib}} &= \frac{C_{\mathrm{p}}^{1}}{\dot{A}_0} \left[\sum_{i=1}^{\infty} (-1)^{i} \frac{F_{\mathrm{C}}^{i}(\Omega)}{C_{\mathrm{g}}^{i}} + \sum_{i=1}^{\infty} (-1)^{i} \frac{F_{\mathrm{S}}^{i}(\Omega)}{C_{\mathrm{g}}^{i}} \right] \\ &= -\frac{C_{\mathrm{p}}^{1}}{dA_0/dt} \left[\sum_{i=1}^{\infty} (-1)^{i} \frac{d\Pi_{\mathrm{C}}^{i}/dt}{C_{\mathrm{g}}^{i}} + \sum_{i=1}^{\infty} (-1)^{i} \frac{d\Pi_{\mathrm{S}}^{i}/dt}{C_{\mathrm{g}}^{i}} \right] \\ &= -\sum_{i=1}^{\infty} (-1)^{i} \frac{d\Pi_{\mathrm{C}}^{i}}{dA_0} \frac{C_{\mathrm{p}}^{1}}{C_{\mathrm{g}}^{i}} - \sum_{i=1}^{\infty} (-1)^{i} \frac{d\Pi_{\mathrm{S}i}}{dA_0} \frac{C_{\mathrm{p}}^{1}}{C_{\mathrm{g}}^{i}} . \end{aligned} \tag{7.86}$$

The ratio $C_{\mathrm{p}}^{1} / C_{\mathrm{g}}^{i}$ is the correction factor for dispersion, where the phase speed of firs-mode flexural wave is $C_{\mathrm{p}}^{1} = \sqrt{\omega_1 \sqrt[4]{EI/(\rho A)}}$ and group speed of ith mode flexural wave is $C_{\mathrm{g}}^{i} = 2\sqrt{\omega_i}\sqrt[4]{EI/(\rho A)}$, giving correction factor for dispersion $f_i = C_{\mathrm{p}}^{1}\big/C_{\mathrm{g}}^{i} = \sqrt{\omega_1/(4\omega_i)}$.

Eq. (7.86) can be expanded into the following form:

$$\begin{aligned} G_{\mathrm{vib}} = {} & \frac{v^2}{4b}\sum_{i=1}^{\infty}(-1)^i\sqrt{\frac{\omega_1}{\omega_i}}\frac{dH_i}{da}\cos(\omega_i t) - \frac{v^2 t}{2b}\sum_{i=1}^{\infty}(-1)^i\sqrt{\frac{\omega_1}{\omega_i}}H_i^{\,2}\frac{d\omega_i}{da}\sin(\omega_i t) \\ & - \frac{v^2}{2b}\sum_{i=1}^{\infty}(-1)^i\sqrt{\frac{\omega_1}{\omega_i}}\frac{dH_i}{da}. \end{aligned} \tag{7.87}$$

Unless t is small, the first and third term of Eq. (7.87) are much smaller than the second term, which increases with time, and therefore

$$G_{\mathrm{vib}} \approx -\frac{v^2 t}{2b}\sum_{i=1}^{\infty}(-1)^i\sqrt{\frac{\omega_1}{\omega_i}}H_i^{\,2}\frac{d\omega_i}{da}\sin(\omega_i t). \tag{7.88}$$

The derivative $d\omega_i/da$ is derived as follows. Recall the determinant D_i for the coefficient matrix in Eq. (7.21) in Section 7.2.1.2, which is a function of the wavenumbers, α_i and β_i, and lengths of the sections, a and L. Since $D_i = 0$, its total derivative is

$$dD_i(\alpha_i,\beta_i,L,a) = \frac{\partial D_i}{\partial\alpha_i}d\alpha_i + \frac{\partial D_i}{\partial\beta_i}d\beta_i + \frac{\partial D_i}{\partial L}dL + \frac{\partial D_i}{\partial a}da = 0. \tag{7.89}$$

Diving Eq. (7.89) by da gives

$$\frac{\partial D_i}{\partial\alpha_i}\frac{d\alpha_i}{da} + \frac{\partial D_i}{\partial\beta_i}\frac{d\beta_i}{da} + \frac{\partial D_i}{\partial L}\frac{dL}{da} + \frac{\partial D_i}{\partial a} = 0. \tag{7.90}$$

Note that $L + a =$ constant, which gives $dL/da = -1$; and that $4\alpha_i^4 = k/EI - \beta_i^4$, which gives $d\alpha_i/da = -\beta_i^3\big/(4\alpha_i^3)(d\beta_i/da)$. By also using $\beta_i^4 = \omega_i^2\rho A\big/(EI)$, $d\omega_i/da$ is obtained as

$$\frac{d\omega_i}{da} = 2\beta_i\sqrt{\frac{EI}{\rho A}}\frac{d\beta_i}{da} = 2\beta_i\frac{\dfrac{\partial D_i}{\partial L} - \dfrac{\partial D_i}{\partial a}}{-\dfrac{\partial D_i}{\partial\alpha_i}\dfrac{\beta_i^3}{4\alpha_i^3} + \dfrac{\partial D_i}{\partial\beta_i}}\sqrt{\frac{EI}{\rho A}}. \tag{7.91}$$

7.2.3.3 Total dynamic energy release

By summing Eqs. (7.79), (7.81) and (7.88), the total dynamic ERR under the above assumptions is approximately

$$G=\frac{9EIv^{2}t^{2}f_{\mathrm{st}}^{\mathrm{U}}}{2ba^{4}}-\frac{33\rho Av^{2}f_{\mathrm{st}}^{\mathrm{K}}}{280b}-\frac{v^{2}t}{2b}\sum_{i=1}^{\infty}\left(-1\right)^{i}\sqrt{\frac{\omega_{1}}{\omega_{i}}}H_{i}^{2}\frac{d\omega_{i}}{da}\sin\left(\omega_{i}t\right). \tag{7.92}$$

Note that Eq. (7.92) is for a crack on the interface between a partially supported beam and an elastic foundation; for a DCB, the ERR is simply twice of Eq. (7.92) due to symmetry.

Also, note the combination of the first two terms of Eq. (7.92) is the ERR due to quasi-static motion G_{st}; and it is a counterpart in the conventional analytical approach in Section 4.2, where

$$G_{\mathrm{st}}=\frac{9EIv^{2}t^{2}f_{\mathrm{st}}^{\mathrm{U}}}{2ba^{4}}-\frac{33\rho Av^{2}f_{\mathrm{st}}^{\mathrm{K}}}{280b}. \tag{7.93}$$

7.2.4 Dynamic factor

Now consider the total dynamic effect of the last two terms in Eq. (7.92), which can be grouped together as G_{dyn}, so $G=G_{\mathrm{st}}^{\mathrm{U}}+G_{\mathrm{dyn}}$, where

$$G_{\mathrm{dyn}}=-\frac{33\rho Av^{2}f_{\mathrm{st}}^{\mathrm{K}}}{280b}-\frac{v^{2}t}{2b}\sum_{i=1}^{\infty}\left(-1\right)^{i}\sqrt{\frac{\omega_{1}}{\omega_{i}}}H_{i}^{2}\frac{d\omega_{i}}{da}\sin\left(\omega_{i}t\right). \tag{7.94}$$

To investigate the dynamic effect, a dynamic factor is defined as

$$\begin{aligned}f_{\mathrm{dyn}}&=\frac{G_{\mathrm{dyn}}}{G_{\mathrm{st}}^{\mathrm{U}}}\\&=-\frac{11f_{\mathrm{st}}^{\mathrm{K}}}{420f_{\mathrm{st}}^{\mathrm{U}}}\frac{\rho A}{EI}\frac{a^{4}}{t^{2}}-\frac{1}{9f_{\mathrm{st}}^{\mathrm{U}}}\frac{1}{EI}\frac{a^{4}}{t}\sum_{i=1}^{\infty}\left(-1\right)^{i}\sqrt{\frac{\omega_{1}}{\omega_{i}}}H_{i}^{2}\sin\left(\omega_{i}t\right)\frac{d\omega_{i}}{da}.\end{aligned} \tag{7.95}$$

Dynamic effects arise due to the kinetic energy of the quasi-static motion and vibration. The former was the focus of the conventional analytical approach (Section 4.2), in which the dynamic factor follows an inverse square law with respect to time and decays very quickly. The latter dynamic effect, the second term of Eq. (7.95), is the focus of this chapter. It is therefore called the dynamic factor due to vibration, denoted by f_{vib}, and is the summation of contributions from all vibration modes.

$$f_{\mathrm{vib}} = -\frac{1}{9 f_{\mathrm{st}}^{\mathrm{U}}} \frac{1}{EI} \frac{a^4}{t} \sum_{i=1}^{\infty} \left(-1\right)^i \sqrt{\frac{\omega_1}{\omega_i}} H_i^{\,2} \sin\left(\omega_i t\right) \frac{d\omega_i}{da}. \tag{7.96}$$

7.2.4.1 Dynamic factor due to vibration and vibration modes

To show the relative contribution from each vibration mode for a rigid interface, a Fourier analysis is conducted using the Fast Fourier Transform algorithm to transform the dynamic factor due to vibration in Eq. (7.96) from the time domain to the frequency domain. For this, the verification case in Section 7.3.1 is used with the dynamic ERR from the time interval of (0 ~ 0.04 s). The first ten vibration modes are shown in Figure 7.4 with the dynamic factor due to vibration normalised by the dynamic factor due to vibration of the first vibration mode. With increasing vibration mode frequency, the dynamic factor decreases monotonically. The first vibration mode makes the greatest contribution, which drops dramatically over the first five modes. The first five vibration modes are therefore adequate to capture the major contributions to the dynamic ERR.

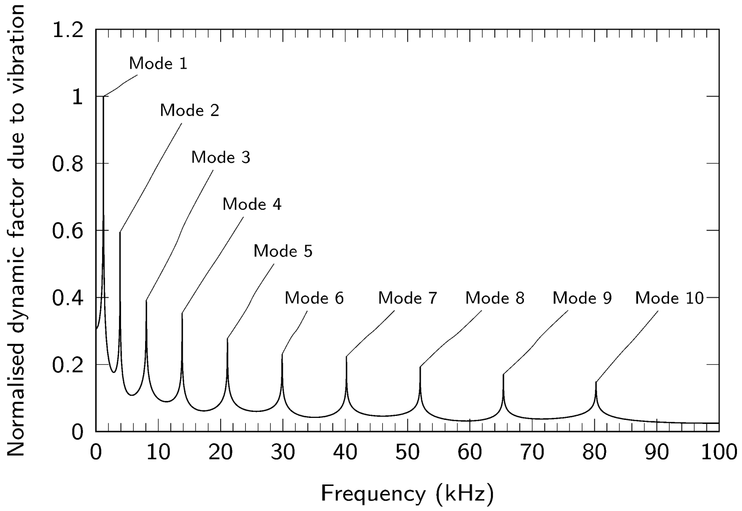

Figure 7.4 Normalised dynamic factor due to vibration first ten modes for rigid interface

7.2.4.2 Dynamic factor due to vibration and foundation stiffness

Now consider the effect of foundation stiffness, Fourier analyses are again conducted on Eq. (7.96) using four levels of foundation stiffness, namely, $k/E = 1$, 0.1, 0.01 and 0.001, and with the same geometry and material properties in Section 7.3.1. The results are normalised by the dynamic factor due to vibration of the first vibration mode with $k/E = 1$, and the numerical values are tabulated in Table 7.6.

Table 7.6 Normalised dynamic factors due to vibration with various foundation stiffnesses

Foundation stiffness	1st vibration mode	2nd vibration mode	3rd vibration mode
$k/E = 1$	1	0.65599	0.48112
$k/E = 0.1$	1.17225	0.67009	0.45369
$k/E = 0.01$	1.19499	0.70870	0.52466
$k/E = 0.001$	1.27728	0.70111	0.49133

The trends for the dynamic factor due to vibration with various foundation stiffness are plotted in Figure 7.5. With decreasing foundation stiffness, the frequency spectra shift to the left, with higher-order vibration modes being more sensitive to the foundation stiffness change. Another characteristic to note is that the contribution from the first vibration mode increase with decreasing foundation stiffness, which indicates that lower-order vibration modes become even more dominant for less stiff foundations.

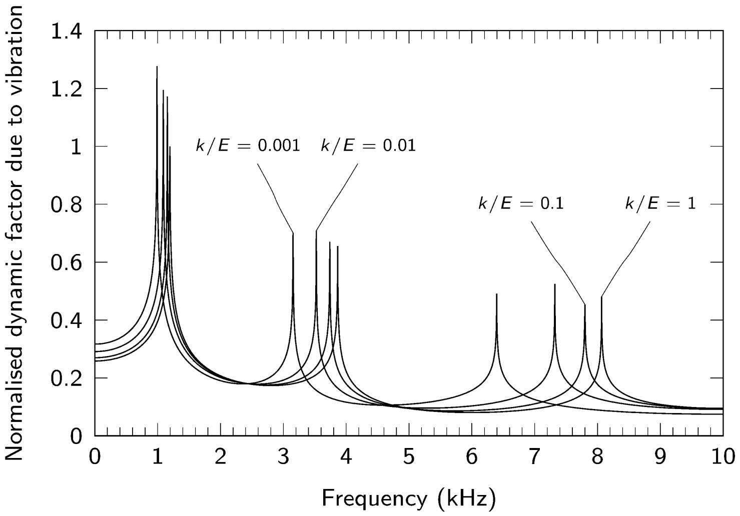

Figure 7.5 Normalised dynamic factors due to vibration versus frequency for various foundation stiffness

7.3 Numerical verification for stationary crack

The FEM simulations were used to verify the theory developed in Section 7.2. Three verification studies were conducted using the geometries shown in Figure 7.6.

(1) To verify that the developed theory agrees with FEM simulations for cracks on rigid interfaces;

(2) To verify that the developed theory agrees with FEM simulations for cracks on non-rigid linear elastic interfaces.

(3) To inspect the fracture mode mixity of a crack between a thin layer and a thick substrate under dynamic loading

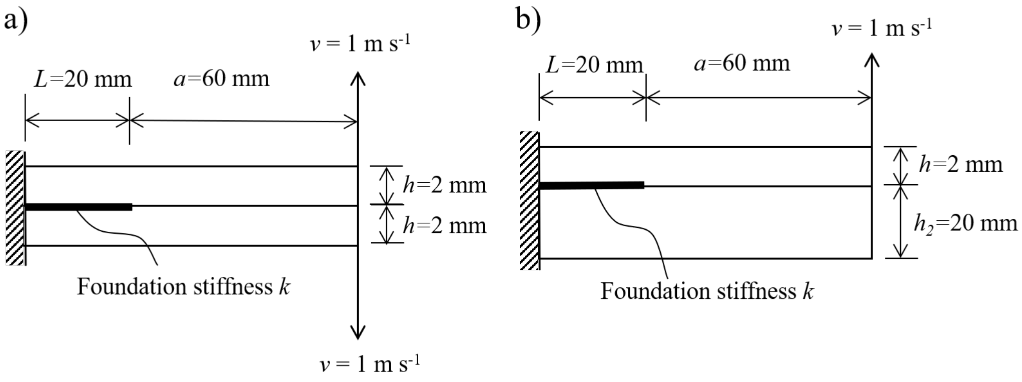

Figure 7.6 (a) DCB geometry for FEM verification studies (1) and (2); (b) thin-layer-on-thick-substrate geometry for FEM verification study (3)

7.3.1 Verification for rigid interface

The DCB geometry shown in Figure 7.6a with a width of 1 mm is used for the first verification study of a crack on a rigid interface. The Young's modulus was 10 GPa, the Poisson's ratio 0.3, and the density 10^3 kg m^{-3}. A linear 2D FEM model was constructed using plane-stress elements (CPS4R) in Abaqus/Explicit with a mesh size of 0.1 mm in accordance with the element size convergence study in Section 5.4.1. The uncracked interface ahead of the crack tip was formed by sharing nodes and no contact was simulated. The VCCT was applied to determine the dynamic ERR.

For the developed theory, an appropriate foundation stiffness that represents a rigid interface needs to be used. An interface stiffness of the same order as the beam material's Young's modulus can be regarded as a rigid interface [63], but there is no unanimous agreement on the exact value in the literature (see, for example, Refs. [166][167]). Kanninen claimed that for DCB of the mono-material under plane-strain condition the foundation stiffness should be taken as $k = 2Eb/h$, since this foundation stiffness provided excellent agreement with well-established experimental data; Cabello et al. [168] derived that under plane-stress condition the foundation stiffness is $k = Eb/h$. Therefore, for the current verification case the foundation stiffness is taken $k = 0.5\ E$ for the geometries of h =2 mm, b =1 mm.

The dynamic ERR versus time results from the FEM and the developed theory are compared in Figure 7.7, with the black line representing the theory (with $k = 0.5E$) and the grey line representing the FEM. The black dashed line represents the ERR from the strain energy of quasi-static motion in Eq. (7.79), that is, the ERR without any dynamic effect. The first one, two, three, four, five, ten, 15 and 20 vibration modes are shown in subfigures a–h of Figure 7.7, respectively. As more vibration modes are considered in the theory, it becomes increasingly closer agreement with the FEM in terms of the overall magnitude of ERR, and the frequencies, phases and amplitudes of oscillation. It is seen that the theory with the first five vibration modes (Figure 7.7e) is adequate to capture the dynamic ERR very accurately; adding more vibration modes (Figure 7.7f-h) provides more detail, but the changes in the amplitude are not significant.

Note that the theory with just the first vibration mode (Figure 7.7a) is close to what was reported in Sections 5.2 and 5.3 for DCBs analysed by effective boundary condition. With effective boundary condition, the developed theory in Sections 5.2 and 5.3 was slightly out-of-phase due to the simplified boundary condition and requires an additional crack length Δ to compensate for crack-tip rotation in Section 5.5. Now with the elastic foundation which allows the crack tip to rotate under externally applied displacement, this phase difference was substantially corrected rather than employing an additional crack length Δ.

For further application of this analytical theory in composite DCB, the interfacial stiffness can be determined by $k = \alpha E_{33}/h_0$, where E_{33} is the transverse modulus, h_0 is the thickness of an adjacent sub-laminate, and α is a parameter much large than 1 [169].

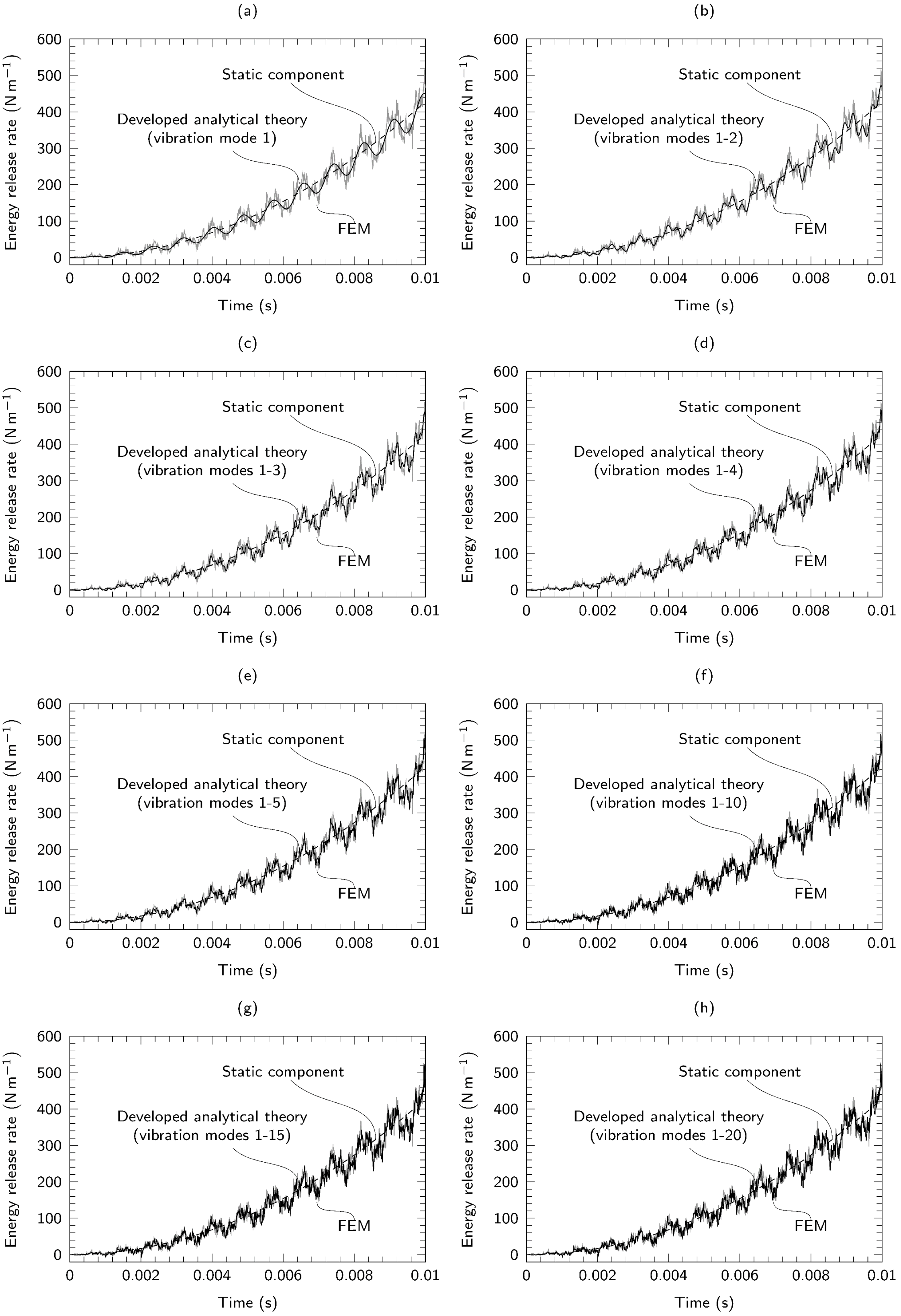

Figure 7.7 Dynamic ERR versus time results from developed theory (black line) and from FEM (grey line) with increasing numbers of vibration modes

7.3.2 Verification for non-rigid interface

The same DCB geometry and material properties were used for the second verification study of cracks on non-rigid linear elastic interfaces. The FEM model was used with the uncracked interface ahead of the crack tip being modelled with cohesive elements (COH2D4), length of which was set to be 0.05 mm after an element size convergence study with 4 elements sizes (0.5 mm, 0.2 mm, 0.1 mm and 0.05 mm) following a similar approach in Section 5.4.1 (see Figure 7.8) and thickness 0.0001 mm, to simulate the linear-elastic interface with a traction-separation law. A crack closure integral was used at the crack tip to determine the dynamic ERR [130], also referred to Eq. (4.14). Note that the density of the cohesive element was set as 1 kg m^{-3}, which is 0.1% of the DCB material, in order not to add significant extra mass to the system.

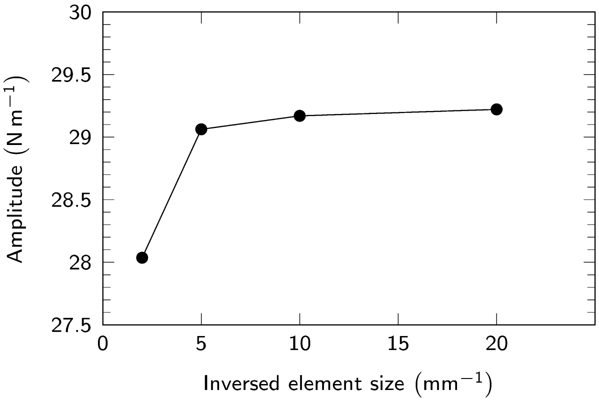

Figure 7.8 Cohesive element size convergence

Since the DCB in Figure 7.6a deforms symmetrically but the developed theory is for a partially-supported beam on an elastic foundation (Figure 7.2), the normal stiffness of the cohesive elements in these FEM simulations must be set as $E_{nn} = 0.5k$. This relationship is a consequence of the symmetric deformation of the DCB (and its interface) under the prescribed loading in comparison to the ‘one-sided’ deformation of a partially supported beam on an elastic foundation, which the developed theory is for. As long as the deformation is symmetrical, this relationship between E_{nn} and k is valid.

Four levels of interface stiffness k were examined, namely, $0.1E$ (1000 MPa), $0.01E$ (100 MPa), $0.001E$ (10 MPa) and $0.0001E$ (1 MPa), and so the corresponding normal stiffnesses E_{nn} for the cohesive elements were 500 MPa, 50 MPa, 5 MPa and 0.5 MPa, respectively.

The dynamic ERR versus time results from the FEM and the developed theory (with the first five vibration modes) are compared in Figure 7.9, with the black line representing the theory and the grey line representing the FEM. There is excellent agreement between the theory and the FEM for the three different foundation stiffnesses shown in Figure 7.9a-c considering the overall magnitude of ERR and the frequencies, phases and amplitudes of oscillation.

Note that the developed theory is only applicable for relatively large foundation stiffness: In Section 7.2.1.2, the general solution of free vibration of the foundation-supported beam section requires that $4\alpha_i^4 = k/EI - \beta_i^4 > 0$. Furthermore, in Section 7.2.3.1, the developed expression for dynamic ERR requires that $\gamma L \gtrapprox 3$. For $k = 0.0001E$ in Figure 7.9d, the condition of $k/EI - \beta_i^4 > 0$ is met only for the first two vibration modes, and then from the third vibration mode onwards, $k/EI - \beta_i^4 < 0$. This accounts for the discrepancy seen between the results from the FEM and the developed theory in Figure 7.9d.

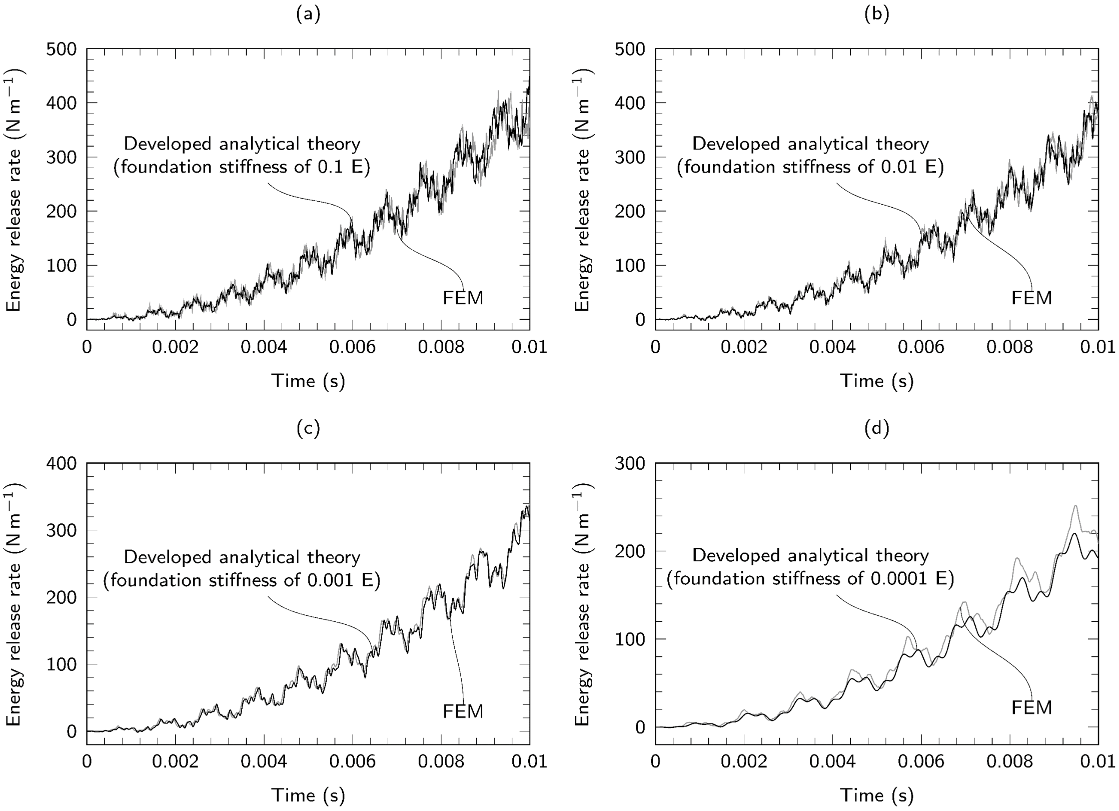

Figure 7.9 Dynamic ERR versus time results from developed theory (black line) and from FEM (grey line) with the first five vibration modes for different foundation stiffnesses

The comparison between Figure 7.7 and Figure 7.9 also indicates that whether ERR is sensitive to the foundation stiffness. When foundation stiffness is within the same order, the amplitude of the ERR is not sensitive to the alteration of the foundation stiffness, and this can be seen by comparing Figure 7.7e ($k = 0.5\,E$) and Figure 7.9a ($k = 0.1\,E$).

7.3.3 Verification for fracture mode mixity

The developed theory also applies to thin layers on thick substrates. Note that this configuration is also known as spalling of a thin layer, which is a typical mixed-mode case, that is, crack-tip subjected to both normal and shear stress due to the asymmetric configuration (relevant literature in Section 3.2.6), where the relative displacements of thin layer and thick substrate at crack tip are both opening (mode-I) and sliding (mode-II) at the same time. The developed theoretical solution, however, provides the total dynamic ERR; since the fracture is mixed mode, the total ERR comprises both fracture modes I (G_I) and II (G_{II}). In this third verification study, the agreement between the developed theory and FEM simulations is checked for a crack on a rigid interface between a thin layer and a thick substrate. Furthermore, the fracture mode mixity (see Section 3.2.6) is calculated and compared against the mixed-mode partition theory in [170], which was developed for quasi-static fracture of thin layers on thick substrates.

The geometry shown in Figure 7.6b with a width of 1 mm was used for the third verification study. The same material properties from the first verification study were used, and the same global mesh size of 0.2 mm was used (without any refinement around the crack tip). The VCCT was applied to determine the two ERR fracture mode components, G_I and G_{II}, with the total ERR being $G = G_I + G_{II}$.

The total dynamic ERR versus time results from the FEM and the developed theory (with $k = 0.5E$ [168] and the first five vibration modes) are compared in Figure 7.10a with the black line representing the developed theory and the grey line representing the FEM. The total dynamic ERR from the developed theory was then partitioned according to [170] (which gives $G_{II}/G_I = 0.6059$) and is compared against the FEM results in Figure 7.10b. Excellent agreement is seen between the developed theory and the FEM for both the total ERR and its partitions, showing that the quasi-static partition theory in [170] is also applicable under dynamic loading.

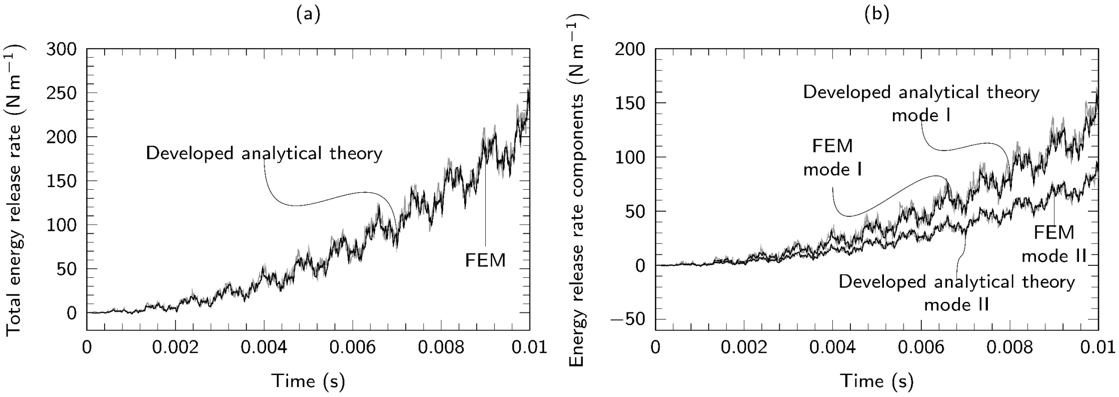

Figure 7.10 Results for (a) total dynamic ERR and (b) its fracture-mode I and fracture-mode II components versus time results from developed theory (black line) and from FEM (grey line).

7.4 Theoretical development for propagating crack

The analytical solution for dynamic ERR of a stationary crack on an elastic foundation is derived in Section 7.2.3, see Eq. (7.92). Its second term is the ERR component due to the kinetic energy of the quasi-static motion; it is constant and only provides a baseline shift down for the total dynamic ERR; in the long run, this term is insignificant, and the total dynamic ERR can be approximated as

$$G = \frac{9EIv^2t^2 f_{\mathrm{st}}^{\mathrm{U}}}{2ba^4} - \frac{v^2 t}{2b}\sum_{i=1}^{\infty}(-1)^i \sqrt{\frac{\omega_1}{\omega_i}} H_i^{\,2} \frac{d\omega_i}{da}\sin(\omega_i t). \tag{7.97}$$

Eq. (7.97) is a counterpart of Eq. (5.37), and, therefore, can be used to develop the dynamic ERR for a propagating crack on the elastic foundation following a similar approach established in Section 6.2.2.2. If the foundation’s stiffness is large, the beam partially supported on elastic foundation in Figure 7.2 degrades into the configuration of a half DCB arm with the effective boundary condition as shown in Figure 5.1b, and Eq. (7.97) becomes equivalent to Eq. (5.37). By analogy to the dynamic ERR solution in Eq. (6.13) (developed in Section 6.2.2.2) and using Eq. (7.97), the dynamic ERR for the propagating crack on the elastic foundation (for a relatively large foundation’s stiffness) is

$$
\begin{aligned}
G = {} & \frac{9EIv^2t^2 f_{\mathrm{st}}^{\mathrm{U}}}{2ba^4}\left(1-\frac{\dot{a}^2}{C_0^2}\right) \\
& -\frac{v^2 t}{2b}\left(1-\frac{\dot{a}^2}{C_0^2}\right)\sum_{i=1}^{\infty}\left(-1\right)^i\sqrt{\frac{\omega_1}{\omega_i}}H_i{}^2\,\frac{d\omega_i}{da}\,f_i'\sin\left[\left(1-\frac{\dot{a}}{C_{\mathrm{p}}^i}\right)\omega_i t\right].
\end{aligned}
\tag{7.98}
$$

Note that f_i' is the correction factor for dispersion for the propagating crack, but it has different values from those in Table 6.1, derived on the assumption that the boundary conditions for the crack increment of the beam section ($a_2 - a_1$) are fixed-fixed.

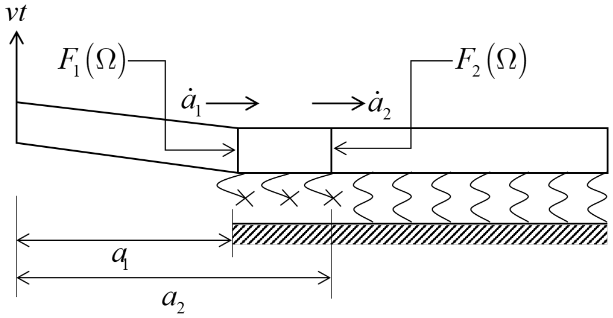

Figure 7.11 Crack propagation from a_1 to a_2 over time interval Δt on elastic interface

For the propagating crack on the elastic foundation, consider a crack propagating from a_1 to a_2 in Figure 7.11. Since the elastic foundation allows crack tips ($x = a_1$ and $x = a_2$) to rotate, the boundary conditions for the crack increment ($a_2 - a_1$) are more free than completely fixed-fixed. But the elastic foundation does not allow the crack tips to rotate completely freely, and this means that the boundary conditions for the crack increment ($a_2 - a_1$) do not achieve the pinned-pinned boundary conditions. Therefore, fixed-fixed and pinned-pinned are two limiting cases for the boundary conditions for the crack increment ($a_2 - a_1$) on the elastic foundation, and the correction factor for dispersion f_i' should be derived between these two limiting boundary conditions. It is also assumed that f_i' can be taken an average value of those from fixed-fixed and pinned-pinned boundary conditions with its values given in Table 7.7.

Table 7.7 Correction factor for dispersion for propagating crack

Mode number	1	2	3	4	5	$i > 5$
Correction factor for fixed-fixed boundary conditions	0.5	0.30115	0.21509	0.16729	0.13687	$\frac{1.50562}{(2i+1)}$
Correction factor for pinned-pinned boundary conditions	0.5	0.25	0.16667	0.125	0.1	$\frac{1}{2i}$
Correction factor for elastic foundation boundary conditions	0.5	0.27558	0.19088	0.14615	0.11844	$\frac{5.011i+1}{4i(2i+1)}$

7.5 Numerical verification for propagating crack

Numerical simulations of a DCB of a PEEK/carbon-fibre composite under 6.5 and 10.0 m s^{-1} opening rate cases in [22] for experiments in [19] and [20] are used to verify the analytical solution Eq. (7.98) for the propagating crack on the elastic foundation. Ref. [22] used ITLSM (Section 4.3.2.3) to model the damage in the interface by overcoming the disadvantage of CZM (Section 4.3.2.2), and numerical details can be found in [22]. Note that these numerical simulations were used previously in this work for verification of the theory developed based on effective boundary condition in Section 6.4.2. The application of Eq. (7.98) requires accurate value of the foundation stiffness. For composite materials, the interlaminar stiffness is highly dependent on the transverse modulus of the composite material, and the foundation stiffness for the interface is derived by compliance calibration against experimental data.

Determination of foundation's stiffness

The foundation stiffness is essential to study the dynamic fracture and to derive the ERR. For CFRPs, Turon et al. [169] proposed a solution for foundation stiffness $k = \alpha E_{33}/h_0$, where E_{33} is the transverse modulus, h_0 is the thickness of an adjacent sub-laminate, and α is a parameter much large than 1; clearly, to employ this foundation stiffness, the parameter α should be known, but currently there is also no exact value for

α in literature. Instead, a compliance calibration method against quasi-static DCB experimental data is developed to determine the foundation stiffness.

Considering the quasi-static component in deflection in Eq. (7.36), the external force under quasi-static loading rate is found to be $P = -vtEIF^{\mathrm{FR}(3)}(L+a)$, and then the compliance is $C = vt/P$, and by combining Eq. (7.78), the following relationship between the compliance and foundation stiffness (represented by γ) can be derived:

$$\left(2a^3 - 6CEI\right)\gamma^3 + 6a^2\gamma^2 + 6a\gamma + 3 = 0, \tag{7.99}$$

where $\gamma = \sqrt[4]{k/\left(4EI\right)}$, and, therefore, $k = 4\gamma^4 EI$. Note that for plane-strain condition E should be substituted by $115/(1 - 0.28^2)$ GPa.

Now consider the PEEK/carbon-fibre composite under constant opening rate of 3.3×10^{-5} m s^{-1} in Figure 4.1a, the compliance is calculated using the initial linearly elastic response, which gives the compliance of 1/28382 m/N. Combining Eq. (7.99), the compliance calibration gives the foundation stiffness $k = 1.18$ GPa.

Therefore, this foundation's stiffness $k = 1.18$ GPa is used in Eq. (7.98) to verify the numerical results for the propagating crack for the PEEK/carbon-fibre composite (which was also been used in Section 6.4.2). The crack length is taken from [22] and the crack-propagation speed is calculated with the central-difference scheme. For the stationary crack before the crack initiation, Eq. (7.92) is used to calculate the dynamic ERR, and, once the crack starts to propagate, Eq. (7.98) is used.

Numerical verification for DCB under 6.5 m s^{-1} loading rate

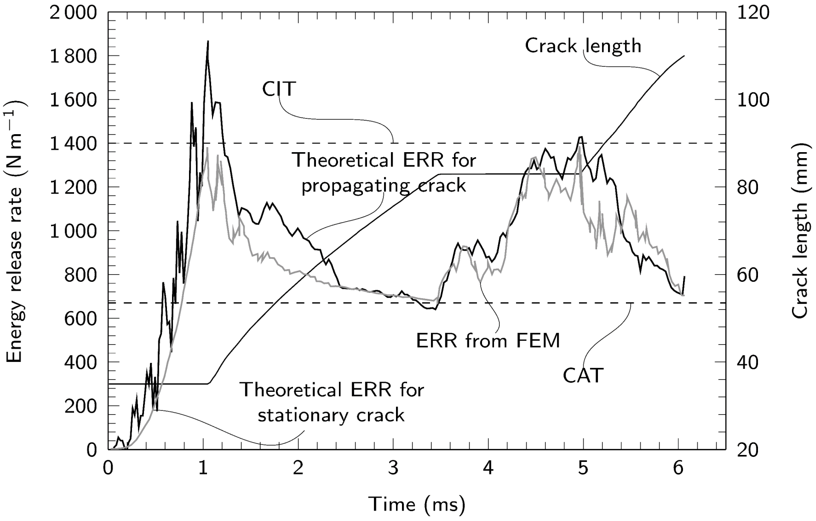

Figure 7.12 Evolution of dynamic ERR and crack length for 6.5 m s^{-1} loading rate based on FEM results for crack-propagation speed using analytical solution for elastic foundation

Figure 7.12 shows an excellent agreement of the dynamic ERR with the analytical solutions for the elastic foundation and numerical results both for the stationary and propagating cracks, although at the crack initiation the analytical solution predicts a higher dynamic ERR compared to that in the numerical results, which is due to isotropic material properties in the analytical model and anisotropic material properties of the FEM model, which makes the FEM model less stiff.

Numerical verification for DCB under 10 m s^{-1} loading rate

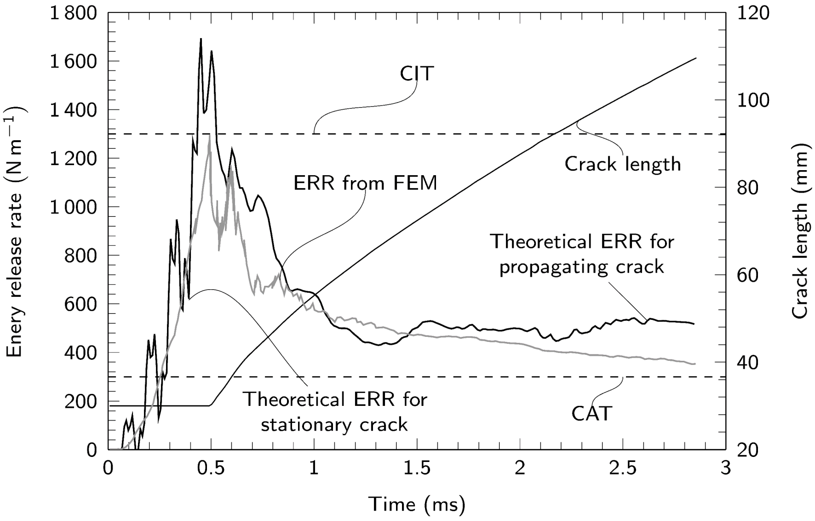

Figure 7.13 Evolution of dynamic ERR and crack length for 10 m s^{-1} loading rate based on FEM results of crack-propagation speed using analytical solution for elastic foundation

Figure 7.13 shows the numerical verification for 10 m s^{-1} loading rate. The dynamic ERR obtained with the analytical theory developed in this chapter for stationary and propagating crack is in a good agreement with the results from the FEM simulation in [22].

Generally, the analytical solution shows an excellent ability to capture the crack behaviours such as propagation, arrest and re-initiation. Another important aspect of this excellent agreement is that it shows that the stiffness of elastic foundation does not depend on the rate, i.e. it is rate-independent, in the contrast to the compensation method with Δ (see Section 6.6), which is rate-dependent (see Table 6.2).

7.6 Relation between foundation stiffness and effective crack length

For a stationary/propagating crack in DCBs with rigid interface under quasi-static loads, the analytical solution for ERR is usually developed with an effective boundary condition, that is, a fixed boundary condition at a crack tip. To compensate the crack-tip rotation, the effective crack length $a_{\mathrm{eff}} = a + \Delta$ is used by including an additional crack length Δ to compensate for this crack-tip rotation, which is determined with the MCC method (see Section 5.5.1). This method also applies to stationary crack under dynamic loads (see Section 5.5.2).

In this chapter, the elastic foundation is introduced to allow the crack tip to rotate and actual crack length is employed to determine the dynamic ERR rather than using the effective crack length with compensation. Note that these two approaches – one with effective crack length and the other with elastic foundation – are supposed to provide the same results for the dynamic ERR for a stationary crack, and, therefore, the dynamic ERR in Eq. (5.32) or (5.37) equals to two-fold of Eq. (7.92) (due to symmetry). Therefore, the respective ERR components should have the same value; for instance, those due to the strain energy of the quasi-static motion (i.e. the first term in Eq. (5.32) or (5.37) and two-fold of the first term in Eq. (7.92)) are equal, giving

$$\frac{9EIv^2t^2}{ba_{\mathrm{eff}}^4}=\frac{9EIv^2t^2f_{\mathrm{st}}^{\mathrm{U}}}{ba^4}, \tag{7.100}$$

where $f_{\mathrm{st}}^{\mathrm{U}}$ is given in Eq. (7.80) with $\gamma=\sqrt[4]{k/(4EI)}$. Solving Eq. (7.100), the additional crack length Δ to compensate for crack-tip rotation is

$$\Delta=a_{\mathrm{eff}}-a=\frac{1}{\gamma}\sqrt[4]{\frac{\left(2a^3\gamma^3+6a^2\gamma^2+6a\gamma+3\right)^2}{4\left(a\gamma+1\right)^2}}-a. \tag{7.101}$$

Eq. (7.101) provides a convenient relation between the additional crack length for crack-tip rotation Δ and the elastic foundation stiffness *k*. It also provides a new method to determine the addition crack length Δ providing the foundation stiffness is known; this is always the case with adhesively bonded DCBs. But note that this relation can be applicable to a stationary/propagating crack under quasi-static loads and a stationary crack under dynamic loads; it cannot be used for a propagating crack under dynamic loads, where Δ is shown to be rate-dependent (see Section 6.6), whereas the stiffness of elastic foundation *k* is rate-independent (see Section 7.5).

The FEM verification cases for symmetric DCBs in Section 5.5.2 with the effective crack length and in Section 7.3.1 with the elastic foundation share the same geometry, material properties and loading conditions. Using the MCC method, the additional crack length compensating for crack-tip rotation Δ is 1.34 mm; using the elastic foundation, its stiffness is found to be 0.5*E*, with Eq. (7.101) giving the additional crack length Δ = 1.52 mm. These two values for Δ are used hereby to generate ERRs again as shown in Figure 7.14, and the difference between these two ERRs for two different values for Δ is not significant. But the value $\Delta = 1.52$ mm gives a more accurate result than $\Delta = 1.34$ mm in terms of the frequency compared to the FEM data.

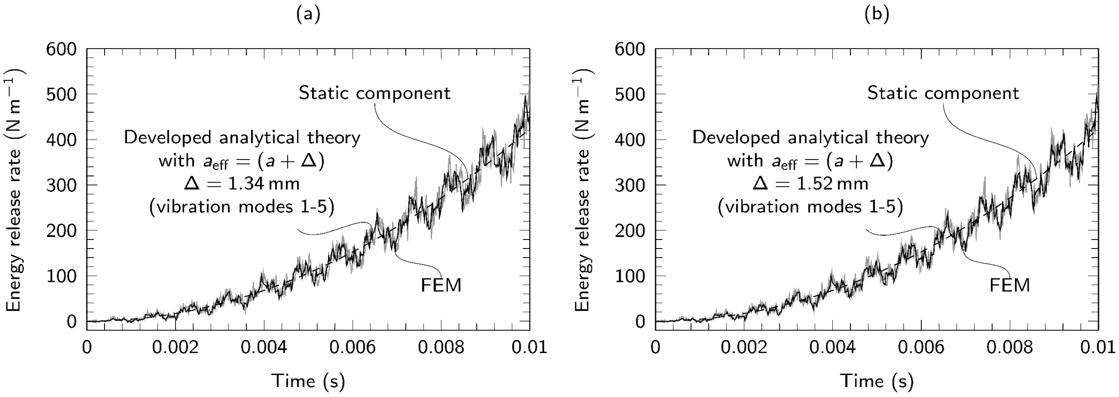

Figure 7.14 Dynamic ERR using effective crack length: (a) MCC method; (b) elastic foundation solution

Another instance demonstrating the relationship between the foundation stiffness k and the additional crack length to compensate for crack-tip rotation Δ in Eq. (7.101) is the DCB test case of the PEEK/carbon-fibre composite under quasi-static loads from [19]. As reported based on the MCC method, the additional crack length $\Delta = 3.6$ mm (see Table 6.2). For this case, the foundation stiffness is $k = 1.18$ GPa (see Section 7.5 for determination of the foundation stiffness), which, according to Eq. (7.101), gives $\Delta = 3.31$ mm.

7.7 Conclusion

In this chapter, the analysis of dynamic fracture at the elastic interface is developed by introducing an elastic foundation to the established analytical framework for dynamic interfacial fracture. The dynamic ERR of a stationary crack at the interface between a partially supported vibrating beam and an elastic foundation with time-dependent displacement applied to the beam's free end is derived, which allows the relationship between the dynamic effect and the foundation stiffness to be studied. Both analytical theories for stationary and propagating cracks were developed based on the established analytical framework developed in Chapters 5 and 6.

For the stationary crack, a series of verification studies were carried out using the FEM for a stationary crack on an elastic foundation. For rigid interfaces, the interface stiffness in the developed theory needs to be of the same order as the Young's modulus of the beam material for a DCB, an interface stiffness $k = 0.5E$ in the developed theory provides the best agreement; for a thin layer on a thick substrate, it is also $k = 0.5E$. With these values of the interface stiffness, an excellent agreement is achieved between the theory and the FEM for a rigid interface considering the overall magnitude of the ERR and the frequencies, phases and amplitudes of oscillation. Furthermore, in the case of a thin layer on a thick substrate, resulting in a mixed-mode fracture, the quasi-static partition theory in [170] is shown to be applicable under dynamic loading to partition the total ERR G into its components, G_{I} and G_{II}. For non-rigid elastic interfaces, the developed theory is only applicable for relatively high levels of the foundation stiffness, that is, the following conditions must be satisfied: $4\alpha_i^4 = k/EI - \beta_i^4 > 0$ and $\gamma L \gtrapprox 3$. Under these conditions, there is also an excellent agreement between the theory and the FEM considering the overall magnitude of ERR and the frequencies, phases and amplitudes of oscillation.

For the propagating crack on the elastic foundation, based on the analytical solution for the stationary crack on the elastic foundation and the same theoretical consideration of the analytical solution for the propagating crack in Chapter 6, the dynamic ERR for the propagating crack at the elastic interface is obtained. This analytical solution is verified against the numerical results showing an excellent agreement. But the accurate estimation of the foundation stiffness is important, especially for composite materials, with their interlaminar stiffness highly dependent on the transverse modulus. The advantage of this theoretical solution with the elastic foundation over the analytical theory for the effective boundary condition with compensation for crack-tip rotation in Chapter 6 is that the foundation stiffness is rate-independent, in contrast to the rate-dependent Δ. Therefore, it is deemed to be able to capture the local crack behaviour rather than the overall average crack behaviour in the compensation method.

The developed analytical solutions can be readily applied to study various engineering problems, for example, to determine the dynamic fracture toughness of layered materials, adhesive and welding bonds in DCB tests, as well as to characterise the fracture behaviour of engineering structures under dynamic loads. Furthermore, the partially supported beam's elastic foundation is particularly relevant for the study of crack process zones, which usually must be studied with the FEM and the CZM.

Chapter 8: Dynamic mode-II interfacial fracture

8.1 Introduction

Laminated composite materials are widely used in aerospace, automotive and naval applications to save weight. Their weak transverse property, however, make them susceptible to damage from transverse loading such as impact, which causes delamination and significant weakening of structural strength. Impact-induced delamination tends to be mode-II-dominant [171], and so it is important to understand the dynamic mode-II fracture behaviour of structures in addition to the corresponding loading rate-dependent fracture toughness of the material.

As pointed out in a recent review paper [89], which also provides a broad review of dynamic mode-II delamination, there is therefore still a clear need for closed-form analytical solutions to study the dynamic mode-II fracture behaviours. Under rapidly applied loads, the arms of the fundamental engineering structures for studying dynamic mode-II fracture, such as ELS and ENF specimens, slide back and forth, generating the oscillating relative displacement and ERR, which conventional analytical solutions do not capture (Section 4.2.2). There is also a disagreement among various experimental studies concerning the rate effects of dynamic mode-II fracture toughness: positive rate effects in [85][172][173], negative in [18][86] and insignificant in [88][174][175][176]. This disagreement might be explained by structural vibration, not considered in the data reduction.

Chapters 3 to 5 show the capability of structural dynamics (vibration and wave propagation) to accurately predict the dynamic ERR in *mode-I* dynamic fracture. In this chapter, structural dynamics and vibration are used to model the dynamic ELS test and to derive the dynamic *mode-II* ERR. It is demonstrated that this is not just a straightforward application of the existing analytical framework developed in previous chapters, but requires additional novel ideas and interpretation, including the handling of contact in the modelling; the representation of the dynamic effect in terms of a *dynamic factor* and a *spatial factor* to facilitate understanding; and the insight regarding dominant vibration modes.

8.2 Theoretical development

In this section, the dynamic mode-II ERR of an ELS specimen is derived analytically considering beam dynamics and structural vibration. Figure 8.1 shows such an ELS specimen in its initial undeformed state, with three beam sections, ①, ② and ③. A time-dependent downwards displacement $w_0(t) = vt$ is applied to free end of beam section ②, where v is a constant displacement rate. The length of beam section ① (the intact region) is L, while beam sections ② and ③ are above and below, respectively, the crack with length a; the total length of the ELS specimen is L_0. In the conventional ELS specimen [14], beam sections ② and ③ have the same thickness h. The x axis is positive to the right, with the crack tip located at $x = L$. The transverse deflections of beam sections ①, ② and ③ are in the x-z plane and denoted $w_1(x, t)$, $w_2(x, t)$ and $w_3(x, t)$, respectively.

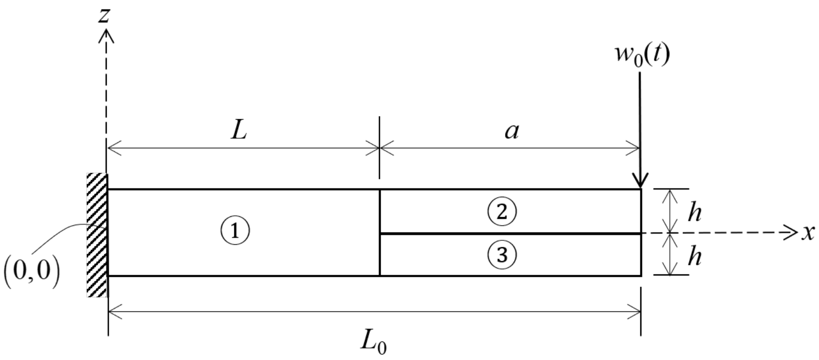

Figure 8.1 Configuration of ELS specimen and prescribed coordinates

As beam section ② deflects downwards according to the applied $w_0(t)$, interfacial contact between beam sections ② and ③ also drives beam section ③ downwards. It is assumed that beam section ③ has the same vertical deflection as beam section ②, and so a pure mode-II fracture is produced. Under the further assumptions of $h << L$ and $h << a$, the Euler-Bernoulli beam assumption is appropriate to derive the respective deflections and, thus, the ERR.

Since the local and dispersion-corrected global approaches are equivalent as demonstrated in Section 5.3.3.2, the local approach using crack-tip bending moment is applied here to determine the dynamic ERR as

$$G=\frac{1}{2bE}\left[\frac{M_2^2(L,t)}{I_2}+\frac{M_3^2(L,t)}{I_3}-\frac{M_1^2(L,t)}{I_1}\right], \tag{8.1}$$

where $M_1(L, t)$, $M_2(L, t)$ and $M_3(L, t)$ are the crack-tip bending moments of beam sections ①, ② and ③, respectively, and $M_1(L,t)=EI_1w_1^{(2)}(L,t)$, $M_2(L,t)=EI_2w_2^{(2)}(L,t)$ and $M_3(L,t)=EI_3w_3^{(2)}(L,t)$ with I_1, I_2 and I_3 being the corresponding second moment of inertia of these sections.

8.2.1 Dynamic response of ELS specimen

Under the applied constant-rate displacement of $w_0(t) = vt$, the dynamic transverse deflections of beam sections ①, ② and ③ take the following forms by introducing shifting functions:

$$w_1(x,t)=w_{1\text{fv}}(x,t)+F_1(x)vt, \tag{8.2}$$

$$w_2(x,t)=w_{2\text{fv}}(x,t)+F_2(x)vt, \tag{8.3}$$

$$w_3(x,t)=w_{3\text{fv}}(x,t)+F_3(x)vt. \tag{8.4}$$

In Eqs. (8.2) to (8.4), $w_{1\text{fv}}(x, t)$, $w_{2\text{fv}}(x, t)$ and $w_{3\text{fv}}(x, t)$ are the free-vibration components of three beam sections ①, ②, ③, respectively; $F_1(x)$, $F_2(x)$ and $F_3(x)$ are the respective shifting functions. The effect of the shifting functions is to distribute the applied displacement of $w_0(t) = vt$ along the three beam sections. Note that in order to satisfy the assumed contact condition that beam sections ② and ③ have the same deflection, that is, $w_2(x, t) = w_3(x, t)$, both their free-vibration components and their shifting functions must be equal, that is, $w_{2\text{fv}}(x, t) = w_{3\text{fv}}(x, t)$ and $F_2(x) = F_3(x)$ by enforcing homogeneous conditions. Therefore, the deflection and shifting function of beam section ③ are replaced by those of beam section ②, which simplifies and facilitates the derivation process.

Combining equation of motion in Eq. (2.6) and deflection assumption in Eq. (8.2) and enforcing homogeneous conditions, the governing equations for the free-vibration components $w_{1\text{fv}}(x, t)$ and the shifting function $F_1(x)$ for beam section ① are derived:

$$EI_1w_{1\text{fv}}^{(4)}(x,t)+\rho A_1\ddot{w}_{1\text{fv}}(x,t)=0, \tag{8.5}$$

$$F_1^{(4)}(x)=0. \tag{8.6}$$

Similarly, the governing equations for the free-vibration component $w_{2\text{fv}}\ (x, t)$ and the shifting function $F_2\ (x)$ for beam section ②, by combining Eqs. (2.6) and (8.3), are

$$EI_2 w_{2\text{fv}}^{(4)}\left(x,t\right)+\rho A_2 \ddot{w}_{2\text{fv}}\left(x,t\right)=0, \tag{8.7}$$

$$F_2^{(4)}\left(x\right)=0. \tag{8.8}$$

For beam section ①, the boundary conditions for the total deflection $w_1\ (x, t)$ are $w_1\ (0, t) = 0$ and $w_1^{(1)}\left(0,t\right)=0$. By using these boundary conditions for $w_1\ (x, t)$ in Eq. (8.2), and enforcing homogeneous conditions, the boundary conditions for the free-vibration component $w_{1\text{fv}}\ (x, t)$ and shifting function $F_1\ (x)$ are obtained in Table 8.1.

Table 8.1 Boundary conditions for beam section ①

Boundary	Total deflection $w_1\left(x,t\right)$	Free-vibration component $w_{1\text{fv}}\left(x,t\right)$	Shifting function $F_1\left(x\right)$
$x=0$	$w_1\left(0,t\right)=0$	$w_{1\text{fv}}\left(0,t\right)=0$	$F_1\left(0\right)=0$
	$w_1^{(1)}\left(0,t\right)=0$	$w_{1\text{fv}}^{(1)}\left(0,t\right)=0$	$F_1^{(1)}\left(0\right)=0$

For the beam section ② with boundary condition $w_2\ (L + a, t) = vt$ and $w_2^{(2)}\left(L+a,t\right)=0$, following the similar approach, using Eq. (8.3), the corresponding boundary conditions for the free-vibration component $w_{2\text{fv}}\ (x, t)$ and shifting function $F_2\ (x)$ are obtained in Table 8.2.

Table 8.2 Boundary conditions for beam section ②

Boundary	Total deflection $w_2\left(x,t\right)$	Free-vibration component $w_{2\text{fv}}\left(x,t\right)$	Shifting function $F_2\left(x\right)$
$x=L+a$	$w_2\left(L+a,t\right)=vt$	$w_{2\text{fv}}\left(L+a,t\right)=0$	$F_2\left(L+a\right)=1$
	$w_2^{(2)}\left(L+a,t\right)=0$	$w_{2\text{fv}}^{(2)}\left(L+a,t\right)=0$	$F_2^{(2)}\left(L+a\right)=0$

Considering the continuity condition at the crack tip $x = L$, the beam section ① shares the same deflection and slope with beam sections ② and ③, but its bending moment and shear force are the sums of those of beam sections ② and ③, respectively. Therefore, the continuity condition for the corresponding free-vibration components and the shifting functions can be derived by enforcing homogeneous condition and given in Table 8.3.

Table 8.3 Continuity conditions for total deflection and its components

Continuity	Total deflection	Free-vibration component	Shifting function
Deflection	$w_1(L,t) = w_2(L,t)$	$w_{1\text{fv}}(L,t) = w_{2\text{fv}}(L,t)$	$F_1(L) = F_2(L)$
Slope	$w_1^{(1)}(L,t) = w_2^{(1)}(L,t)$	$w_{1\text{fv}}^{(1)}(L,t) = w_{2\text{fv}}^{(1)}(L,t)$	$F_1^{(1)}(L) = F_2^{(1)}(L)$
Bending moment	$EI_1 w_1^{(2)}(L,t)$ $= 2EI_2 w_2^{(2)}(L,t)$	$EI_1 w_{1\text{fv}}^{(2)}(L,t)$ $= 2EI_2 w_{2\text{fv}}^{(2)}(L,t)$	$EI_1 F_1^{(1)}(L)$ $= 2EI_2 F_2^{(2)}(L)$
Shear force	$EI_1 w_1^{(3)}(L,t)$ $= 2EI_2 w_2^{(3)}(L,t)$	$EI_1 w_{1\text{fv}}^{(3)}(L,t)$ $= 2EI_2 w_{2\text{fv}}^{(3)}(L,t)$	$EI_1 F_1^{(3)}(L)$ $= 2EI_2 F_2^{(3)}(L)$

8.2.1.1 Solution for free-vibration components and orthogonality

By the method of separation of variables, the solutions for the free-vibration components $w_{1\text{fv}}(x, t)$ and $w_{2\text{fv}}(x, t)$ in Eqs. (8.5) and (8.7) are

$$w_{1\text{fv}}(x,t) = \sum_{i=1}^{\infty} W_{1i}(x) T_i(t), \tag{8.9}$$

$$w_{2\text{fv}}(x,t) = \sum_{i=1}^{\infty} W_{2i}(x) T_i(t), \tag{8.10}$$

where $W_{1i}(x)$ and $W_{2i}(x)$ are the ith normal modes for beam sections ① and ②; and $T_i(t)$ is the modal displacement.

Combining Eqs. (8.5) and (8.9) for beam section ① and Eqs. (8.7) and (8.10) for beam section ②, and introducing natural frequency, the following governing equations for the normal modes and the modal displacement are derived:

$$W_{1i}^{(4)}\left(x\right)-\omega_i^2\frac{\rho A_1}{EI_1}W_{1i}\left(x\right)=0, \tag{8.11}$$

$$W_{2i}^{(4)}\left(x\right)-\omega_i^2\frac{\rho A_2}{EI_2}W_{2i}\left(x\right)=0, \tag{8.12}$$

$$\ddot{T}_i\left(t\right)+\omega_i^2T_i\left(t\right)=0. \tag{8.13}$$

The corresponding boundary conditions for the normal modes $W_{1i}(x)$ and $W_{2i}(x)$ in Table 8.4 are derived from the boundary conditions of their free-vibration components in Table 8.1 and 8.2.

Table 8.4 Boundary conditions for normal modes

Boundary	Normal modes	
	$W_{1i}\left(x\right)$	$W_{2i}\left(x\right)$
$x=0$	$W_{1i}\left(0\right)=0$	-
	$W_{1i}^{(1)}\left(0\right)=0$	-
$x=L+a$	-	$W_{2i}\left(L+a\right)=0$
	-	$W_{2i}^{(2)}\left(L+a\right)=0$

The continuity conditions at the crack tip $x = L$ are listed in Table 8.5.

Table 8.5 Continuity conditions for normal modes

Continuity	Normal modes
Deflection	$W_{1i}\left(L\right)=W_{2i}\left(L\right)$
Slope	$W_{1i}^{(1)}\left(L\right)=W_{2i}^{(1)}\left(L\right)$
Bending moment	$EI_1W_{1i}^{(2)}\left(L\right)=2EI_2W_{2i}^{(2)}\left(L\right)$
Shear force	$EI_1W_{1i}^{(3)}\left(L\right)=2EI_2W_{2i}^{(3)}\left(L\right)$

Now consider the orthogonality conditions. For the beam section ①, multiplying Eq. (8.11) by $W_{1j}(x)$, integrating over the beam section length (0, L) twice by parts, and applying the boundary conditions for normal modes in Table 8.4, gives

$$\begin{aligned}&\omega_i^2\int_0^L \frac{\rho A_1}{EI_1}W_{1i}\left(x\right)W_{1j}\left(x\right)dx\\&=W_{1j}\left(L\right)W_{1i}^{(3)}\left(L\right)-W_{1j}^{(1)}\left(L\right)W_{1i}^{(2)}\left(L\right)+\int_0^L W_{1i}^{(2)}\left(x\right)W_{1j}^{(2)}\left(x\right)dx.\end{aligned} \tag{8.14}$$

For beam section ②, multiplying Eq. (8.12) by $W_{2j}(x)$, integrating over the beam section length (L, $L + a$) twice by parts, and applying the boundary conditions for normal modes in Table 8.4, gives

$$\begin{aligned}&\omega_i^2\int_L^{L+a} \frac{\rho A_2}{EI_2}W_{2i}\left(x\right)W_{2j}\left(x\right)dx\\&=-W_{2j}\left(L\right)W_{2i}^{(3)}\left(L\right)+W_{2j}^{(1)}\left(L\right)W_{2i}^{(2)}\left(L\right)+\int_L^{L+a} W_{2i}^{(2)}\left(x\right)W_{2j}^{(2)}\left(x\right)dx.\end{aligned} \tag{8.15}$$

Multiplying Eq. (8.14) by 4 and summing it with Eq. (8.15), applying continuity conditions at the crack tip in Table 8.5, and then subtracting it from itself with the subscripts i and j exchanged, gives

$$\left(\omega_i^2-\omega_j^2\right)\left[4\int_0^L \frac{\rho A_1}{EI_1}W_{1i}\left(x\right)W_{1j}\left(x\right)dx+\int_L^{L+a}\frac{\rho A_2}{EI_2}W_{2i}\left(x\right)W_{2j}\left(x\right)dx\right]=0. \tag{8.16}$$

Since the natural frequency of the beam system is unique, that is, $\omega_i \neq \omega_j$ for $i \neq j$, therefore

$$4\int_0^L \frac{\rho A_1}{EI_1}W_{1i}\left(x\right)W_{1j}\left(x\right)dx+\int_L^{L+a}\frac{\rho A_2}{EI_2}W_{2i}\left(x\right)W_{2j}\left(x\right)dx=0. \tag{8.17}$$

Now, including the case of $i = j$ and normalising Eq. (8.17), finally the orthogonality of the beam system for ELS specimen is written as

$$4\int_0^L \frac{\rho A_1}{EI_1}W_{1i}\left(x\right)W_{1j}\left(x\right)dx+\int_L^{L+a}\frac{\rho A_2}{EI_2}W_{2i}\left(x\right)W_{2j}\left(x\right)dx=\delta_{ij}. \tag{8.18}$$

8.2.1.2 Solutions for normal modes and frequency equation

For the ith normal mode of the free-vibration component of beam section ①, $W_{1i}(x)$ in Eq. (8.11), the general solution with the available boundary conditions in Table 8.4 applied is

$$W_{1i}\left(x\right)=C_{i1}\left[\cosh\left(\alpha_i x\right)-\cos\left(\alpha_i x\right)\right]+C_{i2}\left[\sinh\left(\alpha_i x\right)-\sin\left(\alpha_i x\right)\right], \qquad (8.19)$$

where $\alpha_i^4=\omega_i^2\,\rho A_1/\left(EI_1\right)$, C_{i1} and C_{i2} are coefficients to be determined.

For the ith normal mode of the free-vibration component of beam section ②, W_{2i} (x) in Eq. (8.12), the general solution with the available boundary conditions in Table 8.4 applied is

$$W_{2i}\left(x\right)=C_{i3}\sinh\left[\beta_i\left(x-L-a\right)\right]+C_{i4}\sin\left[\beta_i\left(x-L-a\right)\right], \qquad (8.20)$$

where $\beta_i^4=\omega_i^2\,\rho A_2/\left(EI_2\right)$, C_{i3} and C_{i4} are coefficients to be determined.

The frequency equation is derived by applying the continuity conditions at the crack tip presented in Table 8.5 to these general solutions for W_{1i} (x) and W_{2i} (x), which gives

$$\begin{bmatrix} \left[\cosh\left(\alpha_i L\right)-\cos\left(\alpha_i L\right)\right] & \left[\sinh\left(\alpha_i L\right)-\sin\left(\alpha_i L\right)\right] & \sinh\left(\beta_i a\right) & \sin\left(\beta_i a\right) \\ \alpha_i\left[\sinh\left(\alpha_i L\right)+\sin\left(\alpha_i L\right)\right] & \alpha_i\left[\cosh\left(\alpha_i L\right)-\cos\left(\alpha_i L\right)\right] & -\beta_i\cosh\left(\beta_i a\right) & -\beta_i\cos\left(\beta_i a\right) \\ 4\alpha_i^2\left[\cosh\left(\alpha_i L\right)+\cos\left(\alpha_i L\right)\right] & 4\alpha_i^2\left[\sinh\left(\alpha_i L\right)+\sin\left(\alpha_i L\right)\right] & \beta_i^2\sinh\left(\beta_i a\right) & -\beta_i^2\sin\left(\beta_i a\right) \\ 4\alpha_i^3\left[\sinh\left(\alpha_i L\right)-\sin\left(\alpha_i L\right)\right] & 4\alpha_i^3\left[\cosh\left(\alpha_i L\right)+\cos\left(\alpha_i L\right)\right] & -\beta_i^3\cosh\left(\beta_i a\right) & \beta_i^3\cos\left(\beta_i a\right) \end{bmatrix}\begin{pmatrix} C_{i1} \\ C_{i2} \\ C_{i3} \\ C_{i4} \end{pmatrix}=\begin{pmatrix} 0 \\ 0 \\ 0 \\ 0 \end{pmatrix}. \qquad (8.21)$$

For this homogeneous system of linear equations to have nonzero solutions, the determinant of the coefficient matrix must be zero, and this gives the frequency equation. Let D_i be the determinant of the coefficient matrix of Eq. (8.21). From $D_i = 0$, the wavenumber α_i and β_i can be determined and thus the natural frequency ω_i via $\omega_i=\alpha_i^2\sqrt{EI_1/\left(\rho A_1\right)}$ or $\omega_i=\beta_i^2\sqrt{EI_2/\left(\rho A_2\right)}$.

By Gaussian elimination, the coefficients C_{i1}, C_{i2} and C_{i3} can be expressed linearly in terms of C_{i4}. Then, by substituting the general solutions in Eqs. (8.19) and (8.20) into the orthogonality condition in Eq. (8.18), C_{i4} can be determined, and, therefore, C_{i1}, C_{i2} and C_{i3} also.

8.2.1.3 Solution for time-dependent modal displacement

The general solution for the time-dependent displacement of ith vibration mode in Eq. (8.13) is

$$T_i\left(t\right)=\frac{\dot{T}_i\left(0\right)}{\omega_i}\sin\left(\omega_i t\right)+T_i\left(0\right)\cos\left(\omega_i t\right), \qquad (8.22)$$

where $T_i(0)$ and $\dot{T}_i(0)$ are the initial values of the modal displacement and modal velocity of the *i*th vibration mode.

The initial modal displacement $T_i(0)$ can be determined by the following procedure: Substitute Eq. (8.22) into Eqs. (8.9) and (8.10), and then combining Eqs. (8.2) and (8.3) to obtain the following deflections for beam sections ① and ②, respectively:

$$w_1(x,t)=\sum_{i=1}^{\infty}W_{1i}(x)\left[\frac{\dot{T}_i(0)}{\omega_i}\sin\omega_i t+T_i(0)\cos\omega_i t\right]+F_1(x)vt, \tag{8.23}$$

$$w_2(x,t)=\sum_{i=1}^{\infty}W_{2i}(x)\left[\frac{\dot{T}_i(0)}{\omega_i}\sin\omega_i t+T_i(0)\cos\omega_i t\right]+F_2(x)vt. \tag{8.24}$$

The initial displacements of beam sections ① and ② are therefore $w_1(x,0)=\sum_{i=1}^{\infty}W_{1i}(x)T_i(0)$ and $w_2(x,0)=\sum_{i=1}^{\infty}W_{2i}(x)T_i(0)$, respectively. Multiply $w_1(x, 0)$ by $4\rho A_1 W_{1j}(x)/(EI_1)$ and integrate over the beam section length $(0, L)$; multiply $w_2(x,0)$ by $\rho A_2 W_{2j}(x)/(EI_2)$ and integrate over the beam section length $(L, L + a)$; sum these two integrals to have

$$\begin{aligned}&\int_0^L 4\frac{\rho A_1}{EI_1}W_{1j}(x)w_1(x,0)dx+\int_L^{L+a}\frac{\rho A_2}{EI_2}W_{2j}(x)w_2(x,0)dx\\&=\int_0^L 4\frac{\rho A_1}{EI_1}W_{1j}(x)\sum_{i=1}^{\infty}W_{1i}(x)T_i(0)dx+\int_L^{L+a}\frac{\rho A_2}{EI_2}W_{2j}(x)\sum_{i=1}^{\infty}W_{2i}(x)T_i(0)dx.\end{aligned} \tag{8.25}$$

Finally, by applying the orthogonality condition in Eq. (8.18) together with the initial conditions that $w_1(x, 0) = 0$ and $w_2(x, 0) = 0$, the *i*th modal displacement is found to be zero, that is, $T_i(0) = 0$. Following a similar procedure, the initial value of the *i*th modal velocity is found to be

$$\dot{T}_i(0)=-vH_i, \tag{8.26}$$

where

$$H_i=\int_0^L 4\frac{\rho A_1}{EI_1}W_{1i}(x)F_1(x)dx+\int_L^{L+a}\frac{\rho A_2}{EI_2}W_{2i}(x)F_2(x)dx. \tag{8.27}$$

H_i represents the coupling of the free vibration and the applied constant loading velocity *v*, that is, how the free vibration of the beam responds to the applied excitation.

But note that H_i is independent of applied velocity v, and thus this is an inherent property representing the beam configuration of ELS specimen.

8.2.1.4 Solutions for shifting functions

The shifting functions are obtained by solving the ordinary differential equations in Eqs. (8.6) and (8.8), together with the available boundary conditions in Table 8.1 and Table 8.2 as well as the continuity conditions Table 8.3 at the crack tip.

The general solutions for $F_1(x)$ and $F_2(x)$ with available boundary conditions applied are

$$F_1(x) = P_1 x^3 + P_2 x^2 , \tag{8.28}$$

$$F_2(x) = P_3 (x - L - a)^3 + P_4 (x - L - a) + 1, \tag{8.29}$$

where P_1, P_2, P_3 and P_4 are coefficients to be determined.

By applying the four continuity condition at the crack tip, $x = L$, listed in Table 8.3, to the general solutions for $F_1(x)$ and $F_2(x)$ in Eqs. (8.28) and (8.29), the following system of equations is obtained.

$$\begin{bmatrix} L^3 & L^2 & a^3 & a \\ 3L^2 & 2L & -3a^2 & -1 \\ 24L & 8 & 6a & 0 \\ 24 & 0 & -6 & 0 \end{bmatrix} \begin{pmatrix} P_1 \\ P_2 \\ P_3 \\ P_4 \end{pmatrix} = \begin{pmatrix} 1 \\ 0 \\ 0 \\ 0 \end{pmatrix}. \tag{8.30}$$

Solving this system of equations gives the coefficients P_1, P_2, P_3 and P_4 as

$$P_1 = -\frac{1}{2\left(L^3 + 3L^2 a + 3La^2 + 4a^3\right)}, \tag{8.31}$$

$$P_2 = \frac{3(L + a)}{2\left(L^3 + 3L^2 a + 3La^2 + 4a^3\right)}, \tag{8.32}$$

$$P_3 = -\frac{2}{\left(L^3 + 3L^2 a + 3La^2 + 4a^3\right)}, \tag{8.33}$$

$$P_4 = \frac{3\left(L^2 + 2La + 4a^2\right)}{2\left(L^3 + 3L^2 a + 3La^2 + 4a^3\right)}. \tag{8.34}$$

The shifting function solutions, given in Eqs. (8.28) and (8.29) together with their coefficient solutions from Eqs. (8.31) to (8.34) show that they are independent of applied velocity v. This indicates that the shifting functions, which represent the distribution of externally applied velocity along the related beam sections, are inherent properties of the beam configurations.

8.2.1.5 Total deflections

The combined results from Sections 8.2.1.1 to 8.2.1.4 give the total deflections for beam sections ① and ② in Eqs. (8.2) and (8.3) as

$$\begin{aligned} w_1(x,t) &= w_{1\text{fv}}(x,t) + F_1(x)vt \\ &= v\left\{-\sum_{i=1}^{\infty}\left[\frac{H_i}{\omega_i}W_{1i}(x)\sin(\omega_i t)\right] + F_1(x)t\right\}, \end{aligned} \tag{8.35}$$

$$\begin{aligned} w_2(x,t) &= w_{2\text{fv}}(x,t) + F_2(x)vt \\ &= v\left\{-\sum_{i=1}^{\infty}\left[\frac{H_i}{\omega_i}W_{2i}(x)\sin(\omega_i t)\right] + F_2(x)t\right\}. \end{aligned} \tag{8.36}$$

It is seen that the beam system's dynamic response is proportional to the externally applied velocity *v*. The terms contained in the braces are determined by the ELS configuration alone.

H_i in Eq. (8.27) can be further simplified by partially integrating and combining Eqs. (8.6), (8.8), (8.11) and (8.12) with boundary conditions in Table 8.4 and continuity conditions in Table 8.5 to

$$H_i = \frac{2}{\omega_i^2}\beta_i^3\left(C_{i3} - C_{i4}\right). \tag{8.37}$$

8.2.2 Dynamic energy release rate for ELS specimen

By combining Eqs. (8.1), (8.35), (8.36) and (8.37), the total dynamic ERR for the ELS specimen shown in Figure 8.1 is obtained as

$$\begin{aligned} G = &\frac{108EI_2a^2v^2t^2}{b\left(L^3+3L^2a+3La^2+4a^3\right)^2} \\ &-\frac{18EI_2av^2t}{b\left(L^3+3L^2a+3La^2+4a^3\right)}\sum_{i=1}^{\infty}\Lambda_i\sin(\omega_i t) + \frac{3EI_2v^2}{4b}\left[\sum_{i=1}^{\infty}\Lambda_i\sin(\omega_i t)\right]^2, \end{aligned} \tag{8.38}$$

where $\Lambda_i = \left(-C_{i3}\sinh\beta_i a + C_{i4}\sin\beta_i a\right)\left(C_{i3}-C_{i4}\right)\left[\rho A_2/\left(EI_2\right)\right]^{3/2}$. In Eq. (8.38), the first term is the ERR component due to the strain energy of the quasi-static motion, which has the same value of static ERR without any dynamic effect; the second term is the ERR component due to coupling between local vibration and quasi-static motion; the last term is the ERR component due to local vibration. These three terms are denoted $G_{\mathrm{st}}^{\mathrm{U}}$, $G_{\mathrm{dyn}}^{\mathrm{cp}}$ and $G_{\mathrm{dyn}}^{\mathrm{loc}}$, respectively, so that $G = G_{\mathrm{st}}^{\mathrm{U}} + G_{\mathrm{dyn}}^{\mathrm{cp}} + G_{\mathrm{dyn}}^{\mathrm{loc}}$.

It should be recognized that the total deflections in Eqs. (8.35) and (8.36) as well as the total dynamic ERR in Eq. (8.38) are vibrational solutions, and as such, assume that sufficient time has passed for all the flexural waves to form standing waves. Chapter 5 derives the dynamic ERR of a DCB employing the dispersion-corrected global approach and the local approach with vibrational solutions. It is shown that for a DCB the difference between the two approaches is essentially zero after 12 times the duration taken for the first-mode flexural wave to travel the crack length, and already very small after just five times. Following this guide from Section 5.3.3.2, the vibrational approach used here is considered justified, as verified in Section 8.3.

To establish the time required for all flexural waves to form standing waves in an ELS specimen, the phase speed of the first-mode flexural wave is considered since it travels slowest. The time needed for this wave to travel from the free end of the ELS specimen to the crack tip is $\tau_1 = a / C_{\mathrm{ap}}^1$, where $C_{\mathrm{ap}}^1 = \omega_1 / \beta_1$ is the phase speed of the first-mode flexural wave in beam section ②. Likewise, the time needed for this wave to travel from the crack tip to the fixed end is $\tau_2 = a / C_{\mathrm{Lp}}^1$, where $C_{\mathrm{Lp}}^1 = \omega_1 / \alpha_1$ is the phase speed of the first-mode flexural wave in beam section ①. Note that $C_{\mathrm{ap}}^1 / C_{\mathrm{Lp}}^1 = \alpha_1 / \beta_1 = 1/\sqrt{2}$. Therefore, the time τ_0 needed for this wave to travel from the free end to the fixed end of the ELS specimen is

$$\tau_0 = \tau_1 + \tau_2 = \frac{1}{\sqrt{\omega_1}} \sqrt[4]{\frac{3\rho}{Eh^2}} \left(\sqrt{2}a + L\right). \tag{8.39}$$

There are two limiting cases, namely, $a \to 0$ and $a \to L_0$, where $L_0 = a + L$ is the constant total length of the ELS specimen. Therefore, the time needed for the first-mode flexural wave to travel from the free end to the fixed end is in the range

$$\tau_0\left(a \to 0\right) < \tau_0 < \tau_0\left(a \to L_0\right), \tag{8.40}$$

where $\tau_0\left(a \to 0\right) = L_0 / C_{\mathrm{Lp}}^1$ and $\tau_0\left(a \to L_0\right) = L_0 / C_{\mathrm{ap}}^1 = \sqrt{2} L_0 / C_{\mathrm{Lp}}^1$. Either of these two limiting cases represents a cantilever beam under constant loading rate, which is the configuration modelled in Chapter 5 (see Figure 5.1b). Therefore, the multiple of 12 can be introduced as guided by the conclusion of Section 5.3.3.2. The minimum time for the developed dynamic ERR solution based on structural vibration to become applicable, or, equivalently, the minimum test time required to post-process experimental results by this method, is therefore

$$t_0 = 12\tau_0 = \frac{1}{\sqrt{\omega_1}}\sqrt[4]{\frac{3\rho}{Eh^2}}\left(\sqrt{2}a + L\right). \tag{8.41}$$

Therefore, the maximum velocity that can be applied in a test is w_{crit}/t_0, where w_{crit} is the critical displacement, at which crack initiates.

8.2.3 Dynamic factor

Since the ERR component due to the strain energy of quasi-static motion $G_{\mathrm{st}}^{\mathrm{U}}$ has the same value as the ERR without any dynamic effect, the total dynamic effect contribution to the ERR is

$$G_{\mathrm{dyn}} = G_{\mathrm{dyn}}^{\mathrm{cp}} + G_{\mathrm{dyn}}^{\mathrm{loc}}. \tag{8.42}$$

The ERR component due to local vibration $G_{\mathrm{dyn}}^{\mathrm{loc}}$ has a maximum value of $3EI_2v^2\left(\sum_{i=1}^{\infty}\Lambda_i\right)^2 \Big/ \left(4b\right)$, while the amplitude of the ERR component due to the coupling of vibration and quasi-static motion $G_{\mathrm{dyn}}^{\mathrm{cp}}$ increases with time t. Therefore, given sufficient time, $G_{\mathrm{dyn}}^{\mathrm{cp}}$ is more significant than $G_{\mathrm{dyn}}^{\mathrm{loc}}$, and, so, in order to better understand the dynamic effect, the total dynamic effect can be taken as $G_{\mathrm{dyn}} \approx G_{\mathrm{dyn}}^{\mathrm{cp}}$. A comparison of these ERR components for verification case in Section 8.3.1 is shown in Figure 8.2.

Note that in Figure 8.2 the ERR component due to dynamic effect in the conventional solution (Section 4.2.2.2) is also plotted (denoted by G_{dyn} in conventional solution); it is the solid horizontal line with a constant value of 6.91 N m^{-1}. This shows the limitation of the conventional approach of using only quasi-static motion to account for the total kinetic-energy contribution to the ERR. This is the reason why the dynamic effect only accounted for 1% of the measured fracture toughness value in [88] and was described as negligible. Therefore, to accurately determine the dynamic mode-II ERR of an ELS specimen, vibration must be considered.

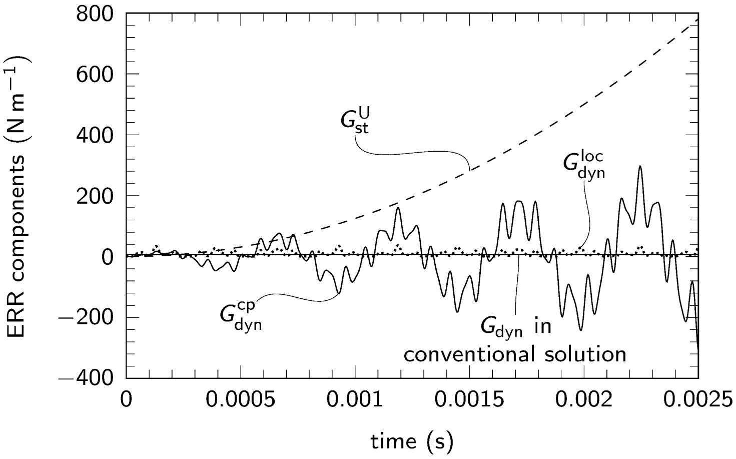

Figure 8.2 Comparison of ERR components of ELS specimen

A *total dynamic factor* for mode-II fracture can be defined as

$$\begin{aligned} f_{\mathrm{dyn}} &= \frac{G_{\mathrm{dyn}}}{G_{\mathrm{st}}^{\mathrm{U}}} \approx \frac{G_{\mathrm{dyn}}^{\mathrm{cp}}}{G_{\mathrm{st}}^{\mathrm{U}}} \\ &= -\frac{\left(L^3 + 3L^2a + 3La^2 + 4a^3\right)}{6at} \sum_{i=1}^{\infty} \Lambda_i \sin\left(\omega_i t\right). \end{aligned} \tag{8.43}$$

Note that $G_{\mathrm{dyn}}^{\mathrm{cp}}$ for the *i*th vibration mode is proportional to parameter Λ_i. Typical values of Λ_i for the verification case in Section 8.3.1 are plotted in Figure 8.3 based on the specified beam configuration and material properties. It can be seen that for the given configuration, the most significant contribution to the total dynamic ERR is from the first vibration mode, whereas the contribution to the total dynamic ERR from the second vibration mode is near zero since $\Lambda_2 \approx 0$, as discussed in Sections 8.2.4 and 8.2.5, and reflected by results presented in Figure 8.8.

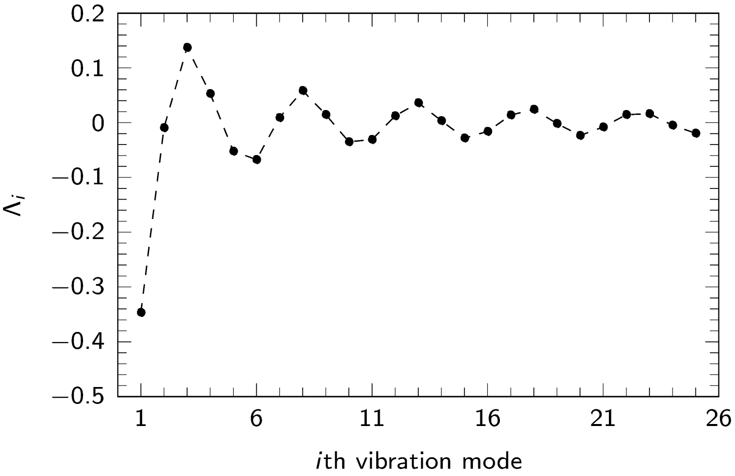

Figure 8.3 Typical value for the parameter Λ_i

From Eq. (8.43), the dynamic factor for the verification case in Section 8.3.1 is plotted in Figure 8.4 for the first vibration mode (dashed line) and the first four vibration modes (solid line). The maximum value for the dynamic factor is found in the first cycle of the first vibration mode, and then it drops dramatically. The dynamic factor with the first four vibration modes oscillates around the dynamic factor of the first vibration mode since the first vibration mode makes the most significant contribution to the total ERR. This indicates the feasibility of using only the first vibration mode to quantify the dynamic ERR for this beam configuration; however, this is not always the case as shown in Section 8.2.5. The dynamic factor based on conventional approach in Section 4.2.2.2 is also plotted in Figure 8.4 as the dotted line. It does not oscillate but decays very quickly to around zero.

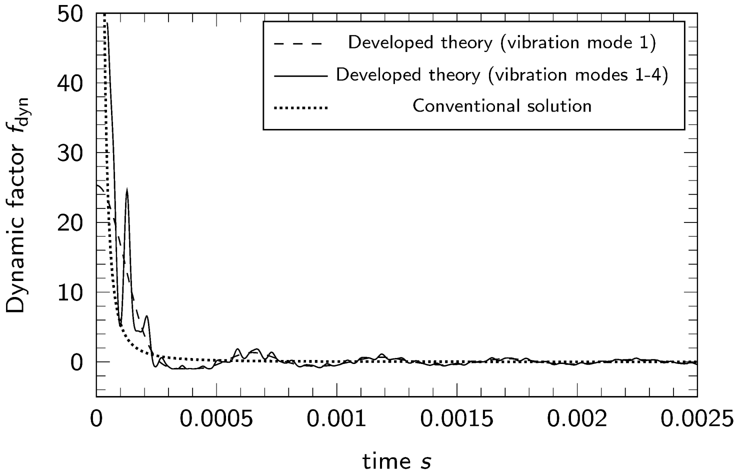

Figure 8.4 Dynamic factor for the verification case in Section 8.3.1

8.2.4 Normal modes and crack-tip loading condition

In Section 8.2.3, the dynamic factor of the *i*th vibration mode is found to be proportional to parameter Λ_i. For the value Λ_i shown in Figure 8.3 (of the verification case in Section 8.3.1), it can be seen that $\Lambda_2 \approx 0$, and accordingly, the dynamic factor of the second vibration mode $f_{\mathrm{dyn}}^{2} \approx 0$ (the superscript 2 denoting the second vibration mode). This means that the second vibration mode does not contribute to the total dynamic ERR in this case.

To understand this phenomenon, the normal mode and its slope of the first three vibration modes of the verification case in Section 8.3.1 were examined to investigate the crack-tip loading condition.

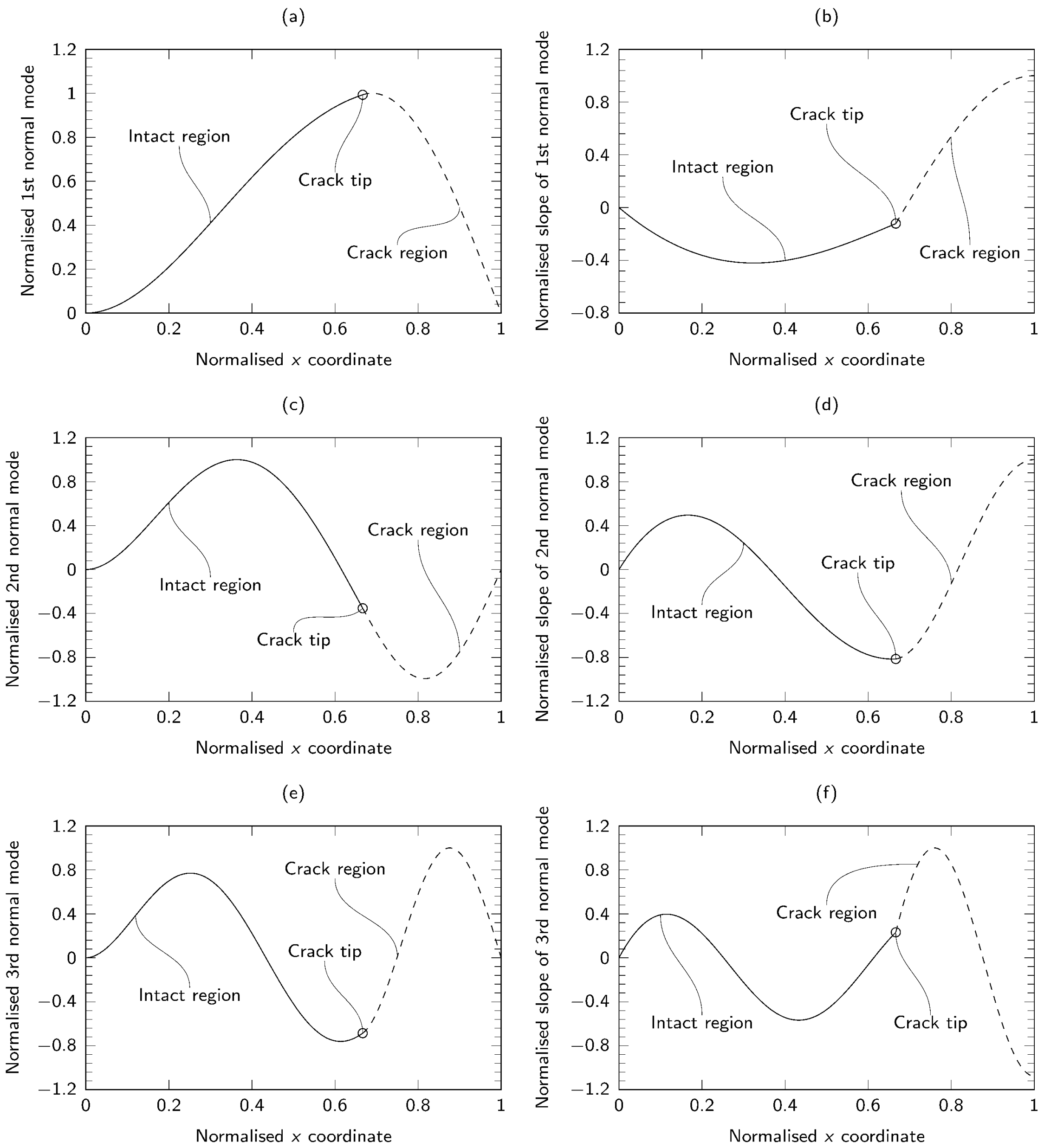

Figure 8.5 Normalised normal modes and slopes for first three vibration modes

It is apparent that the slopes of the first and third normal modes (Figure 8.5b and f) are not smooth at the crack tip (that is, there is a discontinuity of curvature), whereas it is smooth for the second normal mode (Figure 8.5d). This demonstrates that the first and third normal modes contribute to the bending moment at the crack tip and the ERR according to Eq. (8.1).

For the second normal mode, however, $W_{12}^{(2)}(L)=W_{22}^{(2)}(L)$. Since $EI_1W_{12}^{(2)}(L)=2EI_2W_{22}^{(2)}(L)$ (Table 8.5), therefore $W_{12}^{(2)}(L)=W_{22}^{(2)}(L)=0$. This means that, in this configuration, the second vibration mode does not contribute to the bending moment at the crack tip, or to the ERR.

The parameter Λ_i can therefore be interpreted as a description of the crack-tip loading condition. Note that Λ_i is a function of the ELS's configuration, and the second vibration mode does not always give $\Lambda_2 \approx 0$ for different configurations. A more general conclusion about the *i*th vibration modal contribution to ERR is given in Section 8.2.5.

8.2.5 *i*th vibration modal contribution to ERR

The dynamic factor of the *i*th vibration mode is

$$f_{\text{dyn}}^{i} = -\frac{\left(L^3 + 3L^2a + 3La^2 + 4a^3\right)}{6at}\Lambda_i \sin\left(\omega_i t\right), \tag{8.44}$$

which is a sine function decreasing with time as it oscillates (superscript *i* denoting the vibration mode). It is seen that the dynamic effect comes from both the time and the space domains, where the former varies with time, and the latter depends on structural properties. To facilitate understanding of the relationship between the beam configuration and the modal contributions of each vibration mode, a *spatial factor* f_{sp}^{i} can be defined by isolating the structural properties from f_{dyn}^{i} as

$$f_{\text{sp}}^{i} = -\frac{\Lambda_i \left(L^3 + 3L^2a + 3La^2 + 4a^3\right)}{6a}, \tag{8.45}$$

where f_{sp}^{i} has units of seconds, and superscript *i* denotes the vibration mode.

Using the material properties from the verification case in Section 8.3.1 and maintaining the total length of the specimen as L_0 = 60 mm, f_{sp}^{i} was calculated for the first five vibration modes for crack-length ratios, defined as $\eta = a/L_0$, in the range $0.05 \leq \eta \leq 0.95$, and plotted in Figure 8.6.

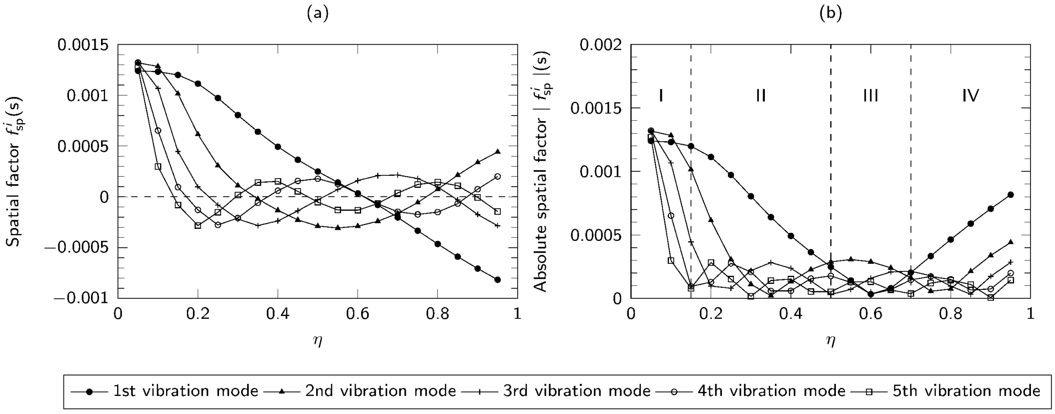

Figure 8.6 Spatial factor of *i*th vibration mode against crack-length ratio η

Figure 8.6a shows the spatial factors of each vibration modes oscillate around zero with crack-length ratio η. Clearly, the first vibration mode has the lowest frequency, and the frequency of f^i_{sp} increases with increasing vibration mode numbers. It is noteworthy that there are some crack-length ratios for which $f^i_{\mathrm{sp}} = 0$, meaning that the *i*th vibration mode does not contribute to the total ERR in this case. Furthermore, for the *i*th vibration mode, there are *i* ratios which produce $f^i_{\mathrm{sp}} = 0$. For example, the first vibration mode has only one crack-length ratio (0.61, approximately) that provides $f^1_{\mathrm{sp}} = 0$; but the second vibration mode has two crack-length ratios (0.34 and 0.78, approximately) that provide $f^2_{\mathrm{sp}} = 0$. Thus, for the verification case in Section 8.3.1 with the crack-length ratio of 0.33, the second mode contribution to the total ERR is close to zero.

The absolute value of f^i_{sp} for various crack-length ratios is presented in Figure 8.6b. The range of this ratio can be divided into four regions, according to relative contribution of each modes, as shown. Note that since f^i_{sp} is independent of the applied loading rate and an inherent property of an ELS specimen with given crack-length ratio η, this classification of regions is general for ELS specimens, and is not just for the specific verification case in Section 8.3.1.

In Region I, where $0.05 \le \eta \le 0.15$, the contribution for each vibration mode is significant, and so all the modes should be taken into account when determining the total dynamic ERR.

In Region II, where $0.15 \le \eta \le 0.5$, the contribution of the first vibration mode is dominant, and the total ERR can be approximated using only the first vibration mode.

In Region III, where $0.5 \le \eta \le 0.7$, the dominant vibration mode contributing to total dynamic ERR is the second vibration mode.

In Region IV, where $0.7 \le \eta \le 0.95$, the dominant vibration mode contributing to the total dynamic ERR changes from the second vibration mode back to the first vibration mode.

This classification of regions is important when designing specimens for high-loading-rate ELS tests to measure the dynamic mode-II fracture toughness of a given material. For example, it may be desirable to design ELS specimen in Region II (with crack-length ratios in the range $0.15 \le \eta \le 0.5$), since then only the first vibration mode would be dominant, simplifying the post-processing of test data, and reducing the amplitude of higher vibration modes, which could be helpful for data recording and regression.

This classification of regions is also important to help understand structural behaviour in the presence of a mode-II crack; for instance, a structure could be designed to avoid certain vibration modes in the presence of certain crack-length ratios. Alternatively, to reduce the total dynamic effect, crack-length ratio in Region III are preferred due to smaller spatial factors of all vibration modes.

8.3 Numerical verification

8.3.1 Verification for isotropic bi-layer composite

FEM simulations were used to verify the analytical theory developed in Section 8.2.2 for the total dynamic ERR. The geometry for the ELS specimen verification case is shown in Figure 8.7. Isotropic elastic material properties were used with the Young's modulus of 10 GPa, the Poisson's ratio of 0.3, and the density of 10^3 kg m^{-3}. The applied constant displacement rate was 5 m s^{-1}.

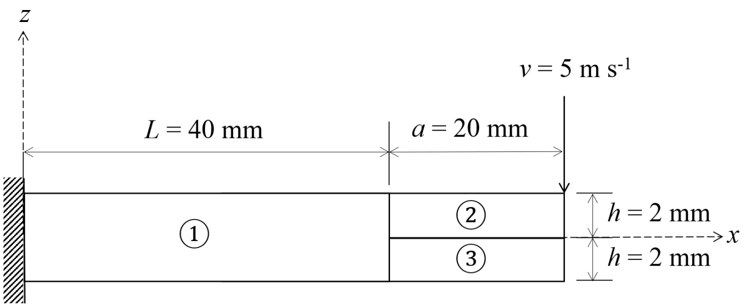

Figure 8.7 ELS geometry for FEM verification

A 2D FEM model was built in Abaqus/Explicit using four-node plane-stress elements (CPS4R) with a uniform mesh size of 0.1 mm, and the total number of elements was 24000. The crack region was modelled using a contact algorithm. To eliminate any damping effect in the dynamic response, the viscosity parameters were set to zero. The total dynamic ERR from the FEM was calculated using the VCCT and compared to the analytical theory.

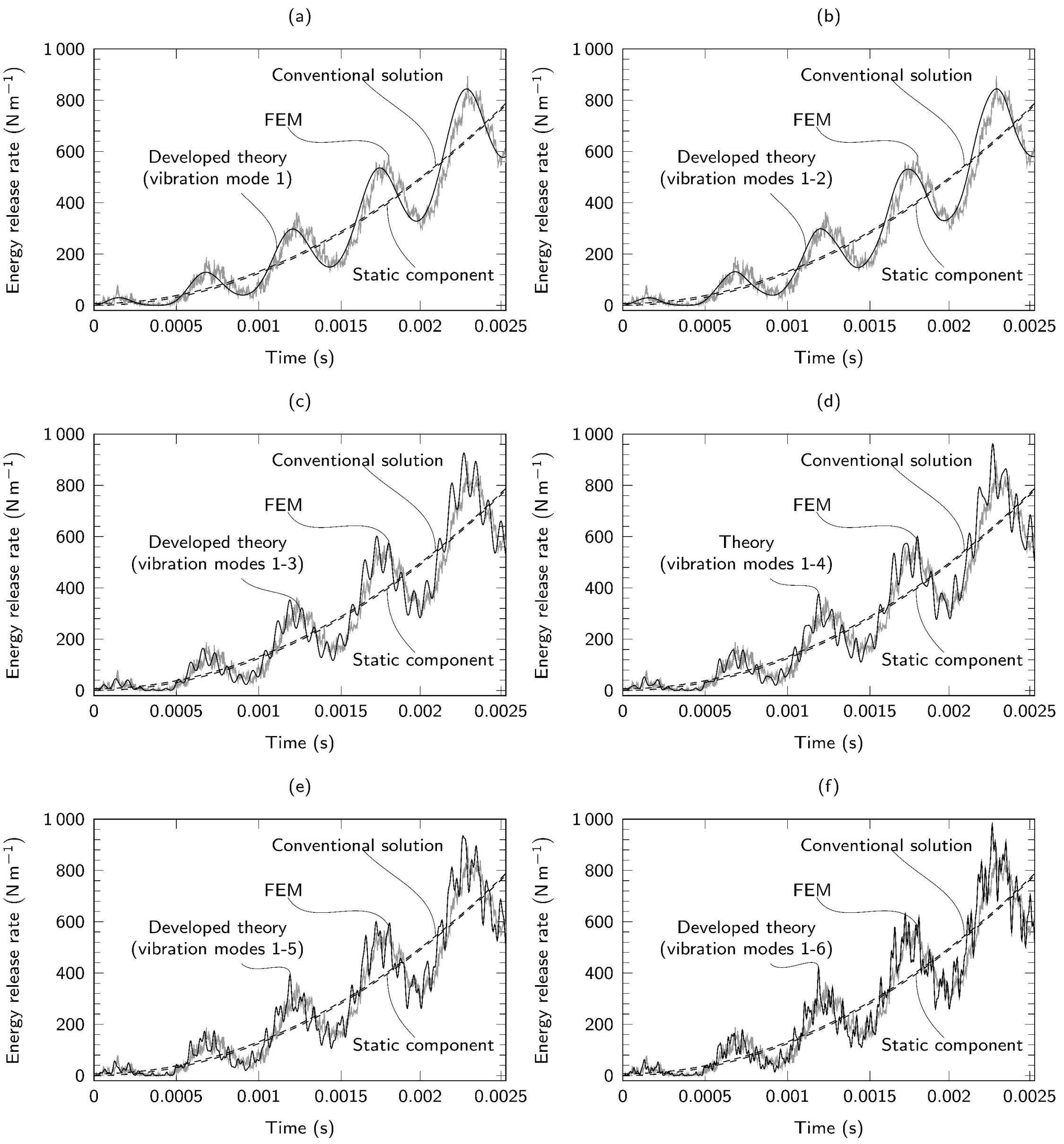

Figure 8.8 Dynamic ERR versus time results from developed theory (black line) and from FEM (grey line) with increasing numbers of vibration modes for an isotropic bi-layer composite

Figure 8.8 shows the comparison of dynamic mode-II ERR from analytical solution developed in Section 8.2.2 (solid black line) and from FEM simulation results (solid grey line) with various numbers of vibration modes. The dashed line represents the static component of ERR. In addition, the conventional solution in Section 4.2.2.2 is also plotted as a dashed line, which almost overlaps with the static component or quasi-static solution with only a baseline upwards shift of 6.91 N m^{-1}. The significant difference between the conventional solution in Section 4.2.2.2 and the developed analytical theory demonstrates the necessity of considering vibration for ELS specimen under dynamic loads.

The developed analytical theory and FEM simulations are in excellent agreement up to, and including, the first four vibration modes. From the fifth vibration mode onwards, the oscillation amplitudes from the analytical solution is slightly larger than that from FEM simulations, suggesting that the assumption in the theory that beam sections ② and ③ share the same deflection is valid for the lower vibration modes, but not quite so accurate for higher-order ones. In addition, Euler-Bernoulli beam theory was used, which overlooks shear and rotational inertia that might become significant for higher modes. Since the actual ERR amplitudes due to higher vibration modes are small however (see Figure 8.3), this discrepancy is not significant in estimating ERR if only the first few vibration modes are used, but the dominant vibration mode must be included as discussed in Section 8.2.5.

The crack-length ratio in this verification case is 0.33, and according to the analysis in Sections 8.2.3, 8.2.4 and 8.2.5, the contribution of the second vibration mode to the total dynamic ERR is close to zero. This is also confirmed by comparing Figure 8.8a and b, where adding the ERR contribution from the second vibration mode in the developed analytical theory does not alter the total ERR.

8.3.2 Verification for orthotropic fibre-reinforced composite

In Section 8.3.1, the numerical verification demonstrates the agreement between the developed theory and FEM simulation for an isotropic bi-layer composite. In this section, the developed theory is verified against a simulation of an orthotropic fibre-reinforced composite material. To apply the developed theory, the conventional method, as in ASTM D5528 [11], is to use the longitudinal modulus of elasticity (if it is dominant and the aspect ratio L/h is high).

The orthotropic material properties of unidirectional T800H/3900-2 carbon-fibre reinforced polymer, as given in Table 8.6, were taken from [177] and adopted for FEM simulation. The ELS dimensions used, in accordance with ISO 15114 [14], were $L = 40$ mm, $a = 60$ mm, $h = 1.5$ mm. The applied loading rate selected was 5 m s^{-1}. The density of T800H/3900-2 was taken as 1.25×10^{3} kg m^{-3} from the manufacturer's data sheet. All other FEM settings were as described in Section 8.3.1.

Table 8.6 Orthotropic material properties of unidirectional T800H/3900-2 graphite/epoxy

E_{11} = 154.72 GPa	E_{22} = 7.58 GPa	E_{33} = 7.58 GPa
G_{12} = 4.27 GPa	G_{13} = 4.27 GPa	G_{23} = 2.88 GPa
ν_{12} = 0.32	ν_{13} = 0.32	ν_{23} = 0.32

For the analytical solution, the modulus of elasticity in the fibre direction (E_{11} in Table 8.6) is used to derive the dynamic mode-II ERR by Eq. (8.38). The comparison between the analytical solution and the FEM simulation results is shown in Figure 8.9.

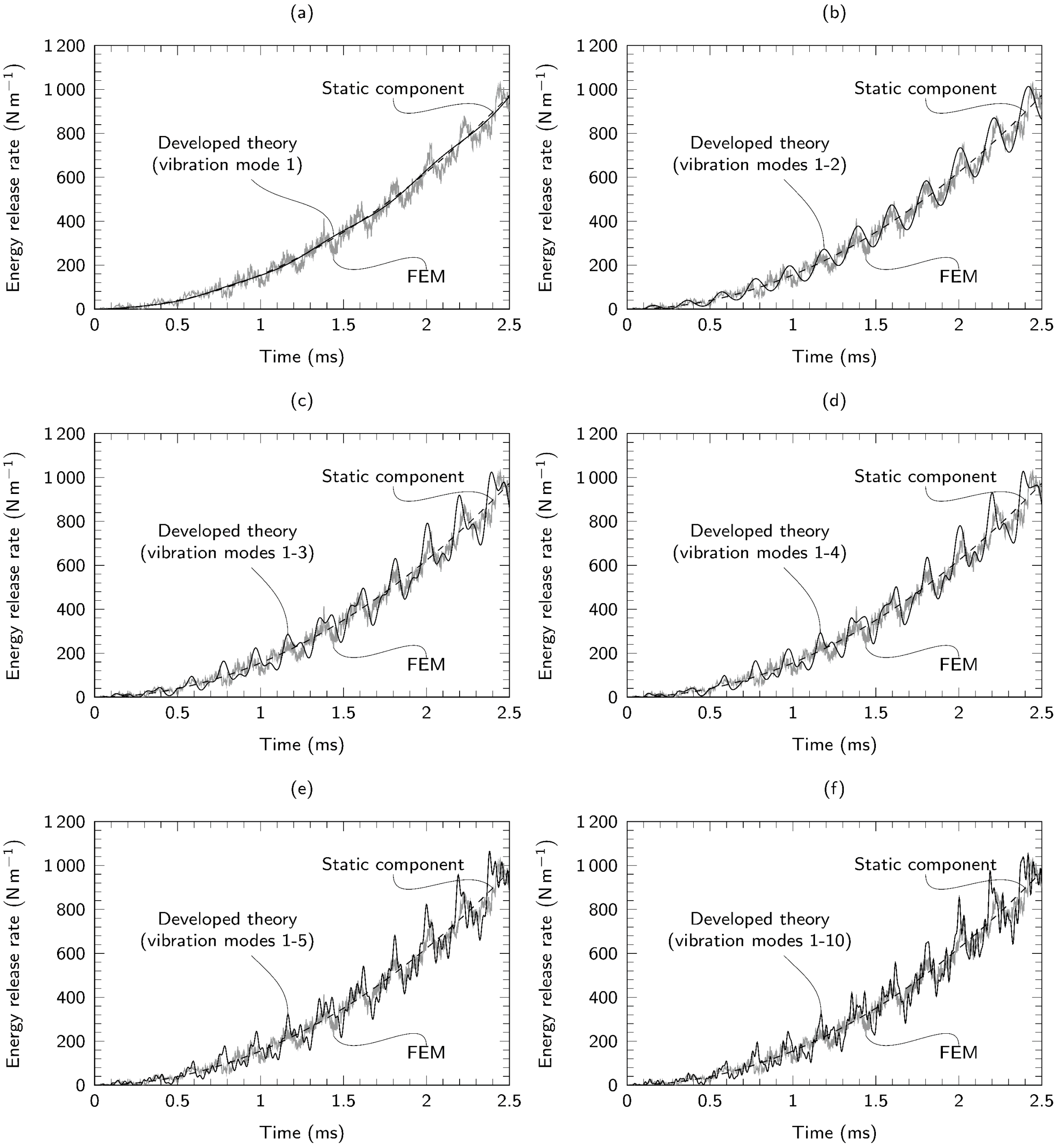

Figure 8.9 Dynamic ERR versus time results from developed theory (black line) and from FEM (grey line) with increasing numbers of vibration modes for an orthotropic fibre-reinforced composite

Results of the analytical solution and the FEM simulation are generally in excellent agreement, although the analytical solution predicts slightly higher amplitudes, which is not significant. The crack-length ratio for this ELS geometry is $\eta = 0.6$. According to Figure 8.6 in Section 8.2.5, the dominant vibration mode should be the second one, with the first vibration mode not contributing to the total ERR since $f_{\text{sp}}^{1} \approx 0$. This is confirmed in Figure 8.9a, in which the analytical solution with the first vibration mode only almost overlaps the static component. Figures 8.9b-f show that by adding more vibration modes, the analytical solution becomes increasingly closer to the FEM simulation results, and that, therefore, the developed theory is also applicable to orthotropic fibre-reinforced composite ELS specimens by the conventional method of using the longitudinal modulus of elasticity.

8.4 Conclusion

The dynamic ERR of a mode-II stationary crack of an ELS specimen is derived analytically by established analytical framework in Chapter 5. They dynamic effect and the contribution of each vibration mode were quantified by defining a *dynamic factor* and a *spatial factor*. They dynamic factor f_{dyn} facilitates understanding of the total dynamic effect. It was found that dynamic factor decreased with time as it oscillates around the dynamic factor-contribution of the dominant vibration mode.

The spatial factor f_{sp}^{i}, which represents the contribution on the total ERR from the ith vibration mode for given structural properties, facilitates understanding the relative contribution of each vibration mode. The spatial factor is a function of the crack-length ratio η. Based on the crack-length ratio, four regions were established with the dominant vibration mode(s) for determining the total dynamic ERR identified in each. In addition, for a given spatial factor, there may exist a certain vibration mode, which makes approximately zero contribution to the ERR.

FEM simulations were used to verify and confirm the analytical solution, and comparison between FEM simulation results and analytical results is in excellent agreement. The comparison of results also demonstrates the importance of including the dominant vibration mode when using the developed theory.

The derived theory is readily applicable in various applications, such as measuring the dynamic mode-II fracture toughness of materials, or designing structures to avoid certain vibration modes in the presence of certain crack length, or reducing the total dynamic effect on the ERR of a structure with a mode-II crack. In addition, the developed theory can guide the design of high-loading-rate ELS tests, the design of specimens to avoid unwanted high-amplitude oscillation from higher-order vibration modes, and can simplify and guide the post-processing of test data.

Chapter 9: Conclusions and future work

9.1 Conclusions

The increasing application of laminated materials such as CFRPs requires a fundamental understanding of the interfacial fracture behaviour in such materials. In the dynamic loading regime, the fracture behaviour was always investigated with a conventional analytical approach or experimental-numerical hybrid schemes. The conventional analytical approach used the global approach including the kinetic energy, accounting for a quasi-static motion, but usually came to different or contradicting results for dynamic fracture toughness. Also, it did not capture the oscillating dynamic ERR that, as the experiments and FEM simulations demonstrate, can be significant. The experimental-numerical hybrid methods generally require extensive computational resources. Therefore, a new analytical framework, which accounts for the structural vibration and wave propagation is developed to study the dynamic interfacial fracture.

The analytical framework for the dynamic interfacial fracture is first developed for DCBs, the most fundamental engineering structure to study the mode-I fracture behaviour. An effective boundary condition was assumed at the crack tip for one DCB arm and the problem of dynamic deflection of this arm was solved by vibration analysis for time-dependent boundary conditions. This dynamic deflection was then used to determine the strain and kinetic energies to assess the dynamic ERR employing the global approach. However, the dynamic ERR obtained in this way shows a non-physical and non-mechanical behaviour: its amplitude diverges with including more vibration modes. Also, only the first-order-accurate dynamic ERR is derived; further examination shows that the global approach overlooked the wave-propagation properties of beams as dispersive waveguides and assumed that all the flexural waves arrived at the crack tip simultaneously. To address this, the dispersive property is included to study the energy flux into the crack tip at a given time, and a correction factor for dispersion is introduced to modify the global approach solution: this method is called *dispersion-corrected global approach*. The dynamic ERR determined with this approach demonstrates a good agreement with results from FEM simulation (but slightly out of phase). So, the method to compensate for crack-tip rotation with the effective crack length (also known as the MCC method and widely used in a quasi-static loading regime) was employed to adjust this and results are in an excellent agreement. The investigation also demonstrates the equivalence between the developed dispersion-corrected global approach and the local approach in determining the dynamic ERR.

The developed analytical framework is then extended further to study the crack-propagation behaviour in mode-I under dynamic loads. For a material with constant fracture toughness, the first-order-accurate dynamic ERR was used to derive the crack-propagation speed and obtain a crack length versus time curve by enforcing $G = G_c$. The analytical solution exhibits a good agreement with the FEM results but cannot predict the crack-arrest phenomenon. For a material with rate-dependent fracture toughness, the dynamic ERR is derived based on the dispersion-corrected global approach and a further assumption of energy conservation as well as a correction of frequency due to the Doppler effect. The developed analytical solution for propagating crack is thus verified against results from experiments and FEM simulations, showing excellent agreement. This analytical solution also allows a study of the limiting crack-propagation speed in the DCBs, which is demonstrated to be a function of aspect ratio r ($r = h/a$, the ratio between the thickness and the crack length) and the Poisson’s ratio. For the conventional DCBs, the limiting crack propagation speed is in the range from $0.02C_R$ to $0.25C_R$ for the given aspect ratio of 0.01 to 0.1. In the analytical solution to determine the ERR, however, the effective crack length is still used. But this effective crack length cannot be derived using the MCC method but by data regression for the experimentally observed crack length against the square root of time, and an additional crack length for the crack-tip-rotation compensation is found to be rate-dependent.

To allow the crack tip to rotate and also to extend the analytical framework to study dynamic fracture at a non-rigid elastic interface, an elastic foundation is introduced into the established analytical framework. This developed analytical solution can be readily applied to study adhesively bonded or welded interfaces. It is found that with decreasing interface stiffness, the ERR decreases, with lower vibration modes becoming more dominant. The developed analytical solutions are verified against the FEM results, demonstrating an excellent agreement. Additionally, the mode-mixity is also studied by applying the quasi-static partition theory to partition the total dynamic ERR derived from the developed theory; the comparison between the ERR components are in excellent agreement with FEM simulation results. For crack propagating on the elastic foundation, the ERR solution is derived by analogy to the solution for the propagating crack in

Chapter 6, and this ERR solution for the propagating crack on the elastic foundation is also verified by FEM simulation.

For dynamic mode-II interfacial fracture, an ELS specimen is investigated with the local approach, that is, using the crack-tip bending moment. The derived analytical solution shows that the contributions to the total ERR of different vibration modes are dependent on the ELS configuration, i.e. crack-length ratio, which is the ratio between the crack length and the total length of the specimen. Accordingly, a *spatial factor* is defined by isolating structural properties in the dynamic factor in the space domain, and the dominant vibration mode for various ranges of the crack-length ratio can be identified. The crack-tip loading condition is also linked to this spatial factor. The finding is essential for designing ELS specimens or engineering structures to avoid specific contributions of vibration mode to the total ERR.

Overall, all of the analytical solutions are readily applicable to engineering applications, such as measuring dynamic fracture toughness in modes I and II, designing engineering structures to avoid certain vibration modes, and reducing the total dynamic effect in structures.

9.2 Future work

This work established an important analytical framework to study dynamic interfacial fracture in the context of engineering structures as waveguides with various analytical solutions. However, there is still some research work for the future:

Experimental investigations In Chapter 6, the experimental verification of the analytical solution developed shows the limitation of inadequate experimental sample points for assessing the crack-propagation speed. Therefore, experiments that can provide adequate experimental sample points and the method to decide the number of these points are desirable. Now experiments suitable for the further study of the theories developed in Chapters 7 and 8 are also required: the experiments for adhesively bonded or welded DCBs would be used to assess and validate the analytical solution for the propagating crack in Chapter 7 as well as the experiments for dynamic mode-II using ELS spcimens to verify the analytical solution in Chapter 8.

Analytical solutions for different engineering structures For engineering structures analysed in this thesis, such as DCB, beam on elastic foundation and ELS configurations, the classical Euler-Bernoulli beam theory (the beams are assumed to be thin) is used to develop the respective analytical solutions for dynamic ERR, which only accounts for transverse inertia of the system. Further investigations to account for rotational inertia can be conducted by using the Rayleigh beam theory, and, to include the shear effect, the Timoshenko beam theory can be used. In addition, the analytical solution for a propagating crack in the ELS specimen can be developed. For other engineering structures, such as circular plates and annular plates, the analytical solutions for dynamic ERR can be obtained, which have different applications for engineering problems, for instance, impact problems.

Analytical solutions for different materials In this thesis, only elastic materials, either isotropic or orthotropic, are studied. Viscoelastic and elastic-plastic materials can be studied together with theoretical frame developed to provide wider applications.

References

[1] J. Pora, "Composite Materials in the Airbus A380," in *13th International Conference on Composite Materials (ICCM-13)*, 2001, pp. 1–10.

[2] M. R. Wisnom, "The role of delamination in failure of fibre-reinforced composites," *Philos. Trans. R. Soc. A Math. Phys. Eng. Sci.*, vol. 370, no. 1965, pp. 1850–1870, 2012.

[3] C. A. J. R. Vermeeren, "An historic overview of the development of fibre metal laminates," *Appl. Compos. Mater.*, vol. 10, no. 4–5, pp. 189–205, 2003.

[4] EASA, "Certification Specifications and Acceptable Means of Compliance for Large Aeroplanes CS-25," 2018.

[5] B. Yuan, C. M. Harvey, R. C. Thomson, G. W. Critchlow, and S. Wang, "A new spallation mechanism of thermal barrier coatings on aero-engine turbine blades," *Theor. Appl. Mech. Lett.*, vol. 8, no. 1, pp. 7–11, 2018.

[6] D. Geng *et al.*, "Delamination formation, evaluation and suppression during drilling of composite laminates: A review," *Compos. Struct.*, vol. 216, pp. 168–186, 2019.

[7] F. Aymerich and P. Priolo, "Characterization of fracture modes in stitched and unstitched cross-ply laminates subjected to low-velocity impact and compression after impact loading," *Int. J. Impact Eng.*, vol. 35, no. 7, pp. 591–608, 2008.

[8] Y. Behnamian *et al.*, "A comparative study on the oxidation of austenitic alloys 304 and 304-oxide dispersion strengthened steel in supercritical water at 650 °C," *J. Supercrit. Fluids*, vol. 119, pp. 245–260, 2017.

[9] B. Park, Y. K. An, and H. Sohn, "Visualization of hidden delamination and debonding in composites through noncontact laser ultrasonic scanning," *Compos. Sci. Technol.*, vol. 100, pp. 10–18, 2014.

[10] ASTM E1820, "Standard Test Method for Measurement of Fracture Toughness," *ASTM International*. 2020.

[11] ASTM D5528, "Standard test method for mode I interlaminar fracture toughness of unidirectional fiber-reinforced polymer matrix composites," *ASTM International*. 2014.

[12] ASTM D7905, “Standard test method for determination of the mode II interlaminar fracture toughness of unidirectional fiber-reinforced polymer matrix composites,” *ASTM International*. 2014.

[13] ASTM D6671, “Standard Test Method for Mixed Mode I-Mode II Interlaminar Fracture Toughness of Unidirectional Fiber Reinforced Polymer Matrix Composites,” *ASTM International*. 2019.

[14] ISO 15114:2014, “Fibre-reinforced plastic composites - Determination of the mode II fracture resistance for unidirectionally reinforced materials using the calibrated end-loaded split (C-ELS) test and an effective crack length approach.,” *Int. Stand. Organ. Geneva, Switz.*, 2014.

[15] M. Colin de Verdiere, A. A. Skordos, M. May, and A. C. Walton, “Influence of loading rate on the delamination response of untufted and tufted carbon epoxy non crimp fabric composites: Mode I,” *Eng. Fract. Mech.*, vol. 96, pp. 11–25, 2012.

[16] M. Colin de Verdiere, A. A. Skordos, A. C. Walton, and M. May, “Influence of loading rate on the delamination response of untufted and tufted carbon epoxy non-crimp fabric composites/Mode II,” *Eng. Fract. Mech.*, vol. 96, pp. 1–10, 2012.

[17] A. J. Smiley and R. B. Pipes, “Rate effects on mode I interlaminar fracture toughness in composite materials,” *J. Compos. Mater.*, vol. 21, no. 7, pp. 670–687, 1987.

[18] A. J. Smiley and R. B. Pipes, “Rate sensitivity of mode II interlaminar fracture toughness in graphite/epoxy and graphite/PEEK composite materials,” *Compos. Sci. Technol.*, vol. 29, no. 1, pp. 1–15, 1987.

[19] B. R. K. Blackman *et al.*, “The failure of fibre composites and adhesively bonded fibre composites under high rates of test - Part I Mode I loading-experimental studies,” *J. Mater. Sci.*, vol. 30, no. 23, pp. 5885–5900, 1995.

[20] B. R. K. Blackman, A. J. Kinloch, Y. Wang, and J. G. Williams, “The failure of fibre composites and adhesively bonded fibre composites under high rates of test: Part II mode I loading - Dynamic effects,” *J. Mater. Sci.*, vol. 31, no. 17, pp. 4451–4466, 1996.

[21] H. Liu, H. Nie, C. Zhang, and Y. Li, “Loading rate dependency of Mode I interlaminar fracture toughness for unidirectional composite laminates,” *Compos.*

Sci. Technol., vol. 167, pp. 215–223, 2018.

[22] Y. Liu, F. P. van der Meer, and L. J. Sluys, “Cohesive zone and interfacial thick level set modeling of the dynamic double cantilever beam test of composite laminate,” *Theor. Appl. Fract. Mech.*, vol. 96, pp. 617–630, 2018.

[23] S. S. Rao, *Vibration of Continuous Systems*. John Wiley & Sons, 2007.

[24] R. D. Blevins, *Formulas for Natural Frequency and Mode Shape*. 1979.

[25] K.F. Graff, *Wave Motion in Elastic Solids*. Oxford University Press, 1991.

[26] V. Giurgiutiu, *Structural Health Monitoring with Piezoelectric Wafer Active Sensors*. Elsevier, 2007.

[27] N. G. Stephen and S. Puchegger, “On the valid frequency range of Timoshenko beam theory,” *J. Sound Vib.*, vol. 297, no. 3–5, pp. 1082–1087, 2006.

[28] D. A. Grant, “Beam vibrations with time-dependent boundary conditions,” *J. Sound Vib.*, vol. 89, no. 4, pp. 519–522, 1983.

[29] Lord Rayleigh, “On waves propagated along the plane surface of an elastic solid,” *Proc. London Math. Soc.*, vol. s1-17, no. 1, pp. 4–11, 1885.

[30] I. A. Viktorov, *Rayleigh and Lamb Waves*. 1967.

[31] H. Lamb, “On waves in an elastic plate,” *Proc. R. Soc. London. Ser. A, Contain. Pap. a Math. Phys. Character*, 1917.

[32] T. Kamas, V. Giurgiutiu, and B. Lin, “Thickness mode EMIS of constrained proof-mass piezoelectric wafer active sensors,” *Smart Mater. Struct.*, vol. 24, no. 11, p. 115035, 2015.

[33] A. M. Kamal, B. Lin, and V. Giurgiutiu, “Exact analytical modeling of power and energy for multimode lamb waves excited by piezoelectric wafer active sensors,” *J. Intell. Mater. Syst. Struct.*, vol. 25, no. 4, pp. 452–471, 2014.

[34] K. Broberg, *Cracks and Fracture*. Academic Press, 1999.

[35] E. E. Gdoutos, *Fracture Mechanics*. Springer, 2005.

[36] L.B.Freund, *Dynamic Fracture Mechanics*. Cambridge University Press, 1990.

[37] K. Ravi-Chandar, *Dynamic Fracture*. Elseveier Science, 2004.

[38] A. A. Griffith, “The phenomena of rupture and flow in solids,” *Philos. Trans. R. Soc. A Math. Phys. Eng. Sci.*, vol. 221, pp. 163–198, 1921.

[39] G. R. Irwin, “Analysis of Stresses and Strains Near the End of a Crack Traversing a Plate,” *J. Appl. Mech.*, vol. 24, pp. 361–364, 1957.

[40] C. G.P, “Crack propagation in continuos media,” *J. Appl. Math. Mech.*, vol. 31, pp. 476–488, 1967.

[41] J. R. Rice, “A path independent integral and the approximate analysis of strain concentration by notches and cracks,” *J. Appl. Mech. Trans. ASME*, vol. 35, no. 2, pp. 379–388, 1964.

[42] A. A. Griffith, “The phenomena of rupture and flow in solids,” *Philos. Trans. R. Soc. A Math. Phys. Eng. Sci.*, vol. 221, no. 1, pp. 163–198, 1921.

[43] C.E.Inglis, “Stresses in a Plate due to presence of Cracks and Sharp Corners,” *Trans. R. Inst. Nav. Archit.*, vol. 60, no. 55, pp. 219–241, 1913.

[44] Westergaard H.M., “Bearing Pressures and Cracks,” *J. Appl. Mech.*, vol. 6, pp. 49–53, 1939.

[45] I. N. Sneddon, “The distribution of stress in the neighbourhood of a crack in an elastic solid,” *Proc. R. Soc. London. Ser. A. Math. Phys. Sci.*, 1946.

[46] M. L. Williams, “The bending stress distribution at the base of a stationary crack,” *J. Appl. Mech. Trans. ASME*, vol. 28, no. 1, pp. 78–82, 1960.

[47] J. R. Reeder, “An Evaluation of Mixed-Mode Delamination Failure Criteria,” *NASA Tech. Memo. 104210*, 1992.

[48] J. R. Reeder, “3D mixed-mode delamination fracture criteria - An experimentalist’s perspective,” in *American Society for Composites - 21st Technical Conference of the American Society for Composites 2006*, 2006.

[49] J. R. Rice, “A path independent integral and the approximate analysis of strain concentration by notches and cracks,” *J. Appl. Mech. Trans. ASME*, vol. 35, no. 2, pp. 379–388, 1964.

[50] J. P. Berry, “Determination of fracture surface energies by the cleavage technique,” *J. Appl. Phys.*, vol. 34, no. 1, pp. 62–68, 1963.

[51] S. Hashemi, A. J. Kinloch, and J. M. Williams, "The analysis of interlaminar fracture in uniaxial fibre-polymer composites," *Proc. R. Soc. London. A. Math. Phys. Sci.*, vol. 427, no. 1872, pp. 173–199, 1990.

[52] A. Russell and K. Street, "Moisture and Temperature Effects on the Mixed-Mode Delamination Fracture of Unidirectional Graphite/Epoxy," in *Delamination and Debonding of Materials*, 1985, pp. 349–370.

[53] R. V. Gol'dstein and R. L. Salganik, "Brittle fracture of solids with arbitrary cracks," *Int. J. Fract.*, vol. 10, no. 4, pp. 507–523, 1974.

[54] J. G. Williams, "On the calculation of energy release rates for cracked laminates," *Int. J. Fract.*, 1988.

[55] R. A. Schapery and B. D. Davidson, "Prediction of energy release rate for mixed-mode delamination using classical plate theory," *Appl. Mech. Rev.*, vol. 43, no. 5, pp. S281–S287, 1990.

[56] J. W. Hutchinson and Z. Suo, "Mixed Mode Cracking in Layered Materials," *Adv. Appl. Mech.*, vol. 29, no. C, pp. 63–191, 1991.

[57] M. D. Thouless, A. G. Evans, M. F. Ashby, and J. W. Hutchinson, "The edge cracking and spalling of brittle plates," *Acta Metall.*, vol. 35, no. 6, pp. 1333–1341, 1987.

[58] Z. Zou, S. R. Reid, S. Li, and P. D. Soden, "General expressions for energy-release rates for delamination in composite laminates," *Proc. R. Soc. A Math. Phys. Eng. Sci.*, vol. 458, no. 2019, pp. 645–667, 2002.

[59] J. Wang and P. Qiao, "Interface crack between two shear deformable elastic layers," *J. Mech. Phys. Solids*, vol. 52, no. 4, pp. 891–905, 2004.

[60] S. Wang and C. M. Harvey, "Mixed mode partition theories for one dimensional fracture," *Eng. Fract. Mech.*, vol. 79, pp. 329–352, 2012.

[61] S. Wang and C. Harvey, "A theory of one-dimensional fracture," *Compos. Struct.*, vol. 94, no. 2, pp. 758–767, 2012.

[62] C. M. Harvey and S. Wang, "Mixed-mode partition theories for one-dimensional delamination in laminated composite beams," *Eng. Fract. Mech.*, vol. 96, pp. 737–759, 2012.

[63] S. Wang, C. M. Harvey, and L. Guan, “Partition of mixed modes in layered isotropic double cantilever beams with non-rigid cohesive interfaces,” *Eng. Fract. Mech.*, vol. 111, pp. 1–25, 2013.

[64] C. M. Harvey, J. D. Wood, and S. Wang, “Brittle interfacial cracking between two dissimilar elastic layers: Part 1-Analytical development,” *Compos. Struct.*, vol. 134, pp. 1076–1086, 2015.

[65] C. M. Harvey, J. D. Wood, S. Wang, and A. Watson, “A novel method for the partition of mixed-mode fractures in 2D elastic laminated unidirectional composite beams,” *Compos. Struct.*, vol. 116, no. 1, pp. 589–594, 2014.

[66] J. D. Wood, C. M. Harvey, and S. Wang, “Partition of mixed-mode fractures in 2D elastic orthotropic laminated beams under general loading,” *Compos. Struct.*, vol. 149, pp. 239–246, 2016.

[67] J. D. Wood, C. M. Harvey, and S. Wang, “Adhesion toughness of multilayer graphene films,” *Nat. Commun.*, vol. 8, no. 1, 2017.

[68] G. A. O. Davies and R. Olsson, “Impact on composite structures,” *Aeronaut. J.*, vol. 108, no. 1089, pp. 541–563, 2004.

[69] L. B. Freund, “Crack propagation in an elastic solid subjected to general loading-III. Stress wave loading,” *J. Mech. Phys. Solids*, vol. 21, no. 2, pp. 47–61, 1973.

[70] N. F. Mott, “Fracture of metals: theoretical considerations,” *Engineering*, vol. 265, pp. 16–18, 1948.

[71] D. K. Roberts and A. A. Wells, “The velocity of brittle fracture,” *Engineering*, vol. 178, pp. 820–821, 1954.

[72] C. Atkinson and J. D. Eshelby, “The flow of energy into the tip of a moving crack,” *Int. J. Fract. Mech.*, vol. 4, no. 1, pp. 3–8, 1968.

[73] B. V. Kostrov and L. V. Nikitin, “Some General Problems of Mechanics of Brittle Fracture,” *Arch Mech Strosowanej*, vol. 22, no. 6, pp. 749–776, 1970.

[74] L. B. Freund, “Energy flux into the tip of an extending crack in an elastic solid,” *J. Elast.*, vol. 2, no. 4, pp. 341–349, 1972.

[75] G. I. Barenblatt and G. P. Cherepanov, “On the wedging of brittle bodies,” *J. Appl. Math. Mech.*, vol. 24, no. 4, pp. 993–1015, 1960.

[76] J. W. Craggs, “On the propagation of a crack in an elastic-brittle material,” *J. Mech. Phys. Solids*, vol. 8, no. 1, pp. 66–75, 1960.

[77] A. A. Aliyu and I. M. Daniel, “Effects of strain rate on delamination fracture toughness of graphite/epoxy,” in *ASTM Special Technical Publication*, 1985, vol. ASTM STP 8, pp. 336–348.

[78] S. Mall, G. E. Law, and M. Katouzian, “Loading rate effect on interlaminar fracture toughness of a thermoplastic composite,” *J. Compos. Mater.*, vol. 21, no. 6, pp. 569–579, 1987.

[79] W. J. Cantwell and M. Blyton, “Influence of loading rate on the interlaminar fracture properties of high performance composites - A review,” *Appl. Mech. Rev.*, vol. 52, no. 6, pp. 199–212, 1999.

[80] G. C. Jacob, J. M. Starbuck, J. F. Fellers, S. Simunovic, and R. G. Boeman, “The effect of loading rate on the fracture toughness of fiber reinforced polymer composites,” *J. Appl. Polym. Sci.*, vol. 96, no. 3, pp. 899–904, 2005.

[81] M. May, “Measuring the rate-dependent mode I fracture toughness of composites - A review,” *Compos. Part A Appl. Sci. Manuf.*, vol. 81, pp. 1–12, 2016.

[82] K. Friedrich, R. Walter, L. A. Carlsson, A. J. Smiley, and J. W. Gillespie, “Mechanisms for rate effects on interlaminar fracture toughness of carbon/epoxy and carbon/PEEK composites,” *J. Mater. Sci.*, vol. 24, no. 9, pp. 3387–3398, 1989.

[83] K. Kageyama and I. Kimpara, “Delamination failures in polymer composites,” *Mater. Sci. Eng. A*, vol. 143, no. 1–2, pp. 167–174, 1991.

[84] T. Kusaka, Y. Yamauchi, and T. Kurokawa, “Effects of strain rate on mode II interlaminar fracture toughness in carbon-fibre/epoxy laminated composites,” *J. Phys. IV JP*, vol. 4, no. 8, 1994.

[85] L. Berger and W. J. Cantwell, “Temperature and loading rate effects in the mode II interlaminar fracture behavior of carbon fiber reinforced PEEK,” *Polym. Compos.*, vol. 22, no. 2, pp. 271–281, 2001.

[86] H. Maikuma, J. W. Gillespie, and D. J. Wilkins, “Mode II Interlaminar Fracture of the Center Notch Flexural Specimen under Impact Loading,” *J. Compos. Mater.*, vol. 24, no. 2, pp. 124–149, 1990.

[87] P. Compston, P. Y. B. Jar, and P. Davies, “Matrix effect on the static and dynamic interlaminar fracture toughness of glass-fibre marine composites,” *Compos. Part B Eng.*, vol. 29, no. 4, pp. 505–516, 1998.

[88] B. R. K. Blackman *et al.*, “The failure of fibre composites and adhesively bonded fibre composites under high rates of test: Part III mixed-mode I/II and mode II loadings,” *J. Mater. Sci.*, vol. 31, no. 17, pp. 4467–4477, 1996.

[89] M. May, H. Channammagari, and P. Hahn, “High-rate mode II fracture toughness testing of polymer matrix composites – A review,” *Compos. Part A Appl. Sci. Manuf.*, vol. 137, p. 106019, 2020.

[90] H. Liu, X. Meng, H. Zhang, H. Nie, C. Zhang, and Y. Li, “The dynamic crack propagation behavior of mode I interlaminar crack in unidirectional carbon/epoxy composites,” *Eng. Fract. Mech.*, vol. 215, pp. 65–82, 2019.

[91] M. F. Kanninen, C. Popelar, and P. C. Gehlen, “Dynamic analysis of crack propagation and arrest in the double-cantilever-beam specimen,” in *ASTM Special Technical Publication*, 1977, no. 627, pp. 19–38.

[92] M. F. Kanninen, “A dynamic analysis of unstable crack propagation and arrest in the DCB test specimen,” *Int. J. Fract.*, vol. 10, no. 3, pp. 415–430, 1974.

[93] P. Davidson, A. M. Waas, and C. S. Yerramalli, “Experimental determination of validated, critical interfacial modes I and II energy release rates in a composite sandwich panel,” *Compos. Struct.*, vol. 94, no. 2, pp. 477–483, 2012.

[94] P. Davidson and A. M. Waas, “Non-smooth mode I fracture of fibre-reinforced composites: An experimental, numerical and analytical study,” *Philos. Trans. R. Soc. A Math. Phys. Eng. Sci.*, vol. 370, pp. 1942–1965, 2012.

[95] C. Sun, M. D. Thouless, A. M. Waas, J. A. Schroeder, and P. D. Zavattieri, “Ductile-brittle transitions in the fracture of plastically-deforming, adhesively-bonded structures. Part I: Experimental studies,” *Int. J. Solids Struct.*, vol. 45, no. 10, pp. 3059–3073, 2008.

[96] R. Palazzetti *et al.*, “Influence of electrospun Nylon 6,6 nanofibrous mats on the interlaminar properties of Gr-epoxy composite laminates,” *Compos. Struct.*, vol. 94, no. 2, pp. 571–579, 2012.

[97] H. Wang and T. Vu-Khanh, “Use of end-loaded-split (ELS) test to study stable fracture behaviour of composites under mode II loading,” *Compos. Struct.*, vol. 36, no. 1–2, pp. 71–79, 1996.

[98] Y. Gong, B. Zhang, S. Mukhopadhyay, and S. R. Hallett, “Experimental study on delamination migration in multidirectional laminates under mode II static and fatigue loading, with comparison to mode I,” *Compos. Struct.*, vol. 201, pp. 683–698, 2018.

[99] H. Maikuma, J. W. Gillespie, and J. M. Whitney, “Analysis and experimental characterization of the center notch flexural test specimen for mode II interlaminar fracture,” *J. Compos. Mater.*, vol. 23, no. 8, pp. 756–786, 1989.

[100] J. Ratcliffe and W. J. Cantwell, “Center notch flexure sandwich geometry for characterizing skin-core adhesion in thin-skinned sandwich structures,” *J. Reinf. Plast. Compos.*, vol. 20, no. 11, pp. 945–970, 2001.

[101] W. J. Cantwell, “The influence of loading rate on the mode II interlaminar fracture toughness of composite materials,” *J. Compos. Mater.*, vol. 31, no. 14, pp. 1364–1380, 1997.

[102] D. R. J. Owen and A. J. Fawkes, *Engineering Fracture Mechanics: Numerical Methods and Applications*. Pineridge Press, 1983.

[103] A. Sedmak, “Computational fracture mechanics: An overview from early efforts to recent achievements,” *Fatigue Fract. Eng. Mater. Struct.*, vol. 41, no. 12, pp. 2438–2474, 2018.

[104] T. Nishioka, “Computational dynamic fracture mechanics,” *Int. J. Fract.*, vol. 86, no. 1–2, pp. 127–159, 1997.

[105] L. B. Lucy, “A numerical approach to the testing of the fission hypothesis,” *Astron. J.*, vol. 82, p. 1013, 1977.

[106] L. D. Libersky, A. G. Petschek, T. C. Carney, J. R. Hipp, and F. a. Allahdadi, “High Strain Lagrangian Hydrodynamics,” *Journal of Computational Physics*, vol. 109, no. 1. pp. 67–75, 1993.

[107] M. B. Liu and G. R. Liu, “Smoothed particle hydrodynamics (SPH): An overview and recent developments,” *Arch. Comput. Methods Eng.*, vol. 17, no. 1, pp. 25–76,

2010.

[108] R. C. Batra and G. M. Zhang, “Search algorithm, and simulation of elastodynamic crack propagation by modified smoothed particle hydrodynamics (MSPH) method,” *Comput. Mech.*, vol. 40, no. 3, pp. 531–546, 2007.

[109] W. W. Yao, X. P. Zhou, and F. Berto, “Continuous smoothed particle hydrodynamics for cracked nonconvex bodies by diffraction criterion,” *Theor. Appl. Fract. Mech.*, vol. 108, 2020.

[110] T. Belytschko, Y. Y. Lu, and L. Gu, “Element-free Galerkin methods,” *Int. J. Numer. Methods Eng.*, vol. 37, no. 2, pp. 229–256, 1994.

[111] T. Belytschko, Y. Y. Lu, L. Gu, and M. Tabbara, “Element-free galerkin methods for static and dynamic fracture,” *Int. J. Solids Struct.*, vol. 32, no. 17–18, pp. 2547–2570, 1995.

[112] R. Brighenti, “Application of the element-free Galerkin meshless method to 3-D fracture mechanics problems,” *Eng. Fract. Mech.*, vol. 72, no. 18, pp. 2808–2820, 2005.

[113] Z. Zhang, K. M. Liew, Y. Cheng, and Y. Y. Lee, “Analyzing 2D fracture problems with the improved element-free Galerkin method,” *Eng. Anal. Bound. Elem.*, vol. 32, no. 3, pp. 241–250, 2008.

[114] B. N. Rao and S. Rahman, “Efficient meshless method for fracture analysis of cracks,” *Comput. Mech.*, vol. 26, no. 4, pp. 398–408, 2000.

[115] I. Guiamatsia, B. G. Falzon, G. A. O. Davies, and L. Iannucci, “Element-Free Galerkin modelling of composite damage,” *Compos. Sci. Technol.*, vol. 69, no. 15–16, pp. 2640–2648, 2009.

[116] Y. Y. Zhang and L. Chen, “Impact simulation using simplified meshless method,” *Int. J. Impact Eng.*, vol. 36, no. 5, pp. 651–658, 2009.

[117] R. D. Henshell and K. G. Shaw, “Crack tip finite elements are unnecessary,” *Int. J. Numer. Methods Eng.*, vol. 9, no. 3, pp. 495–507, 1975.

[118] R. S. Barsoum, “On the use of isoparametric finite elements in linear fracture mechanics,” *Int. J. Numer. Methods Eng.*, vol. 10, no. 1, pp. 25–37, 1976.

[119] D. M. Parks, “A stiffness derivative finite element technique for determination of

crack tip stress intensity factors,” *Int. J. Fract.*, vol. 10, no. 4, pp. 487–502, 1974.

[120] T. K. Hellen, “On the method of virtual crack extensions,” *Int. J. Numer. Methods Eng.*, vol. 9, no. 1, pp. 187–207, 1975.

[121] E. F. Rybicki and M. F. Kanninen, “A finite element calculation of stress intensity factors by a modified crack closure integral,” *Eng. Fract. Mech.*, vol. 9, no. 4, pp. 931–938, 1977.

[122] N. Moës, J. Dolbow, and T. Belytschko, “A finite element method for crack growth without remeshing,” *Int. J. Numer. Methods Eng.*, vol. 46, no. 1, pp. 131–150, 1999.

[123] T. Belytschko and T. Black, “Elastic crack growth in finite elements with minimal remeshing,” *Int. J. Numer. Methods Eng.*, vol. 45, no. 5, pp. 601–620, 1999.

[124] V. Murti and S. Valliappan, “The use of quarter point element in dynamic crack analysis,” *Eng. Fract. Mech.*, vol. 23, no. 3, pp. 585–614, 1986.

[125] H. Nguyen-Vinh *et al.*, “Extended finite element method for dynamic fracture of piezo-electric materials,” *Eng. Fract. Mech.*, vol. 92, pp. 19–31, 2012.

[126] T. Belytschko, H. Chen, J. Xu, and G. Zi, “Dynamic crack propagation based on loss of hyperbolicity and a new discontinuous enrichment,” *Int. J. Numer. Methods Eng.*, vol. 58, no. 12, pp. 1873–1905, 2003.

[127] G. Zi, H. Chen, J. Xu, and T. Belytschko, “The extended finite element method for dynamic fractures,” *Shock Vib.*, vol. 12, no. 1 SPEC. ISS., pp. 9–23, 2005.

[128] J. Réthoré, A. Gravouil, and A. Combescure, “An energy-conserving scheme for dynamic crack growth using the eXtended finite element method,” *Int. J. Numer. Methods Eng.*, vol. 63, no. 5, pp. 631–659, 2005.

[129] B. Prabel, S. Marie, and A. Combescure, “Using the X-FEM method to model the dynamic propagation and arrest of cleavage cracks in ferritic steel,” *Eng. Fract. Mech.*, vol. 75, no. 10, pp. 2984–3009, 2008.

[130] C. J. Jih and C. T. Sun, “Evaluation of a finite element based crack-closure method for calculating static and dynamic strain energy release rates,” *Eng. Fract. Mech.*, vol. 37, no. 2, pp. 313–322, 1990.

[131] J. L. Tsai, C. Guo, and C. T. Sun, “Dynamic delamination fracture toughness in

unidirectional polymeric composites," *Compos. Sci. Technol.*, vol. 61, pp. 87–94, 2001.

[132] Q. Qian and D. Xie, "Analysis of mixed-mode dynamic crack propagation by interface element based on virtual crack closure technique," *Eng. Fract. Mech.*, vol. 74, no. 5, pp. 807–814, 2007.

[133] D. S. Dugdale, "Yielding of steel sheets containing slits," *J. Mech. Phys. Solids*, vol. 8, no. 2, pp. 100–104, 1960.

[134] G. I. Barenblatt, "The Mathematical Theory of Equilibrium Cracks in Brittle Fracture," *Adv. Appl. Mech.*, vol. 7, no. C, pp. 55–129, 1962.

[135] A. Hillerborg, M. Modéer, and P. E. Petersson, "Analysis of crack formation and crack growth in concrete by means of fracture mechanics and finite elements," *Cem. Concr. Res.*, vol. 6, no. 6, pp. 773–781, 1976.

[136] V. Tvergaard and J. W. Hutchinson, "The relation between crack growth resistance and fracture process parameters in elastic-plastic solids," *J. Mech. Phys. Solids*, vol. 40, no. 6, pp. 1377–1397, 1992.

[137] W. Cui and M. R. Wisnom, "A combined stress-based and fracture-mechanics-based model for predicting delamination in composites," *Composites*, vol. 24, no. 6, pp. 467–474, 1993.

[138] A. Needleman, "A continuum model for void nucleation by inclusion debonding," *J. Appl. Mech. Trans. ASME*, vol. 54, no. 3, pp. 525–531, 1987.

[139] X. P. Xu and A. Needleman, "Numerical simulations of fast crack growth in brittle solids," *J. Mech. Phys. Solids*, vol. 42, no. 9, pp. 1397–1434, 1994.

[140] Q. Yang and B. Cox, "Cohesive models for damage evolution in laminated composites," *Int. J. Fract.*, vol. 133, no. 2, pp. 107–137, 2005.

[141] P. W. Harper and S. R. Hallett, "Cohesive zone length in numerical simulations of composite delamination," *Eng. Fract. Mech.*, vol. 75, no. 16, pp. 4774–4792, 2008.

[142] F. Zhou, J. F. Molinari, and T. Shioya, "A rate-dependent cohesive model for simulating dynamic crack propagation in brittle materials," *Eng. Fract. Mech.*, vol. 72, no. 9, pp. 1383–1410, 2005.

[143] J. J. C. Remmers, R. de Borst, and A. Needleman, "The simulation of dynamic

crack propagation using the cohesive segments method," *J. Mech. Phys. Solids*, vol. 56, no. 1, pp. 70–92, 2008.

[144] M. Subasic, "Level Set Methods and Fast Marching Methods," *J. Comput. Inf. Technol.*, vol. 11, no. 1, p. 79, 2003.

[145] F. P. Van der Meer, N. Moës, and L. J. Sluys, "A level set model for delamination - Modeling crack growth without cohesive zone or stress singularity," *Eng. Fract. Mech.*, vol. 79, pp. 191–212, 2012.

[146] F. P. Van Der Meer, L. J. Sluys, and N. Moës, "Toward efficient and robust computation of energy release rate and mode mix for delamination," *Compos. Part A Appl. Sci. Manuf.*, vol. 43, no. 7, pp. 1101–1112, 2012.

[147] N. Moës, C. Stolz, P. E. Bernard, and N. Chevaugeon, "A level set based model for damage growth: The thick level set approach," *Int. J. Numer. Methods Eng.*, vol. 86, no. 3, pp. 358–380, 2011.

[148] A. Parrilla Gómez, N. Moës, and C. Stolz, "Comparison between thick level set (TLS) and cohesive zone models," *Adv. Model. Simul. Eng. Sci.*, vol. 2, no. 1, 2015.

[149] M. Latifi, F. P. van der Meer, and L. J. Sluys, "An interface thick level set model for simulating delamination in composites," *Int. J. Numer. Methods Eng.*, vol. 111, no. 4, pp. 303–324, 2017.

[150] T. Nishioka and S. N. Atluri, "Numerical analysis of dynamic crack propagation: Generation and prediction studies," *Eng. Fract. Mech.*, vol. 16, no. 3, pp. 303–332, 1982.

[151] C. Guo and C. T. Sun, "Dynamic mode-I crack-propagation in a carbon/epoxy composite," *Compos. Sci. Technol.*, vol. 58, no. 9, pp. 1405–1410, 1998.

[152] P. Kumar and N. N. Kishore, "Initiation and propagation toughness of delamination crack under an impact load," *J. Mech. Phys. Solids*, vol. 46, no. 10, pp. 1773–1787, 1998.

[153] S. B. Park and C. T. Sun, "Effect of electric field on fracture of piezoelectric ceramics," *Int. J. Fract.*, vol. 70, no. 3, pp. 203–216, 1995.

[154] V. Govorukha, M. Kamlah, V. Loboda, and Y. Lapusta, *Fracture Mechanics of Piezoelectric Solids with Interface Cracks*. Springer, 2017.

[155] R. Chandra, S. P. Singh, and K. Gupta, “Damping studies in fiber-reinforced composites - a review,” *Compos. Struct.*, vol. 46, no. 1, pp. 41–51, 1999.

[156] S. U. Khan, C. Y. Li, N. A. Siddiqui, and J. K. Kim, “Vibration damping characteristics of carbon fiber-reinforced composites containing multi-walled carbon nanotubes,” *Compos. Sci. Technol.*, vol. 71, no. 12, pp. 1486–1494, 2011.

[157] S. Hashemi, A. J. Kinloch, and J. G. Williams, “Corrections needed in double-cantilever beam tests for assessing the interlaminar failure of fibre-composites,” *J. Mater. Sci. Lett.*, vol. 8, no. 2, pp. 125–129, 1989.

[158] J. W. Dally, W. L. Fourney, and G. R. Irwin, “On the uniqueness of the stress intensity factor - crack velocity relationship,” *Int. J. Fract.*, vol. 27, no. 3–4, pp. 159–168, 1985.

[159] N. L. Balazs, “On the solution of the wave equation with moving boundaries,” *J. Math. Anal. Appl.*, vol. 3, pp. 472–484, 1961.

[160] L. Gaffour, “Analytical method for solving the one-dimensional wave equation with moving boundary – abstract,” *J. Electromagn. Waves Appl.*, vol. 20, pp. 63–73, 1998.

[161] B. Pelloni and D. A. Pinotsis, “Moving boundary value problems for the wave equation,” *J. Comput. Appl. Math.*, vol. 234, pp. 1685–1691, 2010.

[162] I. C. Christov and C. I. Christov, “On mechanical waves and Doppler shifts from moving boundaries,” *Math. Methods Appl. Sci.*, vol. 40, no. 12, pp. 4481–4492, 2017.

[163] C. Hakoda and C. J. Lissenden, “Comparison of quasi-Rayleigh waves and Rayleigh waves, and clarifying the cut-off frequency of quasi-Rayleigh waves,” *Ultrasonics*, vol. 92, pp. 50–56, 2019.

[164] S. Gopalakrishnan, *Wave Propagation in Materials and Structures*. CRC Press, 2017.

[165] D. R. Curran, L. Seaman, and D. A. Shockey, “Dynamic failure of solids,” *Phys. Rep.*, vol. 147, no. 5–6, pp. 253–388, 1987.

[166] A. P. Gallagher, “Bending of a Free Beam on an Elastic Foundation,” *J. Appl. Mech.*, vol. 50, no. 2, p. 463, 2009.

[167] A. B. Vesic, “Beams on Elastic Subgrade and the Winkler’s Hypothesis,” *Proc. 5th Int. Conf. Soil Mech.*, pp. 845–850, 1963.

[168] M. Cabello, J. Zurbitu, J. Renart, A. Turon, and F. Martínez, “A general analytical model based on elastic foundation beam theory for adhesively bonded DCB joints either with flexible or rigid adhesives,” *Int. J. Solids Struct.*, vol. 94–95, pp. 21–34, 2016.

[169] A. Turon, C. G. Dávila, P. P. Camanho, and J. Costa, “An engineering solution for mesh size effects in the simulation of delamination using cohesive zone models,” *Eng. Fract. Mech.*, vol. 74, no. 10, pp. 1665–1682, 2007.

[170] J. D. Wood, C. M. Harvey, and S. Wang, “Adhesion toughness of multilayer graphene films,” *Nat. Commun.*, vol. 8, no. 1, 2017.

[171] G. A. O. Davies and X. Zhang, “Impact damage prediction in carbon composite structures,” *Int. J. Impact Eng.*, vol. 16, no. 1, pp. 149–170, 1995.

[172] J. J. M. Machado, E. A. S. Marques, R. D. S. G. Campilho, and L. F. M. da Silva, “Mode II fracture toughness of CFRP as a function of temperature and strain rate,” *Compos. Part B Eng.*, vol. 114, pp. 311–318, 2017.

[173] R. J. Brambleby, L. A. Louca, and S. E. Mouring, “Influence of loading rate on the mode II fracture toughness of vinyl ester GRP,” *Compos. Part A Appl. Sci. Manuf.*, vol. 93, pp. 153–162, 2017.

[174] H. Zabala, L. Aretxabaleta, G. Castillo, and J. Aurrekoetxea, “Dynamic 4 ENF test for a strain rate dependent mode II interlaminar fracture toughness characterization of unidirectional carbon fibre epoxy composites,” *Polym. Test.*, vol. 55, pp. 212–218, 2016.

[175] P. Compston, P. Y. B. Jar, P. J. Burchill, and K. Takahashi, “Effect of matrix toughness and loading rate on the mode-II interlaminar fracture toughness of glass-fibre/vinyl-ester composites,” *Compos. Sci. Technol.*, vol. 61, no. 2, pp. 321–333, 2001.

[176] X. F. Wu and Y. A. Dzenis, “Determination of dynamic delamination toughness of a graphite-fiber/epoxy composite using hopkinson pressure bar,” *Polym. Compos.*, vol. 26, no. 2, pp. 165–180, 2005.

[177] B. D. Davidson, R. D. Bialaszewski, and S. S. Sainath, “A non-classical, energy release rate based approach for predicting delamination growth in graphite reinforced laminated polymeric composites,” *Compos. Sci. Technol.*, vol. 66, no. 10, pp. 1479–1496, 2006.

Appendix A: Formulas for integrals for mode shapes

For the mode shape of fixed-pinned boundary conditions with the expression in Eq. (2.22), Ref. [24] provides useful formulas for integrals for mode shapes, and they are used to derived relevant physical quantities, such as strain energy, kinetic energy and modal velocity in Chapter 5. These formulas are as follows:

$$\int_0^L \left[\phi_i\left(x\right)\right]^2 dx = L. \tag{A.1}$$

$$\int_0^L \left[\phi_i^{(2)}\left(x\right)\right]^2 dx = \beta_i^4 L. \tag{A.2}$$

$$\int_0^L \left[x\phi_i\left(x\right)\right] dx = \frac{1}{\beta_i^2}\left\{2-\beta_i L\left[\left(-1\right)^i\sqrt{\sigma_i^2+1}+\sqrt{\sigma_i^2-1}\right]\right\}. \tag{A.3}$$

$$\int_0^L \left[x^2\phi_i\left(x\right)\right] dx = \frac{1}{\beta_i^3}\left\{\begin{array}{l} -\beta_i^2 L^2\left[\left(-1\right)^i\sqrt{\sigma_i^2+1}+\sqrt{\sigma_i^2-1}\right] \\ +2\left[\left(-1\right)^i\sqrt{\sigma_i^2+1}-\sqrt{\sigma_i^2-1}\right] \end{array}\right\}. \tag{A.3}$$

$$\int_0^L \left[x^3\phi_i\left(x\right)\right] dx = \frac{L}{\beta_i^3}\left\{\begin{array}{l} -\beta_i^2 L^2\left[\left(-1\right)^i\sqrt{\sigma_i^2+1}+\sqrt{\sigma_i^2-1}\right] \\ +6\left[\left(-1\right)^i\sqrt{\sigma_i^2+1}-\sqrt{\sigma_i^2-1}\right] \end{array}\right\}. \tag{A.4}$$

Appendix B: DCB FEM model

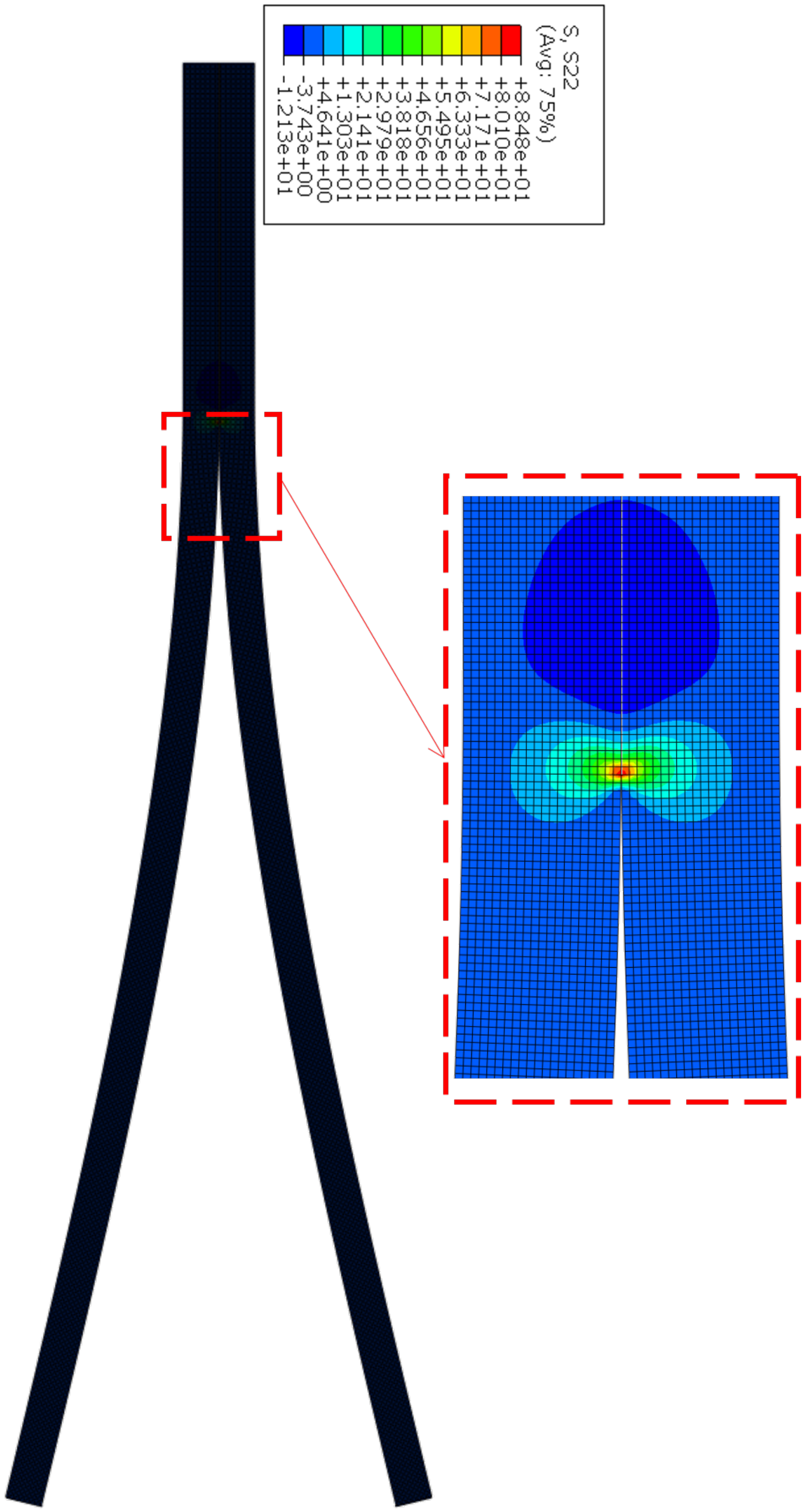
S, S22
(Avg: 75%)
+8.848e+01
+8.010e+01
+7.171e+01
+6.333e+01
+5.495e+01
+4.656e+01
+3.818e+01
+2.979e+01
+2.141e+01
+1.303e+01
+4.641e+00
-3.743e+00
-1.213e+01

Figure B.1 DCB FEM model